3-2008

Velocity Estimate Following Air Data System Failure

Scott A. Mclaren

VELOCITY ESTIMATE FOLLOWING AIR DATA SYSTEM FAILURE

THESIS

Scott A. McLaren, Major, USAF

AFIT/GAE/ENY/08-M21

DEPARTMENT OF THE AIR FORCE
AIR UNIVERSITY

AIR FORCE INSTITUTE OF TECHNOLOGY

Wright-Patterson Air Force Base, Ohio

The views expressed in this thesis are those of the author and do not reflect the official policy or position of the United States Air Force, Department of Defense, or the U.S. Government.

AFIT/GAE/ENY/08-M21

VELOCITY ESTIMATE FOLLOWING AIR DATA SYSTEM FAILURE

THESIS

Presented to the Faculty

Department of Aeronautics and Astronautics

Graduate School of Engineering and Management

Air Force Institute of Technology

Air University

Air Education and Training Command

In Partial Fulfillment of the Requirements for the

Degree of Master of Science in Aeronautical Engineering

Scott A. McLaren, BS

Major, USAF

March 2008

AFIT/GAE/ENY/08-M21

VELOCITY ESTIMATE FOLLOWING AIR DATA SYSTEM FAILURE

Scott A. McLaren, BS

Major, USAF

Approved:

Paul A. Blue, Maj, USAF (Thesis Advisor)	27 Feb 08 Date
Bradley S. Liebst (Committee Member)	27 Feb 08 Date
Donald L. Kunz (Committee Member)	27 Feb 2008 Date
Timothy R. Jorris, Maj, USAF (Committee Member)	27 Feb 08 Date

Abstract

Modern high performance aircraft can provide amazing performance due in part to their advanced flight control systems that require gain scheduling to provide optimum performance over a huge flight envelope. In modern fighter aircraft, this gain scheduling is a function of airspeed, and almost all of the research involving aircraft gain scheduling assumes aircraft airspeed to be a known quantity. The purpose of this research was to investigate a method of determining an aircraft's airspeed in the event of total air data system failure. The process began by combining known aircraft information following an air data system failure to determine an estimate of the inertial velocity. Then, an innovative airspeed estimation algorithm was developed using Kalman filtering with geometric concepts based on the velocity triangle that defines the relationship between airspeed, wind speed, and groundspeed. This algorithm used the inertial velocity and heading and provided a real-time estimate of the current wind and the aircraft's true airspeed, which can be used in the flight control system for gain scheduling. The true airspeed estimate was also converted to calibrated airspeed for display in the cockpit to provide the pilot situational awareness.

The culmination of this effort resulted in a successful flight test program as part of a Test Management Project at the United States Air Force Test Pilot School. The project consisted of two ground test and six flight test evaluation sorties. The average true airspeed error from the estimator algorithm during in-flight maneuvers was determined to be 12 knots, non-divergent, and minimally variable. The results of this research clearly showed the potential of the algorithm to determine an aircraft's airspeed in the event of an air data system failure. Recommendations for future research and improvements to the operation of the velocity estimator algorithm are discussed.

To my wife for making it possible to get this far!

Acknowledgments

I would like to express my appreciation to my thesis advisor, Maj Paul Blue, for his guidance and support throughout the course of this thesis effort. The insight and sincere effort to make it to the end deserve my applause and sincere appreciation.

I would also like to thank Michael Nielsen for his time and technical knowledge. The implementation of the inertial and wind estimators would not have been possible without his efforts.

Finally, I thank Mr. Russ Easter. His technical expertise and dedication were tremendous when faced with the impossible task.

Scott A. McLaren

Table of Contents

Page

List of Figures

Page

List of Tables

Page

VELOCITY ESTIMATE FOLLOWING AIR DATA SYSTEM FAILURE

1. Introduction

1.1 Motivation

Modern advanced fighter aircraft represent the culmination of over fifty years of aircraft flight dynamics and controls research and development. Pilot control inputs are translated by flight control systems into aircraft performance that is optimized to the edge of a safe operating envelope for both the pilot and the aircraft. In the author's opinion, based on 1,300 hours of experience flying the F-16 and the 10 hours of flight testing conducted for this thesis on a variable stability Learjet, modern flight control systems do an amazing job at providing aircraft performance that closely match the pilot's desired aircraft response throughout the aircraft's large flight envelope. Modern fighter aircraft can be flown from an abrupt and violent maneuver at nine times the force of gravity to a precise tracking maneuver in just seconds when commanded by the pilot. Flight control systems with advanced gain scheduling techniques make the connection between the desired response from the pilot and the resulting precise aircraft performance possible, even for inherently unstable aircraft.

In order to make such optimized dynamic flight possible, the flight control system of the aircraft must receive inputs about the environment in which it is flying. Inputs to the flight control system are made possible by aircraft sensors that relay pitot-static information from the aircraft's air data system and inertial measurement information from the Inertial Navigation System (INS). Appropriate flight control gain settings can

be scheduled using this information to optimize control for any flight condition. In the absence of some combination of input information, such as in the case of aircraft air data system failure, appropriate gain settings are not as easily obtained. In fact, to ensure safe and controlled flight remains possible in the event of air data system failures, flight control of the aircraft must be limited to a less than optimal, degraded performance state.

The gain scheduling for the degraded performance state is known as standby gain scheduling. Because of an aircraft system failure, a necessary component of the current flight condition is unknown. If air data input values from current flight conditions are unknown, the aircraft flight control computer cannot determine its true velocity and altitude, and cannot properly schedule gain settings. Therefore, standby gain settings, usually in the form of a single, default solution for a certain airspeed and altitude, are forwarded to the flight control computer for continued safe operation. If the aircraft is operated at a different airspeed or altitude than the one corresponding to the standby gains, its performance will be limited and the response of the aircraft may not match the pilot's expectations. The default method of standby gain scheduling is a compromise solution that is practical for flight conditions up to and including the default values for airspeed and altitude. Limited performance is traded for gain settings that allow for safe flight operations over a wider expanse of flight conditions.

To further complicate the degraded operating mode, the standby gain schedule may not be set correctly by the flight control computer for the current phase of flight. Three typical phases of flight for standby gain settings are cruise, air refueling, and takeoff and landing gains. In the event of air data system failure during cruise conditions

for example, the flight control computer could default to air refueling gains. This could cause an aircraft response that feels abrupt to the pilot. The pilot would then be required to set cockpit controls to correct the standby gain schedule based on the feel of the aircraft response to control inputs. Based on which portion of the mission the failure occurred, the pilot may have limited time available to remove his hands from the flight controls and make the required switch actuation to find the correct standby gain setting. The solution offered here is to estimate the aircraft's airspeed using information still available from the aircraft and use the estimated operating condition for gain scheduling.

1.2 Problem Statement

The purpose of this work is to develop an algorithm to accurately estimate the unknown air data information resulting from an aircraft system failure. The algorithm will use inertial data to estimate the aircraft's encountered wind and true airspeed. The true airspeed will be continuously updated, converted to calibrated airspeed, and available for gain scheduling and display in the cockpit. The goal of this research is to develop a velocity estimate algorithm and conduct flight tests to determine the potential of its use for gain scheduling in the absence of air data.

1.3 Research Objectives

Inertial and Global Positioning System (GPS) sensors cannot measure an aircraft's relative flight conditions; as a result, if an aircraft's air data system fails, it is not possible to directly measure its true airspeed, making automatic gain scheduling impossible. The objective of this research is to develop an algorithm that will use inertial

or GPS sensors to automatically generate an estimate of airspeed to be used as an input for gain scheduling in the event of an air data system failure.

1.3.1 Develop an Algorithm to Estimate True Airspeed

Available information following an air data system failure will be used as inputs into the developed algorithm. The algorithm will continuously estimate the aircraft's true airspeed.

1.3.2 Validate the Airspeed Algorithm with Simulation and Flight Data

The airspeed estimate from the developed algorithm will be compared to airspeeds from a Learjet simulator and true airspeeds recorded from Learjet flight data.

1.3.3 Assess the Potential of Using Estimated Airspeed for Gain Scheduling

A gain scheduled stick force gradient will be developed for the variable stability Learjet used at the United States Air Force Test Pilot School. This gain scheduled system will incorporate the estimated airspeed obtained from the algorithm developed in the first objective, so its potential for use in gain scheduling can be assessed during flight testing. Pilot comments will be collected while performing operationally representative maneuvers using the estimated airspeed for gain scheduling.

1.4 Approach

The starting point for this research was to define what information would still be available for velocity calculations after the time of air data system failure. The available information includes a last known aircraft state prior to the failure, aircraft accelerations and angular rates from the flight control computer, and position from GPS. The accelerations and rates are used to form a GPS updated inertial state estimate of position,

velocity, and attitude. Then, the inertial state is used along with the geometric relationship between airspeed, wind speed, and groundspeed to develop an algorithm that provides estimates of the current wind and airspeed. Due to the multi-axis, unbounded nature of flight, an aircraft will continually get farther and farther away from the flight conditions that existed at the time of air data system failure. Consequently, the last known wind velocity at the time of air data system failure will only supply accurate true velocity information for a relatively short time period. Therefore, the algorithm was optimized to continuously provide the smallest error from actual wind magnitude and direction. All of the algorithms developed were incorporated into the velocity estimate (VEST) algorithm, which provides the inertial, wind, and true velocity estimate from available aircraft information. The next step was to assess the accuracy of the VEST algorithm in aircraft simulation. Inertial and wind portions of the algorithm were optimized to contend with simulated flight conditions. The final step was to assess the algorithm performance in flight test. During flight testing, the airspeed estimates obtained from the VEST algorithm were compared to air data provided true airspeed, and were used to assess the potential of gain scheduling using an estimated airspeed.

1.5 Preview of Results and Implications

An innovative airspeed estimate algorithm was developed using geometric concepts based on the velocity triangle that defines the relationship between airspeed, wind speed, and groundspeed. The results of this research clearly show the potential of the VEST algorithm to determine an aircraft's airspeed in the event of an air data system failure. The average true airspeed error from the VEST algorithm during in-flight

maneuvers was determined to be 12 knots, non-divergent, and minimally variable. Therefore, the estimated airspeed from the VEST algorithm makes a viable substitute for true airspeed in gain scheduling, and can be displayed to the pilot to provide situational awareness.

A new method of backup gain scheduling could be made possible by this research. Current augmented aircraft gain schedules work from a two-tiered methodology where primary flight condition dependent gains are used for normal operating conditions, and standby gains are used for the baseline default, back up settings. When air data information is not available, current airspeed and altitude information is not displayed in the cockpit, and standby gains replace primary flight control gains. Airspeed and altitude information are required for more effective mission accomplishment and safer recovery. Flight in a standby gain scheduling mode could result in poor aircraft performance when better performance is desired. This research incorporates an alternative input to gain scheduling algorithms. Instead of a baseline default airspeed value used for backup gain scheduling, an accurately estimated airspeed could bring aircraft performance back up to more effective levels. Then, a three-tiered gain scheduling methodology could be used – primary mode: standard gains scheduled with true airspeed for normal operating conditions, secondary mode: standard gains scheduled with estimated airspeed for air data system failures, and tertiary mode: standby gains using the backup default settings.

1.6 Thesis Overview

A background of theory and concepts used during this research is presented in the next chapter. The theory and concepts as applied to VEST algorithm development are presented in Chapter 3. Chapter 4 shows the theory and specific aircraft simulation results. Flight test methodology and algorithm results are presented in Chapter 5. Research conclusions and future application directions are discussed in Chapter 6. The appendices provide detailed information on developed algorithm Matlab® Simulink® block diagrams and time history error plots from simulation and flight test.

2. Background

2.1 Overview

The purpose of this Chapter is to provide a review of basic theory applicable to the velocity estimate (VEST) algorithm developed and analyzed in the remainder of this thesis. Concepts needed for initial algorithm design in terms of reference frames, equations of motion, and velocity triangles describing the vector relationship between airspeed, wind speed, and groundspeed are discussed. Estimation techniques introduced here will be further developed in Chapter 3 to determine algorithm performance in simulation and flight test.

2.2 Aircraft Dynamic Motion

The dynamic motion of an aircraft can be described by a variety of different modeling techniques. Similarly, the specific model chosen to predict the aircraft motion can depend on just as many different specifications such as the aircraft type to be modeled, the flight conditions to be expected, fidelity of the model that is required, application of model outputs, and level of operator and airframe interaction. Regardless of the modeling technique or application used to describe the aircraft motion, a reference frame must be established to build and further describe the aircraft's movement. The equations of motion can then be developed to describe the translational and rotational aircraft movement. From the equations of motion, specific model requirements and applications can be further developed and refined.

2.2.1 Reference Frames

The flight of an aircraft through the air mass can be described in specific coordinate systems [Nelson 1998]. To determine how the aircraft is moving according to Newton's laws, a non-rotating non-accelerating reference frame needs to be established [Kayton and Fried 1997]. The Earth Centered Inertial (ECI) frame has its origin at the center of the earth, the z-axis points to the north star, the x-axis is on the equatorial plane and points to the first star of Aires, and the y-axis is orthogonal to both and lies on the equatorial plane. The ECI frame is considered non-rotating in inertial space relative to the stars [Kayton and Fried 1997].

The following reference frames can be used to define the position of the aircraft on the earth. The Earth Centered Earth Fixed (ECEF) frame has its origin at the center of the earth, the z-axis points to the north pole, the x-axis points to the Greenwich meridian on the equatorial plane, and the y-axis points to ninety degrees east longitude on the equatorial plane. The North East Down (NED) frame is a local reference frame used commonly for navigation [Stevens and Lewis 2003]. Its origin is fixed to the surface of the Earth, the z-axis points down normal to the spheroid, the x-axis points to north and the y-axis points to east.

The Body Fixed (BF) frame is rigidly fixed to the aircraft and is rotating and translating with the aircraft through the air mass. Its origin is at the aircraft's center of gravity, the z-axis points out the bottom of the aircraft, the x-axis points in the direction of the nose of the aircraft, and the y-axis points in the direction of the right wing. The Stability frame is similar to the BF frame in that it also has its origin at the aircraft's

center of gravity and its y-axis pointing in the direction of the right wing; however, the x-axis and z-axis of the Stability frame are rotated about the y-axis from the BF frame by the angle of attack. Further, the Wind axis is described by rotating the Stability axis about its z-axis by the angle of sideslip. Using these reference frames, the position and motion of the aircraft can be described over any point of the Earth. Equations of motion describing the aircraft's dynamics are typically derived for a reference frame such as the BF frame that is fixed to the aircraft [Nelson 1998]. Moreover, the frame that is most useful for describing the aircraft motion of interest is used as a starting point for the equations of motion. In order to sum all forces and moments defined in different axis systems, those forces and moments must be rotated to a common axis system. The aircraft's orientation defined in one reference frame can be described in other reference frames through a sequence of ordered rotations.

For example, a rotation from the NED frame to the BF frame can be accomplished using Euler angles [Nelson 1998]. Euler angles are angular rotations describing the roll (Φ) about the x-axis, pitch (Θ) about the y-axis, and yaw (Ψ) about the z-axis. The order of rotation from NED to BF is yaw, pitch, then roll. The order of rotation from BF to NED is just the opposite roll, pitch, then yaw. Similarly, the BF frame is rotated in pitch through the angle of attack to the Stability frame, and the Stability frame is rotated in yaw through the sideslip angle to the Wind frame.

2.2.2 Equations of Motion

The aircraft equations of motion (EOM) are used to describe bare airframe responses to specific control surface deflections and aerodynamic forces, changes in

thrust levels, and changes in atmospheric conditions and gravity. The aircraft response will be calculated in translation and rotation. These translational and rotational responses are defined by movement along or about a specific axis system as described above. The starting point in defining the translational and rotational movement is Newton's Second law of motion. For translation, the force is proportional to the time rate of change of the momentum

$$\vec{F} = \frac{d}{dt}\left(m\vec{V}\right), \tag{1}$$

and for rotation, the moment is proportional to the time rate of change of the angular momentum [Nelson 1998]

$$\vec{M} = \frac{d}{dt}\left(\vec{H}\right). \tag{2}$$

The basic forces and moments acting on an aircraft can be derived [Nelson 1998] to describe aircraft motion. In the BF frame, the forces and moments acting on the aircraft are illustrated below:

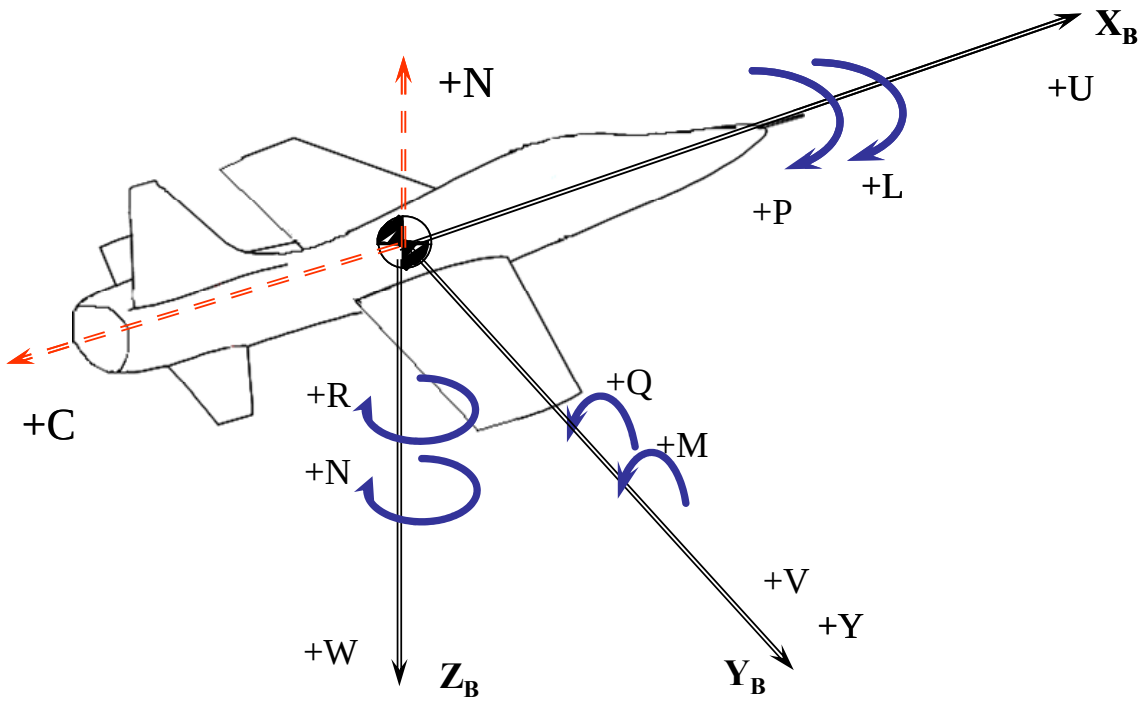

Figure 2.1. Aircraft Forces and Moments

where X_B, Y_B, and Z_B describe the BF frame axes; C, Y, and N represent the aerodynamic forces; L, M, and N represent the moments acting on the aircraft; U, V, and W represent the translational velocities; and P, Q, and R represent the rotational velocities. A few assumptions are made to develop the typical Six Degrees of Freedom (6 DOF) aircraft equations of motion [Stevens and Lewis 2003].

1. The mass of the aircraft does not change over a specified short period of time
2. The aircraft is a rigid body
3. A flat, non-rotating Earth reference frame is a suitable inertial reference frame
4. The atmosphere is at rest
5. The BF x-z plane is a plane of symmetry

Applying these assumptions in the BF frame, the translational equations become [Nelson 1998]

$$\begin{aligned}
\dot{U} &= -QW + RV - \frac{C}{m} + \frac{T_X}{m} - g\sin\Theta \\
\dot{V} &= -RU + PW + \frac{Y}{m} + \frac{T_Y}{m} + g\cos\Theta\sin\Phi \\
\dot{W} &= -PV + QU - \frac{N}{m} + \frac{T_Z}{m} + g\cos\Theta\cos\Phi
\end{aligned} \quad , \tag{3}$$

where g is the acceleration due to gravity, and m is the aircraft mass, and T is the thrust force. The rotational equations become

$$\begin{aligned}
\dot{P} &= \frac{I_{yy} - I_{zz}}{I_{xx}} QR + \frac{I_{xz}}{I_{xx}}\left(\dot{R} + PQ\right) + \frac{L_T}{I_{xx}} + \frac{L}{I_{xx}} \\
\dot{Q} &= \frac{I_{zz} - I_{xx}}{I_{yy}} PR - \frac{I_{xz}}{I_{yy}}\left(P^2 - R^2\right) + \frac{M_T}{I_{yy}} + \frac{M}{I_{yy}} \\
\dot{R} &= \frac{I_{xx} - I_{yy}}{I_{zz}} PQ + \frac{I_{xz}}{I_{zz}}\left(\dot{P} - QR\right) + \frac{N_T}{I_{zz}} + \frac{N}{I_{zz}}
\end{aligned} \quad , \tag{4}$$

where I_{xx}, I_{yy}, and I_{zz} are the mass moments of inertia and of the aircraft about the BF frame x, y, and z axes respectively, I_{XZ} is the product of inertia, and L_T, M_T, and N_T represent the moments acting on the aircraft due to thrust. These equations are known as the 6 DOF equations of motion [DoD 2002]. The 6 DOF equations are used to describe aircraft motion in flight simulators. The equations are six nonlinear coupled equations, for which there is no closed form solution. Flight simulators continuously integrate the equations from a set of given conditions to form a numerical solution that describes the aircraft motion [Stevens and Lewis 2003]. The 6 DOF equations can be further refined to

describe particular aircraft dynamics using additional assumptions such as trim conditions and linearization for transfer function analysis. The specific assumptions applied depend on the application and dynamics to be modeled and type of analysis being conducted.

For example, using stability derivative analysis, the aerodynamic forces *C*, *Y*, and *N* from the translational equations above can be expanded as follows [DoD 2002]:

$$\begin{aligned}
\dot{U} &= -QW + RV - \frac{\bar{q}S}{m}\left(C_{C_0} + \frac{2}{V_T} C_{C_u} U + C_{C_\alpha}\alpha + C_{C_{\delta_e}}\delta_e \right) + \frac{T_X}{m} - g\sin\Theta \\
\dot{V} &= -RU + PW + \frac{\bar{q}S}{m}\left(C_{Y_0} + C_{Y_\beta}\beta + C_{Y_{\delta_a}}\delta_a + C_{C_{\delta_r}}\delta_r \right) + \frac{T_Y}{m} + g\cos\Theta\sin\Phi \\
\dot{W} &= -PV + QU - \frac{\bar{q}S}{m}\left(C_{N_0} + \frac{2}{V_T} C_{N_u} U + C_{N_\alpha}\alpha + C_{N_{\delta_e}}\delta_e \right) + \frac{T_Z}{m} + g\cos\Theta\cos\Phi
\end{aligned} \quad . \qquad (5)$$

Additionally, if the aircraft is to be modeled in a straight and level, unaccelerated flight (SLUF) condition (and there is no thrust in the z-direction), then the rates are zero ($\dot{U} = \dot{V} = \dot{W} = P = Q = R = 0$) and the bank angle is zero ($\Phi = 0$). The $\dot{W}$ equation reduces to

$$0 = -\frac{\bar{q}S}{m}\left(C_{N_0} + \frac{2}{V_T} C_{N_u} U + C_{N_\alpha}\alpha + C_{N_{\delta_e}}\delta_e \right) + g\cos\Theta\,, \qquad (6)$$

and by rearranging,

$$\bar{q}S\left(C_{N_0} + \frac{2}{V_T} C_{N_u} U + C_{N_\alpha}\alpha + C_{N_{\delta_e}}\delta_e \right) = mg\cos\Theta\,. \qquad (7)$$

Recognizing that $C_N = C_{N_0} + \frac{2}{V_T} C_{N_u} U + C_{N_\alpha}\alpha + C_{N_{\delta_e}}\delta_e$, is the aerodynamic force normal to the x-y plane in the BF frame, and that the acceleration of gravity times the aircraft mass

is its weight, then

$$\bar{q}SC_N = Weight\cos\Theta. \tag{8}$$

In SLUF, the angle Θ is equal to the angle of attack. When $\bar{q}SC_N$ is rotated about the BF y-axis by the angle of attack , it is equal to the net lifting force, $\bar{q}SC_L$ in the Wind frame. By a similar rotation, the Wind frame portion of the right side of the equation is *Weight* . Equation 8 in the Wind frame then becomes $\bar{q}SC_L = Weight$. Therefore, the net lifting force, *lift*, is equal to the aircraft *weight*, and the familiar equation

$$Lift = Weight \tag{9}$$

is described from the 6 DOF equations of motion for a SLUF condition. Analyzing the $\dot{U}$ equation would reveal that thrust equals drag for an aircraft operating in a SLUF condition. In a similar manner, aircraft motion with changing inputs and flight conditions can be modeled in simulators.

2.3 Aircraft Systems

Modern fighter aircraft are capable of extreme levels of performance. Complex flight control computers smoothly blend pilot inputs into appropriate and acceptable flight control surface deflections to produce desired aircraft performance. Air data systems are one of many necessary components that contribute to producing such desired aircraft performance. To create the desired performance, the flight control computers take existing information from the environment to make appropriate gain scheduling routines [Stevens and Lewis 2003]. The gain scheduling routines optimize aircraft control surface deflections based on existing conditions. In the event of air data system

failure, gain scheduling cannot be optimized for actual conditions since actual conditions are unknown. Therefore, for safety of operation, the flight control computer determines an appropriate gain schedule whether the system is functioning normally or in a failure mode of operation.

2.3.1 Air Data Systems

The air data system determines the aircraft's airspeed, Mach number, altitude, and vertical velocity trend. Air data systems receive total and static pressure inputs from a pitot-static system. A typical pitot tube, as shown below, receives total pressure (P_T) from the open ended portion of the tube in the airstream. Static pressure (P_S) can be obtained from static pressure ports or holes either on the pitot tube or aircraft's fuselage oriented such that the ports are perpendicular to the airstream.

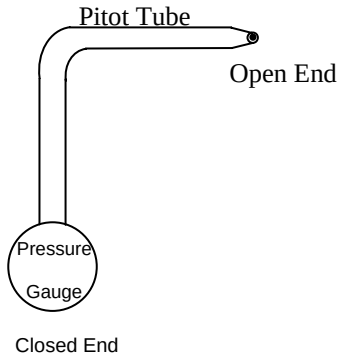

Figure 2.2. Pitot Tube

The pressure information can be converted directly to altitude, airspeed, Mach, and vertical velocity using calibrated gauges or indicator displays in the cockpit.

Alternatively, the total and static pressure information can be converted to airspeed, altitude, Mach, and vertical velocity in aircraft equipped with an air data system computer.

To display the aircraft's airspeed, the air data computer combines the pressure information described above with temperature information. Because the ambient temperature of the air surrounding the aircraft is difficult to measure [Anderson 2005], the air data computer uses sea level reference values from the standard atmosphere for airspeed calculations. Three airspeeds that can be determined are calibrated airspeed (V_C), equivalent airspeed (V_E), and true airspeed (V_T). Calibrated airspeed for subsonic, compressible flow [Erb 2005] is displayed in the cockpit as

$$V_C = \sqrt{\left(\frac{1}{\rho_{SL}}\right) 7 P_{SL} \left(\left(\frac{P_T - P_A}{P_{SL}} + 1 \right)^{\frac{2}{7}} - 1 \right)}, \tag{10}$$

where ρ_{SL} and P_{SL} are standard sea-level values of density and pressure respectively. P_A is the ambient pressure surrounding the aircraft. The exact ambient pressure is difficult to measure. Static pressure, as described above, is used to approximate the ambient pressure [Erb 2005]. The difference between the actual ambient pressure and the measured static pressure is called the position error of the instrument. The position error is calculated by flight testing and is applied along with the known mechanical instrument error to correct the measured static pressure to a more accurate ambient pressure value. The reference values for calibrated airspeed are sea level pressure and density. Calibrated airspeed does not change with changes in altitude. Therefore, a pilot can fly

the same final approach speed whether landing at sea level or at a higher pressure altitude.

Similarly, equivalent airspeed [Erb 2005] is defined as

$$V_E = \sqrt{\left(\frac{1}{\rho_{SL}}\right) 7 P_A \left(\left(\frac{P_T - P_A}{P_A} + 1 \right)^{\frac{2}{7}} - 1 \right)}. \tag{11}$$

The reference value for equivalent airspeed is sea level density. Equivalent airspeed is used to determine aircraft performance speeds such as stall speed that are altitude independent. The dynamic pressure, *q*, can be defined as [Erb 2005]

$$q = \frac{\rho_{SL} V_E^2}{2}. \tag{12}$$

Air loads correspond to a certain dynamic pressure and are independent of altitude. Therefore, equivalent airspeed for air load dependent tasks, such as lowering the landing gear and flaps, does not change with altitude.

True airspeed [Erb 2005] is defined by the following equation:

$$V_T = \sqrt{\left(\frac{1}{\rho_A}\right) 7 P_A \left(\left(\frac{P_T - P_A}{P_A} + 1 \right)^{\frac{2}{7}} - 1 \right)}. \tag{13}$$

True airspeed has no standard atmosphere reference values, and therefore changes with altitude. The density at current flight conditions must be available to directly calculate true airspeed. Air data computers use measured temperature and pressure to calculate the density using the equation of state. True airspeed is not used specifically by pilots, but is

essential for scheduling gains in the flight control system, and is useful in calculating groundspeed.

Mach number can be defined for subsonic flow [Kayton and Fried 1997] and for supersonic flow [Erb 2005] as follows:

when Mach < 1,

$$M = \sqrt{5\left(\frac{P_T - P_A}{P_A} + 1\right)^{\frac{2}{7}} - 1} \tag{14}$$

and when Mach > 1,

$$M = 0.881284\sqrt{\left(\frac{P_T - P_A}{P_A} + 1\right)\left(1 - \frac{1}{7M^2}\right)^{\frac{5}{2}}}\ . \tag{15}$$

The altimeter uses measured static pressure to determine the current aircraft pressure altitude. Pressure altitude for a given elevation changes on a given day due to local weather conditions. As in airspeed instruments, position error is present because of inexact ambient pressure measurements, and can be corrected. Using an altimeter setting of 29.92, the altitude that the sensed pressure would correspond to on a standard day is displayed in the cockpit [Anderson 2005].

The vertical velocity gauge uses multiple static pressure ports to display the vertical velocity. The static pressure from one of the ports is restricted to slow the effective change in static pressure as altitude varies. The resulting difference in static pressure is displayed on the cockpit indicator. The effect of restricting the flow to get a pressure differential results in a display of vertical velocity that lags behind actual

conditions [Erb 2005]. The vertical velocity can also be calculated in the air data computer from changes in static pressure with time [Erb 2005]. Such calculations can include much noise and require filtering prior to cockpit display. The filtering process also introduces lag to the computer calculated vertical velocity.

2.3.2 Velocity Triangle

Groundspeed describes how fast an aircraft is traveling over the ground. It is primarily used for navigation calculations such as time of arrival and wind corrected drift headings. The ground velocity vector (V_G) is typically determined from inertial measurements [Kayton and Fried 1997], and can be combined with the true airspeed vector (V_T) using the vector equation

$$V_G = V_T + V_W , \tag{16}$$

to determine the wind velocity vector (V_W). Using equation 16, the vector equation for V_G , a basic velocity triangle is shown below [Kayton and Fried 1997].

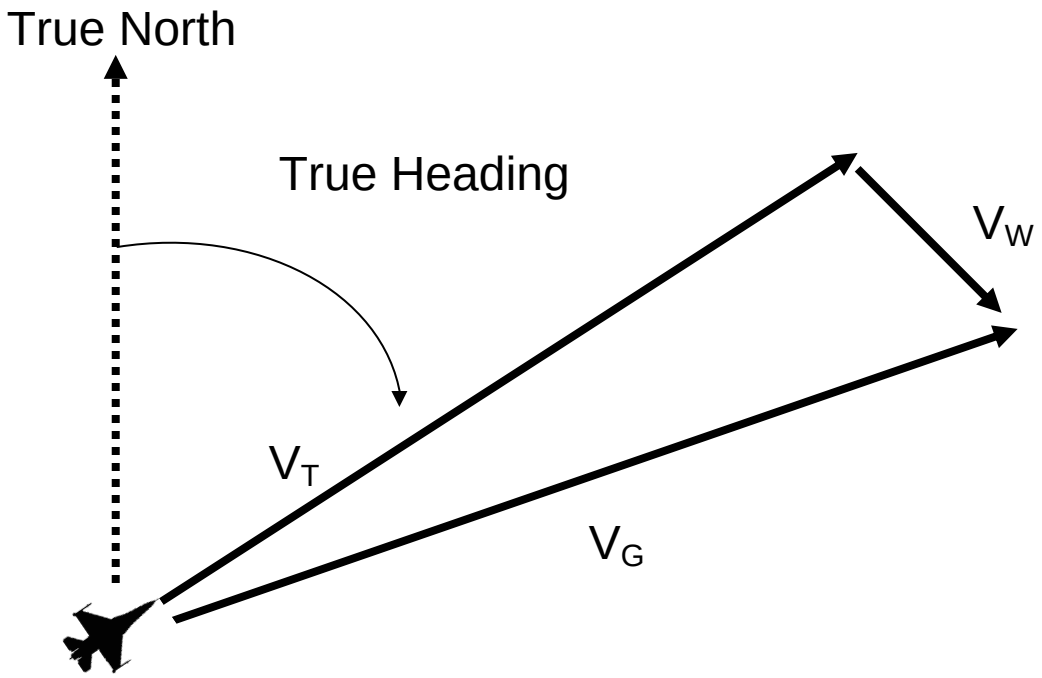

Figure 2.3. Velocity Triangle

In the velocity triangle, V_T represents the aircraft's true velocity vector. The aircraft points and flies along its true velocity vector under no sideslip conditions. The wind vector, V_W, diverts the aircraft's track over the ground by its direction and magnitude. The resultant ground velocity, V_G, is then made up of the vector sum of the true velocity and the wind velocity.

Going one step further, an aircraft's cockpit displayed true heading with zero sideslip is determined by the angle from true north to the true velocity vector, V_T. An aircraft's ground track heading is the angle from true north to the ground velocity vector, V_G. The difference between the two headings is a result of current wind conditions as shown in Figure 2.3.

2.3.3 Inertial Navigation System

Another aircraft system, the inertial navigation system (INS), is used to keep track of the aircraft's position, velocity, and attitude over time. Gyroscopes and accelerometers are fixed to the aircraft in a strapdown INS [Kayton and Fried 1997]. The gyroscopes and accelerometers track aircraft rotation and accelerations in the BF frame. Then, the INS transforms them from the BF frame to the NED frame. Once in the desired frame, the accelerations can be integrated to give velocity and position relative to a fixed position on the Earth. A modern INS typically incorporates position data from a Global Positioning System (GPS) receiver to reduce degraded position and velocity information over time [Kayton and Fried 1997].

The velocity output of the INS is the same as the groundspeed described in section 2.3.2. An INS relates movement of an object with respect to the Earth. Therefore a consistent and accurate model of parameters describing the Earth is necessary. The Department of Defense World Geodetic System 1984 (WGS-84) is one set of data that can be used to model the shape of the Earth. The WGS-84 estimates the Earth as an oblate spheroidal model. The following parameters are used in the WGS-84 model [Stevens and Lewis 2003]:

$$
\begin{aligned}
&a \equiv 6378.137 \quad km \\
&f = \frac{a-b}{a} \equiv \frac{1}{298.257223563} \\
&b = 6356.752 \quad km \\
&e = \frac{(a^2 - b^2)^{1/2}}{a} \approx 0.08181919 \\
&\omega_e = 7.2921150 \times 10^{-5} \quad rad/s \\
&GM \equiv 3986004.418 \times 10^8 \quad m^3/s^2
\end{aligned}
\tag{17}
$$

where a is the semi-major axis, b is the semi-minor axis, f is the flattening, e is the eccentricity, ω_e is the sidereal rate of rotation, and GM is the gravitation constant. The Earth's gravitational field varies as the model of the spheroid shape varies. Therefore, gravitation which is the combination of mass attraction and centrifugal force experienced by a body moving with the Earth's surface [Stevens and Lewis 2003], must be accounted for in an INS. When the gravitational field vector is combined with the Earth's rotation vector, the local gravity vector is

$$
m\mathbf{g}_l = m\mathbf{G} - m\boldsymbol{\omega}_{ei} \times \left(\boldsymbol{\omega}_{ei} \times \mathbf{p}_e\right) \tag{18}
$$

where $\mathbf{g}_l$ is the local gravity vector, $\mathbf{G}$ is the gravitational attraction, and $m\,\boldsymbol{\omega}_{ei} \times \left(\boldsymbol{\omega}_{ei} \times \mathbf{p}_e\right)$ is the centripetal acceleration [Stevens and Lewis 2003]. An INS will use the local gravity to manipulate force data measured on aircraft accelerometer sensors. The value used by the INS will be the sum of the inertial acceleration experienced by the body and the local gravity [Lin 1991]. In this way, the inertial velocity output of the INS corresponds to the aircraft's ground velocity.

In addition to position and velocity, the INS also keeps track of the aircraft attitude. Gyroscopes keep track of the rotation of the aircraft and drive an algorithm that maintains vehicle orientation in roll, pitch, and azimuth [Kayton and Fried 1997]. The aircraft's azimuth from true north corresponds to the true heading in the velocity triangle from section 2.3.2. The INS does not measure wind information directly, but can combine its inertial velocity calculation with true airspeed from the air data system to solve for current wind conditions [Lin 1991]. Using INS position, velocity, and attitude; along with air data measurements; airspeed, heading, and wind information, can be displayed in the cockpit. True airspeed can be sent to the flight control computer for use in gain scheduling so pilot inputs can be translated into desired aircraft responses.

2.3.4 Flight Control Gain Scheduling

From first flight to the breaking of the sound barrier, aircraft design and performance have both experienced tremendous change. As the performance envelope of the aircraft increased, the dependence on human power for flight controls gave way to mechanically assisted flight control actuators. Additionally, safe operation near the edges of the envelope required aircraft stability augmentation. This idea is developed in Stevens and Lewis, *Modern Aircraft Control* [Stevens and Lewis 2003]. Large changes in dynamic pressure over the operational envelope correspond to significant changes for coefficients in the EOMs that characterize the aircraft's motion. Aerodynamic coefficients change with Mach number and mass properties continuously change as fuel is consumed [Stevens and Lewis 2003]. These changes in aircraft dynamics create conditions that alter the aircraft's stability over its operating envelope.

To ensure that the desired performance is achieved despite changes in aircraft dynamics, the following gain scheduling technique is applied in aircraft flight controls. Aircraft motion variables are sensed and used to generate signals that are fed into control surface actuators [Stevens and Lewis 2003]. The feedback control varies with flight conditions to create a feedback control gain schedule. The scheduled flight control gains maintain desired stability and performance as flight conditions change. The scheduling dependent variable will normally be measured dynamic pressure and/or Mach number, which are functions of true airspeed [Stevens and Lewis 2003]. Modern aircraft employing highly augmented flight control systems can therefore provide the desired performance and keep an aircraft within desired stability criteria using a dynamic pressure (determined from true airspeed) dependent gain schedule.

2.3.5 Aircraft Failure Modes

Aircraft operating in dynamic environments and near the edge of their safe operating flight envelopes require a backup mode of operation to account for mechanical failures. In a basic sense, aircraft employing even the most advanced technology available, are mechanical structures that are vulnerable to failure at some level. Once the aircraft has shifted to an alternate mode of operation following an aircraft system failure or degradation, it is known to be operating in an aircraft failure mode. Therefore, resolutions to aircraft failure modes are necessary for safe flying operations.

Failure modes exist for many primary aircraft systems such as thrust, control, landing, and environmental systems. To reduce susceptibility to failures, some systems have redundant or multiple redundant components. Augmented control systems are

responsible for maintaining aircraft stability [Stevens and Lewis 2003]. Therefore, primary and backup modes of operation are typically required. The primary mode is used for normal operation when all information necessary for proper flight control is available. The backup mode is used when some portion of the required information, such as air data is unavailable. Most backup flight control systems for augmented aircraft use a default or assumed air data value for gain scheduling in order to keep the aircraft controllable in a safe operating envelope. The assumed value is referred to as a standby gain value, and the system is said to be employing a standby gain schedule. The standby gain schedule is not varying gains with flight conditions, but uses a single value for the scheduling dependent variable. Depending on how far actual air data conditions differ from the assumed standby value, less than optimum performance could result.

2.3.6 Pilot Interfaces

Controls are sent to avionics systems through many ways. Traditional controls have dedicated panels throughout the cockpit. Some panels are within arm's reach similar to a radio volume in an automobile. Other panels are more difficult to access, and may even require crew members other than the pilot for access in flight. On the opposite extreme, some avionics can be controlled by use of switches and knobs that are located directly on the flight controls. These avionics allow the pilot to maintain control of the aircraft and have control of the avionics at the same time. Avionics employing this type of control are described as using a Hands on Throttle and Stick (HOTAS) type arrangement. Multiple functions and controls can be operated by each finger. HOTAS systems in a fighter aircraft give the pilot control of various aircraft, communication, and

weapon functions in a demanding and hostile environment [Sanders 1993]. Time critical communications, weapons functions, and dynamic maneuvers can be accomplished simultaneously.

HOTAS systems offer many advantages over non-HOTAS systems [Sanders 1993]. The operator does not have to observe the control to operate it. Hands remain in contact with primary flight controls throughout critical operations. Auxiliary controls are available without loss of physical contact with primary controls. Any remaining controls require the pilot to remove hands from the primary flight controls, possibly require attention to be focused inside the cockpit, and result in slower reaction time to events occurring outside the cockpit.

2.4 Dynamic Inversion

Wind velocity can be estimated using the velocity triangle from section 2.3.2, and a known ground velocity vector to determine true velocity. Another method can be used to solve for true velocity directly using dynamic inversion for parameter estimation. The dynamic motion of an aircraft can be described by a combination of linear or nonlinear equations. Numeric techniques used to solve these equations could be time consuming and inefficient for real time implementation. Dynamic inversion is a technique that can be used as an alternate solution method to provide an estimate of true velocity. The background theory for dynamic inversion applied to controls is presented first, and the concept applied to parameter estimation is presented in section 2.4.2.

2.4.1 Dynamic Inversion for Control

An aircraft nonlinear model can be characterized as follows:

$$\begin{aligned} \dot{\mathbf{x}} &= F\left(\mathbf{x},\mathbf{u}\right) \\ \mathbf{y} &= H(\mathbf{x}) \end{aligned} \tag{19}$$

where $\mathbf{x}$ represents the state vector, $\mathbf{u}$ is the control vector, and $\mathbf{y}$ is the output vector. For the case where there are small perturbations from the trim condition, the function F is affine in $\mathbf{u}$ [Ito 2002]. Now the expression can be re-written as

$$\dot{\mathbf{x}} = f(\mathbf{x}) + \mathbf{g}(\mathbf{x})\mathbf{u}\,. \tag{20}$$

If $\mathbf{g}(\mathbf{x})$ is invertible for all values of $\mathbf{x}$, then $\mathbf{u}$ can be solved for as

$$\mathbf{u} = \mathbf{g}^{-1}(\mathbf{x})\left[\dot{\mathbf{x}} - f(\mathbf{x})\right]. \tag{21}$$

This gives an expression for the control vector as a function of the aircraft state and its derivative. If the desired state derivative is used to replace the actual derivative, the desired command based on the aircraft state can be determined as

$$\mathbf{u}_{command} = \mathbf{g}^{-1}(\mathbf{x})\left[\dot{\mathbf{x}}_{desired} - f(\mathbf{x})\right]. \tag{22}$$

The principle is shown in block diagram form below [Ito 2002].

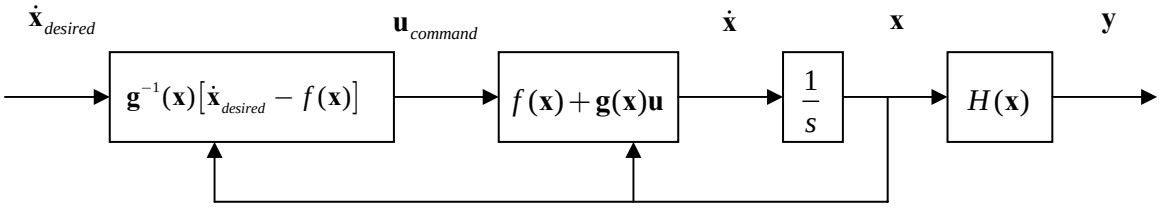

Figure 2.4. Dynamic Inversion Block Diagram

2.4.2 Dynamic Inversion for Parameter Estimation

The concept described in 2.4.1 is typically put to use for nonlinear control, but can also be used for parameter estimation. To do this, an equation that is an implicit function of the parameter to be estimated is inverted as described above to obtain a new function that gives the value of the parameter as a function of measurable variables. If the following represents the nonlinear equations of motion for a system,

$$\dot{\mathbf{x}} = a(\mathbf{x}) + b(\mathbf{x}) \cdot u \tag{23}$$

where $\mathbf{x}$ represents a state vector, and u is a parameter (or vector of parameters) to be estimated. Then if $\dot{\mathbf{x}}$ and $\mathbf{x}$ can be measured, the concept of dynamic inversion can be used to obtain an expression to estimate u;

$$u = \frac{1}{b(x)}\left(\dot{\mathbf{x}} - a(\mathbf{x})\right). \tag{24}$$

Note that dynamic inversion can also be applied to equations that are not affine in u, but it is not as straight forward.

To demonstrate the concept of dynamic inversion for parameter estimation, the procedure is applied below to obtain an angle of attack estimator. An aircraft linear

longitudinal pitching moment equation [Nelson 1998], is given by

$\dot{q} = M_{\alpha}\alpha + M_{q}q + M_{\delta_e}\delta_e$, which can be inverted to solve for the angle of attack as

$$\alpha = \frac{\dot{q} - M_{q}q - M_{\delta_e}\delta_e}{M_{\alpha}}. \tag{25}$$

2.5 Simultaneous Linear Equations

A set of simultaneous linear equations can be used to estimate a solution to the velocity triangle relationship from section 2.3.2. The matrix representation of a set of linear equations can be written in the form $\mathbf{Ax} = \mathbf{b}$ where $\mathbf{A}$ is a known matrix with real or complex coefficients and has *m* rows and *n* columns. When the $\mathbf{b}$ vector is known with *m* rows and one column, $\mathbf{x}$ is the required solution vector with *n* rows and one column. The set of linear equations has a unique solution when $m = n$ and $\mathbf{A}$ is nonsingular [Wylie 1960]. The typical solution uses matrix inversion and takes the form $\mathbf{x} = \mathbf{A}^{-1}\mathbf{b}$.

2.5.1 Over-determined Case

The over-determined case occurs when there are more equations than unknowns, or when the $\mathbf{A}$ matrix takes on the form $m > n$. There will be no solution if the equations are inconsistent, that is if the $\mathbf{b}$ vector components are measured inaccurately or the relationship assumed to exist between $\mathbf{A}$ and $\mathbf{b}$ is oversimplified or incorrect [Brogan 1991]. In this case, an approximate solution to the $\mathbf{x}$ vector can be determined. The least squares solution method places equal weight on each equation assuming that any errors will average out to produce a good approximation for $\mathbf{x}$. The error vector $\mathbf{e}$ is

introduced as $\mathbf{e} = \mathbf{b} - \mathbf{A}\mathbf{x}$ and an $\mathbf{x}$ can be found that minimizes the sum of the squares of the $\mathbf{e}_i$ components [Brogan 1991], as

$$\|\mathbf{e}\|^2 = (\mathbf{b} - \mathbf{A}\mathbf{x})^T (\mathbf{b} - \mathbf{A}\mathbf{x}). \tag{26}$$

By calculus of variations [Boas 2006], $\|\mathbf{e}\|^2$ can be minimized by $\mathbf{x}$ in the form

$$\mathbf{x} = (\mathbf{A}^T \mathbf{A})^{-1} \mathbf{A}^T \mathbf{b}. \tag{27}$$

2.5.2 Weighted Least Squares

A weighted least squares approximation for $\mathbf{x}$ can be determined when all equations are used but some equations are determined more reliable than others. Here a covariance matrix $\mathbf{R}$ is used to represent the noise on the vector $\mathbf{b}$ [Brogan 1991], and $\mathbf{x}$ minimizes the relationship

$$\mathbf{e}^T \mathbf{R}^{-1} \mathbf{e} = (\mathbf{b} - \mathbf{A}\mathbf{x})^T \mathbf{R}^{-1} (\mathbf{b} - \mathbf{A}\mathbf{x}). \tag{28}$$

Using the method of orthogonal projections, the weighted least squares solution takes the form [Brogan 1991]

$$\mathbf{x} = (\mathbf{A}^T \mathbf{R}^{-1} \mathbf{A})^{-1} \mathbf{A}^T \mathbf{R}^{-1} \mathbf{b}. \tag{29}$$

2.5.3 Recursive Weighted Least Squares

Instead of using all equations together in one batch solution for $\mathbf{x}$, a recursive weighted least squares method can be found using each new set of data as it is received. For this case, a set of *m* equations,

$$\mathbf{z}_k = \mathbf{A}\mathbf{x} + \mathbf{e}, \tag{30}$$

can be solved using the weighted least squares estimate for $\mathbf{x}$. Here, the solution $\mathbf{x}$ is of the same form as the weighted least squares solution described above, but there is a new solution for each new set of data. The solution is denoted $\mathbf{x}_k$, and takes the form

$$\mathbf{x}_k = \left(\mathbf{A}^T\mathbf{R}^{-1}\mathbf{A}\right)^{-1}\mathbf{A}^T\mathbf{R}^{-1}\mathbf{z}_k. \tag{31}$$

If additional data for **z** becomes available, then

$$\mathbf{z}_{k+1} = \mathbf{H}_{k+1}\mathbf{x}_k + \mathbf{e}_{k+1} \tag{32}$$

where $\mathbf{H}_{k+1}$ represents the matrix **A** from equation 30 that corresponds to $\mathbf{z}_{k+1}$. Then, a new estimate of $\mathbf{x}$ can be obtained to minimize

$$J = \begin{bmatrix}\mathbf{e}^T & \mathbf{e}_{k+1}^T\end{bmatrix}\begin{bmatrix}\mathbf{R}^{-1} & \mathbf{0}\\ \mathbf{0} & \mathbf{R}_{k+1}^{-1}\end{bmatrix}\begin{bmatrix}\mathbf{e}\\ \mathbf{e}_{k+1}\end{bmatrix} \tag{33}$$

in the form of $\mathbf{x}_{\mathbf{k+1}}$. Here, $\mathbf{R}_{k+1}^{-1}$ is the weighting matrix applied to the new data $\mathbf{z}_{k+1}$. Then the solution using new data is of the form

$$\mathbf{x}_{k+1} = \mathbf{x}_k + \mathbf{K}_{k+1}\left[\mathbf{z}_{k+1} - \mathbf{H}_{k+1}\mathbf{x}_k\right] \tag{34}$$

where $\mathbf{K}_{k+1} = \mathbf{P}_k\mathbf{H}_{k+1}^T\left[\mathbf{H}_{k+1}\mathbf{P}_k\mathbf{H}_{k+1}^T + \mathbf{R}_{k+1}\right]^{-1}$ and $\mathbf{P}_k \triangleq \left(\mathbf{A}^T\mathbf{R}^{-1}\mathbf{A}\right)^{-1}$,which is available from $\mathbf{x}_k$. If the process continues and more equations are needed, then the expression

$$\mathbf{P}_{k+1} = \mathbf{P}_k - \mathbf{K}_{k+1}\mathbf{H}_{k+1}\mathbf{P}_k \tag{35}$$

is also needed [Brogan 1991].

2.5.4 Kalman Filter

When data are received sequentially over time, each new group of data can be used to improve the estimate of $\mathbf{x}$. In this case, the $\mathbf{P}_{k+1}$ and $\mathbf{K}_{k+1}$ presented above become very small. Then, corrections made to $\mathbf{x}_k$ in order to determine $\mathbf{x}_{k+1}$ get small regardless of new measurement values. So to prevent the estimate from failing to respond to new measurement values, data de-weighting can be used. A new matrix $\mathbf{M}_k$ is defined as $\mathbf{M}_k = \mathbf{P}_k + \mathbf{Q} \cdot \Delta t$ for additive de-weighting and is used in place of $\mathbf{P}_k$ in equation 35, where Δt is the time between samples. The new form of $\mathbf{P}_{k+1}$ becomes

$$\mathbf{P}_{k+1} = \mathbf{M}_k - \mathbf{M}_k \mathbf{H}_{k+1}^T \left[\mathbf{H}_{k+1} \mathbf{M}_k \mathbf{H}_{k+1}^T + \mathbf{R}_{k+1} \right]^{-1} \mathbf{H}_{k+1} \mathbf{M}_k \tag{36}$$

When the $\mathbf{P}$, $\mathbf{Q}$, and $\mathbf{R}$ matrices are given the appropriate statistical interpretation [Brogan 1991], then the recursive equations presented above represent an example of discrete Kalman filtering equations. Kalman filter theory is used to estimate state variables of linear systems based on noisy measurements of output variables [Brogan 1991]. The assumption is that all error states can be modeled as zero mean noise processes with known variances, power spectral densities, and time correlation parameters so that error quantities and measurement noises are random processes with a known correlation structure [Kayton and Fried 1997].

An extended Kalman filter may be employed when the system dynamics are represented more appropriately using a nonlinear model. Let the nonlinear **h** replace the linear **H** relationship from equation 32 as follows [Maybeck 1982]

$$\mathbf{z}_{k+1} = \mathbf{h}_{k+1}(\mathbf{x}) + \mathbf{e}_{k+1} \tag{37}$$

so that a linearization of the nonlinear $\mathbf{h}(\mathbf{x})$ with respect to **x** yields a Jacobian matrix $\mathbf{H}_{k+1}$, which can be used to provide a perturbation measurement model [Maybeck 1982]

$$\delta\mathbf{z}_{k+1} = \left[\mathbf{H}_{k+1}\right]\delta\mathbf{x} + \mathbf{e}_{k+1}. \tag{38}$$

The development of the extended Kalman filter [Maybeck 1982] can be shown to change the update equation for $\mathbf{x}_{k+1}$ as shown above (equation 34) to be of the form

$$\mathbf{x}_{k+1} = \mathbf{x}_k + \mathbf{K}_{k+1}\left[\mathbf{z}_{k+1} - \mathbf{h}_{k+1} - \mathbf{H}_{k+1}\mathbf{x}\right]. \tag{39}$$

2.6 Summary

The ideas developed in this chapter were used to provide a background of mathematical concepts and aircraft system interactions. Each basic concept was used either in the development or testing of the VEST algorithm. The general theory will be applied to specific algorithm construction in the following chapters.

3. Methodology

3.1 Overview

The purpose of this chapter is to show how basic concepts presented in Chapter 2 were used to develop the VEST algorithm. Multiple approaches were used to refine the wind estimate portion of the algorithm. The refined designs were tested in simulation. Finally, necessary revisions were made and applications developed for algorithm flight testing.

3.2 Estimating True Airspeed from Wind Estimate

Recall that an air data system provides necessary information to a number of aircraft systems for primary modes of operation. If the air data system fails, systems that use air data may degrade operation or fail completely without input air data. The purpose of the VEST algorithm was to provide an estimate of the air data to avoid degradation or failure of systems that use air data inputs. The algorithm used a last known aircraft state prior to failure and flight control computer accelerations and rates to estimate the aircraft's true velocity. Specifically, accelerations and rates were continuously converted to inertial velocity and heading using a loosely coupled, GPS aided INS. This inertial estimator was separate from the aircraft's INS so that the VEST algorithm could be used as a stand alone system. Next it used the inertial velocity, which is also the ground velocity, and inertial heading to estimate the current wind velocity. The ground velocity was combined with the wind velocity to form the true velocity estimate as described in

section 2.3.2. Three approaches were developed to estimate the wind velocity: Three-Vector Approach, Two-Vector Approach, and Kalman Filter Approach.

3.2.1 Three-Vector Approach

An aircraft's encountered wind and true airspeed can be determined using three known ground velocity vectors [Gray 1998] by combining three velocity triangles from section 2.3.2. The tip of each ground velocity vector is superimposed to intersect at a single point. Assuming the true airspeed is held constant by a constant power setting and stabilized ground speed, and that the winds are constant, the true airspeed can be determined. As shown in the figure below [Gray 1998],

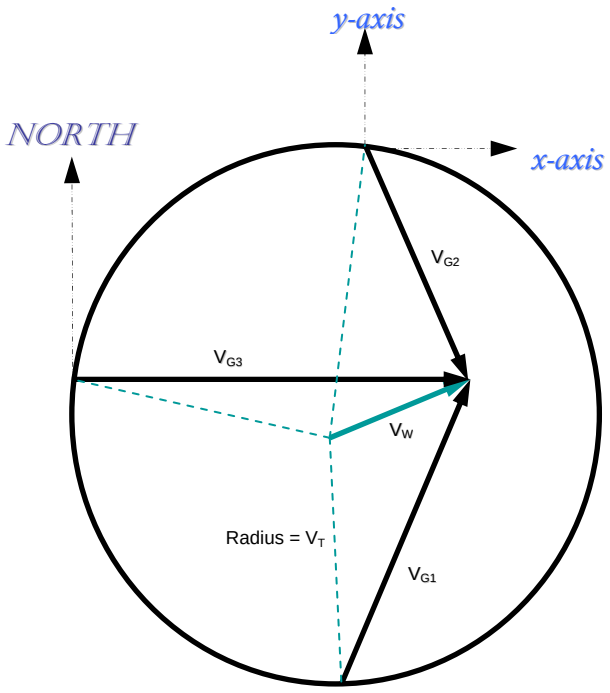

Figure 3.1. Three Combined Velocity Triangles

a constant wind and true airspeed can be determined trigonometrically by solving for the center and radius of a circle that intersects the tails of the three groundspeed vectors.

Then, the true airspeed is the radius of the circle, and the wind is the vector that completes each of the three velocity triangles by connecting the center of the circle to the tips of the groundspeed vectors [Gray 1998].

If many ground velocity vectors are sampled, a least squares approximation from section 2.5.1 can be used to find the circle that best fits all the ground velocities as oriented on the figure above. For the equation of a circle,

$$\left(x_i - x_c\right)^2 + \left(y_i - y_c\right)^2 = R^2 \tag{40}$$

x_c, y_c, and R can be found that best fit the set of points $\left(x_i, y_i\right), i = \left[1,...,n\right]$ defined by ground velocity vectors where n is the number of vectors sampled. The data are arranged such that

$$\begin{bmatrix} x_1 & y_1 & 1 \\ \vdots & \vdots & \vdots \\ x_i & y_i & 1 \\ \vdots & \vdots & \vdots \\ x_n & y_n & 1 \end{bmatrix} \begin{bmatrix} C_1 \\ C_2 \\ C_3 \end{bmatrix} = \begin{bmatrix} -x_1^2 & -y_1^2 \\ \vdots & \vdots \\ -x_i^2 & -y_i^2 \\ \vdots & \vdots \\ -x_n^2 & -y_n^2 \end{bmatrix} \tag{41}$$

is in the form $\mathbf{Ax} = \mathbf{b}$. Then the solution without weighting any particular equation can be found by least squares as

$$\mathbf{x} = \left(\mathbf{A}^{\mathbf{T}}\mathbf{A}\right)^{-1}\mathbf{A}^{\mathbf{T}}\mathbf{b}\,. \tag{42}$$

To determine the radius R, the solution vector is defined by

$$
\begin{aligned}
C_1 &= -2x_c \\
C_2 &= -2y_c \\
C_3 &= x_c{}^2 + y_c{}^2 - R^2
\end{aligned}
\tag{43}
$$

so that

$$
\begin{aligned}
x_c &= -0.5C_1 \\
y_c &= -0.5C_2 \\
R &= \left(x_c{}^2 + y_c{}^2 - C_3 \right)^{0.5}
\end{aligned}
\tag{44}
$$

and R is the true airspeed that is determined from ground velocity vector inputs.

3.2.2 Two Vector Approach

For this research, the Two-Vector Approach was designed to eliminate the constant true airspeed assumption from the Three-Vector Approach. The combined velocity triangle concept was used as a starting point to develop the two vector approach. Inputs required for this technique were two ground velocity vectors and two aircraft headings. The aircraft heading would be supplied by the INS as the angle from true north to the direction the aircraft's nose is pointing. Two ground velocity vectors were combined as in the Three-Vector Approach, with the intersection of their tips defining a geometric origin. Input headings defined the direction from the tails of the ground velocity vectors to the true velocity vectors. The true velocity vectors intersect at a single point in two dimensions. Therefore the vector from the intersection of the true velocity vectors to the origin is the wind velocity as shown below.

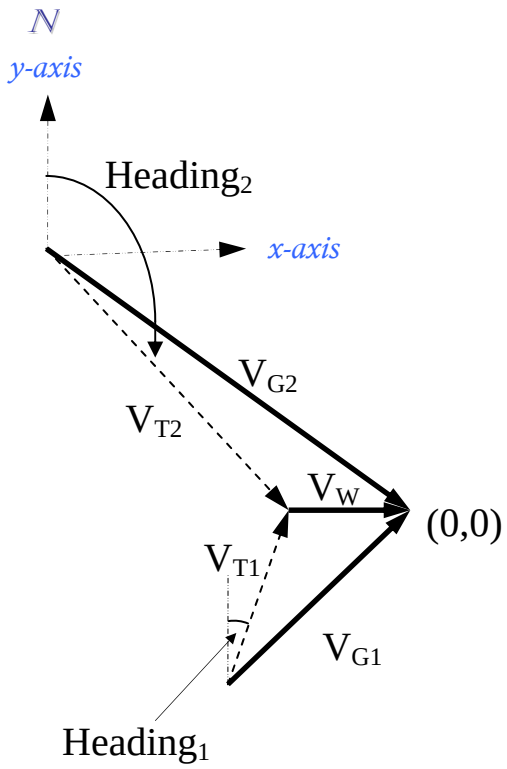

Figure 3.2. Two Combined Velocity Triangles

Using this setup, the constant true airspeed constraint is no longer required.

Continuing, the intersection of the velocity vectors defines a point (x_p, y_p), and the tails of the ground velocity vectors define the points (x_1, y_1) and (x_2, y_2). If more than two vectors are sampled, the process would continue with input angles and points as seen below.

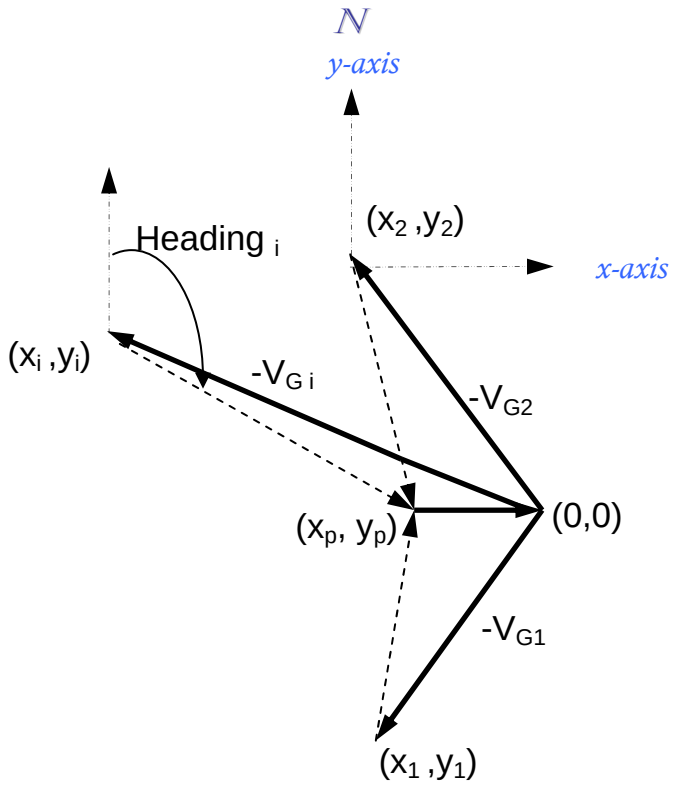

Figure 3.3. Sampled Two Vector Approach

A least squares approximation similar to the three vector approach was developed as follows. The heading, ψ_i, to the true velocity vector for each sample can be described by

$$\tan\psi_i = \frac{\left(x_p - x_i\right)}{\left(y_p - y_i\right)}. \tag{45}$$

Similarly, the point $\left(x_1, y_1\right)$ can be described by $x_i = V_{G_i}\sin\left(\chi_i + \pi\right)$, and $y_i = V_{G_i}\cos\left(\chi_i + \pi\right)$, where χ_i is the heading to the ground velocity vector for each

sample. Then equation 45 can be rearranged as $\tan(\psi_i) y_p - \tan(\psi_i) y_i = x_p - x_i$ and can be further reduced to

$$\tan(\psi_i) y_p - x_p = \tan(\psi_i) y_i - x_i . \tag{46}$$

Substituting in x_i and y_i into equation 46, the following relation is developed

$$\tan(\psi_i) y_p - x_p = \tan(\psi_i) V_{G_i} \cos(\chi_i + \pi) - V_{G_i} \sin(\chi_i + \pi) . \tag{47}$$

The equation is now in the familiar $\mathbf{Ax} = \mathbf{b}$ form

$$\begin{bmatrix} \tan(\psi_i) & -1 \end{bmatrix} \begin{bmatrix} y_p \\ x_p \end{bmatrix} = \mathbf{b}_i \tag{48}$$

where $\mathbf{b}_i$ is the quantity $\tan(\psi_i) V_{G_i} \cos(\chi_i + \pi) - V_{G_i} \sin(\chi_i + \pi)$. Then the solution without weighting any particular equation can be found by least squares as

$$\mathbf{x} = \left(\mathbf{A}^{\mathbf{T}} \mathbf{A}\right)^{-1} \mathbf{A}^{\mathbf{T}} \mathbf{b} . \tag{49}$$

With an estimate of the point (x_p, y_p) available, the true velocity vector, V_T, is thus determined as is the wind velocity vector, V_W, from Figure 3.3. The true airspeed is the magnitude of V_T.

3.2.3 Kalman Filter Approach

A recursive weighted least squares estimation was set up as the Kalman Filter Approach. An extended Kalman filter model was set up using the estimation process from section 2.5 to estimate the **x** that minimizes the error in equation 37. As developed

here, the components of the wind, $V_{W\,x}$ and $V_{W\,y}$ are estimated as each new set of data is sampled, so $\mathbf{x}_k$ has the form

$$\mathbf{x}_k = \left[V_{wind}\right] = \begin{bmatrix} V_{W_x} \\ V_{W_y} \end{bmatrix}. \tag{50}$$

The inputs to the Kalman filter are outputs from the inertial estimator block and include the heading of the true airspeed vector (denoted **z** here) and the ground velocity vector, in its north ($V_{G\,x}$) and east ($V_{G\,y}$) components. The nonlinear measurement model **h(x)** is set up in the form

$$\mathbf{h}_k = \tan^{-1}\left(\frac{V_{true\,y}}{V_{true\,x}}\right) \tag{51}$$

which is the heading of the true velocity from true north. Rewriting equation 51 as

$$\mathbf{h}_k = \tan^{-1}\left(\frac{V_{G\,y} - V_{W\,y}}{V_{G\,x} - V_{W\,x}}\right), \tag{52}$$

where $V_{G\,x}$ and $V_{G\,y}$ are measured values, and $V_{W\,x}$ and $V_{W\,y}$ are estimated values. The inertial estimator provides the heading of the BF frame x-axis from true north, which differs from the heading of the true velocity given in equation 52 during turns. To account for sideslip, roll, and bank encountered during turns, as given by the inertial estimator, $\mathbf{h}_k$ is modified as follows:

$$\mathbf{h}_k = \tan^{-1}\left(\frac{V_{G\,y} - V_{W\,y}}{V_{G\,x} - V_{W\,x}}\right) + \cos(\theta)\left[\sin(\phi)\alpha - \beta\right]. \tag{53}$$

Then, $\mathbf{z}_{k+1} = \mathbf{h}_{k+1}(\mathbf{x}) + \mathbf{e}_{k+1}$ becomes

$$\mathbf{z} = HDG = \tan^{-1}\left(\frac{V_{G\,y} - V_{W\,y}}{V_{G\,x} - V_{W\,x}}\right) + \cos(\theta)\left[\sin(\phi)\alpha - \beta\right] + \mathbf{e}_{k+1} \tag{54}$$

The **H**, required for the update equation, defines the linear relationship between the measurements, **z** and the state to be estimated, **x** [Kayton and Fired 1997]. **H** is defined as

$$\mathbf{H}_k = \frac{\partial \mathbf{h}}{\partial \mathbf{x}} = \frac{\partial \mathbf{h}}{\partial V_{wind}} \tag{55}$$

or in component form

$$\mathbf{H}_k = \left[\frac{\partial \mathbf{h}}{\partial V_{W\,x}}, \frac{\partial \mathbf{h}}{\partial V_{W\,y}}\right]. \tag{56}$$

From section 2.5.4, $\mathbf{P}$, $\mathbf{Q}$, and $\mathbf{R}$ must be defined. **P** is the error covariance matrix, **Q** is the growth in the wind estimate uncertainty, and **R** is the noise on the input heading measurement. The rest of the model is developed and updated according to section 2.5 as follows:

$$\begin{aligned}
&\mathbf{M}_k = \mathbf{P}_k + \mathbf{Q} \cdot \Delta t \\
&\mathbf{x}_{k+1} = \mathbf{x}_k + \mathbf{K}_{k+1}\left(\mathbf{z}_{k+1} - \mathbf{h}_{k+1} - \mathbf{H}_{k+1}\mathbf{x}_k\right) \\
&\mathbf{P}_{k+1} = \mathbf{M}_k - \mathbf{M}_k\mathbf{H}_{k+1}^T\left[\mathbf{H}_{k+1}\mathbf{M}_k\mathbf{H}_{k+1}^T + \mathbf{R}_{k+1}\right]^{-1}\mathbf{H}_{k+1}\mathbf{M}_k
\end{aligned} \tag{57}$$

Then as the sampled data was updated, the wind velocity, V_W, was continuously estimated from $\mathbf{x}_k$. Finally, V_T was obtained from the vector triangle equation by subtracting V_W from V_G.

3.3 Dynamic Inversion Algorithm

The dynamic inversion approach relies on specific aircraft information remaining available following the loss of air data. Because much of the needed information would be unavailable following an air data system failure, the steady, level, unaccelerated flight condition was investigated. In section 2.2, the equation for this condition was developed where $Weight = \bar{q}SC_L$. By expanding $\bar{q}$ and C_L to known lift coefficients, the equation becomes

$$Weight = \frac{1}{2}\rho V_T{}^2 S\left(C_{L_o} + C_{L_q}\frac{q\bar{c}}{2V_T} + C_{L_\alpha}\alpha + C_{L_{\delta e}}\delta_e + C_{L_{\delta f}}\delta_f \right) \tag{58}$$

where ρ is the density, V_T is the true velocity, S is the wing area, q is the pitch rate, $\bar{c}$ is the mean aerodynamic chord, α is angle of attack, δ_e is elevator deflection, δ_f and is flap deflection. Following an air data system failure, two of the unknowns from equation 58, ρ and α, were calculated from available inertial, position, and velocity values, assuming standard day conditions. The dynamic inversion concept from 2.4.2 was then used to develop an expression for the remaining unknown in the equation, V_T. An estimation of the wind was not required using this approach since the true airspeed was directly calculated.

3.4 Testing Airspeed Estimation Theory

The Three-Vector, Two-Vector, and Kalman Filter Approaches for true airspeed estimation were tested using a Matlab® Simulink® model (Appendix A). An aircraft model was used to create ground and wind velocity vectors from input values of actual true and wind velocities. The outputs simultaneously fed model blocks that contained the three wind estimation approaches using the following as inputs: ground velocities for the Three-Vector Approach, and ground velocities and true headings for the Two-Vector and Kalman Filter Approaches. The wind velocity estimate from each of the approaches was then compared to the actual input wind velocity. Input values of true airspeed were varied from 100 to 400 knots, wind was varied from 10 to 30 knots, and the number of samples used to solve the estimation problem was varied from 150 to 350.

The dynamic inversion algorithm was tested using recorded outputs from a T-38 aircraft pilot-in-the-loop simulator provided by the Air Force Research Laboratory. The aircraft was flown straight and level with a constant calibrated airspeed at altitudes from 5,000 to 30,000 feet. During post processing of recorded values, accelerations and rates from the simulator fed the inertial portion of the VEST algorithm. North and east ground velocity components transformed to BF frame velocity components U and W were used to estimate the angle of attack, and the inertial altitude was used to estimate density. An expression for V_T from equation 58 was determined symbolically in Matlab®. Recorded aircraft deflections, coefficients, and estimated values were combined to produce a V_T estimate during straight and level flight conditions. The estimated V_T was compared to the recorded simulator value of V_T and to Kalman Filter Approach V_T estimate.

The true airspeed errors for the three different approaches and dynamic inversion algorithm were compared to determine which technique to employ in the VEST algorithm. Chapter 4 will show that the Kalman Filter Approach consistently produced the smallest wind direction and speed errors throughout testing. Thus, the Kalman Filter Approach was implemented for further VEST algorithm development.

3.5 True Airspeed Estimate in Simulation

In preparation for flight test, the VEST algorithm was coupled to a Learjet simulator in Matlab® Simulink® (Appendix C). A concept block diagram is shown below.

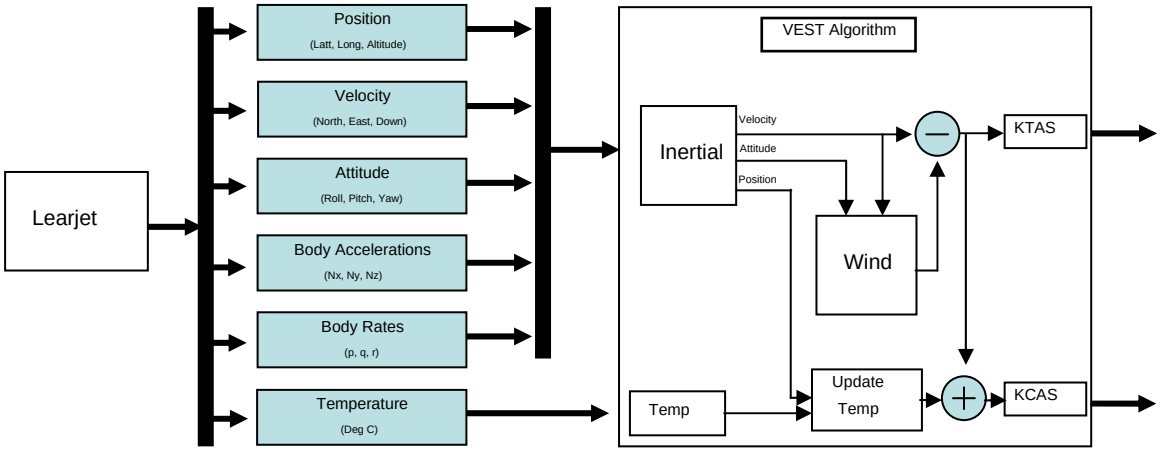

Figure 3.4. VEST Algorithm Block Diagram

The purpose of the VEST algorithm was to continuously estimate true airspeed following a complete air data system failure. The complete air data system failure meant that all sensors providing airspeed, altitude, temperature, angle of attack, and pressure readings

were no longer available. The algorithm had three parts. The first part used available information to estimate the inertial position, velocity, and attitude. The pieces of available information were flight control computer accelerometer and rate gyroscope outputs, and last known position, velocity, attitude, and temperature. The algorithm used accelerometer and rate gyroscope outputs to propagate the last known state forward to give the current inertial position, velocity, and attitude. The second part of the algorithm used the inertial information to continuously estimate the wind speed and direction. Angle of attack and sideslip were estimated and included in the wind estimate to account for the fact that the true airspeed vector is not aligned with the true heading estimate in turns. Finally, the true airspeed was determined using the inertial airspeed estimate and the wind estimate in the vector equation that relates all three velocities. The third part of the algorithm continuously estimated calibrated airspeed. Current temperature was estimated using a standard lapse rate based on inertial altitude deviation from last known altitude and temperature. The current temperature estimate was used to determine current density for use in converting true airspeed to calibrated airspeed [McLaren 2007].

The algorithm was tested during two simulated flight maneuvers: during simulated climbs and descents, and through two level turning maneuvers, then back to level flight. Time history error plots were created for inertial position, velocity, attitude, angle of attack, and angle of sideslip to test the inertial portion of the VEST algorithm. Noise, based on Learjet sensor specifications, was added to the simulated accelerations and rates for additional time history error plots. Wind was then added to the simulation to test the wind portion of the VEST algorithm and to compare the estimated true

airspeed to the actual true airspeed. Time history error plots for wind speed and direction, and true airspeed were then created. All maneuvers began from straight and level, unaccelerated flight, heading north at 10,000 feet altitude and 530 knots true airspeed. Actual wind conditions were either 10 knots at 090 degrees, or 40 knots at 090 degrees. Varying starting conditions for aircraft heading, altitude, airspeed, and actual wind conditions had little effect on resulting wind and true airspeed estimates. Varying values of last known wind conditions made the most significant impact on wind and airspeed estimates. Therefore, last known wind speed and direction were varied from actual wind conditions. Wind speed varied from within 1 knot of actual conditions, to 35 knots from actual wind speed. Wind direction varied from within 1 degree of actual conditions, to 315 degrees from actual wind direction.

3.6 Summary

The methods formulated for the three wind estimator approaches and dynamic inversion algorithm were developed. The resulting errors from each of the techniques were compared to decide which to apply in the wind portion of the VEST algorithm. The Kalman Filter approach was chosen for use in the wind portion of the algorithm, and tested using a Learjet simulator. The results from the simulation tests are presented in the next chapter.

4. Simulation Results and Analysis

4.1 Overview

The four techniques investigated for use in the VEST algorithm included the Three-Vector, Two-Vector, and Kalman Filter Approaches, and the Dynamic Inversion Algorithm. The results from the Three-Vector, Two-Vector, and Kalman Filter Approaches were directly comparable since the time history error plots were all created from the same input source (outlined in section 3.4) and are presented in the next section. The results from the Dynamic Inversion Algorithm were generated from a separate input source (outlined in section 3.4), compared to the Kalman Filter Approach, and are presented in section 4.3. The results for the wind and true airspeed estimates from the Learjet simulator are discussed in section 4.4.

4.2 Wind Estimator Approach Results

The purpose of the Three-Vector, Two-Vector, and Kalman Filter Approaches was to estimate wind velocity, as described in section 3.2. Time history error plots of estimated wind direction and speed were generated for the Three-Vector, Two-Vector, and Kalman Filter Approaches. Wind speed, aircraft true airspeed, and number of samples used per update were varied with time over 400 second intervals for different simulation runs. The following figure shows an example time history error plot for estimated wind direction with input values of 100 knots aircraft true airspeed, 10 knots wind speed, and 150 samples used per update for the Three-Vector and Two-Vector estimators.

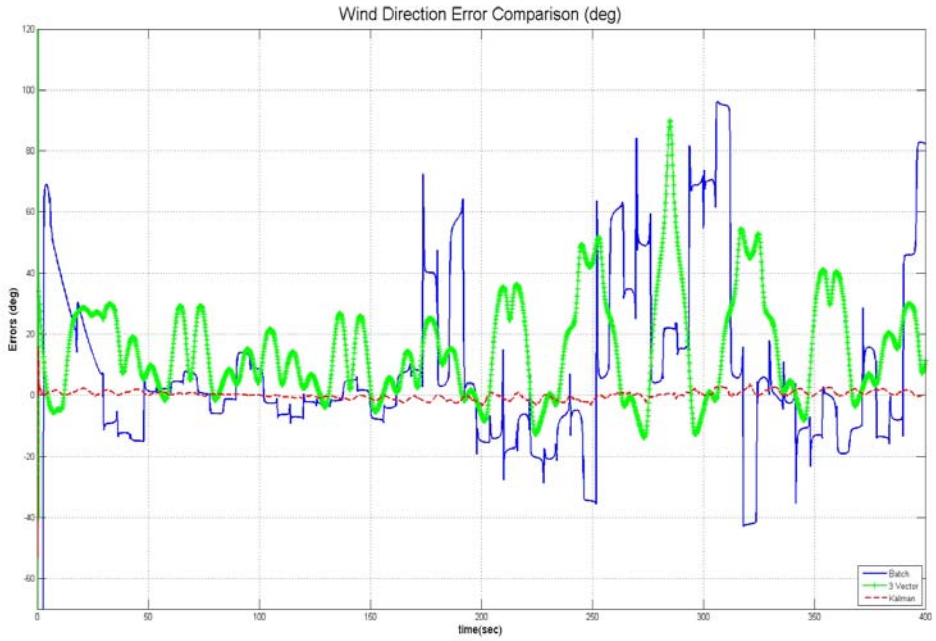

Figure 4.1. Sample Wind Direction Comparison

From the legend, the solid blue line corresponds to the Two-Vector results, the marked green line corresponds to the Three-Vector results, and the dashed red line corresponds to the Kalman Filter results. The set of time history error plots can be found in Appendix B. The results from the three approaches are presented in the following table.

Table 4.1. Three Approach Results

Approach	Average Wind Speed Error (knots)	Average Wind Direction Error (degrees)
Three Vector	16.9	8.3
Two Vector	9.5	4.9
Kalman Filter	0.073	0.045

The Kalman Filter Approach demonstrated the smallest average wind speed and direction error. Certain combinations of aircraft true airspeed, wind speed, and number of samples taken using the Two-Vector Approach produced comparable results to the Kalman Filter results. However, the intent of the algorithm was to minimize constraints to allow favorable operation over a wide flight envelope. Therefore, the Three-Vector and Two-Vector Approaches were not investigated further. The Kalman Filter Approach was used for continuing VEST algorithm development.

4.3 Dynamic Inversion Results

The purpose of the Dynamic Inversion technique was to estimate true airspeed directly from the equation of motion, as described in section 3.3. Four straight and level unaccelerated flight conditions were flown in a T-38 pilot-in-the-loop simulator for this technique. The conditions for the four runs respectively, were as follows: 5,000 feet, 250 knots calibrated airspeed, wind 10 knots at 90 degrees; 10,000 feet, 300 knots calibrated airspeed, wind 10 knots at 120 degrees; 20,000 feet, 350 knots calibrated airspeed, wind 20 knots at 180 degrees; and 30,000 feet, 300 knots calibrated airspeed, wind 30 knots at 360 degrees. The inertial portion of the VEST algorithm provided an estimate of angle of

attack to the dynamic inversion algorithm, and all other inputs were taken from recorded simulator values. The inertial portion of the algorithm also provided velocity and heading information to the wind portion of the algorithm, which made use of the Kalman Filter Approach. The results of the true airspeed estimate from the Dynamic Inversion Algorithm were compared to the VEST algorithm using the Kalman Filter Approach to estimate winds to determine a true airspeed estimate. An example true airspeed error comparison plot is shown below for the first run.

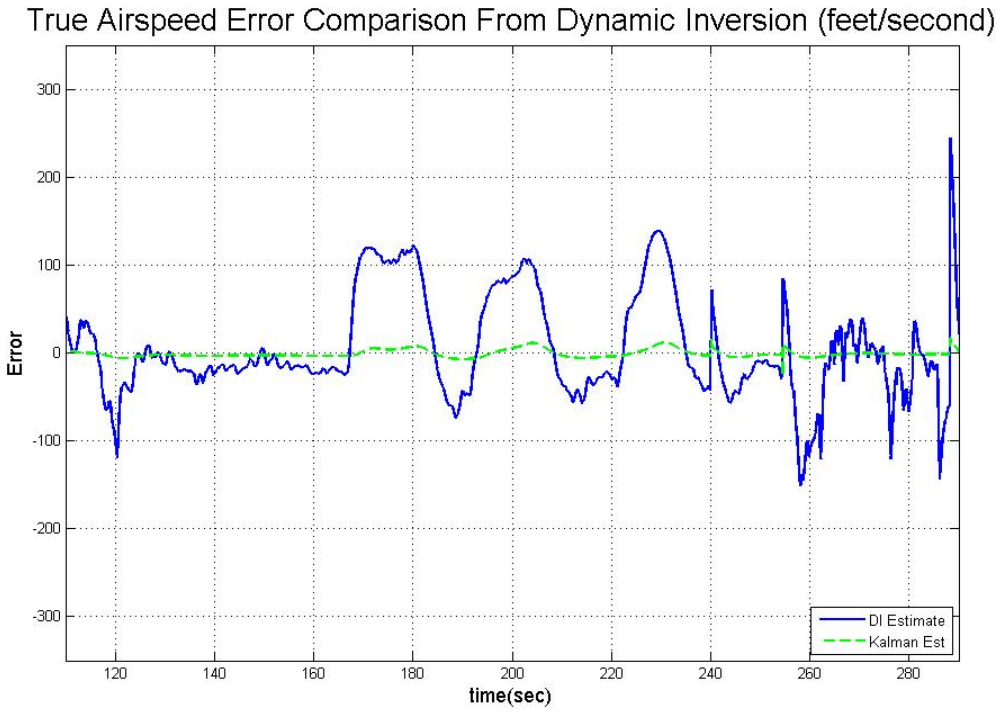

Figure 4.2. True Airspeed Comparison for Dynamic Inversion

The complete set of time history error plots can be found in Appendix B. Dynamic Inversion estimate fluctuations resulted from the pilot's efforts to maintain straight and level, unaccelerated flight based on T-38 simulator generated and displayed attitude,

altitude, and airspeed. The dynamic inversion airspeed estimate results for the four runs are presented in the following table.

Table 4.2. Dynamic Inversion Results

Approach	Average True Airspeed Error (knots)
Dynamic Inversion	7.76
Kalman Filter	0.983

The dynamic inversion airspeed errors were on the same order of magnitude as errors observed with the Two-Vector Approach. Additionally, coefficient values for the lift equation were dependent on aircraft altitude, necessitating the use of a look up table for coefficients. The altitude dependence was viewed as adding an additional constraint to that of the Two-Vector technique, and therefore was not developed further. Consequently, the Kalman Filter Approach was used for VEST algorithm development in the Learjet simulator.

4.4 Learjet Simulation Results

The Learjet ground simulator allowed for testing of both the inertial and wind portions of the VEST algorithm. A series of inputs were made to produce two simulated aircraft maneuvers, a climbing and descending maneuver and a level turning maneuver. The inertial portion was tested first, and the results are presented in section 4.4.1. The wind portion and overall true airspeed estimate were tested second, and the results are presented in section 4.4.2.

4.4.1 Inertial Estimate

The inertial estimate was tested versus simulator position, velocity, attitude, angle of attack (alpha), and angle of sideslip (beta) during two simulated aircraft maneuvers. All maneuvers began from straight and level, unaccelerated flight, heading north at 10,000 feet altitude and 530 knots true airspeed. Inertial estimates were generated from initial conditions and simulated accelerometer and rate gyroscope inputs. Time history error plots for each inertial estimate were created. An example error plot for inertial north and east velocity during a turning maneuver is shown below.

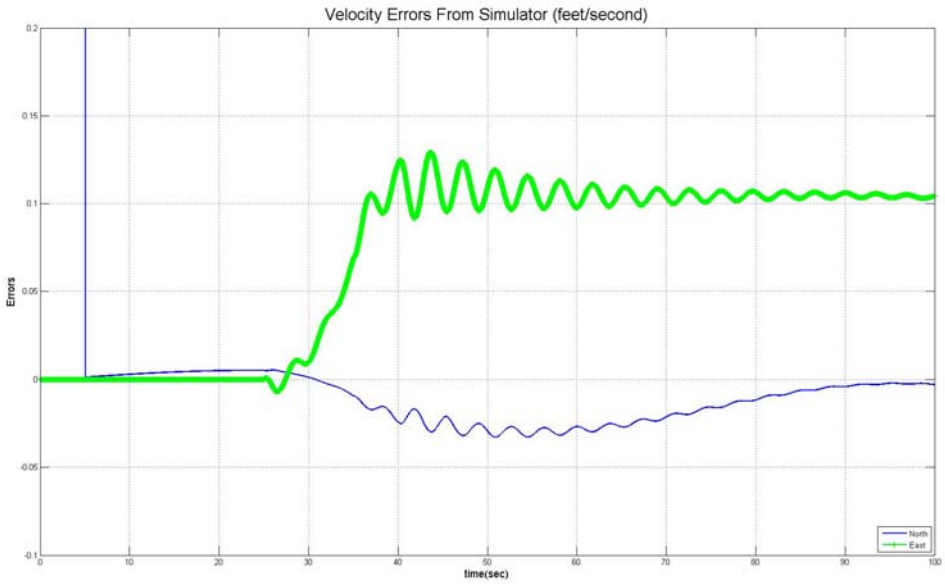

Figure 4.3. Inertial Velocity Error

The time history error plots for each inertial parameter can be found in Appendix D. The results for the two maneuvers are shown in the following table.

Table 4.3. Inertial Estimate (without noise) Results

Estimate Parameter	Average Error During Climb and Descent Maneuver	Average Error During Turning Maneuver
North Position (degrees)	0.004	0.004
East Position (degrees)	0.01	0.01
Altitude (feet)	14.33	9.09
North Velocity (feet/second)	0.01	0.005
East Velocity (feet/second)	0	0.07
Down Velocity (feet/second)	2.76	3.72
Roll (degrees)	0	3.76×10^{-4}
Pitch(degrees)	5.44×10^{-4}	3.21×10^{-4}
Yaw (degrees)	0	6.22×10^{-4}
Alpha (degrees)	0.04	0.04
Beta (degrees)	0	0.03

These average errors were produced without noise on the simulated accelerometer and rate gyroscope inputs. Then, simulated white noise was added to the accelerometer and rate gyroscope inputs according to the Learjet aircraft sensor specifications. Then the process was repeated.

The following are the results after noise (as described in section 3.5) was added to the simulated Learjet accelerometer and rate gyroscope inputs. An example error plot for inertial north and east velocity during a turning maneuver is shown below.

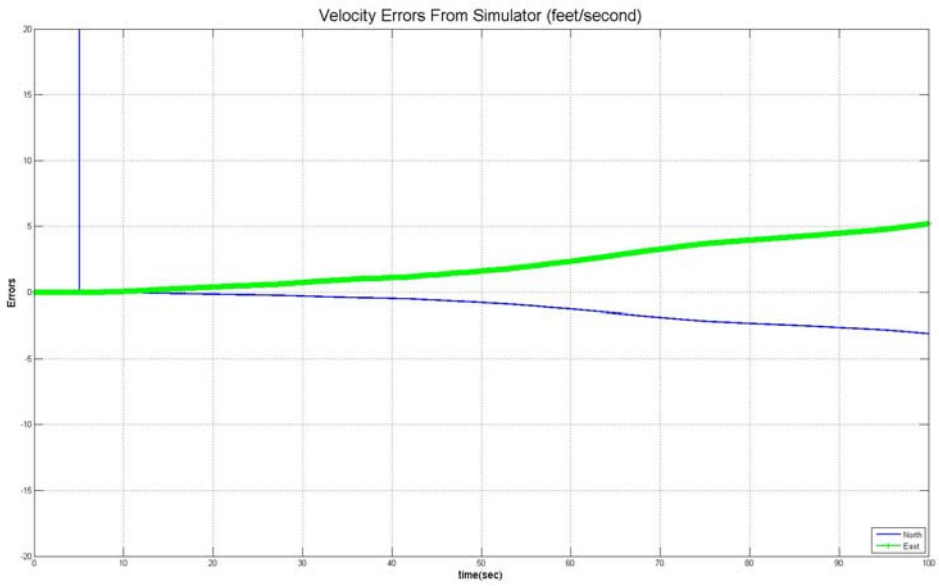

Figure 4.4. Inertial Velocity Error with Noise

The time history error plots for each inertial parameter (with noise) can be found in Appendix D. The results for the two maneuvers are shown in the following table.

Table 4.4. Inertial Estimate (with noise) Results

Estimate Parameter	Average Error During Climb and Descent Maneuver	Average Error During Turning Maneuver
North Position (degrees)	0.004	0.004
East Position (degrees)	0.01	0.01
Altitude (feet)	15.74	1.34
North Velocity (feet/second)	0.86	1.22
East Velocity (feet/second)	2.23	2.21
Down Velocity (feet/second)	6.45	6.16
Roll (degrees)	0.34	0.36
Pitch(degrees)	0.13	0.07
Yaw (degrees)	0.12	0.12
Alpha (degrees)	0.10	0.07
Beta (degrees)	0.72	0.83

The inertial estimate for north and east velocity, and yaw were used as inputs to the wind portion of the VEST algorithm. The errors on these parameters that included noise were considered more flight representative than the parameter errors that did not consider sensor noise. Therefore, further simulations included the noise on the sensors for the wind estimator analysis.

4.4.2 Wind and True Airspeed Estimate

The ground simulation was continued to investigate the wind portion of the VEST algorithm and the resulting true airspeed estimate. Estimated wind speed and direction and true airspeed were compared to simulated conditions. Last known wind conditions were used as initial conditions for the Kalman Filter technique in the wind estimator, and were varied in speed and direction. The average results for the climb and descent maneuvers and the turning maneuvers are shown in the following table.

Table 4.5. Wind and True Airspeed Estimate Results

Actual Wind Condition (knots)	Maneuver	Average Wind Magnitude Error (knots)	Average Wind Heading Error (degrees)	Average True Airspeed Error (knots)
40	Climb and Descent Maneuver	6.59	21.30	17.47
40	Turning Maneuver	3.77	19.16	14.60
10	Climb and Descent Maneuver	3.46	21.73	9.04
10	Turning Maneuver	1.66	16.51	6.35

The time history error plots for varied input wind conditions can be found in Appendix D. Those plots show that the smallest errors for all three parameters were produced when accurate last known wind values were used as inputs. The last known wind magnitude had less of an effect on the estimate errors than the last known heading. Last known heading values within approximately 10 degrees of actual wind heading produced true

airspeed errors less than 2 knots, while last known wind values within approximately 45 degrees of actual wind heading produced true airspeed errors on the order of 10 knots. Worst case conditions that produced the largest true airspeed errors occurred when last known wind direction was ± 90 degrees from actual wind direction. Also, wind and true airspeed errors tended to decrease following each turning maneuver.

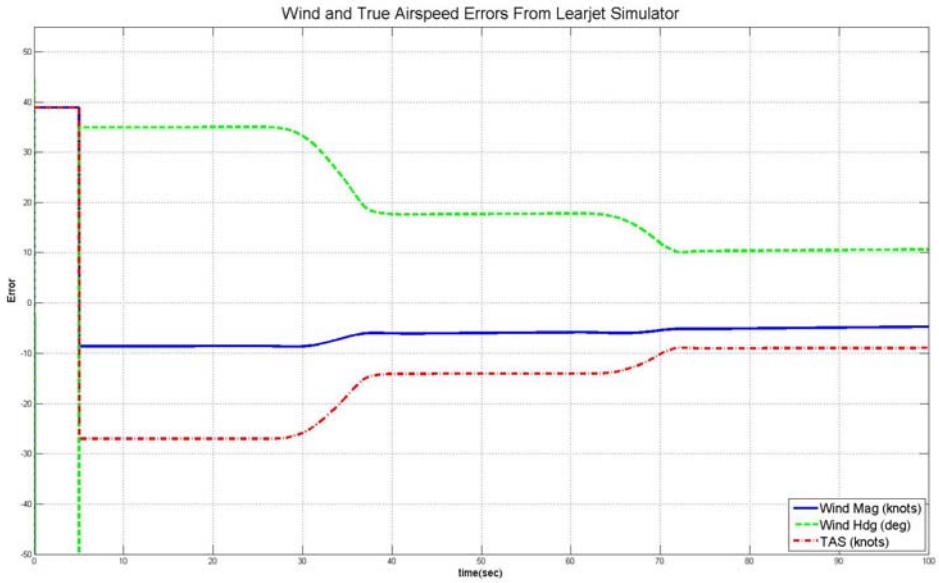

Figure 4.5. Wind and True Airspeed Errors

In Figure 4.5 for example, a turn occurred at approximately 30 and 70 seconds. All three errors decreased following each turn at these conditions.

4.5 Summary

The resulting wind and true airspeed estimates from the Three-Vector, Two-Vector, Kalman Filter, and Dynamic Inversion techniques were used to refine the technique for further VEST algorithm development. The Kalman Filter Approach consistently produced the smallest estimated wind errors compared to actual values. The

Kalman Filter technique was incorporated into the wind portion of the VEST algorithm, and was used to ready the algorithm for flight test using a Learjet aircraft. Flight test employment and results using the VEST algorithm are presented in the next chapter.

5. Flight Test

5.1 Chapter Overview

As part of the author's joint AFIT-TPS program, the VEST algorithm presented in the previous chapters was tested as part of the test management project, "*Backup Velocity Estimate Following Air Data System Failure, Project Have VEST*" [McLaren 2007] at USAF Test Pilot School; the author served as the program manager for the flight test project. A total of 11.3 hours of flight test were flown on a variable stability Learjet during six test sorties at Edwards Air Force Base in September 2007. The tests were set up to determine the accuracy of VEST algorithm inertial, wind, and airspeed estimates, and to employ the airspeed estimate during real time gain scheduling. A build up approach was employed assessing algorithm performance on the ground, airborne, and during operationally representative maneuvers. The next section discusses the testing methodology and section 5.3 presents the flight test results. The methodology, data, analysis, and results presented below were reported in Project Have VEST Final Technical Information Memorandum [McLaren 2007].

5.2 Methodology

The VEST algorithm was prepared for flight test aboard a Learjet, owned and operated by Calspan. Modification and testing took place from February to September 2007.

Figure 5.1. Calspan Variable Stability Learjet

The Calspan Variable Stability Learjet [Ball 2006], as seen in Figure 5.1, was a modified Learjet designed to serve as a three axis in-flight simulator, where normal operations included the use of a safety pilot and an evaluation pilot. The safety pilot's controls (left seat) were standard, but the evaluation pilot's controls (right seat) were replaced with components of fly-by-wire, response feedback, variable stability, and variable control systems. The response feedback flight control system used the Learjet control surfaces to augment the stability characteristics of the basic Learjet.

The Variable Stability System (VSS) on the Learjet was divided into two independent parts, a variable feel system and a response feedback system. The variable feel system provided the evaluation pilot with the stick and rudder pedal forces, gradients, and displacements, while the response feedback flight control system augmented the normal Learjet dynamics to represent those of the vehicle being simulated. The evaluation pilot's inputs were fed into the flight control system through the feel

system, and the resulting control surface movements produced the aircraft response. The loop was closed by sensing the aircraft's motions and feeding back signals proportional to these motions, thus modifying the response to the pilot's inputs. Angle of attack vanes, sideslip vanes, rate and attitude gyros, and air data information were all used as the sensor elements. The VSS flight control modes were as follows: VSS Mode, Emergency Fly By Wire (FBW) Mode, Evaluation Pilot Manual Disengage Mode, Safety Pilot Manual Disengage Mode, and Force Disengage Mode.

For purposes of this flight test, the VSS Mode was set to the basic aircraft parameters. A modified stick-command gain was scheduled in the speed range between 200 and 300 knots, in order to highlight estimated airspeed errors. Existing safety trips were not affected and remained in place.

In the event the safety pilot becomes incapacitated or certain control cable failures occurred, the evaluation pilot can fly the aircraft as a normal Learjet using the FBW mode. All basic Learjet systems (gear, flaps, spoilers, brakes, etc.) were available. The handling characteristics were those of the basic aircraft with the yaw damper on. All safety trips were disabled and no feedback loops were used except rudder deflection per sideslip rate for yaw damping.

The evaluation pilot had the ability to electrically disengage the VSS and return control of the aircraft to the safety pilot. A disengage switch was located on the right seat center stick.

The safety pilot had the ability to disengage the VSS by depressing any of the following: wheel master switch, glare shield disengage switch, or throttle quadrant disengage switch.

A large force input by the safety pilot to the normal Learjet wheel/column would cause the VSS to disengage [McLaren 2007].

Modifications were made from the simulator version to account for flight test input formats. Additionally, modifications were made to ensure compatibility with the LearjetVSS. The VEST algorithm was developed as a Simulink® model that called Matlab® scripts for execution. For VSS compatibility, all called scripts were converted to embedded scripts to create a stand-alone Simulink® model. To reduce run time on the VSS, all lines of code from embedded scripts were converted to individual Simulink® blocks by Calspan. Modified blocks were compared to corresponding blocks from the original algorithm for proper function. Tests were performed both on the ground and in flight.

The following data collection and analysis techniques were used for the ground and flight test points. The test matrix listed in Appendix E describes each of the test points flown. For each test point, eleven performance variables were analyzed. Position errors were determined in the north, east, and vertical direction. North and east position errors were determined in coordinate degrees while the vertical position error was determined in feet. Velocity errors were determined in the north, east, and vertical directions and were determined in feet per second. Heading and wind direction errors were determined in degrees and presented between -180 and +180 degrees. Calibrated

airspeed and wind speed errors were determined in knots. Finally, true airspeed was determined in feet per second. All errors for flight test results were calculated by subtracting the Learjet recorded value (considered the truth source) from the Velocity Estimate (VEST) algorithm calculated value (estimate). Note that even though the Learjet's recorded values were considered the truth source, analysis showed (as will be discussed in more detail below) that the Learjet's recorded wind data (speed and heading) were inaccurate.

Appendix F presents the time history error plots for airspeed and heading, and Appendix G presents error plots for the remaining nine variables corresponding to each completed test point. Data were smoothed using a sliding average technique. Data were collected every 20 milliseconds. A single data point consisted of the average estimated value minus the truth source value over 400 milliseconds plotted at the midpoint of time. Figure 5.2 illustrates the process.

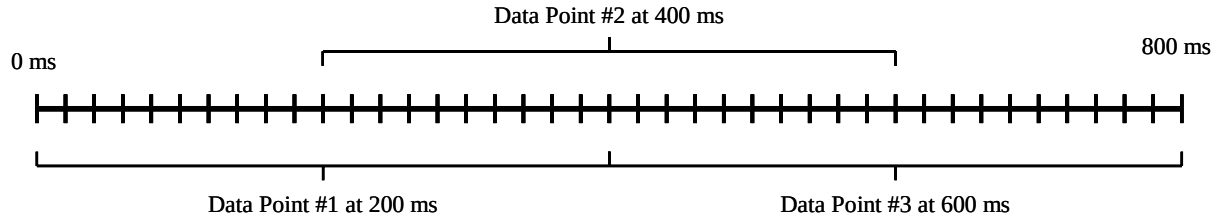

Figure 5.2. Sliding Average Method

For each plot, the x-axis represents time in seconds for the duration of the maneuver. The y-axis scale was selected as a compromise between showing appropriate

detail and attempting to maintain constant scaling for all plots. Figure 5.3 is a representative airspeed and heading error time history plot [McLaren 2007].

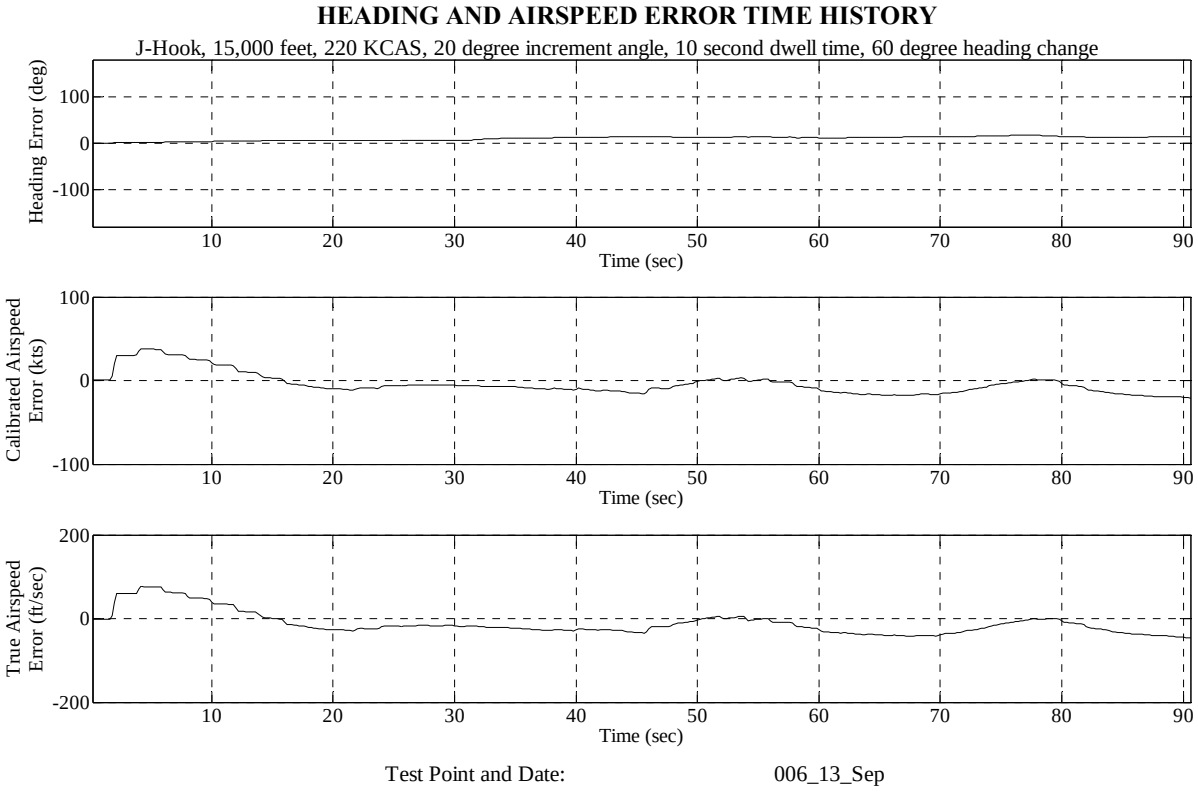

Figure 5.3. Representative Time History Plot

5.2.1 Ground Inertial Estimate

The purpose of the ground test was to check VEST algorithm compatibility with the VSS and to determine inertial estimate performance in a ground taxi. Three power ups of the VEST algorithm implemented on the VSS from the complete power off condition were performed. VSS operation and VEST algorithm specific parameters were

monitored throughout. Next, the accuracy of the VEST algorithm inertial estimate was determined during multiple taxi runs. The aircraft GPS was used as the truth source for position and velocity. To verify the accuracy of the GPS, surveyed points were used as references for stationary aircraft position. The aircraft installed attitude and heading reference system (AHRS) was used as a truth source aircraft heading. The aircraft was taxied for 5 minutes and time histories of inertial speeds were recorded for analysis. To calculate the accuracy of the VEST algorithm, inertial north, east, and vertical speeds were subtracted from the GPS speeds and plotted against time. Inertial heading was compared to AHRS heading in a similar manner. This procedure was repeated both with and without GPS updates to aid the inertial estimates.

5.2.2 Airborne Inertial Estimate

The airborne testing focused on determining the accuracy of the VEST algorithm inertial and wind estimates. The inertial estimate portion provided the ground velocity vector (V_G) element to the $V_G = V_T + V_W$ vector equation from section 2.3. The inertial velocity and heading were also used as inputs to the wind estimate. Due to the importance of accurate inertial estimates, four flight test techniques (FTT) were set up to observe the accuracy of the inertial speed and heading estimates. Three of the four FTTs included turning maneuvers to provide axis observability in inertial estimates. The fourth FTT was developed to evaluate the VEST algorithm's performance during straight and level, unaccelerated flight.

The J-Hook maneuver was flown as the primary maneuver to determine algorithm performance. The maneuver was a combination of level flight durations and incremental

heading changes. The test aircraft was trimmed at the flight condition (A) dictated by the test matrix using the Learjet air data system. The maneuver began with the Velocity Estimate (VEST) algorithm providing its estimate to the Variable Stability System (VSS) feel system. The aircraft was flown straight and level for the dwell time (B) and then heading was incrementally changed (C) as dictated by the test matrix. This combination of straight flight and heading change was continued until a total turn (D) was completed. The maneuver terminated after the last level flight duration elapsed. The J-Hook Flight Test Technique (FTT) is graphically depicted in Figure 5.4 [McLaren 2007].

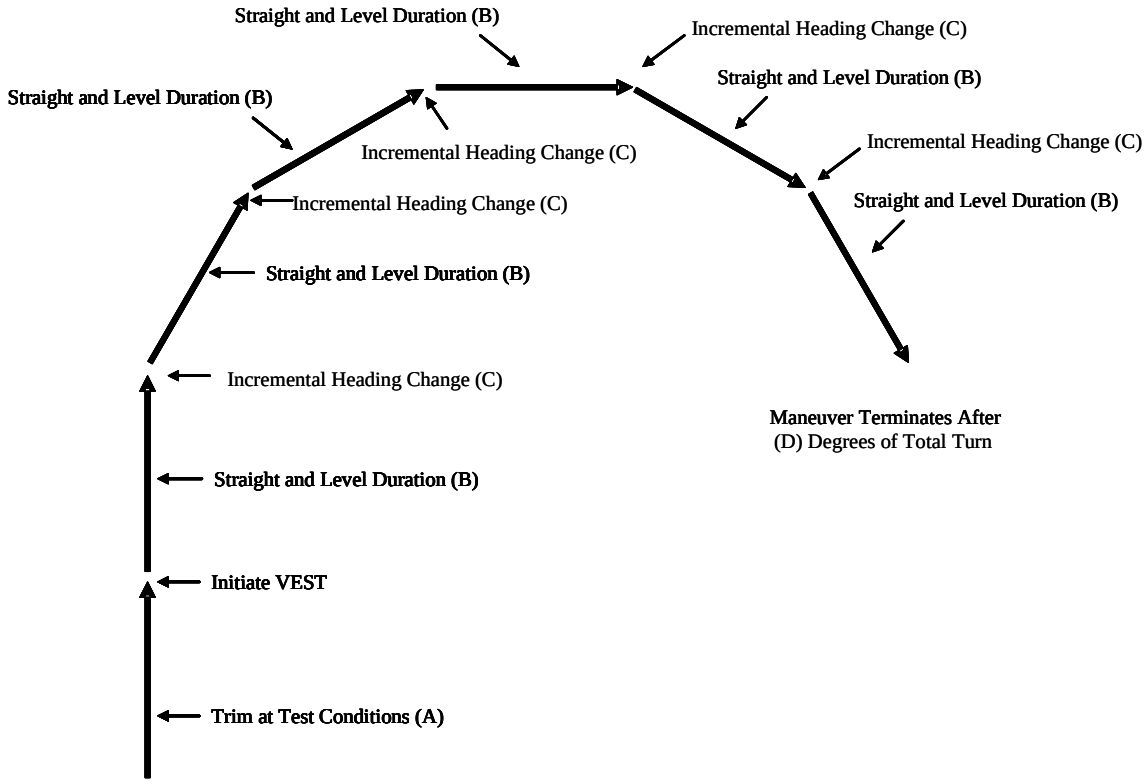

Figure 5.4. J-Hook Flight Test Technique

The Container maneuver was flown as the build-up to approach to landing test points and determined algorithm performance in the landing phase. The Container maneuver was conducted at the flight conditions (A) defined in the test matrix. The test aircraft established a constant heading to simulate a downwind leg of a landing approach. The maneuver began with the VEST algorithm providing its estimate to the VSS feel system. The test aircraft delayed for 10 seconds and turned 90 degrees to configure with gear and flaps for a normal approach. The test aircraft then turned 90 degrees in the same direction and began an 800-1000 feet/minute descent for 2000 feet. The Container FTT is graphically depicted in the Figure 5.5 [McLaren 2007].

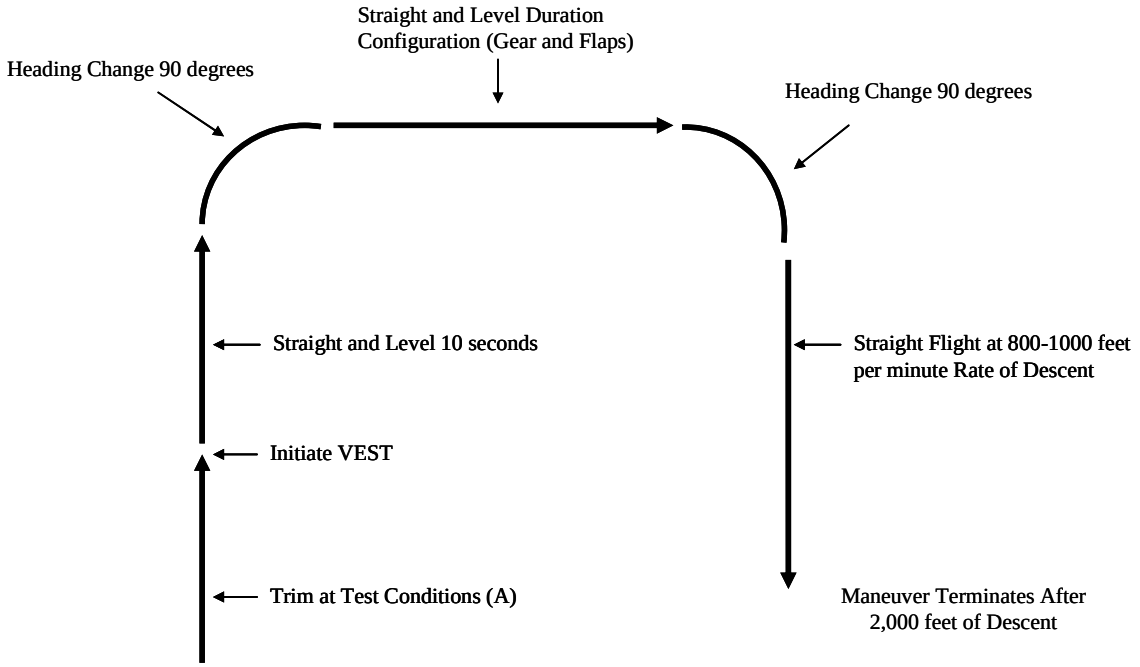

Figure 5.5. Container Flight Test Technique

The Sliceback maneuver was flown as the primary maneuver to determine algorithm performance during dynamic flight conditions. The maneuver was a combination of altitude, angle of bank, and normal acceleration changes. The test aircraft was trimmed at the flight conditions (A) dictated by the test matrix using the Learjet air data system. The maneuver began with the VEST algorithm providing its estimate to the VSS feel system. The pilot delayed for 10 seconds and then increased angle of bank to 60-70 degrees in a slight descent. Once in the bank angle, the pilot increased normal acceleration to approximately 2g. The maneuver terminated when 10 seconds of level flight after 180 degrees of heading change was achieved. The Sliceback FTT is graphically depicted in Figure 5.6 [McLaren 2007].

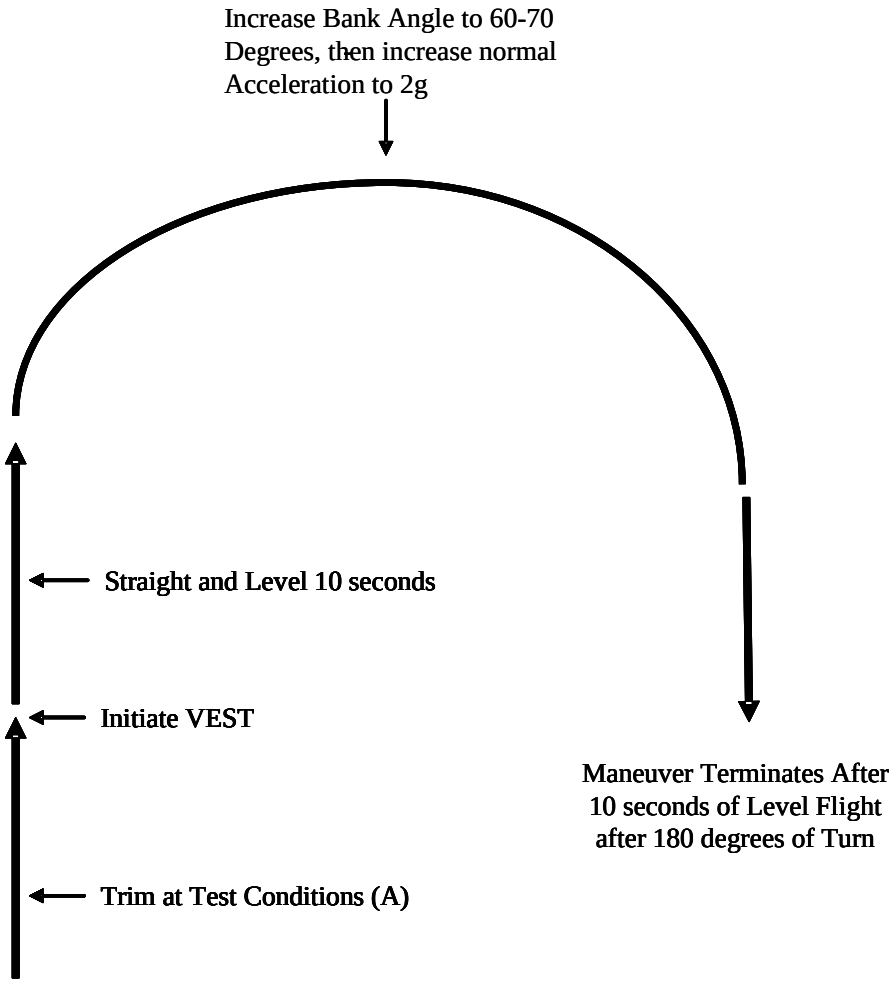

Figure 5.6. Sliceback Flight Test Technique

The Long Shot maneuver was flown as the primary maneuver to determine algorithm performance during straight and level, unaccelerated flight conditions. The test aircraft was trimmed at the flight condition dictated by the test matrix using the Learjet air data system. The maneuver began with the VEST algorithm providing its estimate to the VSS feel system. The test aircraft established a constant heading at the altitude and airspeed delineated in the test matrix. The test aircraft then flew straight and level

maintaining a constant heading and airspeed for 70 nautical miles or until it was determined that in-flight VEST algorithm errors had grown to a maximum value [McLaren 2007].

The procedure used to calculate the accuracy of the VEST algorithm in flight was similar to that described for ground testing. The inertial north, east, and vertical speeds were subtracted from the GPS speeds and plotted against time. Inertial heading was compared to AHRS heading in a similar manner. However, post flight data analysis from flights 1 and 2 indicated that the inertial estimate portion of VEST algorithm was not properly integrated with the Learjet VSS. Recall that the VEST algorithm was developed in Simulink® and then converted to run on the Learjet VSS by Calspan. Inertial estimates observed during flight (algorithm integration with VSS) did not match post-processed inertial estimates (algorithm integration with Simulink® model that drove VSS). The disparity was investigated for the remainder of the flight test schedule, but was not resolved. Therefore, the airborne accuracy of the VEST algorithm's inertial estimate, as presented in the results below, was determined by post-processing using the Simulink® model.

5.2.3 Airborne Wind and Airspeed Estimate

The wind (magnitude and direction) estimate was determined from the wind portion of the VEST algorithm. The wind estimate portion provided the wind velocity vector (V_W) element to the $V_G = V_T + V_W$ vector equation from section 2.3. The same four FTTs used to determine the inertial estimate accuracies were used to evaluate the airborne accuracy of the VEST algorithm wind estimate. The inputs used by the wind

portion of the VEST algorithm to continuously estimate the current winds were aircraft north speed, east speed, and heading from the inertial estimates. The outputs were north and east wind components of the wind velocity. The north and east wind components were converted to magnitude (speed) and direction for comparison to Learjet provided wind truth source. As already mentioned, the wind information provided by the Learjet was an unreliable truth source, so it was not possible to completely analyze the accuracy of the VEST wind estimate by itself; however, since the wind estimate plays an integral part in obtaining the airspeed estimate, the accuracy of the wind estimate can be indirectly determined by analyzing the accuracy of the airspeed estimate.

Using estimated values of V_G and V_W, the airspeed (V_T) could then be calculated using the $V_G = V_T + V_W$ vector equation from section 2.3. The true airspeed estimate was determined as the magnitude of V_T and compared to the true airspeed provided by the Learjet's air data system, which was a very accurate truth source. The calibrated airspeed estimate was determined from the true airspeed estimate and the estimated current flight conditions from the VEST algorithm. Equation 13 was rearranged to solve for ($P_T - P_A$), then the quantity was substituted into equation 10 to solve for the calibrated airspeed, V_C. Standard day values of density and pressure were determined based on the estimated inertial altitude.

5.2.4 Gain Scheduling

To test the utility of the VEST algorithm, a gain schedule was set up in the VSS to change the command gain. The command gain was a gain on the stick that adjusted the magnitude of the pilot's commanded input. The command gain schedule fed back

calibrated airspeed to set the appropriate gain. There were three possible sources of calibrated airspeed: Learjet air data, VEST, and a constant value to simulate standby gains. The command gain was multiplied by the actual air data value of calibrated airspeed raised to the fourth power, then normalized by one of the three sources of fed back calibrated airspeed also raised to the fourth power, referred to as a "V^4/V^4 control law". In this way, the command gain on the stick would be increased or decreased based on the value of calibrated airspeed from one of the three sources. If one of the sources provided a calibrated airspeed value that was different from the actual value, then the command gain on the stick would increase or decrease. If the fed back calibrated airspeed was the same as the actual value, then a constant command gain would result. The amount of change that would be noticeable by the pilot was set during the calibration portion of the first flight.

The intent for this schedule was that maneuvers would be flown in sequence using each of the three calibrated airspeed sources and observed handling qualities would be compared while accomplishing specific tasks. Magnitude of airspeed errors would be perceived as changes in stick sensitivity while variations in airspeed errors would result in unpredictable aircraft responses. The figure below shows the implementation of this concept into the VSS.

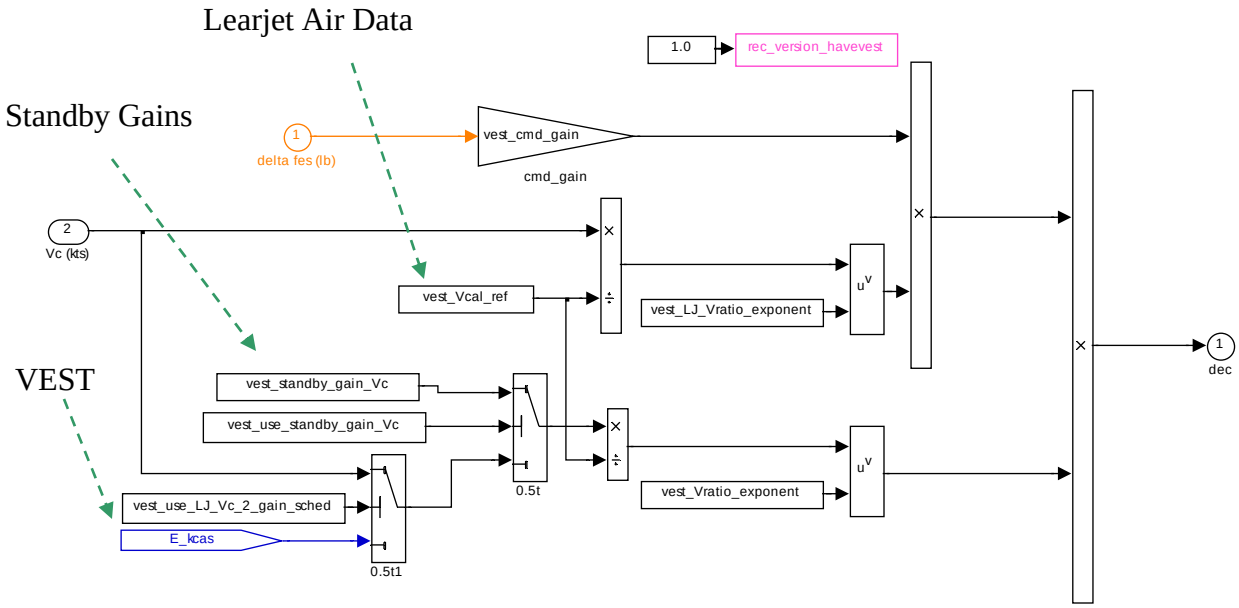

Figure 5.7. VSS Gain Schedule Implementation

Stick forces (*Fs*) and deflections were measured before and after the calibration flight. The calibration flight was performed at 15,000 feet and airspeeds of 200 to 300 KCAS to effectively calibrate the feel system for the gain scheduler. Pitch doublets, pitch captures, and rollercoaster maneuvers were performed at 220, 250, and 280 KCAS for familiarization of the basic Learjet control laws. Next a constant stick force per *g* (V^4/V^4) was flown for pilot familiarization. Maneuvers were flown at varying airspeeds using the V^4/V^4 control law to investigate the resulting *Fs/g*. The intent was to ensure the control laws were properly implemented to increase stick sensitivity as airspeed increased from 250 KCAS and became less sensitive at airspeeds less than 250 KCAS.

The utility of the VEST algorithm was observed during the following operationally representative maneuvers: air refueling, air-to-air, and air-to-ground

tracking tasks. Each maneuver was flown with three different gain schedules for comparison of the corresponding aircraft response. Three gain schedules were created using fed back calibrated airspeed values from the Learjet air data system (ADS), the VEST algorithm, and 250 knots to represent standby gains in the V^4/V^4 control law. Pilot comments were noted during each of the maneuvers and ratings were recorded for analysis. The analog scales and Pilot in the Loop Oscillation (PIO) rating scales can be found in Appendix H.

The inertial estimate of the VEST algorithm was not correctly integrated onto the VSS. Outputs from the inertial estimate were key parameters in the VEST algorithm and the stick command gain schedule was based on the corresponding VEST output airspeed. Therefore, GPS speed and AHRS heading information fed the wind estimator portion of VEST algorithm for these real time evaluations. The post-processed average inertial speed errors were within 2 percent of the input GPS ground speed and the heading error was within 1 percent of input AHRS heading.

5.3 Results and Analysis

The accuracy of the VEST algorithm was determined using flight test data. The results for inertial, wind, and resulting airspeed estimates are presented below. The ultimate goal was to test the VEST algorithm's ability to produce an accurate airspeed estimate without using the Learjet's air data system; however, as previously mentioned, a build up approach was employed during testing to verify accuracy incrementally. The results presented below follow the same build up that was used during testing.

Additionally, pilot comments for the implemented airspeed estimate used for gain scheduling during operationally representative maneuvers are presented.

5.3.1 Ground Inertial Estimate

Time history plots for inertial position (north, east, and altitude), velocity (north, east, and down), and attitude (roll, pitch, and yaw) were generated from flight test data, and can be found in Appendix G. Figure 5.8 is a sample time history plot of north velocity error with eighty percent confidence interval with and without GPS.

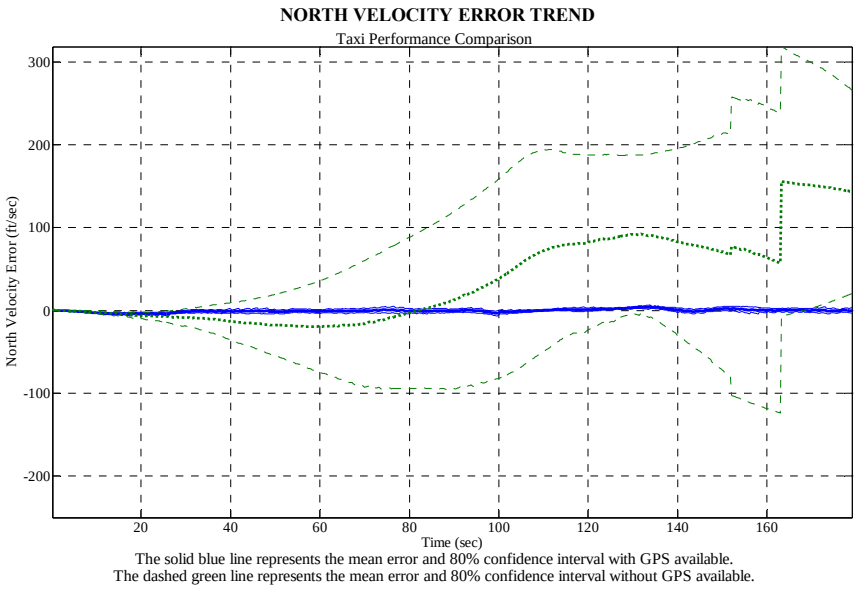

Figure 5.8. North Velocity Error Trend with and without GPS

When GPS updates were not available, the VEST algorithm experienced drift in all three axes. Results showed that the algorithm required GPS to provide an estimate to eliminate the effects of drift. Based on the error observed in the inertial speed estimate, test points without GPS updates were omitted from flight test.

5.3.2 Airborne Inertial Estimate

The VEST algorithm was updated by GPS every two seconds and as such the position errors were on the order of a thousandth of a coordinate degree. The magnitude of the north and east position errors remained relatively constant throughout all of the accomplished maneuvers, and was not a function of airspeed or maneuver. Figure 5.9 is a representative position error time history plot. Additional time histories can be found in Appendix G.

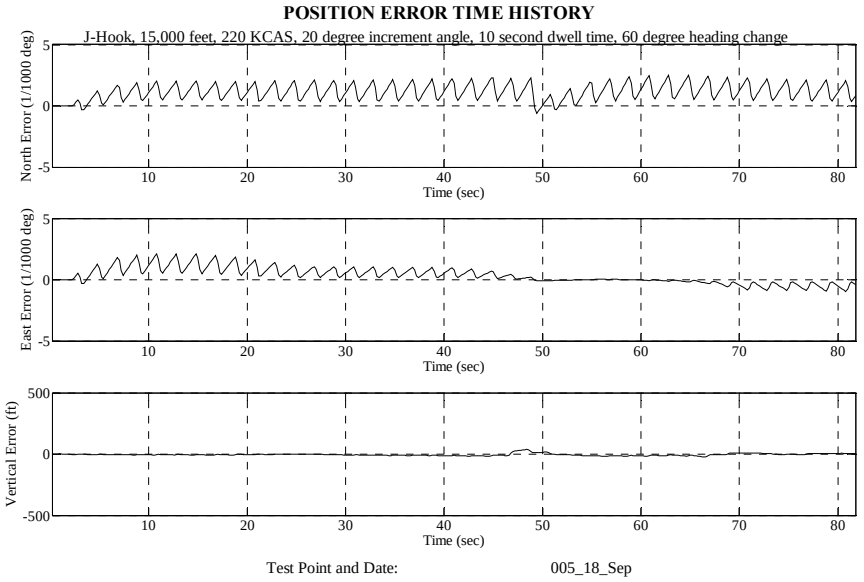

Figure 5.9. Position Error Time History

North and east velocity components of the inertial estimator were evaluated. Error trends for all of the accomplished maneuvers were similar, and the error was not a function of airspeed. Additionally it was observed that the magnitude of the errors were

similar in both the north and east directions. Neither aircraft maneuvers nor airspeeds affected the VEST inertial estimate error profiles. Figure 5.10 is a representative plot of velocity error time history for a J-Hook maneuver. Additional results for velocity errors are presented in Appendix G.

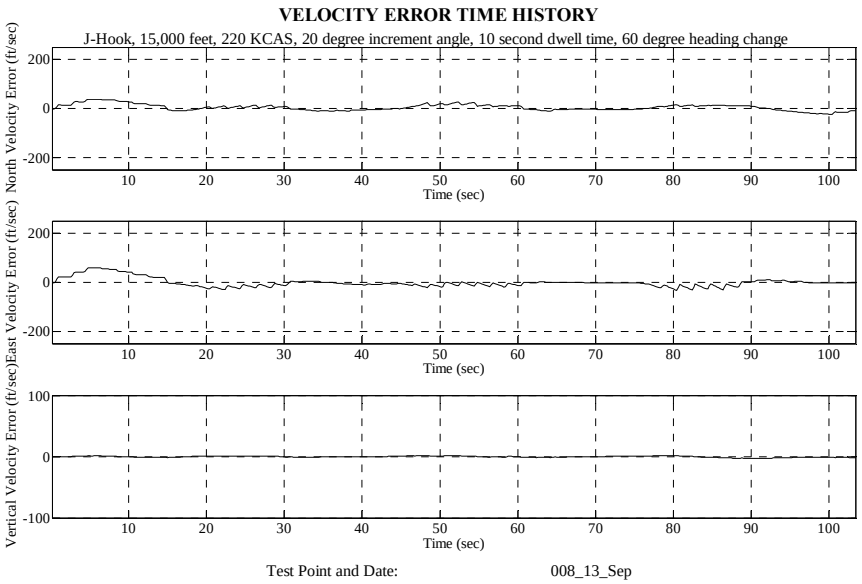

Figure 5.10. Velocity Error Time History

The magnitude of heading errors from the VEST algorithm remained relatively constant for all of the accomplished FTTs except for the Long Shot. Typically they remained less than ninety degrees, but errors in heading of up to 150 degrees were noted during the Long Shot maneuvers. The inertial estimator was expected to drift similar to an actual INS during the Long Shot Maneuvers due to the lack of aircraft accelerations in straight and level, unaccelerated flight. For all of the other FTTs, the heading error

tended to zero with time, but with increasing variability. The results indicate that some level maneuvering is required for the inertial estimate part of the VEST algorithm; however, this would be less of an issue with modern fighter aircraft which have state-of-the-art INS systems (something the Learjet did not have). Airspeed was also a significant factor in algorithm performance during the Sliceback maneuver. The higher speed test points resulted in a more desirable heading error profile (smaller magnitude and less variability). The complete set of heading error time history plots are presented in Appendix F.

5.3.3 Airborne Wind Estimate

The wind estimate was the second element needed in order to generate a true airspeed estimate. The VEST wind estimate was compared to the Learjet wind estimate but the Learjet provided wind did not consistently represent accurate wind conditions. As a result, no accurate truth source was available for the wind, so the accuracy of the VEST wind estimate could not be determined directly. However, the quality of the VEST airspeed estimate depends on the accuracy of the wind estimate, so the accuracy of the wind estimate can be indirectly evaluated based on the accuracy of the airspeed estimate presented in the next section. For completeness, the time history "wind error" plots for each of the maneuvers flown can be found in Appendix G. However, the "wind error" refers to the difference between the Learjet wind estimate and the VEST wind estimate (not actual wind and VEST wind). In the instances where the "wind error" was large, the corresponding VEST true airspeed error does not contain the errors seen in the "wind

error," indicating that the VEST wind estimate was accurate and the observed "wind error" was due to inaccuracies in the Learjet wind estimate.

A sample time history of Learjet wind and VEST wind estimates for a J-Hook maneuver is shown below in Figure 5.11.

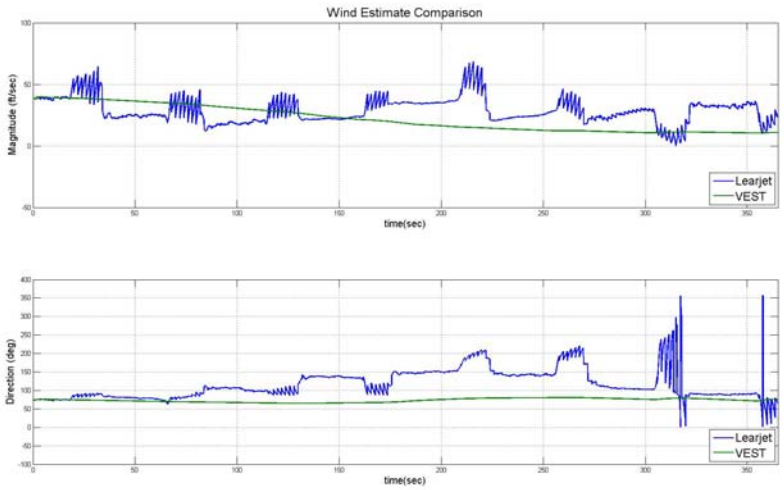

Figure 5.11. Learjet and VEST Wind Time History

In figure 5.11, the Learjet provided wind generated larger estimate variations than the VEST wind, and was not consistent with the actual wind profile. The corresponding "wind error" time history during the same J-Hook maneuver is shown below; the large errors in figure 5.12 are projected from Learjet wind estimate errors.

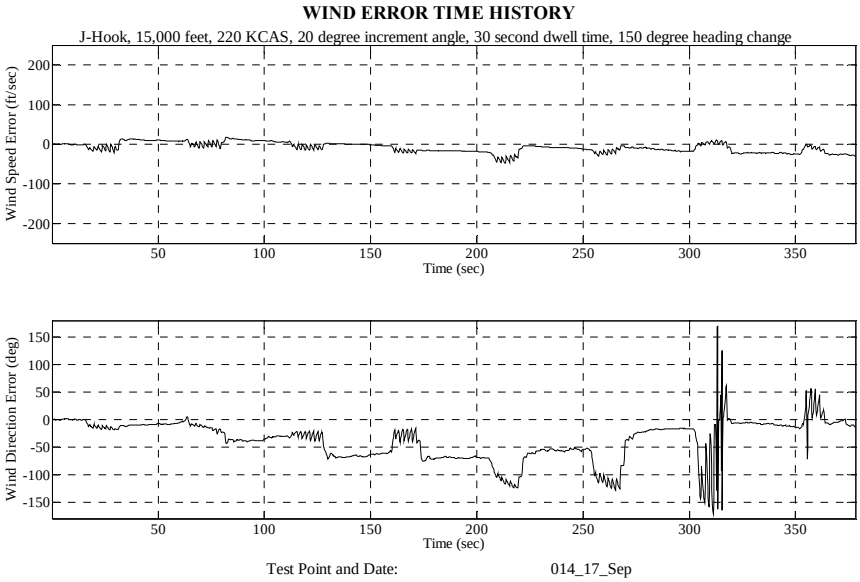

Figure 5.12. Wind Error Time History During J-Hook

5.3.4 Airborne Airspeed Estimate

The goal of the VEST algorithm was to provide a usable airspeed estimate following an air data system failure. The accuracy of the VEST algorithm airspeed estimate was determined from airspeed errors between the VEST algorithm airspeeds and Learjet air data values. Airspeed data from each maneuver tested, including all FTTs, operationally representative maneuvers, and landing approach tasks, were used in the analysis. Airspeed error time history plots, representing the primary results of this research, were created for each maneuver and can be found in Appendix F. An airspeed error time history plot for a J-Hook maneuver is shown below.

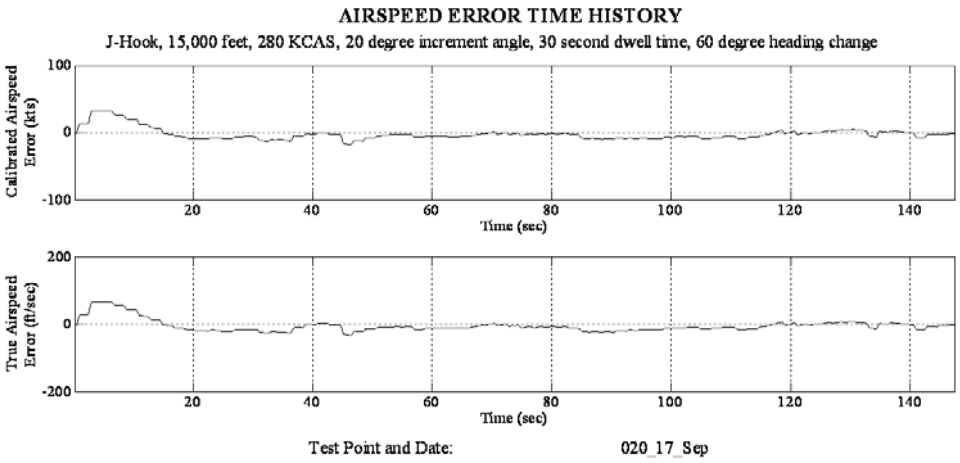

Figure 5.13. J-Hook Airspeed Error Time History

Similar error profiles were generated for both benign and dynamic maneuvers. For example, during benign air refueling maneuvers, the airspeed error profile tended to decrease once the aircraft was stabilized in the desired position, as seen in the figure below.

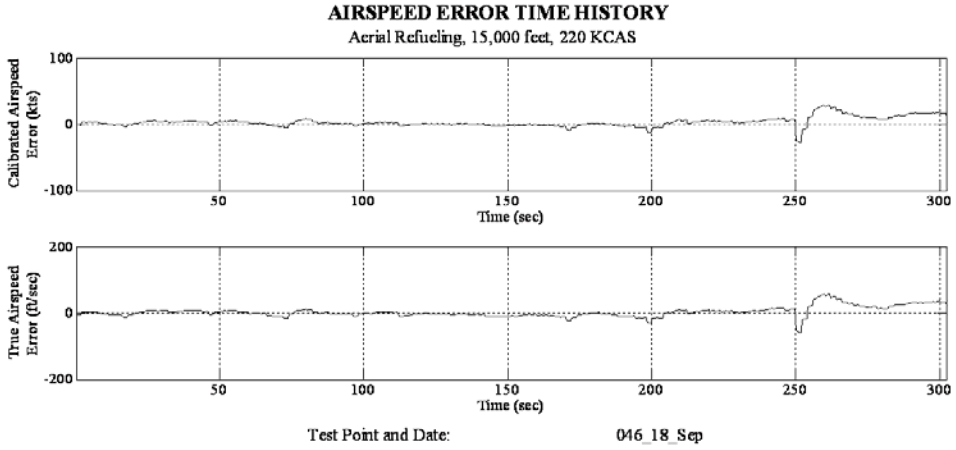

Figure 5.14. Air Refueling Airspeed Error Time History

Similarly, during a dynamic air-to-air tracking maneuver, errors tended to decrease once the aircraft was in a stabilized position. As seen in Figure 5.15, significant aircraft maneuvers produced airspeed error excursions at 105, 145, and 195 seconds respectively.

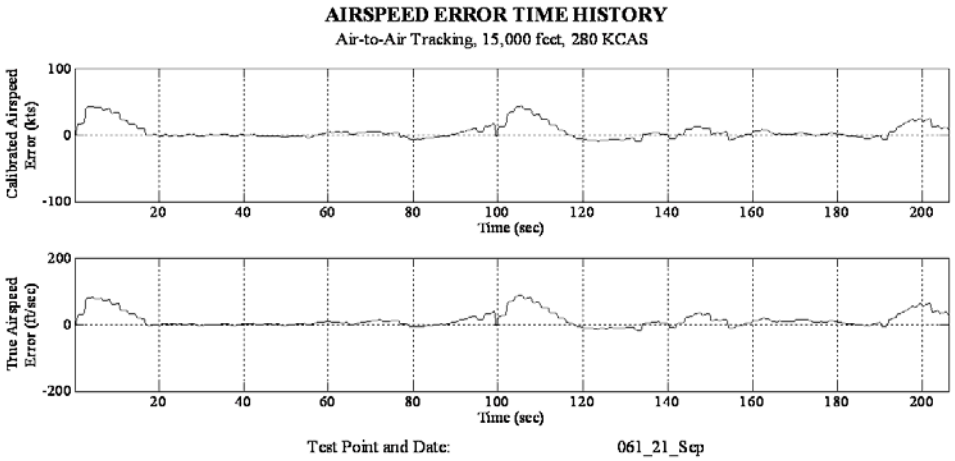

Figure 5.15. Air-to-Air Tracking Airspeed Error Time History

Less significant aircraft motions, such as between 20 and 90 seconds in Figure 5.15, did not create as large an impact on the error profile.

Overall, airspeed error excursions were a combination of inertial and wind estimate errors. The errors were largest during the turning portion of the maneuvers, and decreased after the aircraft was returned to a wings level attitude. Table 5.1 summarizes the average errors calculated during each maneuver.

Table 5.1. Average Airspeed Errors

Maneuver	Average TAS Error (knots)	Standard Deviation	Average CAS Error (knots)	Standard Deviation
J-Hook	2.2	8.2	1.9	6.7
Long Shot	42.1	43.8	32.9	36.1
Sliceback	15.3	24.4	11.7	20.8
Container	9.1	13.4	7.3	11.5
Air to Air Tracking	10.3	11.7	9.7	10.1
Air Refueling	3.3	17.8	4.3	15.3
Air to Ground Tracking	12.6	13.3	10.2	11.4
Landing Approach	6.4	21.4	7.15	18.2

Individual airspeed excursions during turning portions of the maneuvers were typically in excess of the average errors shown above. The excursions were a function of both inertial and wind estimate errors, with the wind estimate providing the largest portion of the error. Following the turning portions of the maneuvers, airspeed errors were reduced significantly.

The largest average error determined was during the Long Shot maneuver. The primary source of error during this maneuver occurred after five minutes of non-maneuvering flight. Ground and wind velocity estimate errors during the Long Shot maneuvers were as much as 150 feet per second after 15 minutes. The large errors were due to the design of the VEST algorithm. Non-maneuvering flight was expected to challenge the algorithm outputs due to the nature of inertial estimation. Inertial heading and estimated airspeeds diverged after approximately five minutes of non-maneuvering flight, as seen below.

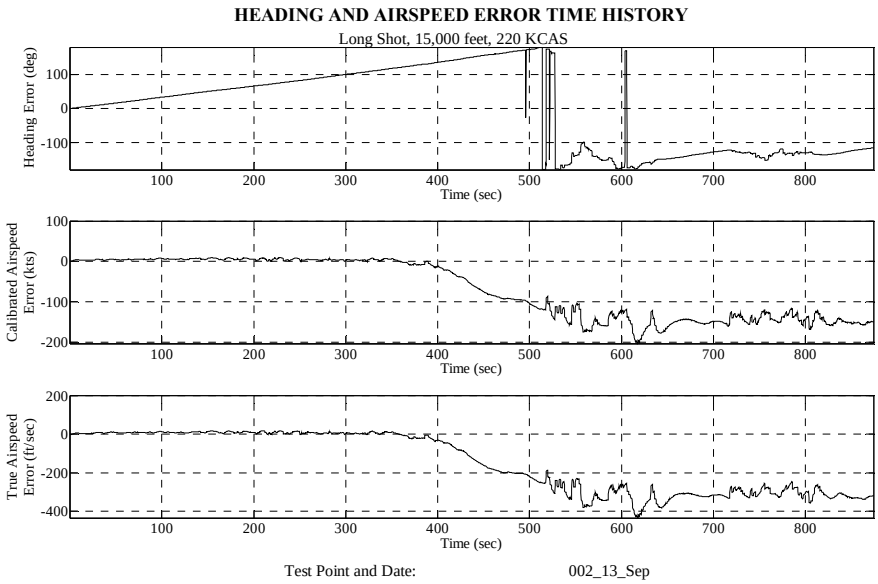

Figure 5.16. Heading and Airspeed Error Divergence

The refueling (lasting five minutes) and the landing approaches (lasting over eleven minutes) did not involve significant amounts of maneuvering; heading changes during these maneuvers were as small as four degrees for up to two minute time periods. However, the small maneuvers performed during these tasks were sufficient, compared to the Long Shot maneuver, for the VEST algorithm to continue to provide airspeed estimates, as seen in the figure below.

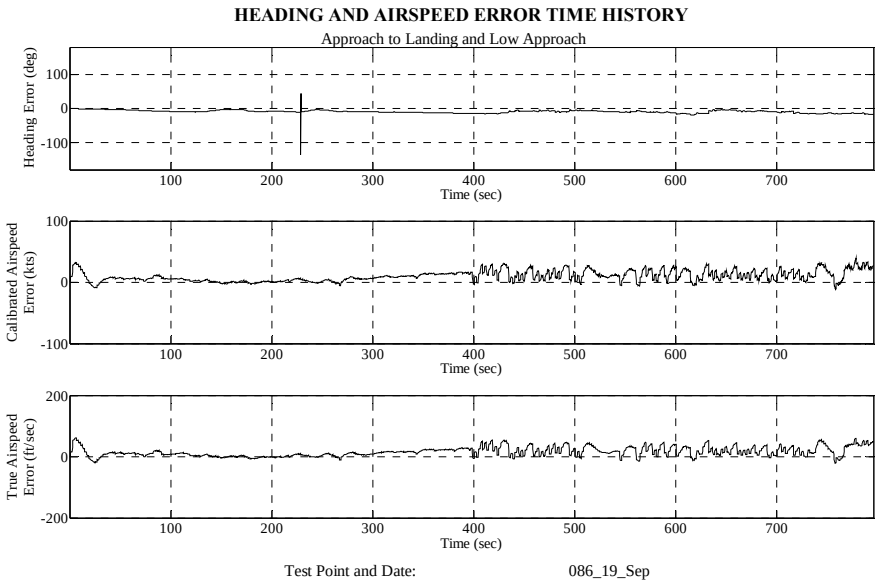

Figure 5.17. Heading and Airspeed Error, Bounded

The lowest average true airspeed error occurred during the J-Hook maneuvers. However, there was no correlation determined between maneuver type and airspeed error. The less dynamic maneuver, and short maneuver duration, during the J-Hooks resulted in a lower average airspeed error than during straight and level or continuous turning maneuvers. While the J-Hook maneuvers had the smallest airspeed errors, the J-Hooks also had the shortest maneuver duration.

Overall, the airborne accuracy of the VEST algorithm was determined. The average true airspeed accuracy was 21 feet per second (12 knots). The average calibrated airspeed was 10 knots (17 feet per second). The VEST airspeed estimate accuracy was determined to be independent of maneuver type, so long as some type of maneuvering was accomplished.

5.3.5 Gain Scheduling Pilot Comments

The results for gain scheduling using the VEST estimated airspeed were divided into the following three operationally representative tasks: air refueling, air-to-air tracking, and air-to-ground tracking. A description of each of the maneuvers along with corresponding pilot comments are presented next.

5.3.5.1 Air Refueling

The maneuver started with the target T-38 aircraft stabilized on conditions at 15,000 feet pressure altitude, 220 knots calibrated airspeed (KCAS), with the test aircraft at a simulated observation position. The first task was to maneuver to the pre-contact position approximately 100 feet in trail. After stabilizing for 30 seconds, the test aircraft closed into the contact position, 50 feet in trail. After stabilizing for 30 seconds straight and level, the target was tracked through 90 degrees of turn using 15 degrees bank. The maneuver was repeated using 280 KCAS.

When using the Air Data System (ADS) schedule, the control force required to produce a desired pitch response was higher than expected, but predictable. There was no delay in the pitch response. Further, there was no tendency to overshoot or undershoot and typically minimal workload was encountered when flying to the desired position. No undesirable motions were noticed (Pilot in the Loop Oscillation Rating (PIOR) 1). This performance met expectations as the V^4/V^4 control law, with ADS airspeed fed back, demonstrated a constant stick force per *g* throughout the maneuver.

Using the VEST schedule, the control force required to produce a desired pitch response was less than the ADS gain schedule, and a high stick sensitivity was apparent.

There was no noticeable delay in the pitch response and some unpredictability was noticeable during precise maneuvers in the contact position. There was a mild tendency to overshoot and typically tolerable workload was encountered when flying to the desired position throughout the refueling task. Due to the sensitivity and predictability, there was a tendency for undesirable motion to be induced easily (PIOR 3). Stick sensitivity resulted when the fed back airspeed was faster or slower than actual values. Unpredictability resulted from variability of error in the fed back VEST airspeed.

Using the Standby Gain schedule, the control force required to produce a desired pitch response was higher as compared to VEST schedule case, and a high stick sensitivity was apparent. There was no noticeable delay in the pitch response and it was predictable. The higher control forces increased the workload and this led to task saturation. Typically, a high workload was encountered to obtain adequate performance throughout the refueling task. Due to the stick forces, there was a tendency for undesirable motion to be induced easily (PIOR 3). The high stick sensitivity was due to the large and fixed error in fed back airspeed. There was no variability in the fed back airspeed (due to the constant airspeed standby gain) and the aircraft response was predictable.

5.3.5.2 Air-to-Air Tracking

The Learjet was equipped with an optical sight that was used during air-to-air tracking. The test aircraft set up 3,000 feet in trail and 1,000 feet below the target T-38 aircraft. The first task was to capture the jet nozzle of the target with the upper mark of the sight. Once the capture task was complete and the aircraft were co-altitude, the next

task was to track the target's canopy through 180 degrees of turn with the target using 50 degrees of bank. During the turn, the target varied pitch to maintain altitude within 1,000 feet of the starting altitude.

Using the ADS schedule, the control force required to produce a desired pitch response was marginally high but not objectionable. There was no noticeable delay in the pitch response and it was predictable. There was no tendency to overshoot or undershoot and typically minimal workload was encountered when tracking the target. No undesirable motions were observed (PIOR 1).

Using the VEST schedule, the control force required to produce a desired pitch response was less than as compared to the ADS schedule, and a high stick sensitivity was apparent. There was no noticeable delay in the pitch response but predictably remained in question. In one of the tracking tasks, the response was highly predictable in the first 90 degrees of turn. Subsequently, there was a change in the stick forces and the response became unpredictable. Despite this unpredictability, the target tracking was achieved at the cost of extensive workload. Due to the sensitivity and unpredictability, there was a tendency for undesirable motion to be induced easily (PIOR 3).

Using the Standby Gain schedule, the control force required to produce a desired pitch response was higher as compared to the VEST schedule and a high stick sensitivity was apparent. There was no noticeable delay in the pitch response and it was predictable. The higher control forces increased the workload and this led to task saturation. Typically, a high workload was encountered to obtain adequate performance throughout

the air-to-air tracking task. Due to the stick forces, there was a tendency for undesirable motion to be induced easily (PIOR 3).

5.3.5.3 Air-to-Ground Tracking

The Learjet's optical sight was used during air-to-ground tracking. Operationally representative ground attack maneuvers were conducted at 220 and 280 KCAS for a descent of 4,000 feet. Since 20 degree dives resulted in speeds rapidly approaching 300 KCAS at idle power, shallower dive angles were used. Initial test points were conducted by a simulated ramp delivery (straight ahead push) at the dive angle required to maintain speed. The dives were shallow, so the pilot attempted to evaluate the gain schedules by rapidly changing aim points in the dive. Recovery was conducted with a 2.0 *g* level pull with mild heading changes during the climb. The control inputs required to complete these shallow angle dives were all small. The inputs were so small in fact that the pilot noticed very little difference among the three gain schedules. Minimal calibrated airspeed error was observed during the VEST test points thereby showing the ADS and VEST gain schedules to perform similarly (indistinguishable). With the standby gain schedule, flying faster than the reference airspeed (250 knots) resulted in increased stick sensitivity, while flying at lower speeds resulted in less objectionable stick sensitivity.

The test points were repeated by selecting a simulated target area that had multiple targets separated by approximately one mile. The test aircraft was then flown to a point roughly perpendicular to the attack axis at 200 KCAS. An aggressive roll to approximately 120 degrees, and subsequent pull (2.0 *g*) was accomplished to aggressively capture a target on the near side of the target area. Power was reduced to

idle. As airspeed increased through 220 KCAS, the aim-point was shifted to the far side of the target area (stabilizing the airspeed). Then the dive angle was aggressively increased to a third aim-point. As airspeed increased through 280 KCAS, a fourth target on the far side of the target area was tracked until 300 KCAS was achieved. A wings level pull to 2.0 *g* was used to recover followed by a heading change of approximately 90 degrees. The process is illustrated below.

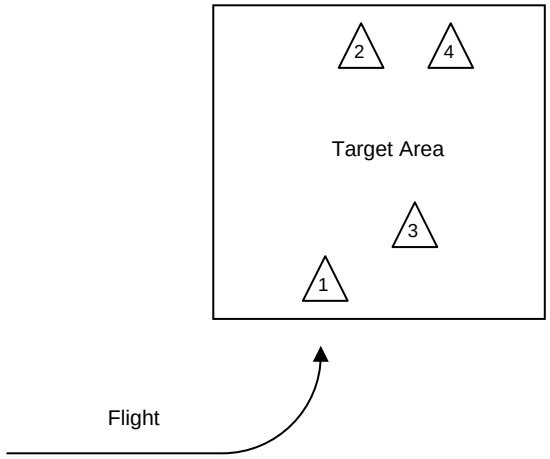

Figure 5.18. Air-to-Ground Target Area Description

This technique highlighted the gain schedule differences as airspeeds changed during the task of ground attack. Once again, the calibrated airspeed error observed with VEST gain scheduling was small (approximately 10 knots) and the ADS and VEST gain schedules were both assessed as desirable. The standby gain schedule, however, was not as predictable or desirable. At the slow speed roll in, the aircraft was very sluggish and difficult to change pitch attitude. At the higher speed tracking and recovery, the aircraft

was extremely sensitive resulting in a stair-stepped pitch response. The tracking task became more difficult as the feel of the aircraft changed through the dive.

Aircraft flying these operational maneuvers would typically be fighters with a speed range in excess of 600 knots. Due to the VSS envelope on the Learjet, the standby gain schedule was tested over a 100 knot speed range with increased stick sensitivity to simulate a wider speed range. The increased stick sensitivity was used to highlight the effect of VEST algorithm errors. The VEST algorithm demonstrated the capability to reduce the magnitude of airspeed error over standby gains (to reduce sensitivity effect) at the cost of inducing variability. The effect of the variability was extremely exaggerated due to the implemented gain schedule.

5.4 Summary

This chapter presented the methods and results of implementing the VEST algorithm in flight test. The accuracy of the VEST algorithm airspeed estimate was determined by flying specially developed FTTs and operationally representative tasks. The three operationally representative tasks highlighted the capabilities and limitations of the VEST algorithm. The true airspeed estimate results in section 5.3.4 demonstrated very positive VEST algorithm performance. Errors in airspeed magnitude (more common in fed back Standby Gain airspeeds) resulted in stick sensitivities which adversely affected handling qualities. Errors in airspeed variability (more common in fed back VEST airspeeds due to the exaggerated gain schedule) resulted in unpredictable aircraft response which adversely affected handling qualities. Therefore, for operationally representative tasks, the advantage of the VEST algorithm over a single

airspeed standby gain could not be fully evaluated. However, based on the accuracy of the VEST airspeed estimate and the difficulties observed during air-to-ground tracking when using standby gains amidst large and rapid flight condition changes, it is reasonable to assess that the VEST algorithm would provide a noticeable advantage over standby gains when used in an unexaggerated gain scheduling control system. Conclusions and directions for possible future applications are presented in the next chapter.

6. Discussion

6.1 Overview

The objective of this research was to develop an algorithm to estimate airspeed following an air data system failure. The Velocity Estimate (VEST) algorithm was developed to provide the airspeed estimate. The estimate would need to be accurate enough for use in the cockpit and for gain scheduling. The algorithm used known techniques to produce an inertial estimate. Then, the inertial estimate was used in a new wind estimation technique to further produce a continuous wind estimate, and ultimately a true airspeed estimate. The VEST algorithm concept could provide a valuable piece of unknown information when air data is unavailable, that could be used before resorting to standby gains or the use of an atmospheric wind model estimate. Possible future research areas include improved inertial estimate formulation (or demonstration on an aircraft with an INS), airspeed estimate filtering, and incorporation of a broader testing envelope.

6.2 Conclusions of Research

The purpose of the VEST algorithm was to continuously estimate true airspeed following a complete air data system failure. Following an air data system failure, all sensors providing airspeed, altitude, temperature, angle of attack, and pressure readings would be unavailable for use by aircraft systems. The VEST algorithm was developed from theory, refined in simulation, and implemented in flight test to provide an estimate of the lost air data information. The airspeed estimate was used to schedule gains appropriate to the estimated flight condition. Airspeed and altitude information were also

displayed in the cockpit. The average true airspeed error from flight test was 21 feet per second (12 knots) and the average calibrated airspeed error was 10 knots (17 feet per second).

No correlation was determined between maneuver type and overall true airspeed error. However, some maneuvering was required to reduce the effect of drift on the inertial speed and heading estimates. Inertial estimates during long duration straight and level flight diverged after approximately five minutes of non-maneuvering flight. Observed maneuvers, exceeding five minutes in duration during operationally representative and approach to landing maneuvers, that resulted in heading changes on the order of four degrees were enough to prevent the inertial estimate divergence. Overall, the VEST wind and resulting true airspeed estimates were most accurate in a wings level attitude following maneuvers.

The VEST algorithm airspeed estimate was used to schedule stick command gain during operationally representative maneuvers. Aircraft handling qualities were evaluated during air refueling, air-to-air tracking, and air-to-ground tracking tasks. The tasks were accomplished comparing the VEST airspeed estimate to the single airspeed value representing standby gains. The VEST airspeed estimate produced airspeed variability errors that resulted in unpredictable aircraft response. The standby gain airspeed value produced errors in airspeed magnitude that resulted in increased stick sensitivity as compared to the same tasks accomplished with the VEST estimate. However, the effect of the VEST variability errors was exaggerated due to the implemented gain schedule, and therefore the operational value of the reduced sensitivity

compared to a standby gains default airspeed could not be conclusively evaluated. However, the VEST airspeed estimate was very accurate. Additionally, the undesirable, sluggish aircraft response observed during air-to-ground tracking tasks using standby gains, made the tasks difficult to accomplish. Therefore it is reasonable to conclude that the VEST algorithm would provide a noticeable advantage over standby gains when used in an unexaggerated gain scheduling control system.

6.3 Significance of Research

Modern aircraft rely on air data information for normal flight operations. Because many systems rely on accurate air data information, much time is devoted to the proper calibration of the aircraft's air data system in the early phases of flight test [Erb 2005]. When the air data system fails, the VEST algorithm offers an alternate airspeed solution. Apart from starting conditions, air data is not a requirement for the VEST algorithm airspeed estimate. The performance of the VEST algorithm demonstrates the potential of this type of airspeed estimation as a back up system following air data failures.

In addition, much research has been accomplished in the past to determine aircraft position and inertial speed using an inertial navigation system (INS). A tightly coupled INS can make inertial velocity (aircraft groundspeed) very accurate. However, even with the best aided INS solution, groundspeed alone is unusable for high performance aircraft gain scheduling [Webster 2007]. Similarly, a true airspeed solution using INS groundspeed and last known winds (or an atmospheric wind model) would not account for realistic changes in wind from high altitudes to landing conditions, and would also be unusable for gain scheduling [Webster 2007].

The innovative VEST algorithm presented in this thesis combined Kalman filtering with geometric concepts based on the relationship between airspeed, wind speed, and groundspeed to continuously estimate actual wind conditions. The sum of the inertial groundspeed and the continuous estimate of wind formed the true airspeed estimate. The estimated airspeed was not based on last known wind, and was not based on an assumed wind model; rather, the airspeed continuously represented an accurate estimate of actual conditions. The VEST algorithm provided a true airspeed estimate that when converted to calibrated airspeed, was used successfully to schedule stick command gain during the performance of operationally representative tasks.

Applying the three-tiered gain scheduling methodology from section 1.5, an aircraft could experience an air data system failure, switch to gain scheduling using the VEST algorithm estimate, and never require input from the pilot to find the correct gain schedule. The pilot's attention could remain focused on the tactical situation until time was available to address implications of the air data system failure and associated non-HOTAS related tasks. The standby gain scheduling could remain in place for safety considerations following a VEST failure, as a third line of defense.

Going one step further, hypersonic applications that require airspeed information beyond the region where probes sensing air data can function [Stevens and Lewis 2003], could make use of the VEST algorithm. As the vehicle is transiting a slower speed region, the air data system could be used to initiate the VEST algorithm. Since the VEST algorithm does not require air data information to continue operation, it could be used to provide airspeed as the vehicle accelerates to hypersonic speeds. Although the wind

magnitude component would be small compared to the hypersonic true airspeed component, the potential to use the VEST algorithm concept does exist.

6.4 Recommendations for Future Research

The inertial portion of the VEST algorithm used flight control computer accelerations and rates to provide position, velocity, and attitude estimates. The sensors provided less than INS quality information, and inertial estimates required an update from GPS for implementation in flight test. Without an update to the inertial estimate, the algorithm's performance was inadequate for aircraft airspeed estimation. With the updates however, the algorithm produce the airspeed results shown above. The average 12 knot true airspeed error could be reduced further by improving performance of the inertial portion of the VEST algorithm or by incorporating the use of the VEST algorithm on an aircraft with an existing INS.

The VEST algorithm airspeed estimate produced errors in airspeed variability that were noticeable in the implemented gain schedule. The variability errors resulted in unpredictable aircraft responses that adversely affected handling qualities. The airspeed errors resulted from a combination of inertial and wind estimates, the latter of which were susceptible to large errors during turning maneuvers. The wind estimate errors encountered during turns contributed to the overall airspeed variability. No effort was made to filter the VEST estimated airspeed values before use in gain scheduling. Future research could filter airspeed, either constantly or during turning maneuvers, to smooth the airspeed variability and decrease unpredicted aircraft response.

Due to the VSS envelope, the standby gain schedule was tested over a 100 knot speed range with increased stick sensitivity (V^4/V^4 law) to simulate a wider speed range. The increased stick sensitivity was used to highlight the effect of VEST algorithm errors. The VEST algorithm demonstrated the capability to reduce the magnitude of airspeed error over standby gains (to reduce sensitivity effect) at the cost of inducing variability. The implemented gain schedule had large gain changes within a small airspeed region; therefore, the airspeed variability from the VEST algorithm led to unpredictability in aircraft control. As a result, the effect of VEST reduced magnitude airspeed errors versus fixed standby gain errors could not be determined. To investigate the operational advantage of the VEST reduced magnitude airspeed errors over standby gains, algorithm performance could be tested in a less exaggerated gain schedule over a wider speed envelope.

6.5 Summary

The VEST algorithm demonstrated a new method of estimating airspeed without the use of air data information. VEST estimated airspeeds closely matched actual conditions throughout maneuvers during flight testing on the N101VS variable stability Learjet. The usefulness of VEST algorithm airspeed estimates over standby gains, for use in gain scheduling, could be better determined over a wider speed envelope where a less exaggerated schedule could be employed. Allowing for modifications, the application of the VEST algorithm has potential beyond the subsonic airspeed estimates demonstrated in this research.

Bibliography

Anderson, John D. *Introduction to Flight, Fifth Edition*. New York: McGraw-Hill, Incorporated, 2005.

Ball, J., C. Berthe, S. Buethe, P. Deppe, R. Easter, L. Knotts, M. Parrag, J. Peer. *Learjet Flight Syllabus and Background Material for the USAF/SUN Test Pilot School Variable Stability Programs*. Niagara Falls: Calspan Flight Research Group, 2006.

Boas, Mary L. Mathematical Methods in the Physical Sciences, Third Edition. New Jersey: John Wiley and Sons, Incorporated, 2006.

Brogan, William L. *Modern Control Theory, Third Edition*. New Jersey: Prentice Hall, 1991.

Erb, Russell. *Pitot-Statics and the Standard Atmosphere*. Edwards AFB, CA: USAF Test Pilot School Pitot-Statics Textbook, 2005.

Department of Defense (DoD). *USAF Test Pilot School Flying Qualities Phase Textbook, Part IV*. Air Force Flight Test Center, Edwards AFB, CA, 2002.

Gray, Doug. "Using GPS to Accurately Establish True Airspeed," unpublished paper available at http://www.ntps.edu/HTML/Downloads, 1998.

Ito, Daigoro, Jennifer Georgie, John Valasek, Donald T. Ward. Reentry Vehicle Flight Controls Design Guidelines: Dynamic Inversion. NASA/TP- 2002-210771.

Kayton, Myron and Walter R. Fried. *Avionics Navigation Systems, Second Edition*. New York: John Wiley & Sons, Incorporated, 1997.

Lin, Ching-Fang. *Modern Navigation, Guidance, and Control Processing*. New Jersey: Prentice Hall, 1991

Maybeck, Peter S. *Stochastic Models, Estimation, and Control, Volume 2*. New York: Academic Press Incorporated, 1982.

McLaren, Scott A., Corey Beaverson, William Rothermel, Sreeram Jayashankar, Donald Powers. *Backup Velocity Estimate Following Air Data System Failure*. AFFTC-TIM-07-09. Final Technical Information Memorandum, 2007.

Nelson, Robert C. *Flight Stability and Automatic Control, Second Edition*. Boston: McGraw-Hill, Incorporated, 1998.

Sanders, Mark S. and Ernest J. McCormick. *Human Factors in Engineering and Design, Seventh Edition*. New York: McGraw Hill, Incorporated, 1993.

Stevens, Brian L. and Frank L. Lewis. *Aircraft Control and Simulation, Second Edition*. New Jersey: John Wiley & Sons, Incorporated, 2003.

Webster Fred. AFFTC Flight Control Systems Technical Expert / YD-3, 773 TS/ENFA, Edwards Air Force Base, CA, 661-277-6627. Personal interview. 9 July 2007.

Wylie, C.R., Jr. *Advanced Engineering Mathematics, Third Edition*. New York: McGraw-Hill Book Company, 1960.

Vita

Major Scott A. McLaren graduated from Bowie High School in Bowie, Maryland. He entered undergraduate studies at the United States Air Force Academy in Colorado Springs, Colorado, where he graduated with a Bachelor of Science degree in Engineering Sciences in May 1996. Upon graduation, he was commissioned as a 2nd Lieutenant in the United States Air Force.

He served nine months at Headquarters Air Force Space Command at Peterson Air Force Base, Colorado before beginning Specialized Undergraduate Pilot Training at Laughlin AFB, Texas. In April 1999, he was assigned to the 77th Fighter Squadron, Shaw Air Force Base, South Carolina where he flew the F-16. In 2002 he arrived at Luke Air Force Base, Arizona to serve as an instructor pilot for basic F-16 Training. In August 2005, he entered the Graduate School of Engineering and Management, Air Force Institute of Technology to complete course work and initial research. From January through December 2007 he was enrolled as a student at the United States Air Force Test Pilot School. Upon graduation, he will be assigned to the 445th Flight Test Squadron, Edwards Air Force Base, California.

Appendix A. Airspeed Estimation Theory Model

In the figure below, the Three-Vector Approach is depicted in green, the Two-Vector Approach is depicted in gray, and the Kalman Filter Approach is depicted in orange.

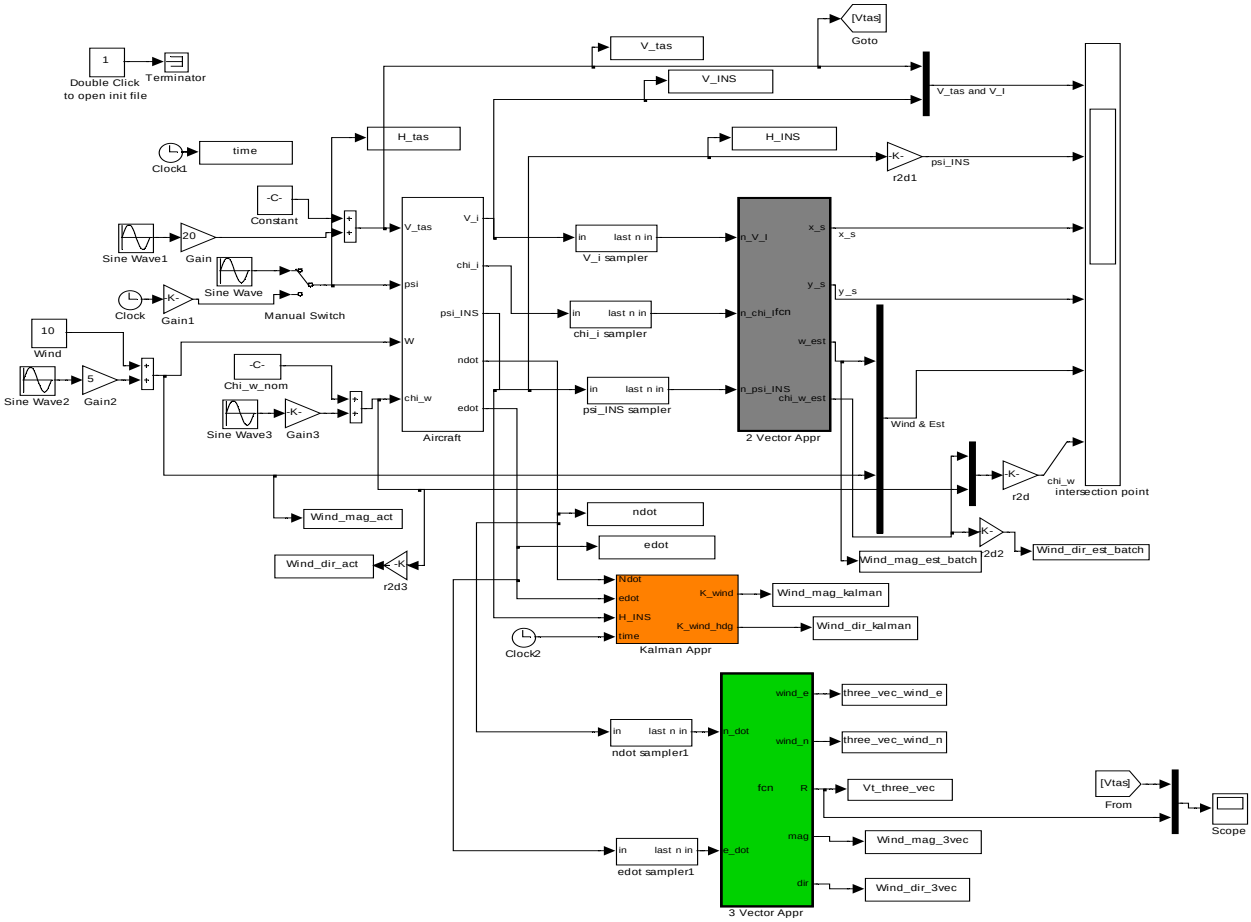

Figure A.1. Model for Wind Estimate Comparison

Appendix B. Airspeed Estimation Theory Plots

The first set of plots (section B.1) were taken from the three wind estimation techniques described in Chapter 3, the Three-Vector (Green data on each plot), Two-Vector (blue data), and Kalman Filter (Red data) Approaches. The plots are arranged together by the number of samples taken (sections B.1.1 – B.1.3) and are labeled with input wind and true airspeed conditions. The second set of plots (section B.2) were taken from the dynamic inversion technique and the Kalman Filter Approach.

B.1. Wind Estimator Results

B.1.1. Wind Direction and Speed Using 150 Samples

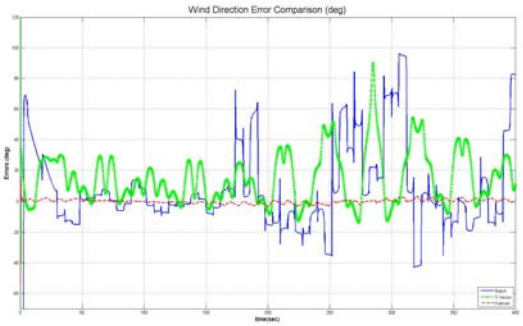

10 knot Wind, 100 knot True Airspeed

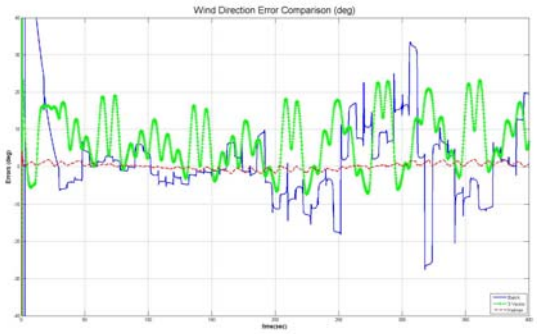

20 knot Wind, 100 knot True Airspeed

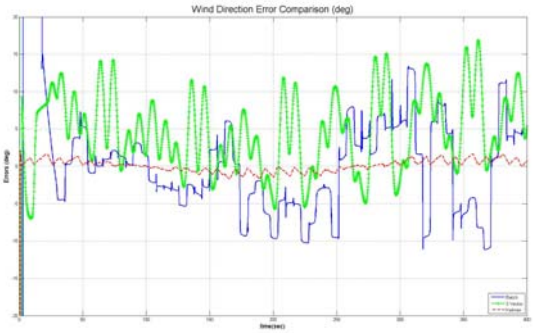

30 knot Wind, 100 knot True Airspeed

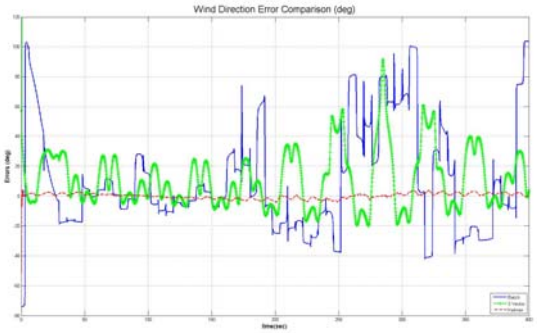

10 knot Wind, 200 knot True Airspeed

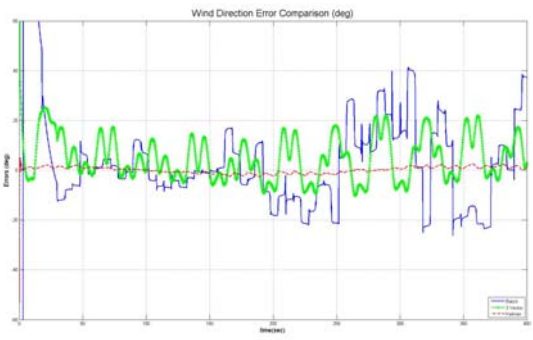

20 knot Wind, 200 knot True Airspeed

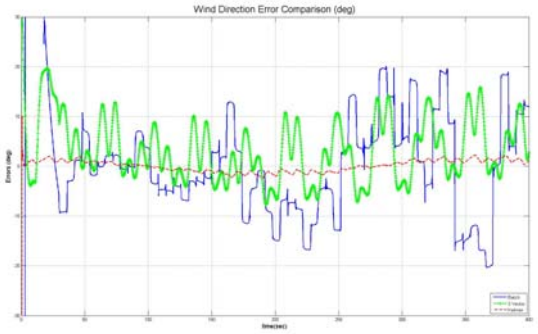

30 knot Wind, 200 knot True Airspeed

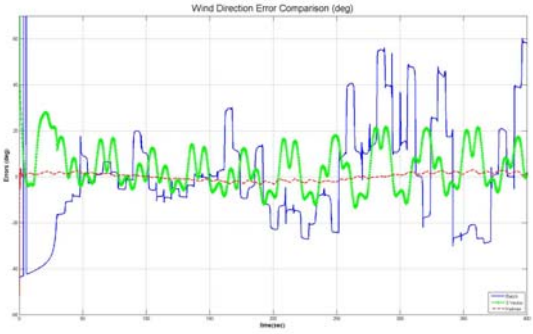

10 knot Wind, 300 knot True Airspeed

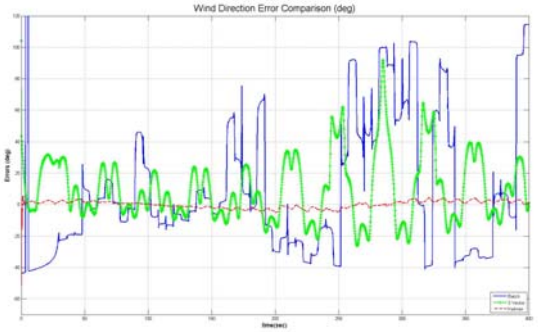

20 knot Wind, 300 knot True Airspeed

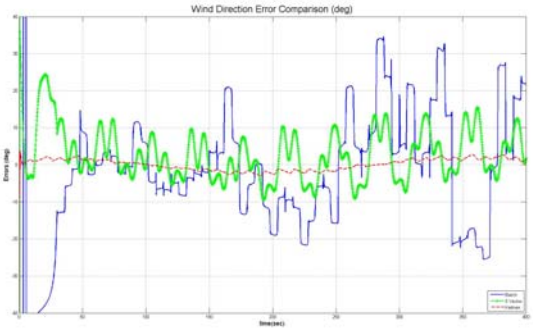

30 knot Wind, 300 knot True Airspeed

Wind Speed Using 150 Samples

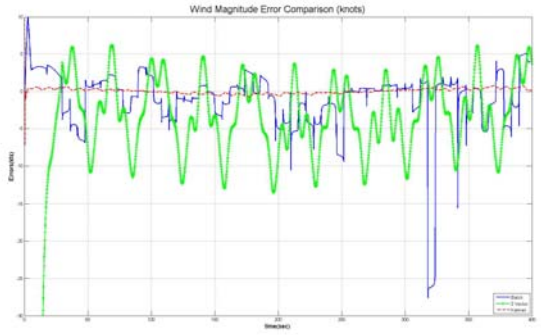

10 knot Wind, 100 knot True Airspeed

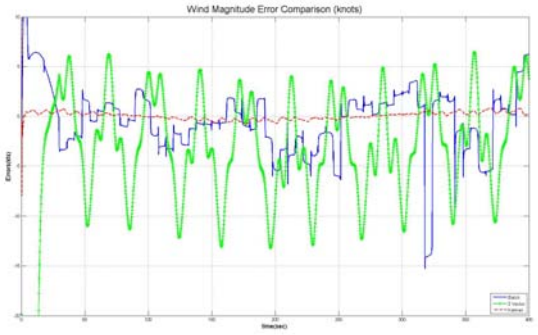

20 knot Wind, 100 knot True Airspeed

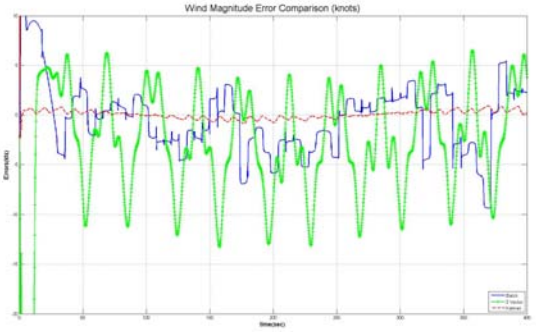

30 knot Wind, 100 knot True Airspeed

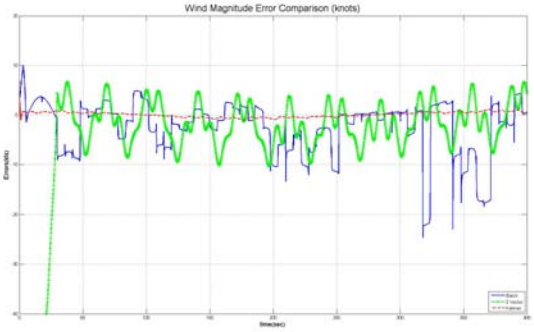

10 knot Wind, 200 knot True Airspeed

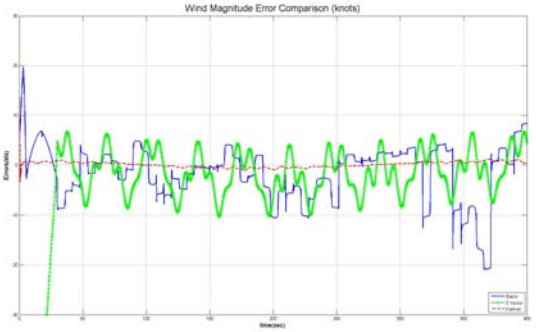

20 knot Wind, 200 knot True Airspeed

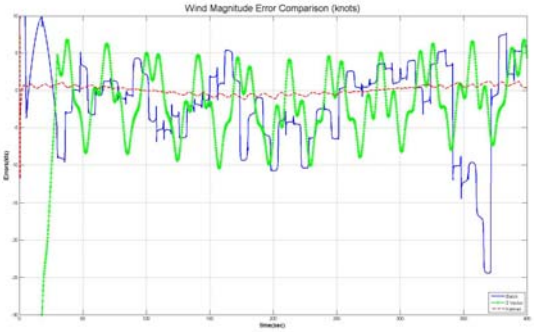

30 knot Wind, 200 knot True Airspeed

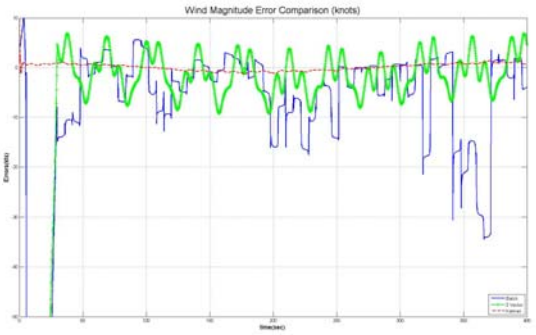

10 knot Wind, 300 knot True Airspeed

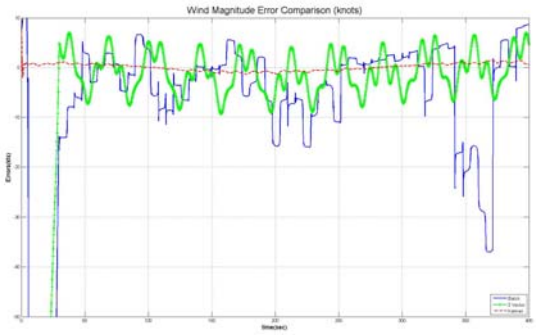

20 knot Wind, 300 knot True Airspeed

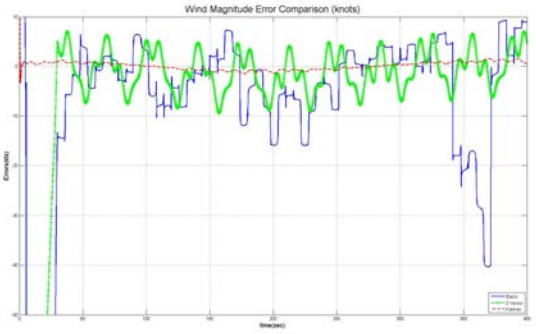

30 knot Wind, 300 knot True Airspeed

B.1.2. Wind Direction and Speed Using 250 Samples

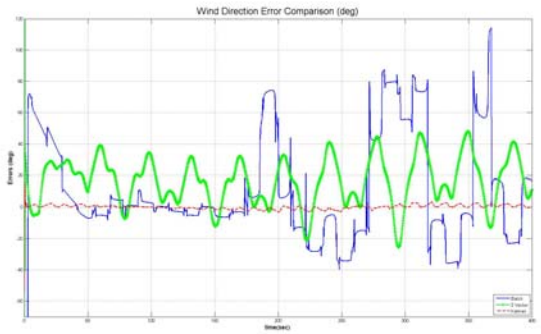

10 knot Wind, 100 knot True Airspeed

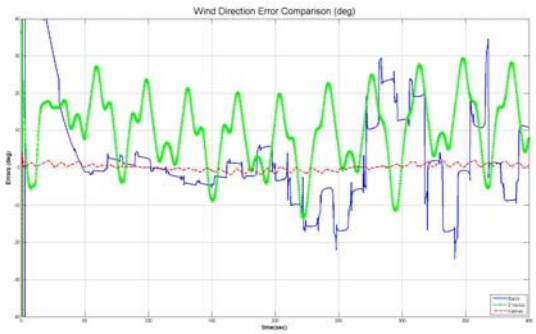

20 knot Wind, 100 knot True Airspeed

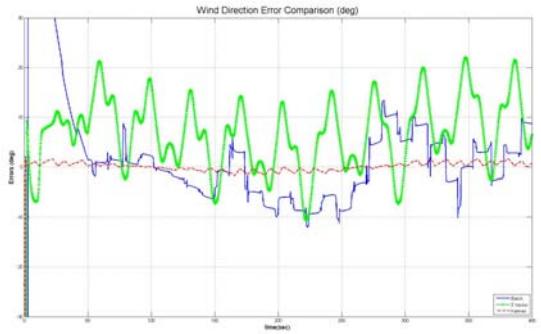

30 knot Wind, 100 knot True Airspeed

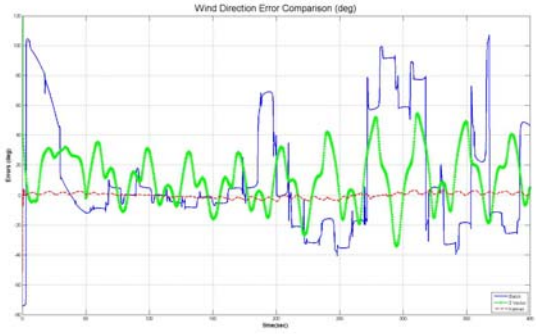

10 knot Wind, 200 knot True Airspeed

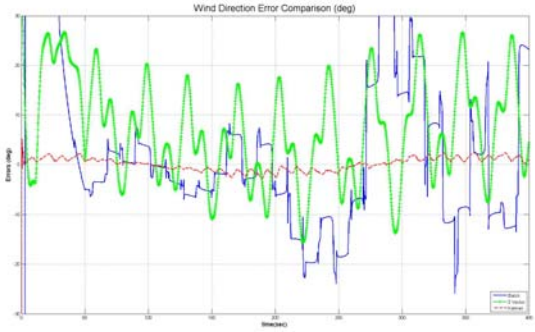

20 knot Wind, 200 knot True Airspeed

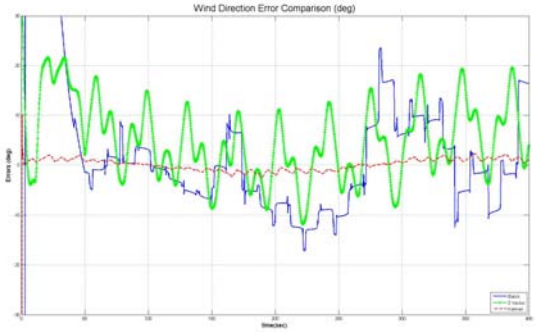

30 knot Wind, 200 knot True Airspeed

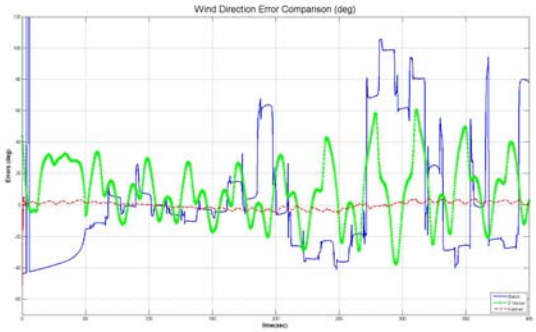

10 knot Wind, 300 knot True Airspeed

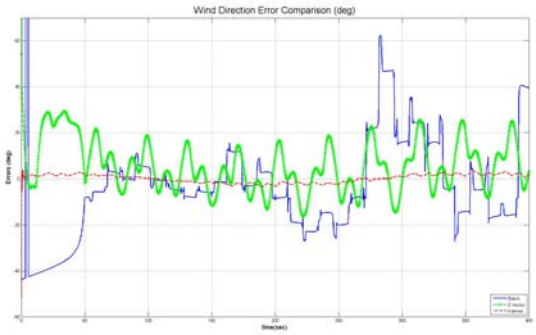

20 knot Wind, 300 knot True Airspeed

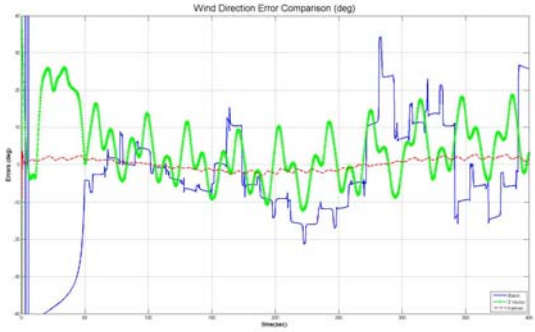

30 knot Wind, 300 knot True Airspeed

Wind Speed Using 250 Samples

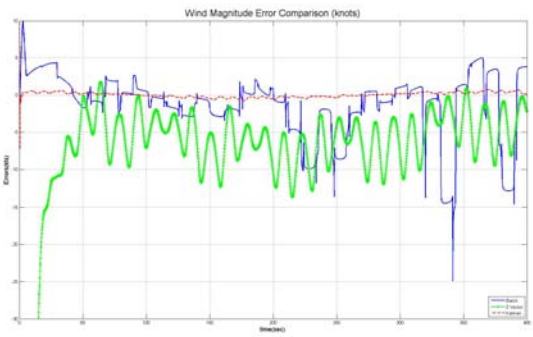

10 knot Wind, 100 knot True Airspeed

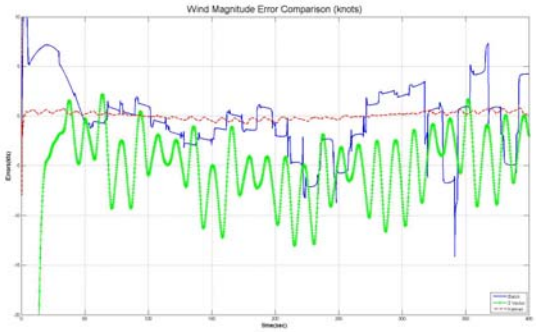

20 knot Wind, 100 knot True Airspeed

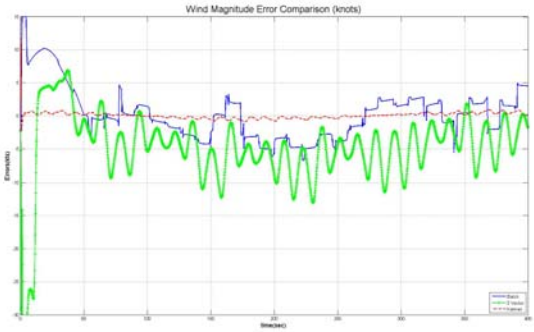

30 knot Wind, 100 knot True Airspeed

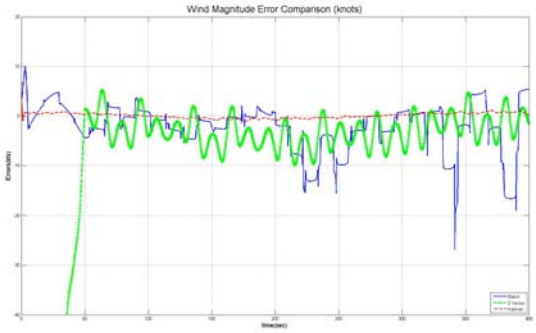

10 knot Wind, 200 knot True Airspeed

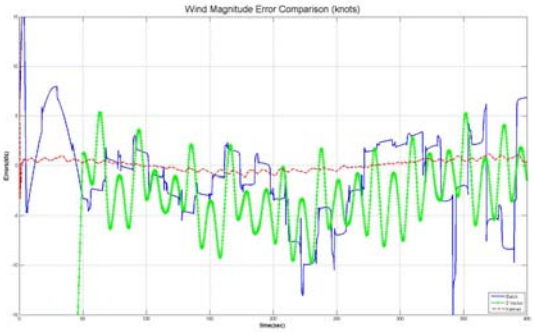

20 knot Wind, 200 knot True Airspeed

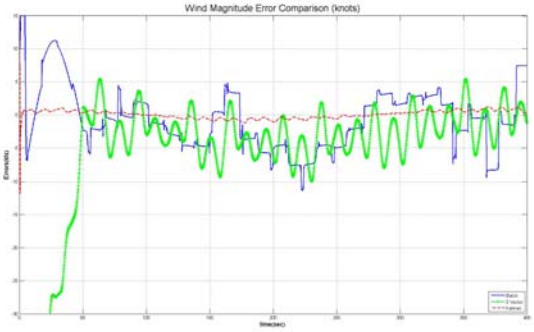

30 knot Wind, 200 knot True Airspeed

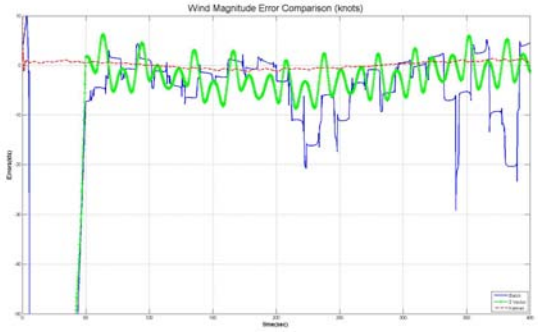

10 knot Wind, 300 knot True Airspeed

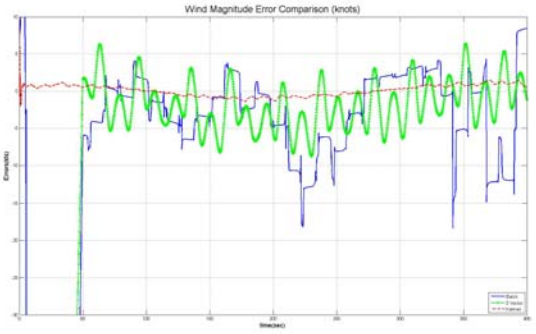

20 knot Wind, 300 knot True Airspeed

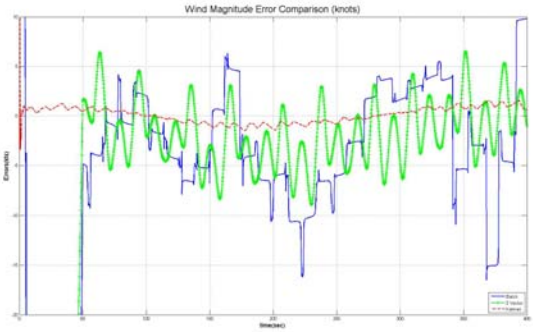

30 knot Wind, 300 knot True Airspeed

B.1.3. Wind Direction and Speed Using 350 Samples

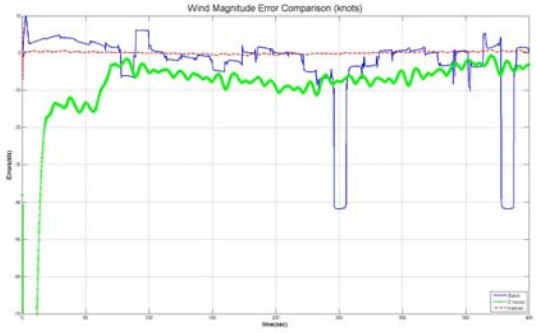

10 knot Wind, 100 knot True Airspeed

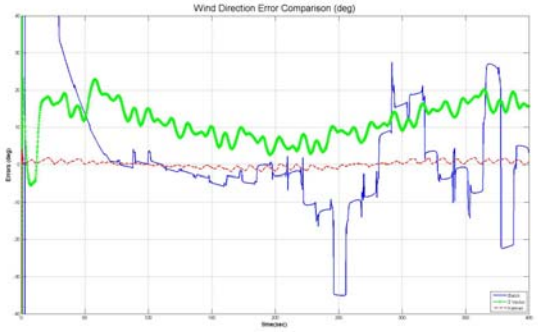

20 knot Wind, 100 knot True Airspeed

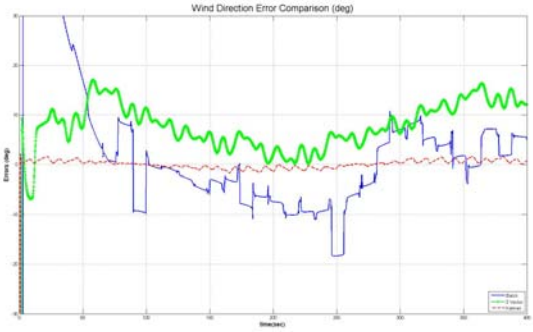

30 knot Wind, 100 knot True Airspeed

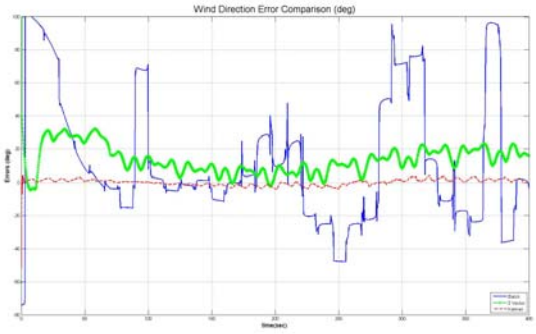

10 knot Wind, 200 knot True Airspeed

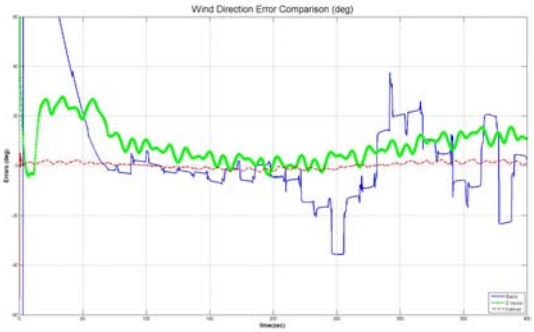

20 knot Wind, 200 knot True Airspeed

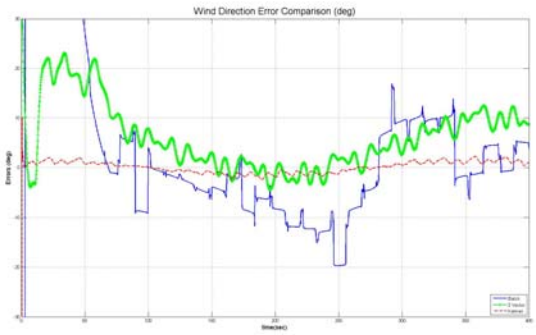

30 knot Wind, 200 knot True Airspeed

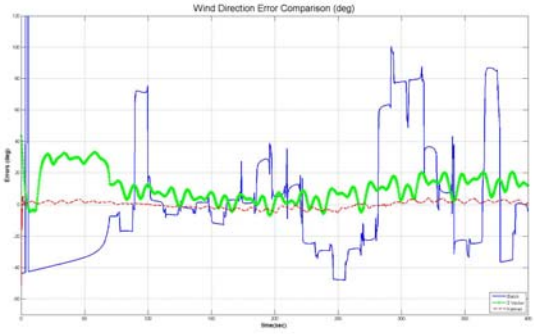

10 knot Wind, 300 knot True Airspeed

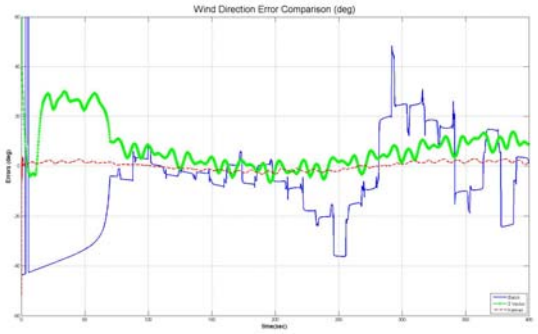

20 knot Wind, 300 knot True Airspeed

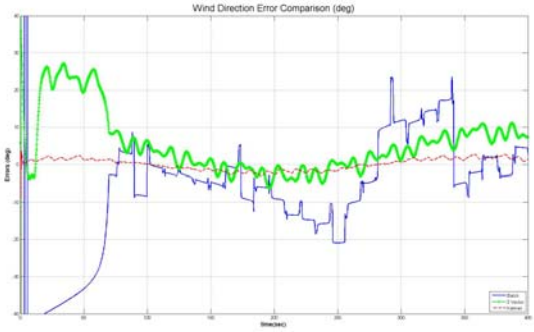

30 knot Wind, 300 knot True Airspeed

Wind Speed Using 350 Samples

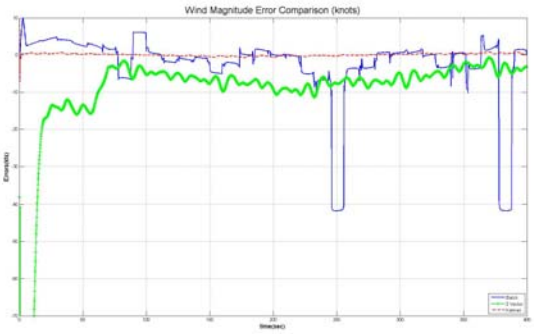

10 knot Wind, 100 knot True Airspeed

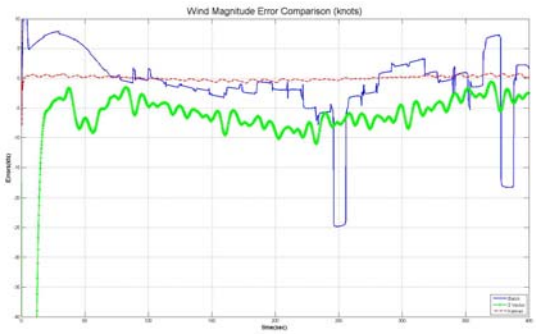

20 knot Wind, 100 knot True Airspeed

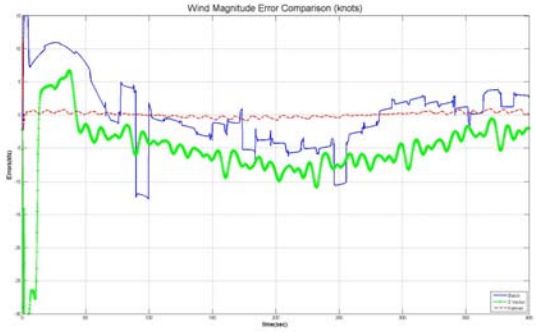

30 knot Wind,100 knot True Airspeed

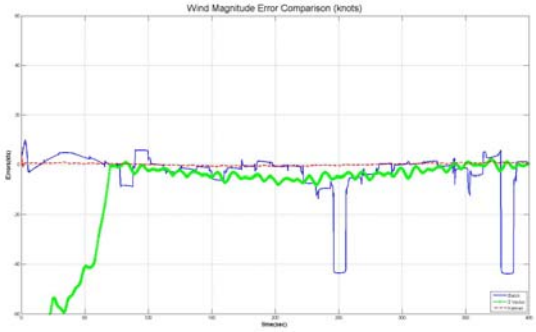

10 knot Wind, 200 knot True Airspeed

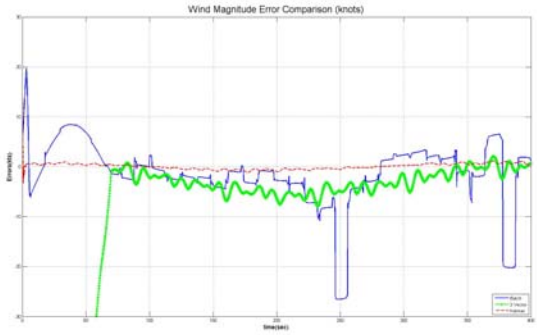

20 knot Wind, 200 knot True Airspeed

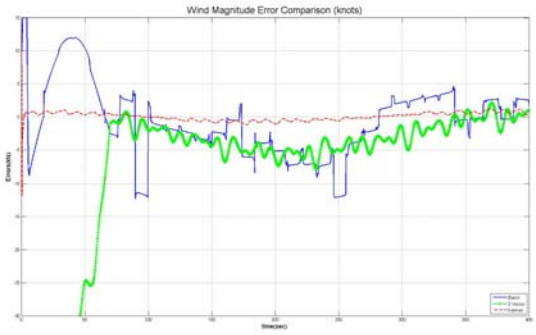

30 knot Wind, 200 knot True Airspeed

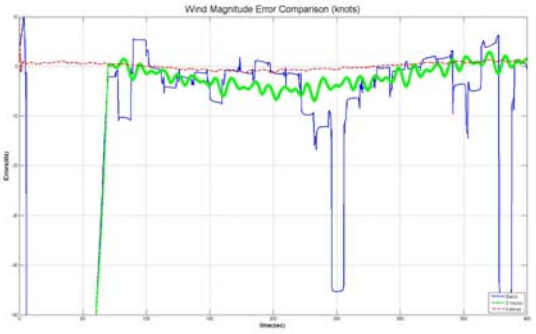

10 knot Wind, 300 knot True Airspeed

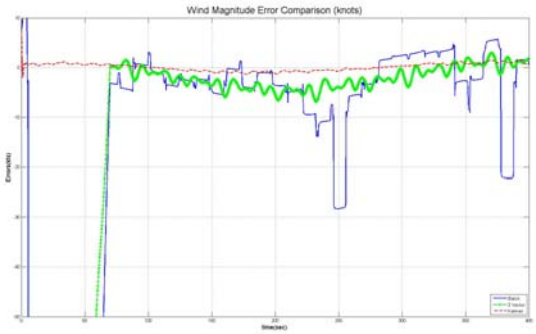

20 knot Wind, 300 knot True Airspeed

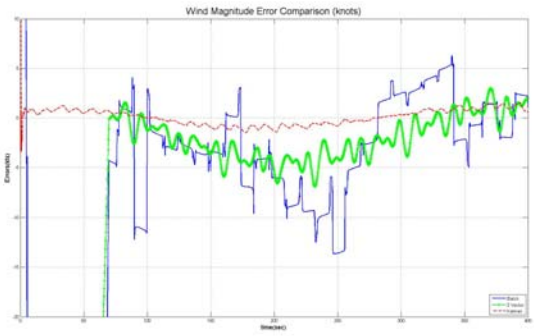

30 knot Wind, 300 knot True Airspeed

B.2. Dynamic Inversion True Airspeed Results

Four straight and level unaccelerated flight conditions were evaluated for dynamic inversion. The results for dynamic inversion were compared with the Kalman Filter results for true airspeed estimate. The conditions for the four runs are labeled with each plot.

Run 1 - 5,000 feet, 250 knots calibrated airspeed, wind 10 knots at 90 degrees

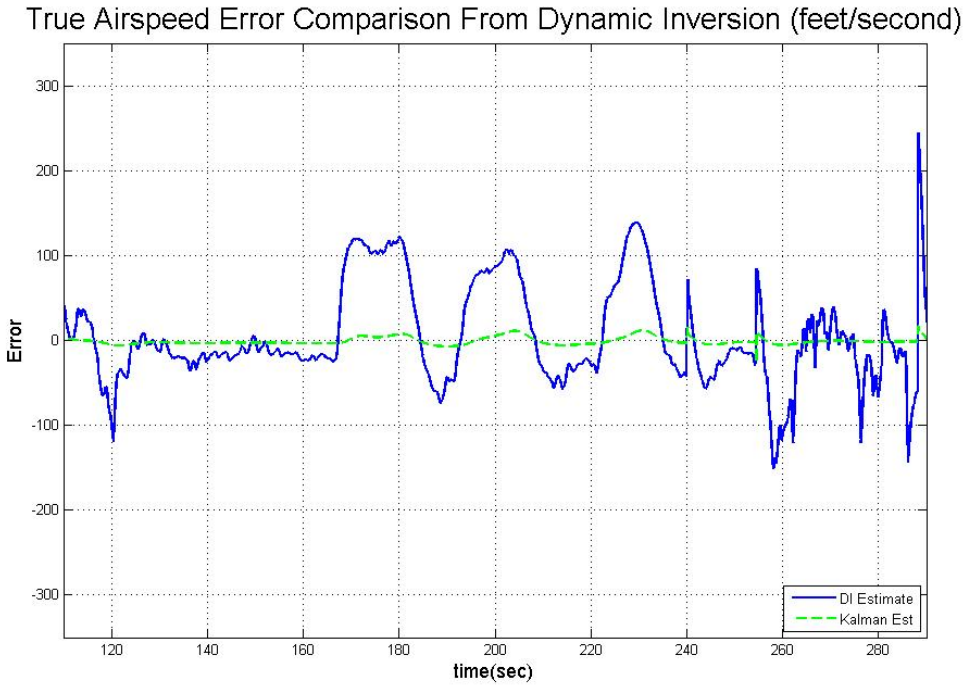

Run 2 - 10,000 feet, 300 knots calibrated airspeed, wind 10 knots at 120 degrees

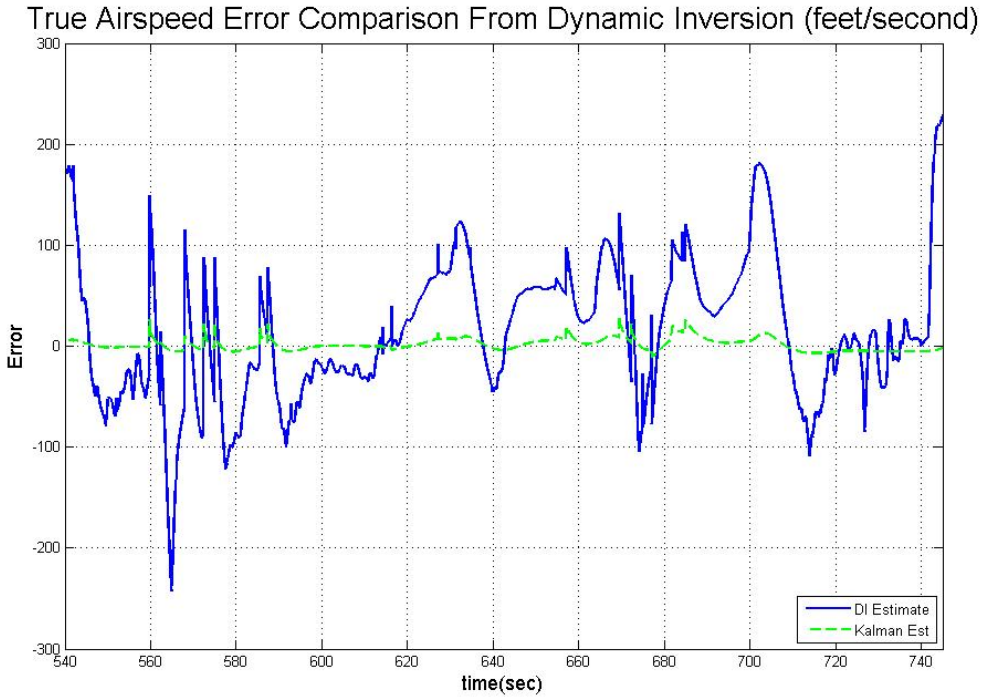

Run 3 - 20,000 feet, 350 knots calibrated airspeed, wind 20 knots at 180 degrees

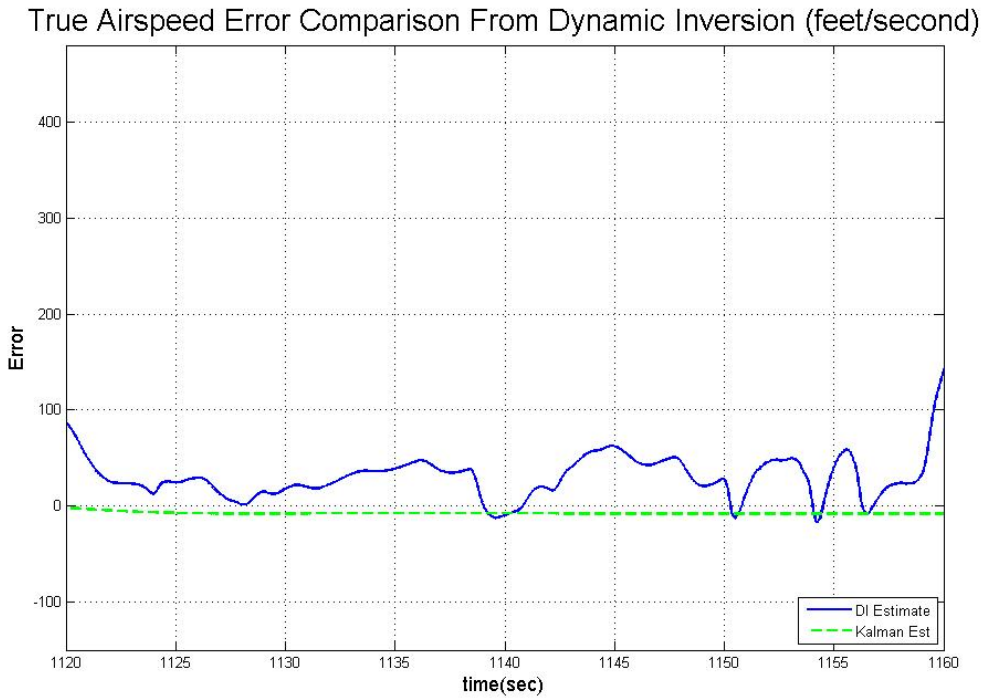

Run 4 - 30,000 feet, 300 knots calibrated airspeed, wind 30 knots at 360 degrees

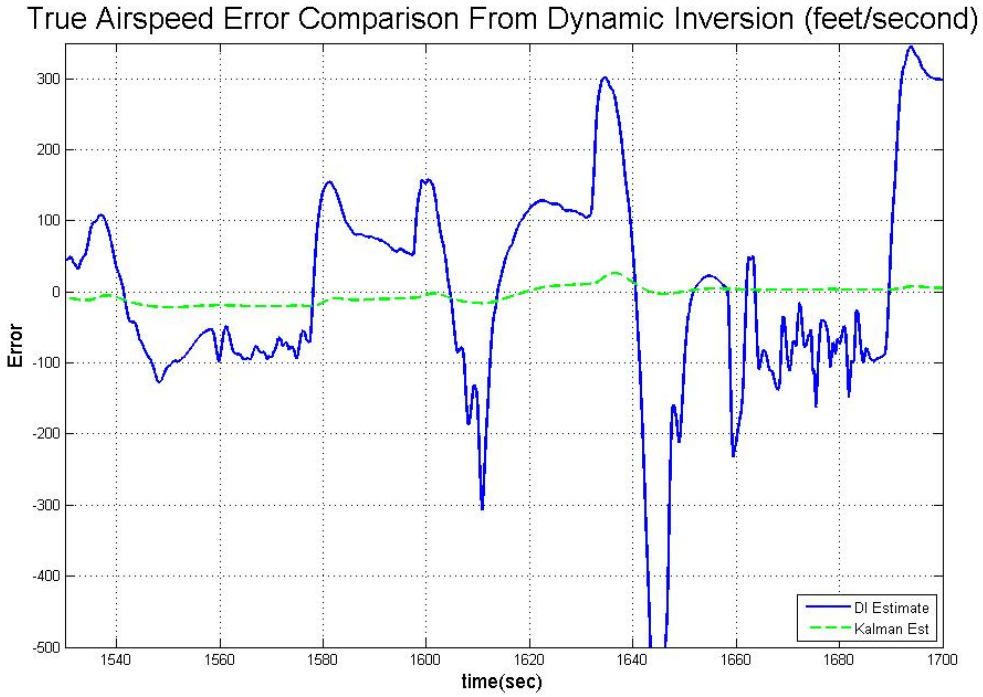

Appendix C. Simulation Model

In the figure below, the Learjet simulator is depicted in green, the inertial components of the VEST algorithm are depicted in gray, the wind portion of the VEST algorithm is in orange, and the airspeed outputs are depicted in red.

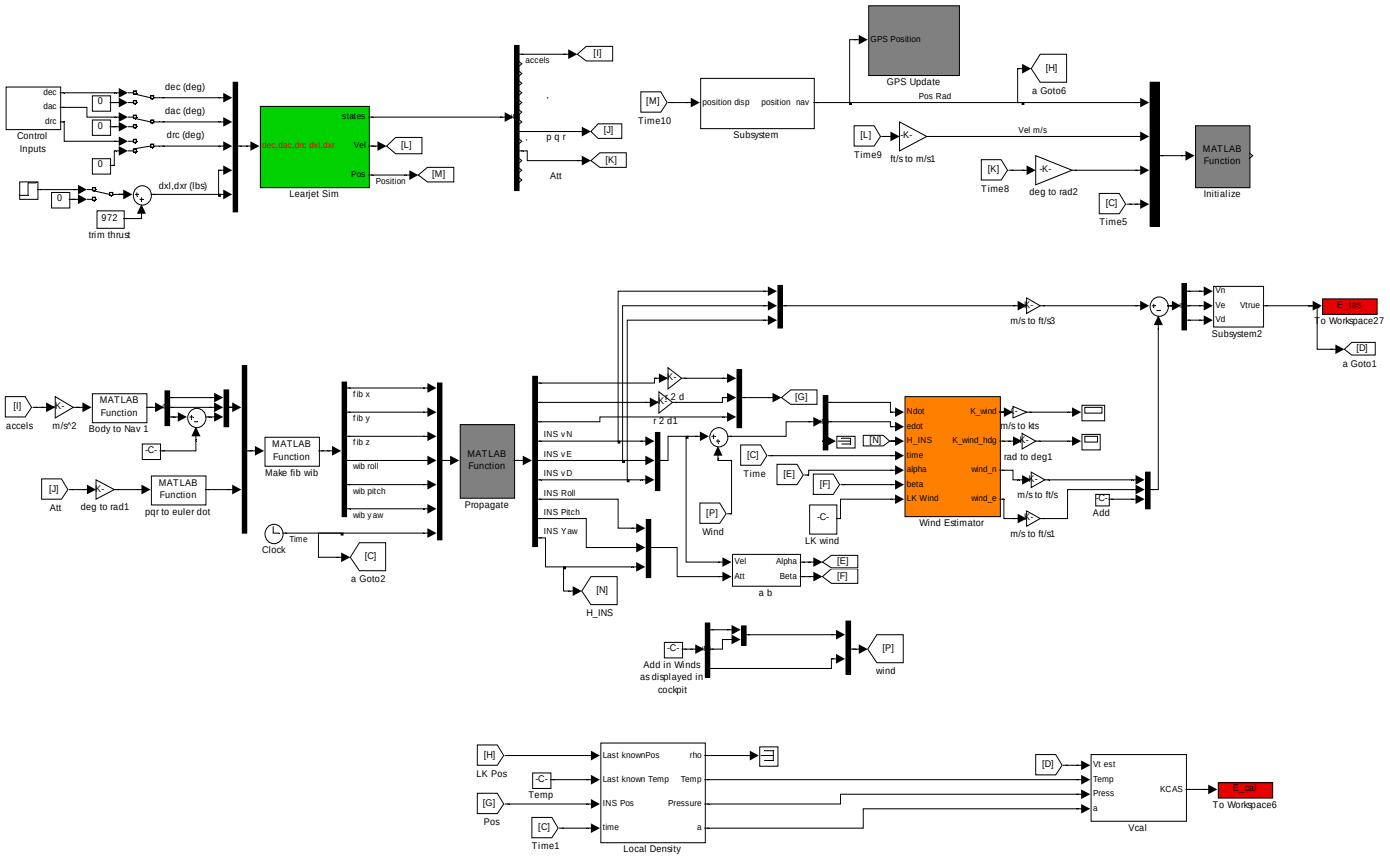

Figure C.1. Learjet Simulation Model for VEST Algorithm

Appendix D. Simulation Plots

The following plots are separated into four sections. The first section has results for inertial estimates from Learjet simulation runs. Section D.2 repeats the first section, with added noise to the input acceleration and rate sensors. The inertial estimate sections are divided into turning maneuvers and climb and descent maneuvers (sections D.1.1 and D.1.2 for turning and climb and descent maneuvers, respectively).

The last two sections present results for wind and overall true airspeed estimate errors. Section D.3 has results for the 40 knot actual wind conditions. The fourth section has results for the 10 knot actual wind conditions. Each plot is labeled with algorithm initial condition input values and simulated aircraft maneuvers. For example, a plot with last known wind magnitude value within of 10 knots of the actual wind magnitude, a last know wind heading value 10 degrees different from actual wind heading, and a simulated turning maneuver would have the following label: Magnitude within 10 knots, Heading 10 degrees off, Turning Maneuver.

D.1. Inertial Estimates, without Noise

D.1.1. Inertial Estimates, No Noise, Turning Maneuvers

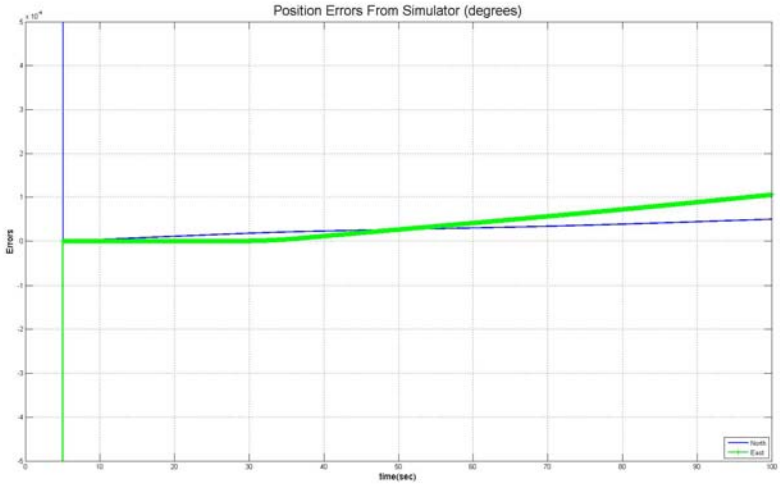

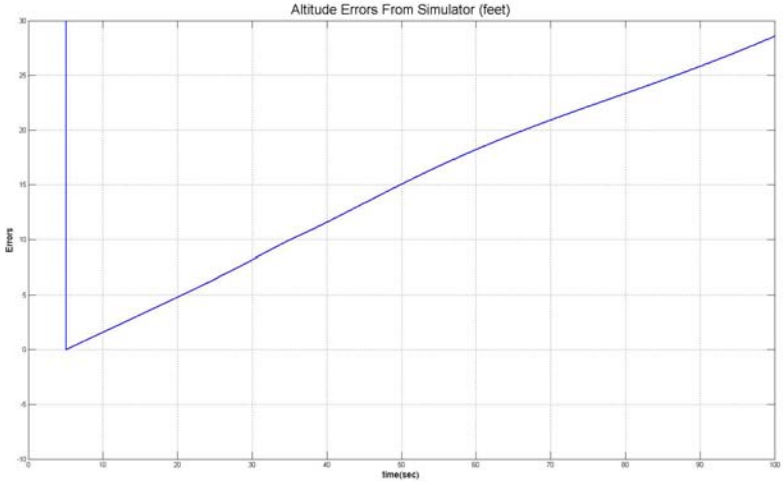

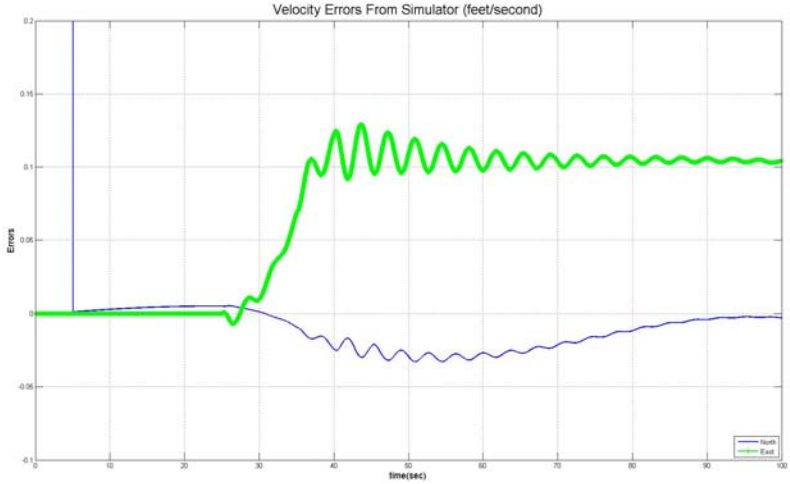

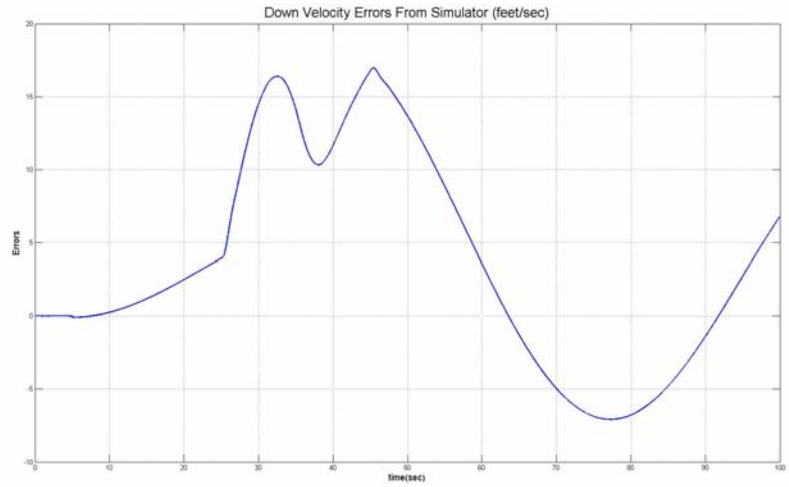
Down Velocity Errors From Simulator (feet/sec)
Errors
time(sec)

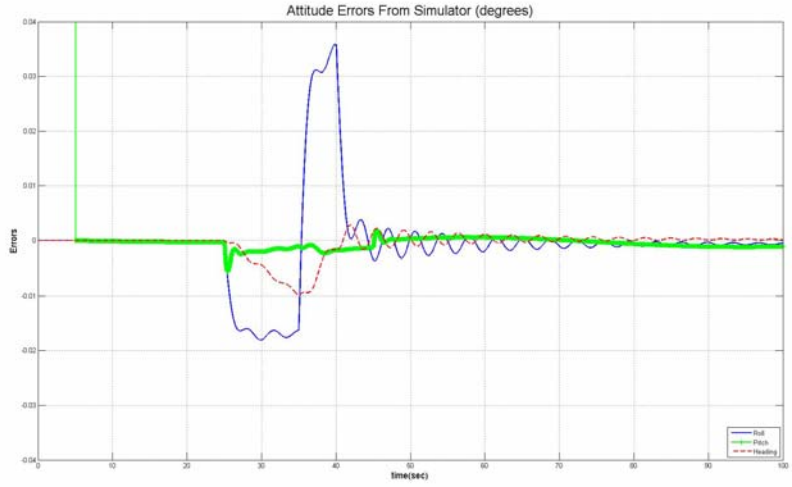
Attitude Errors From Simulator (degrees)
Errors
time(sec)
Roll
Pitch
Heading

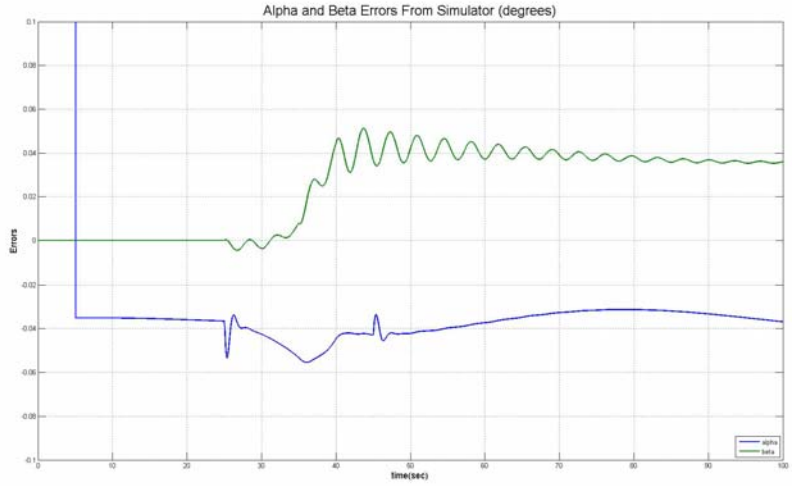
Alpha and Beta Errors From Simulator (degrees)
Errors
time(sec)
alpha
beta

D.1.2. Inertial Estimates, No Noise, Climb and Descent Maneuvers

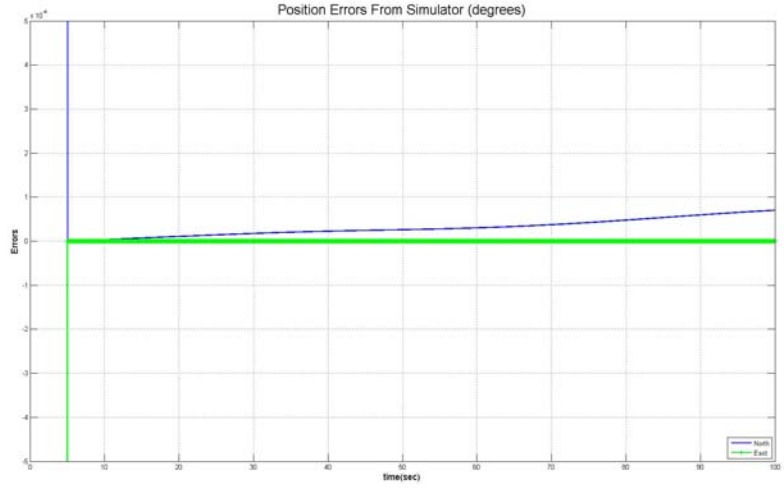

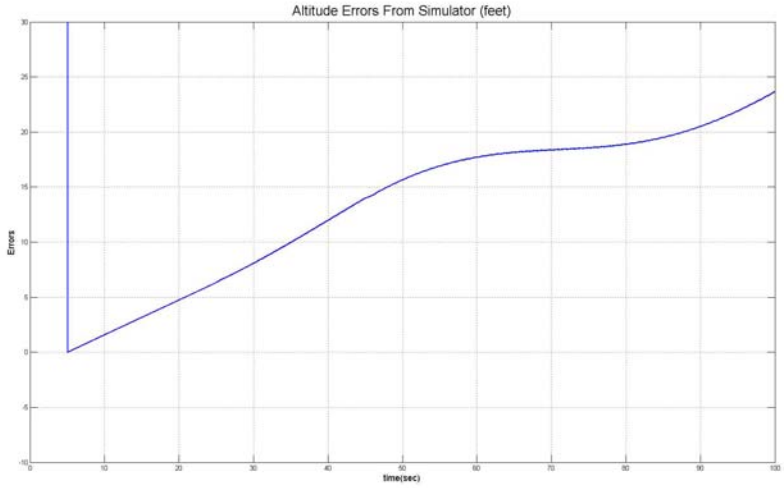

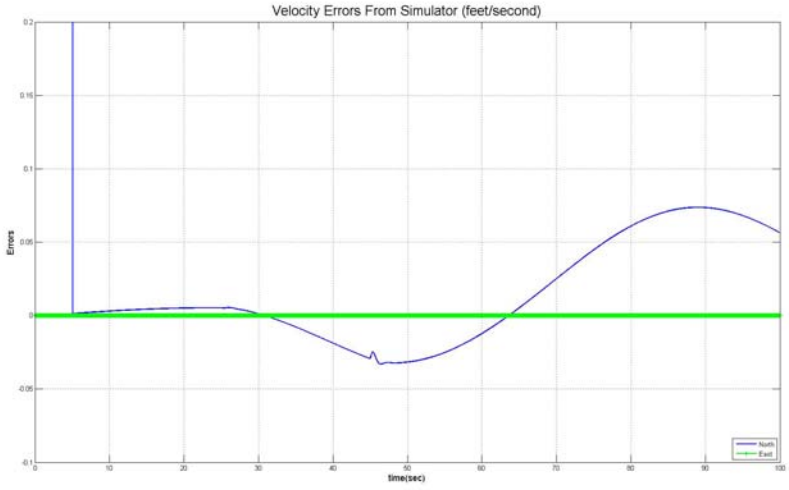

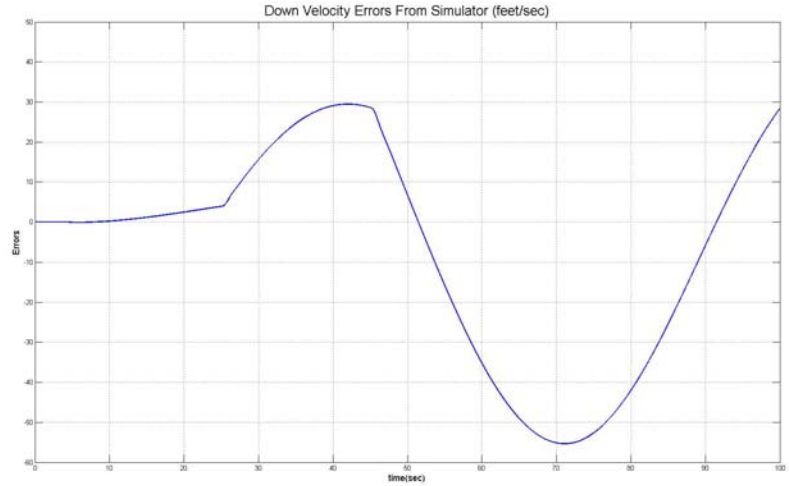
Down Velocity Errors From Simulator (feet/sec)
Errors
time(sec)

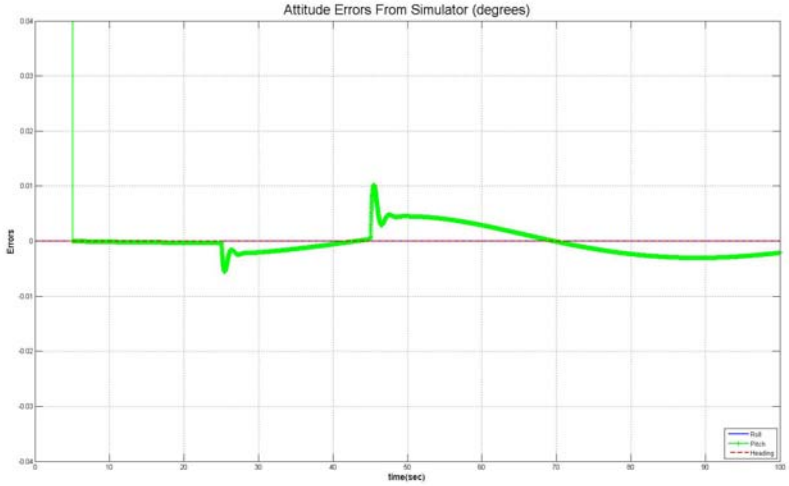
Attitude Errors From Simulator (degrees)
Errors
time(sec)
Roll
Pitch
Heading

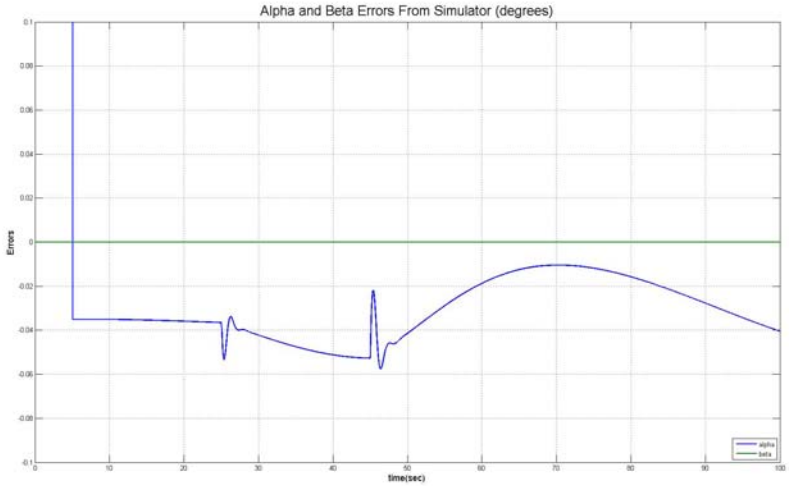
Alpha and Beta Errors From Simulator (degrees)
Errors
time(sec)
alpha
beta

D.2. Inertial Estimates with Noise

D.2.1. Inertial Estimates, with Noise, Turning Maneuvers

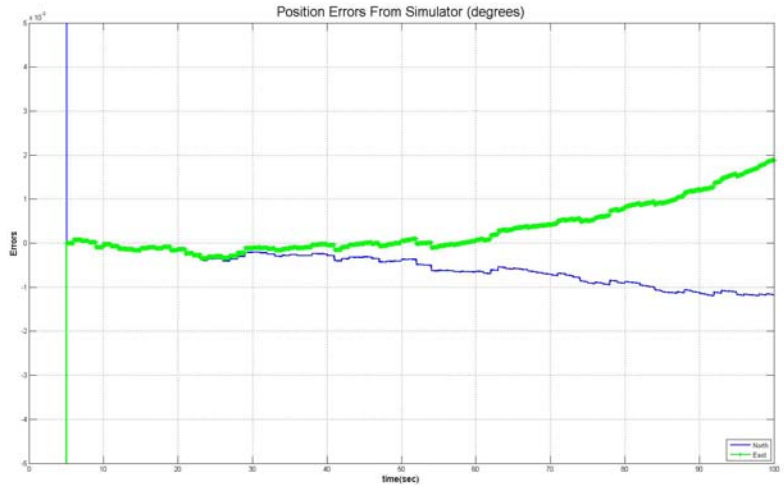

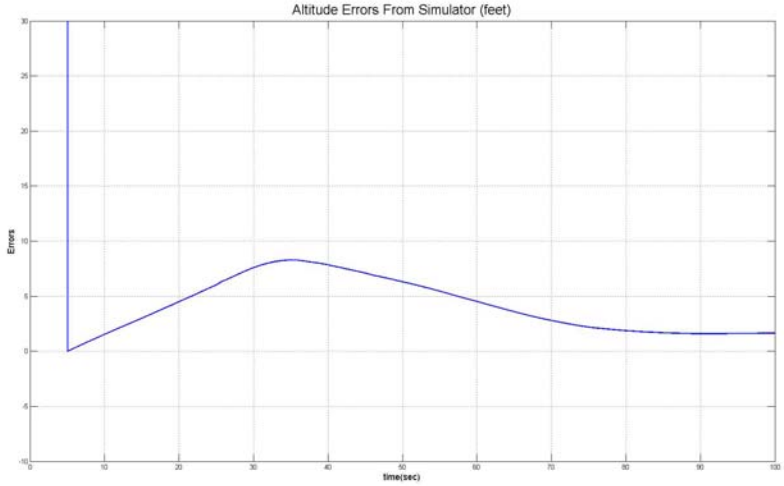

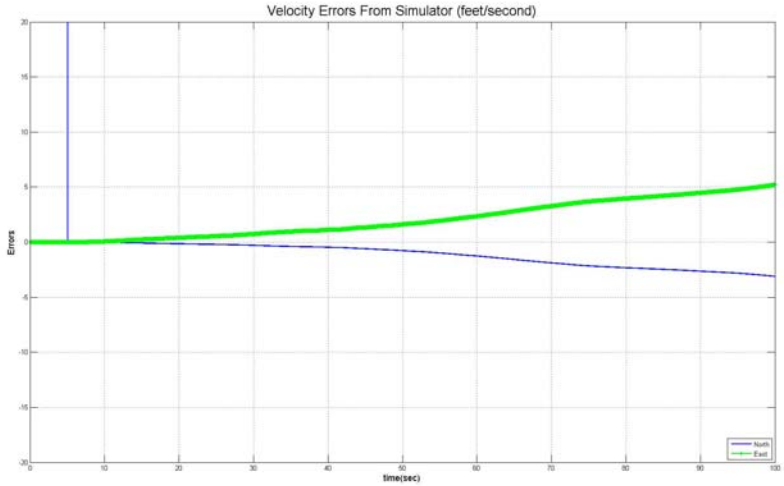

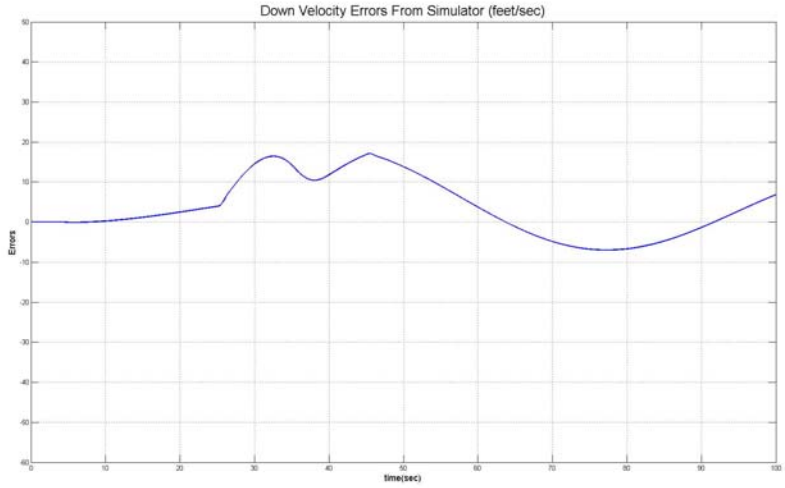
Down Velocity Errors From Simulator (feet/sec)
Errors
time(sec)

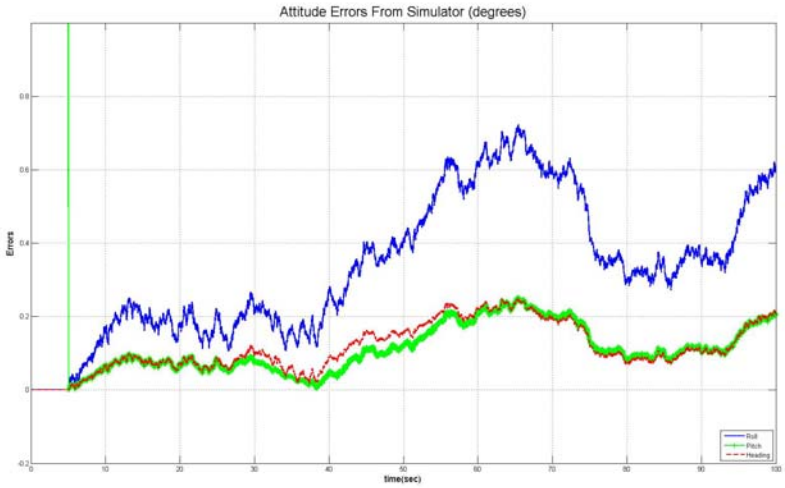
Attitude Errors From Simulator (degrees)
Errors
time(sec)
Roll
Pitch
Heading

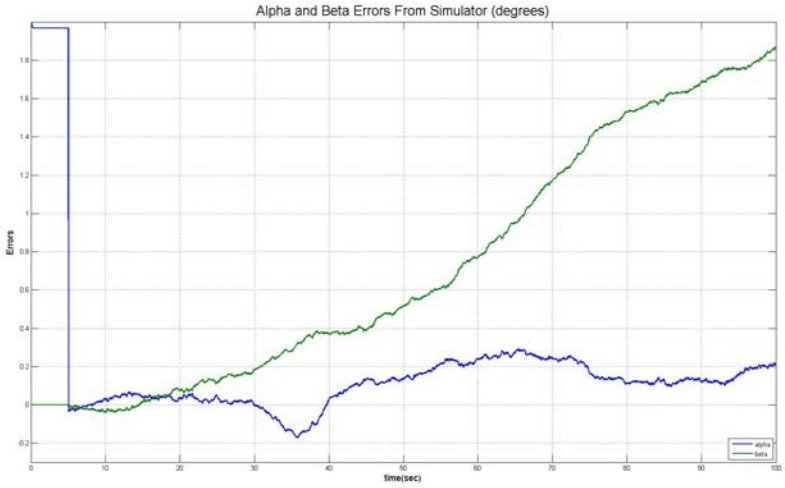
Alpha and Beta Errors From Simulator (degrees)
Errors
time(sec)
alpha
beta

D.2.2. Inertial Estimates, with Noise, Climb and Descent Maneuvers

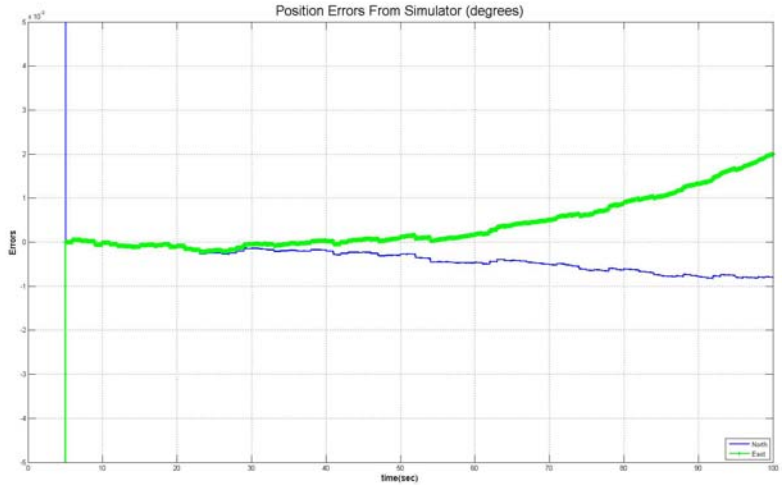

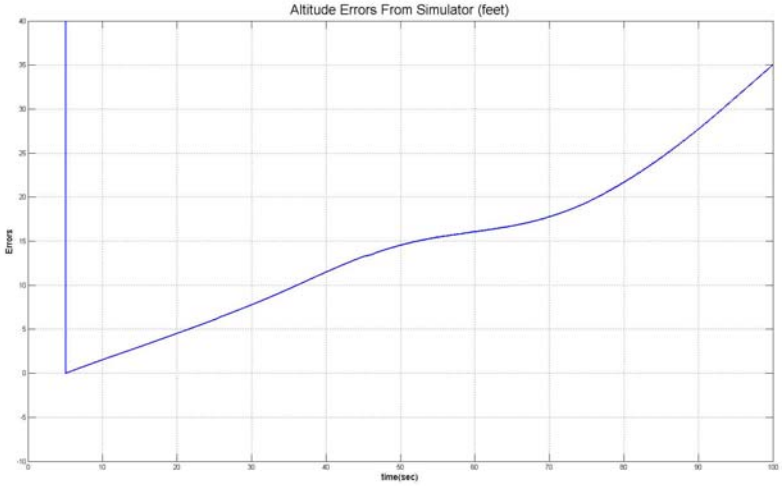

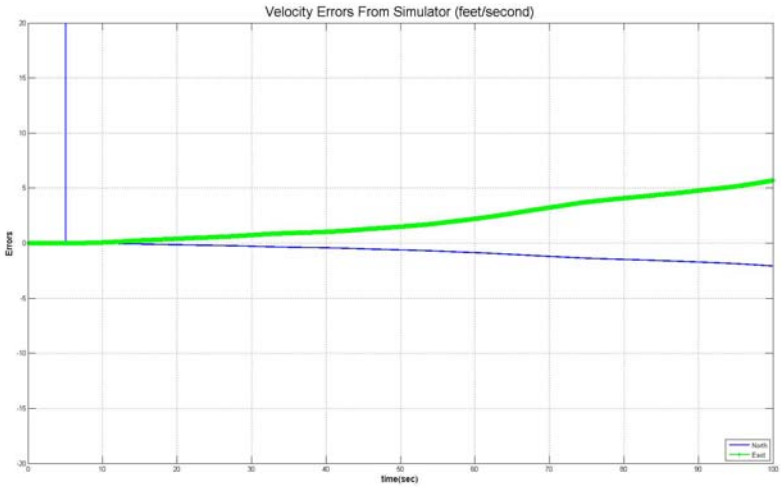

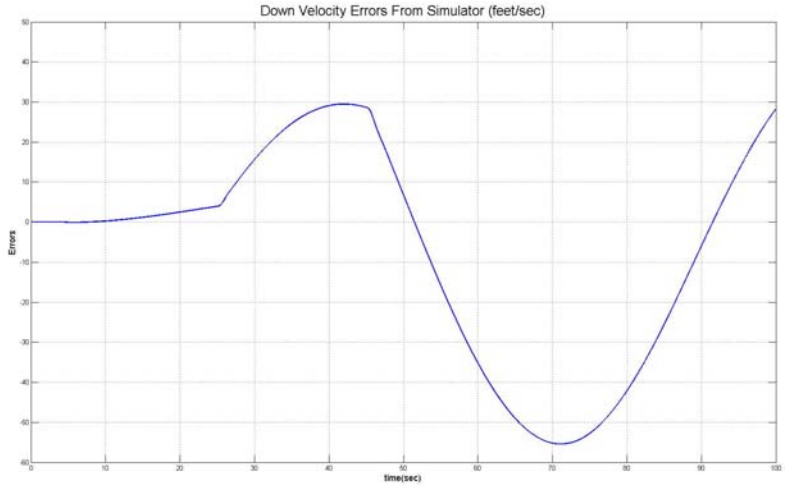
Down Velocity Errors From Simulator (feet/sec)
Errors
time(sec)

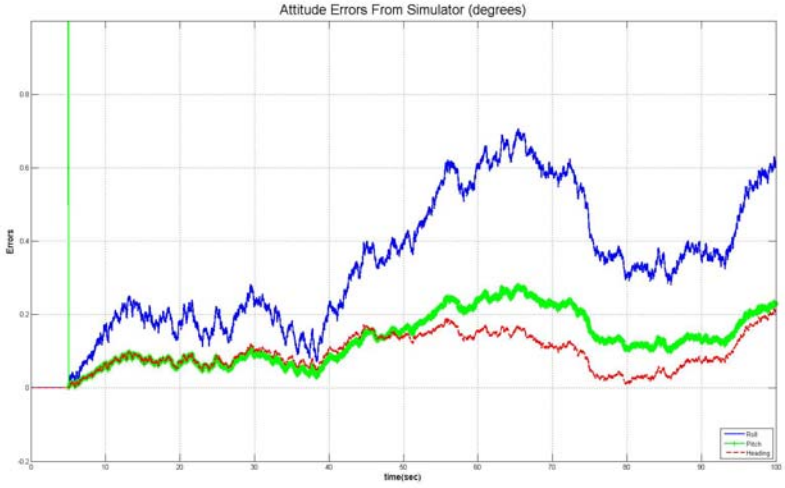
Attitude Errors From Simulator (degrees)
Errors
time(sec)
Roll
Pitch
Heading

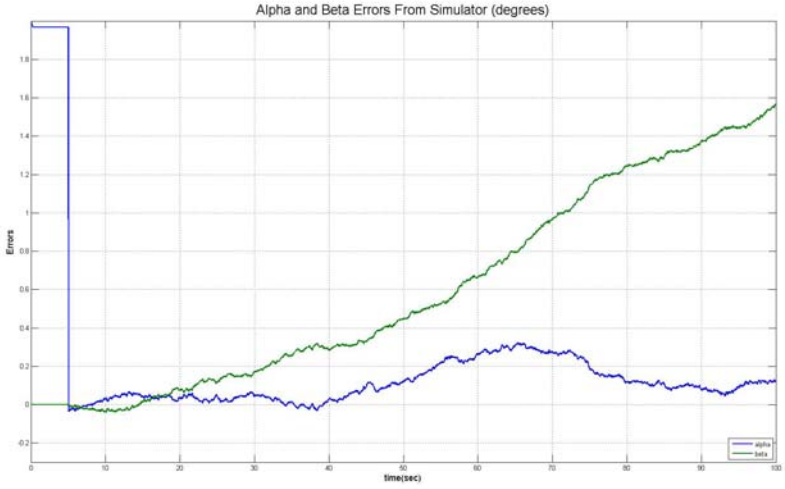
Alpha and Beta Errors From Simulator (degrees)
Errors
time(sec)
alpha
beta

D.3. Wind and True Airspeed Results, 40 knot Actual Wind

Starting Conditions: 40 knot Wind, 10,000 feet Altitude, 530 knots True Airspeed

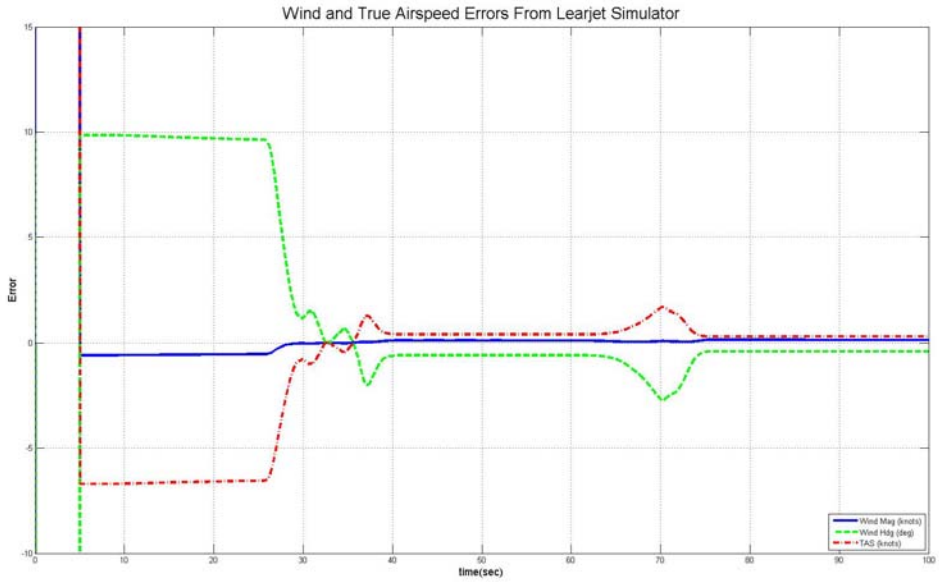

Magnitude within 1 knot, Heading within 1 degree, Turning Maneuver

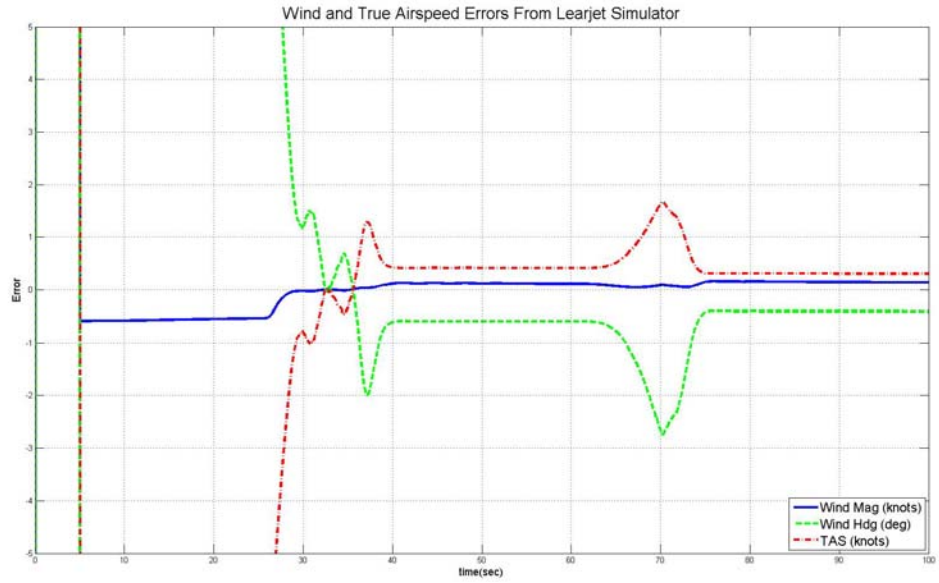

Magnitude within 10 knots, Heading 10 degrees off, Turning Maneuver

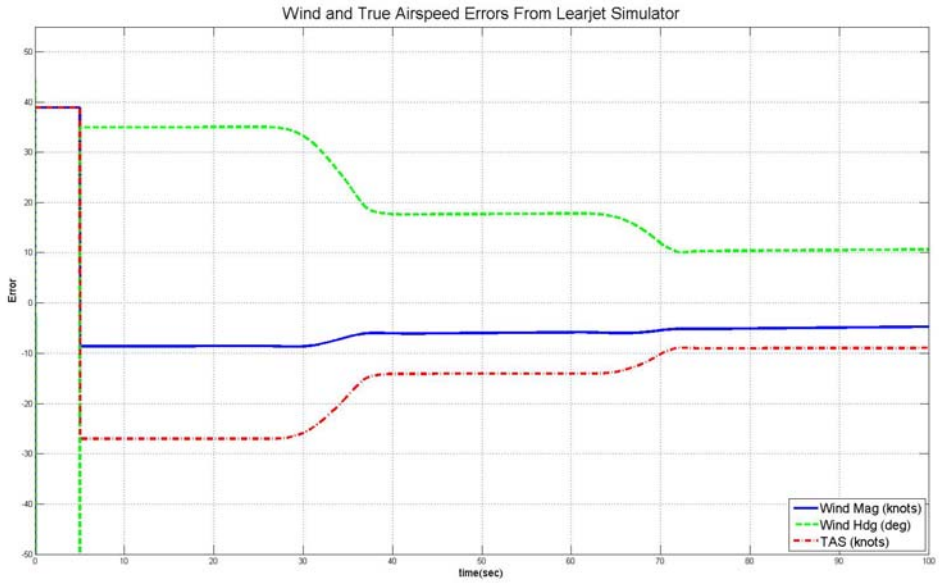

Magnitude within 10 knots, Heading 45 degrees off, Turning Maneuver

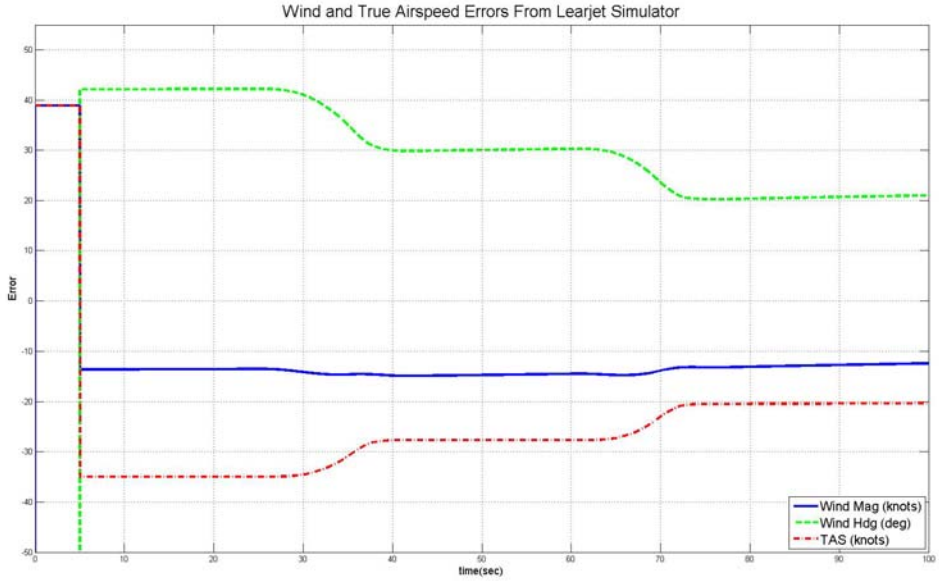

Magnitude within 10 knots, Heading 90 degrees off, Turning Maneuver

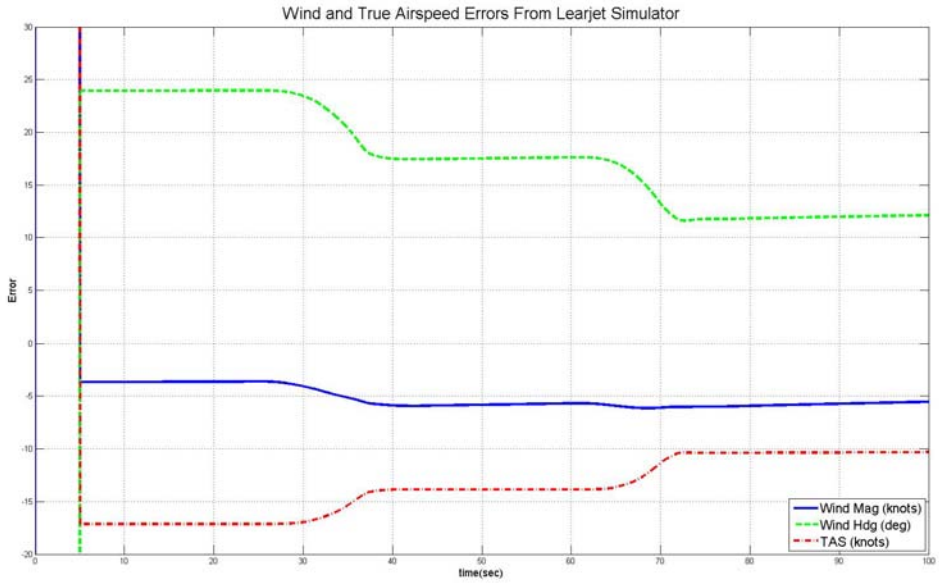

Magnitude within 10 knots, Heading 135 degrees off, Turning Maneuver

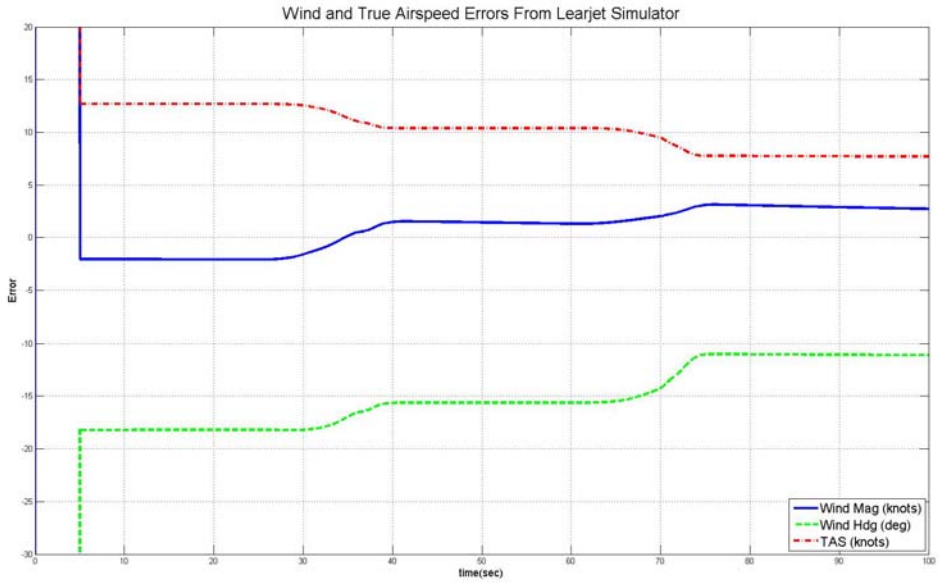

Magnitude within 10 knots, Heading 180 degrees off, Turning Maneuver

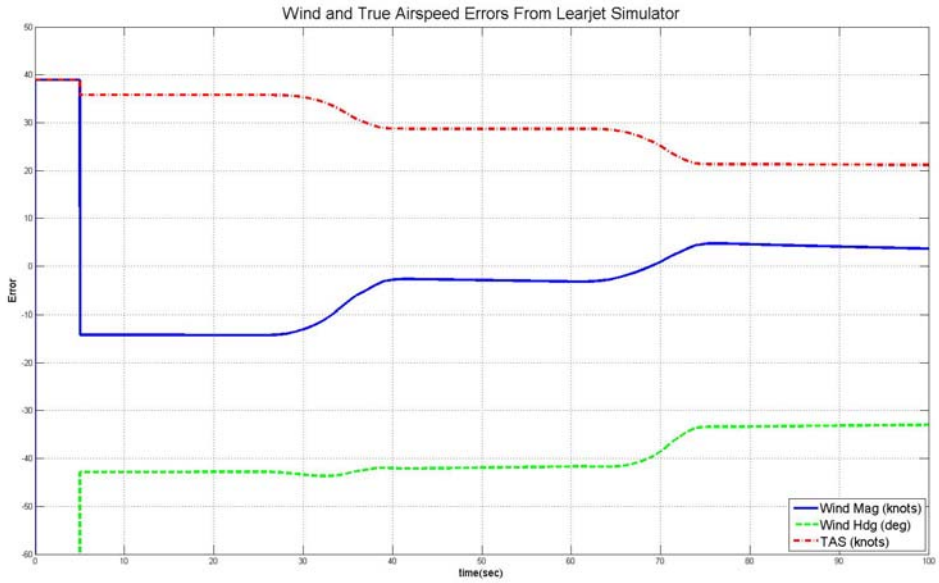

Magnitude within 10 knots, Heading 225 degrees off, Turning Maneuver

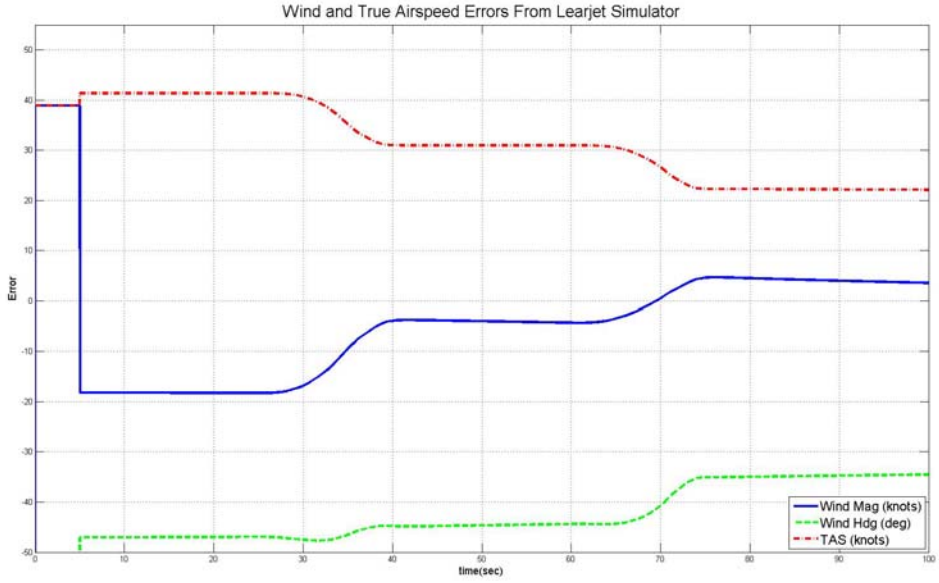

Magnitude within 10 knots, Heading 270 degrees off, Turning Maneuver

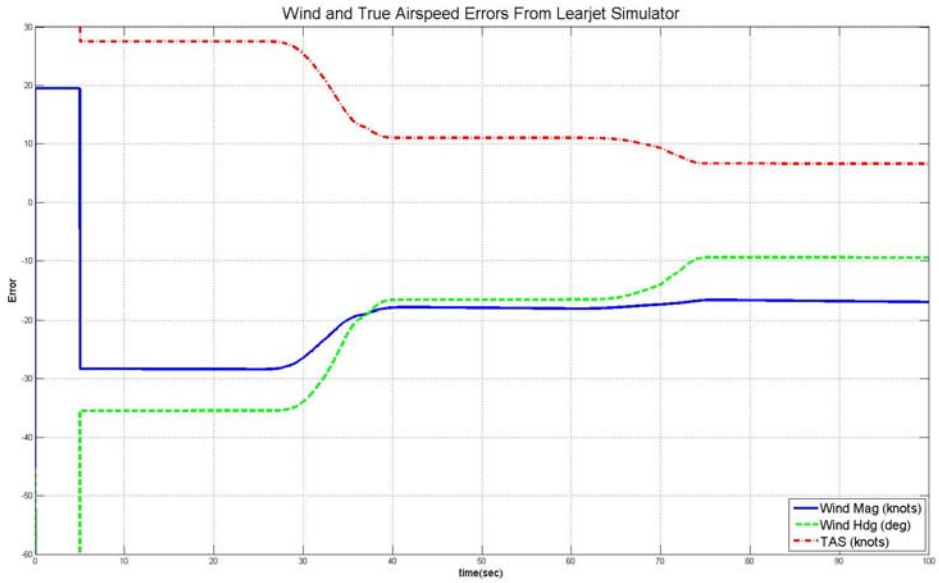

Magnitude within 10 knots, Heading 315 degrees off, Turning Maneuver

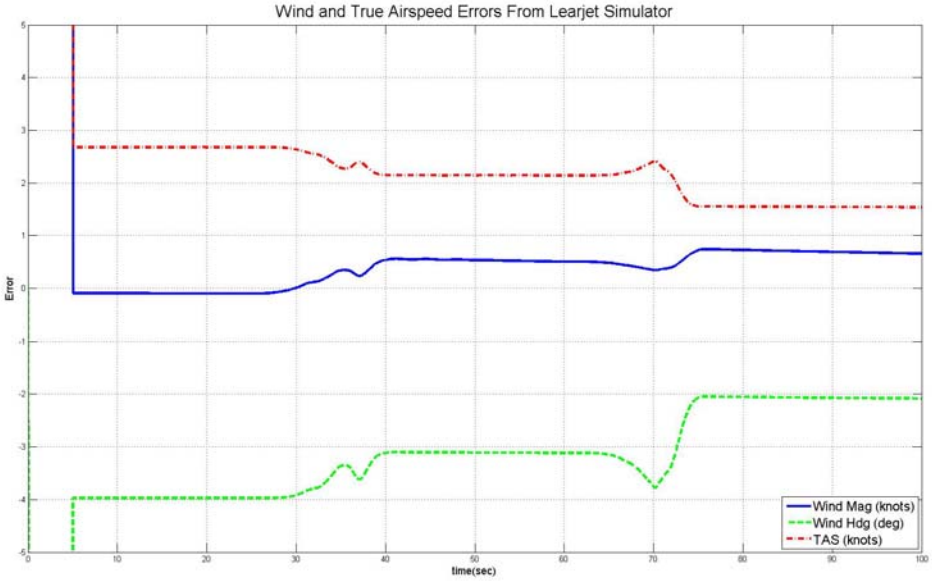

Magnitude off 35 knots, Heading within 1 degree, Turning Maneuver

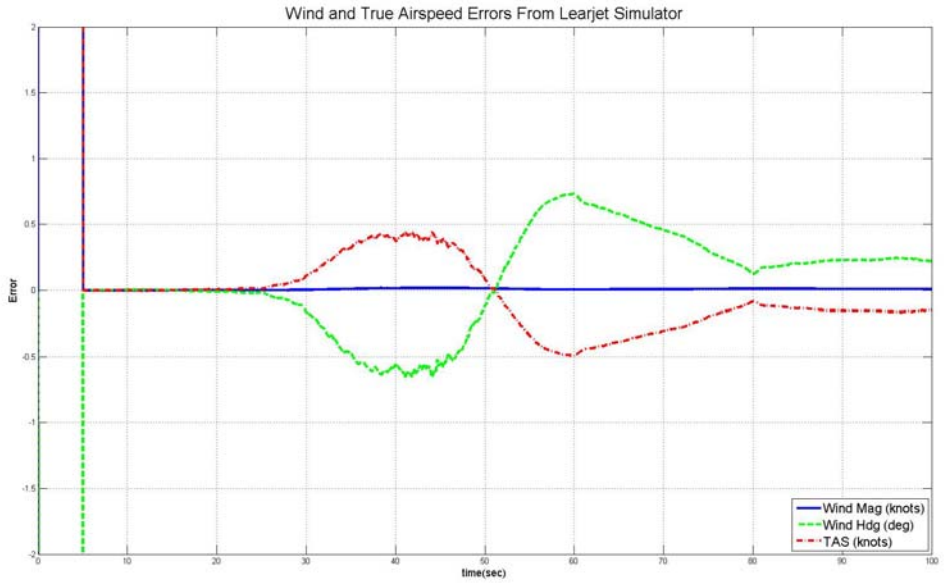

Magnitude within 10 knots, Heading within 1 degree, Climb and Descent Maneuver

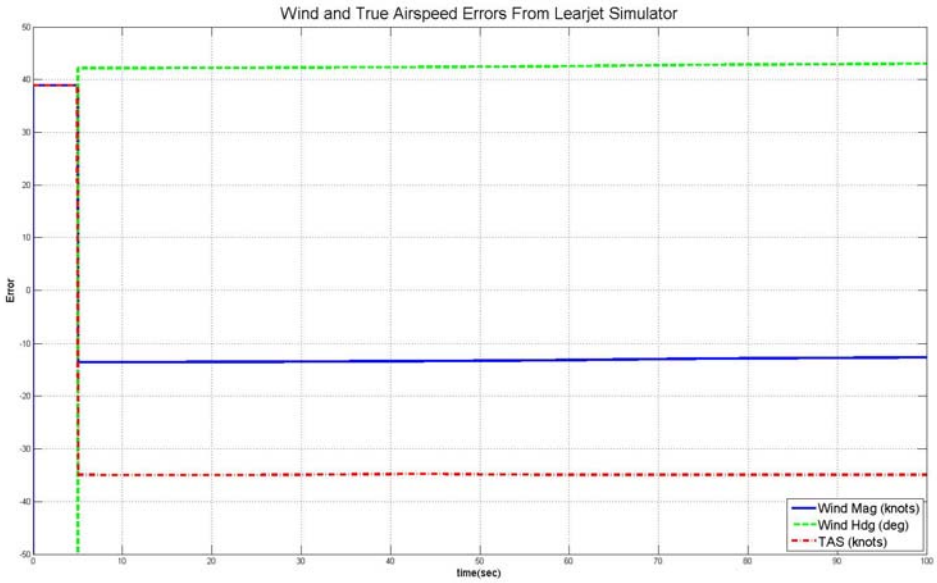

Magnitude within 10 knots, Heading 90 degrees off, Climb and Descent Maneuver

D.4. Wind and True Airspeed Results, 10 knot Actual Wind

Section 4: Conditions: 10 knot Wind, 10,000 feet Altitude, 530 knots True Airspeed

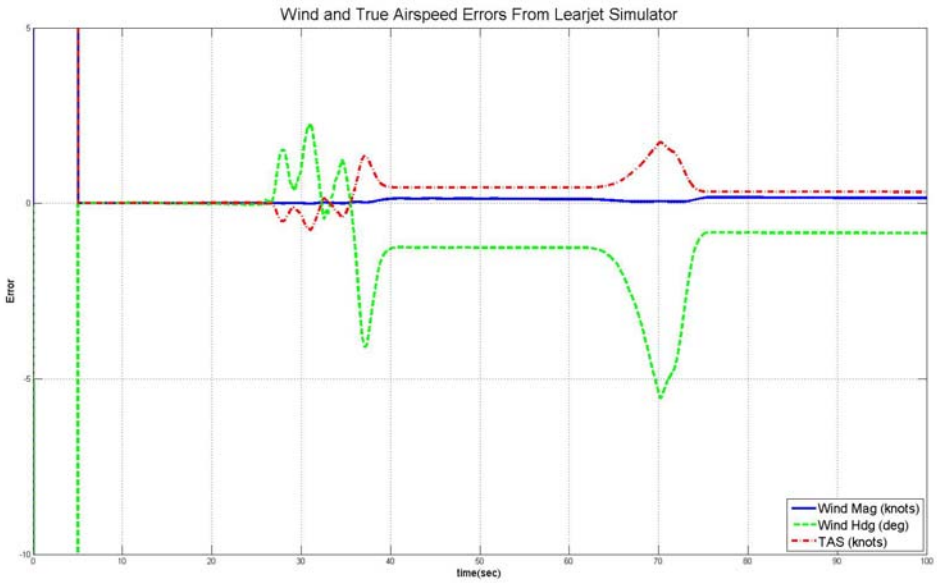

Magnitude within 1 knot, Heading within 1 degree, Turning Maneuver

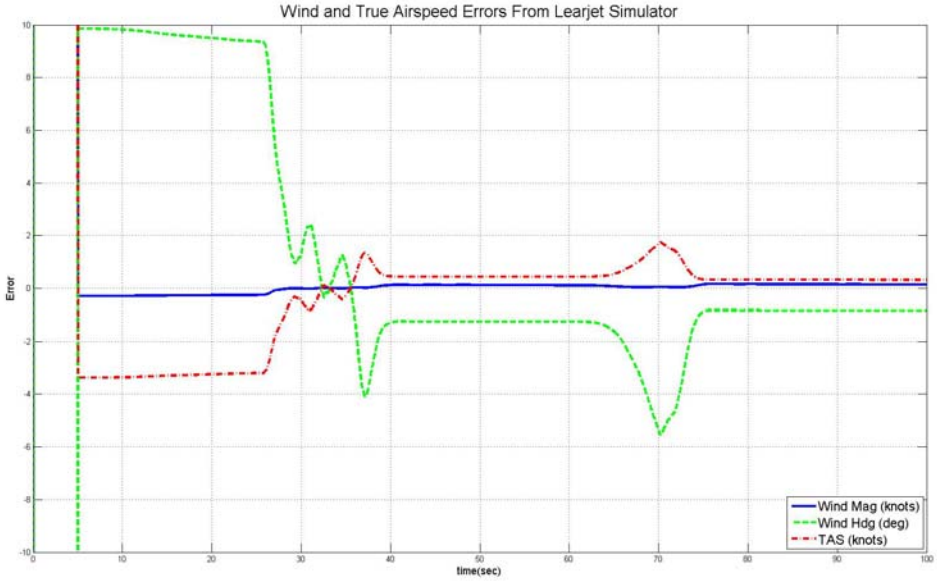

Magnitude within 10 knots, Heading 10 degrees off, Turning Maneuver

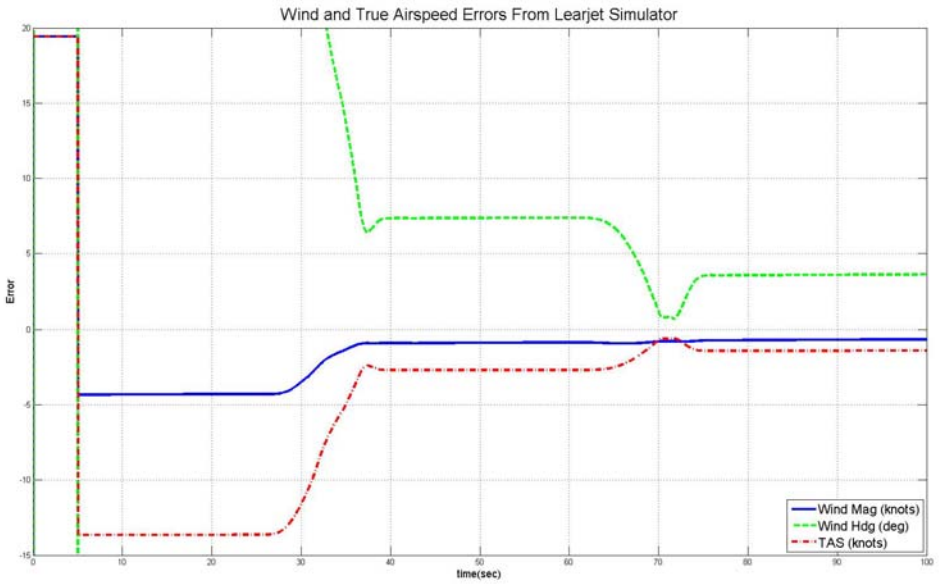

Magnitude within 10 knots, Heading 45 degrees off, Turning Maneuver

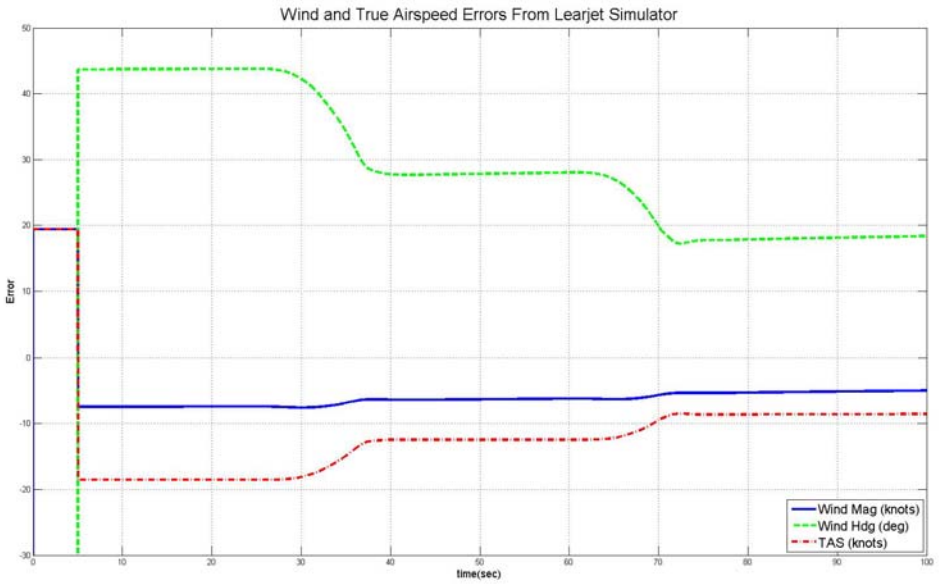

Magnitude within 10 knots, Heading 90 degrees off, Turning Maneuver

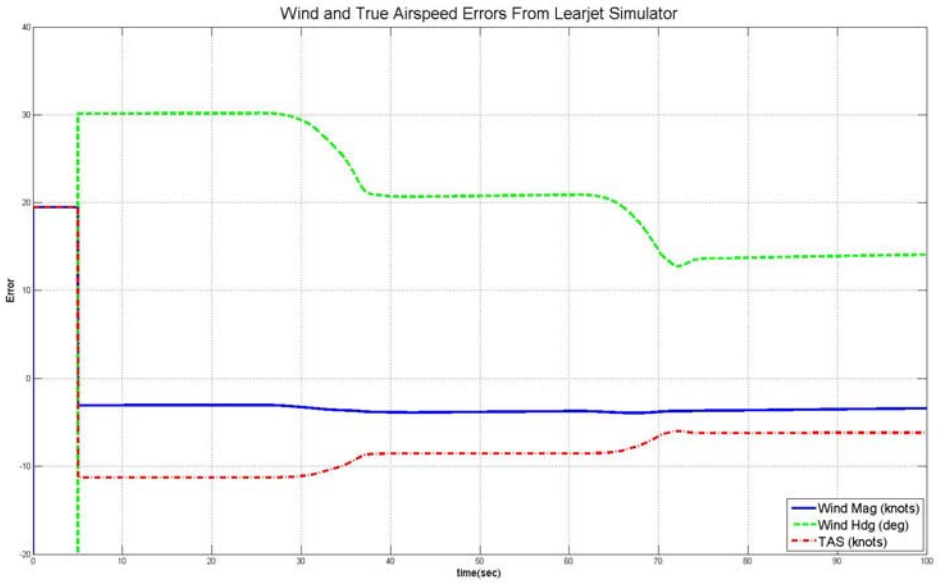

Magnitude within 10 knots, Heading 135 degrees off, Turning Maneuver

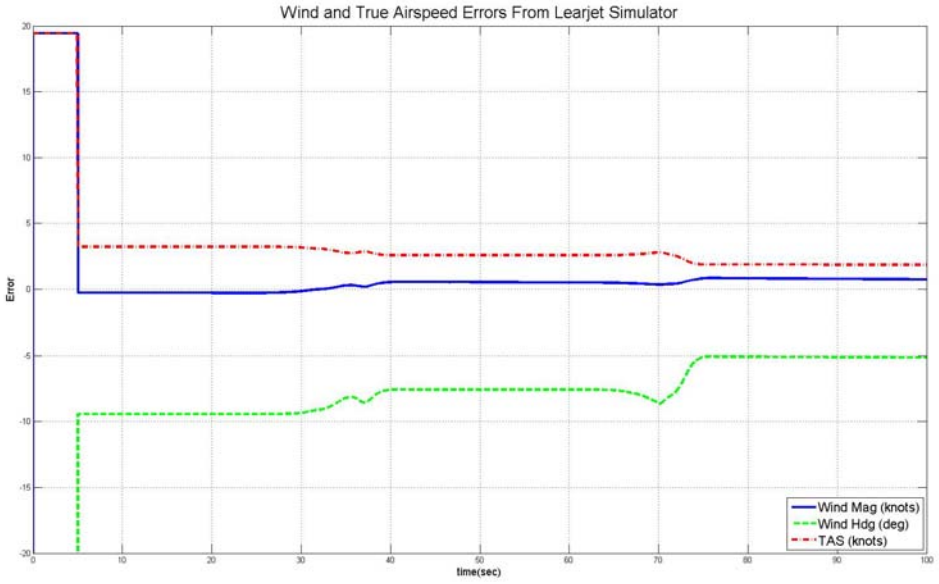

Magnitude within 10 knots, Heading 180 degrees off, Turning Maneuver

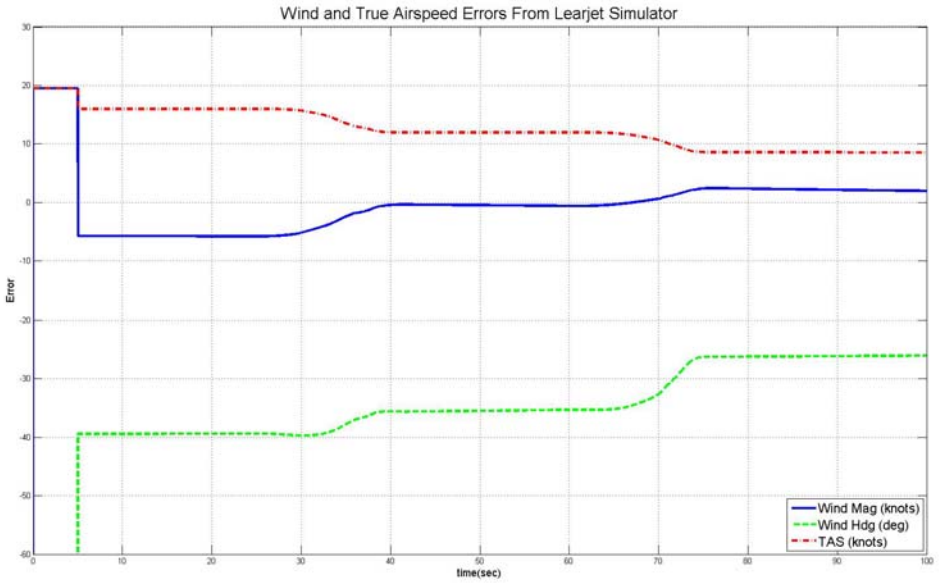

Magnitude within 10 knots, Heading 225 degrees off, Turning Maneuver

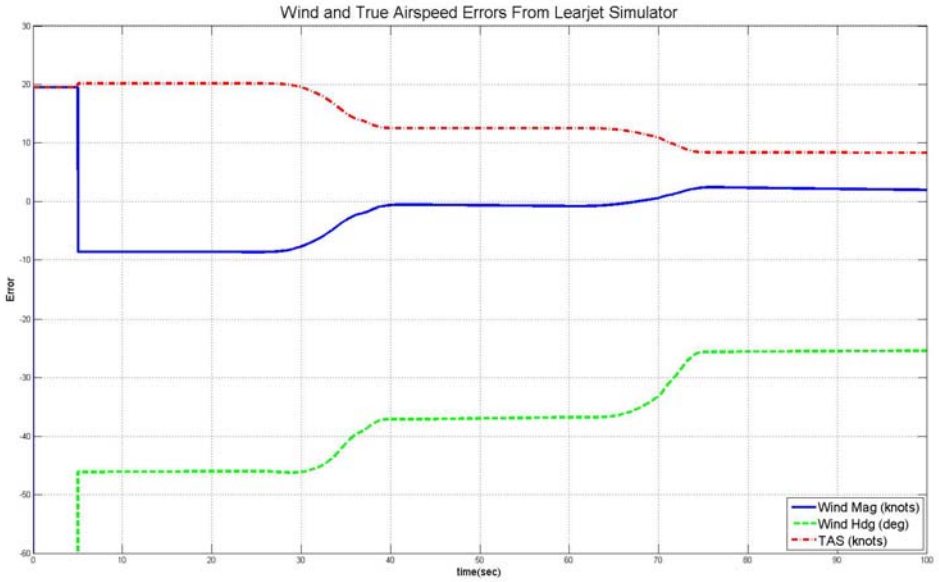

Magnitude within 10 knots, Heading 270 degrees off, Turning Maneuver

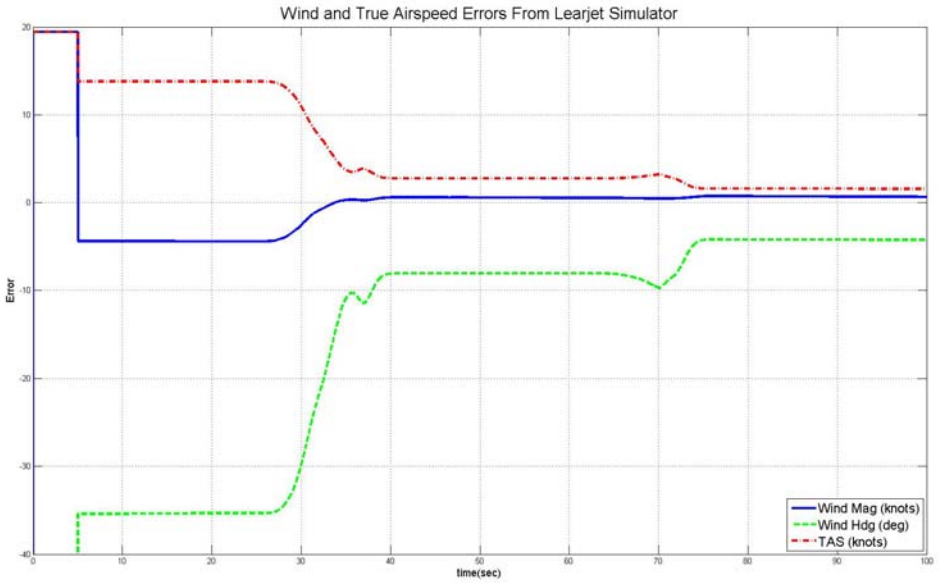

Magnitude within 10 knots, Heading 315 degrees off, Turning Maneuver

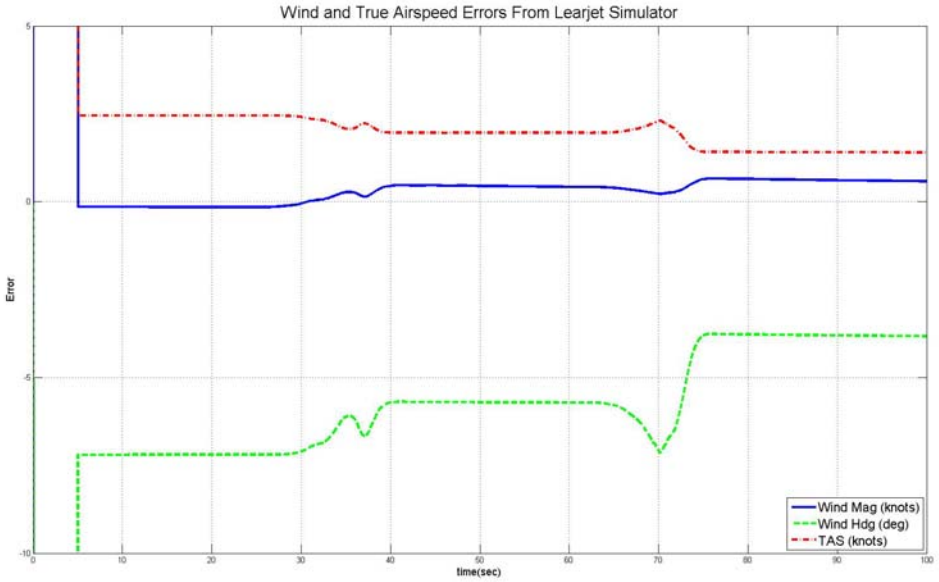

Magnitude off 35 knots, Heading within 1 degree, Turning Maneuver

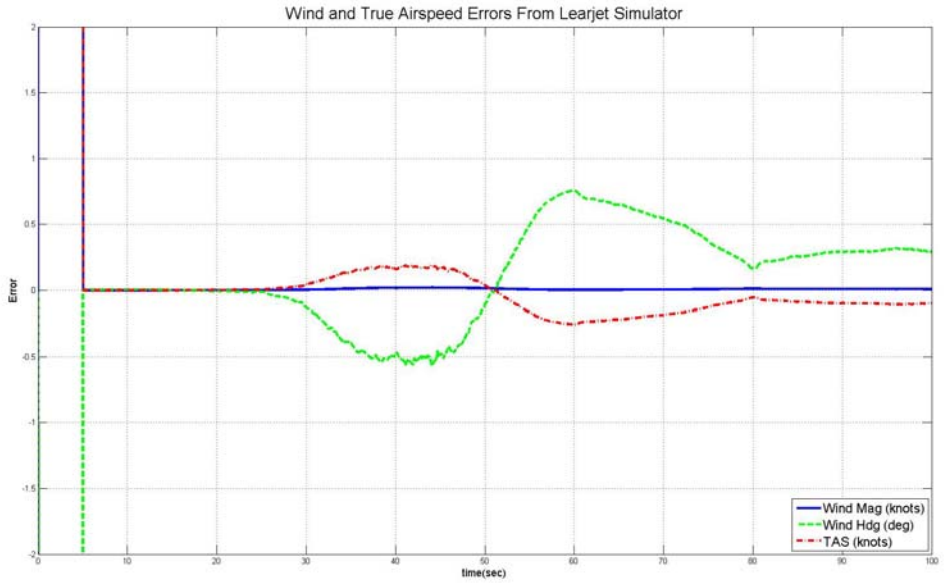

Magnitude within 1 knot, Heading within 1 degree, Climb and Descent Maneuver

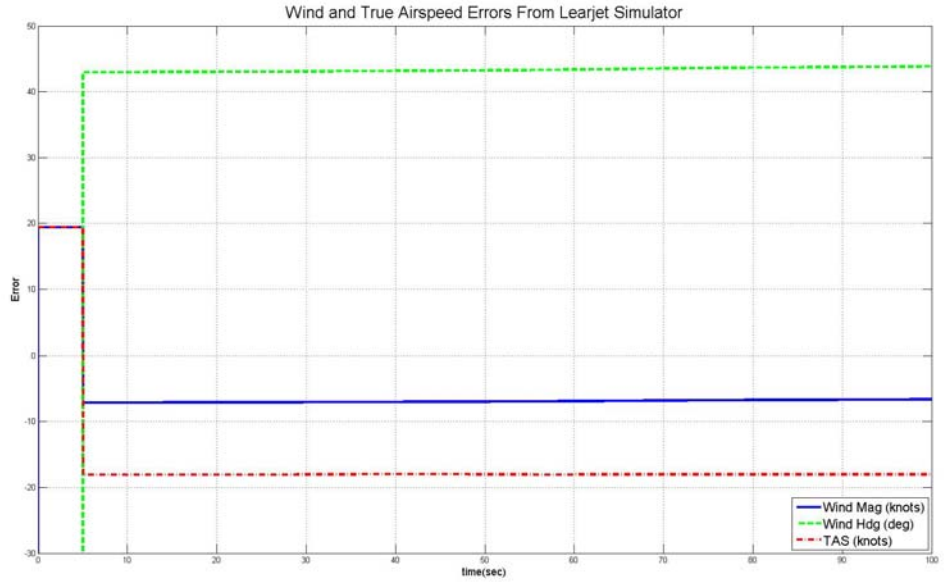

Magnitude within 10 knots, Heading 90 degrees off, Climb and Descent Maneuver

Appendix E. Flight Test Point Matrix

Description: Long Shot FTT - Straight and Level, VEST Data and Characterization

Test Point:

1	13_Sep_Rec_14
2	13_Sep_Rec_3
3	17_Sep_Rec_17
4	19_Sep_Rec_2

Description: J-Hook FTT - Heading Changes, Straight Times, VEST Data and Characterization

Test Point:

5	18_Sep_Rec_1, 21_Sep_Rec_16
6	13_Sep_Rec_10
7	13_Sep_Rec_11
8	13_Sep_Rec_9
9	17_Sep_Rec_23
10	19_Sep_Rec_3
11	17_Sep_Rec_19
12	17_Sep_Rec_21
13	13_Sep_Rec_6
14	17_Sep_Rec_4
15	13_Sep_Rec_5
16	19_Sep_Rec_4

17	18_Sep_Rec_20
18	13_Sep_Rec_17
19	17_Sep_Rec_20
20	17_Sep_Rec_18
21	13_Sep_Rec_7
22	13_Sep_Rec_4
23	13_Sep_Rec_8
24	18_Sep_Rec_2
25	18_Sep_Rec_21
26	17_Sep_Rec_12, 21_Sep_Rec_17
27	18_Sep_Rec_22
28	17_Sep_Rec_13
29	17_Sep_Rec_3
30	18_Sep_Rec_3
31	17_Sep_Rec_2
32	18_Sep_Rec_4
33	17_Sep_Rec_24
34	17_Sep_Rec_14
35	17_Sep_Rec_15
36	17_Sep_Rec_22

Description: Container FTT - Workup to Approach Task, Simulated Instrument Pattern, VEST Data and Characterization

Test Point:

37 21_Sep_Rec_15

38 17_Sep_Rec_9

39 13_Sep_Rec_12

Description: Sliceback FTT - Mild Maneuvering, Workup to Operational Respresentative Tasks, VEST Data and Characterization

Test Point:

40 13_Sep_Rec_13

41 17_Sep_Rec_7

42 17_Sep_Rec_8

43 13_Sep_Rec_18

44 17_Sep_Rec_10

45 17_Sep_Rec_11

Description: Operationally Representative Air Refueling Tasks, VEST Data and Handling Qualities

Test Point:

46 18_Sep_Rec_6

47 18_Sep_Rec_9

48 21_Sep_Rec_4b

49 21_Sep_Rec_2

Description: Operationally Representative Aerial Refueling Tasks, VEST Data and Handling Qualities

Test Point:

50 18_Sep_Rec_5

51 18_Sep_Rec_8

52 21_Sep_Rec_4a

53 21_Sep_Rec_1

54 18_Sep_Rec_7

55 18_Sep_Rec_11

56 21_Sep_Rec_5

57 21_Sep_Rec_3

Description: Operationally Representative Air-to-Air Tracking, VEST Data and Handling Qualities

Test Point:

58 18_Sep_Rec_13

59 18_Sep_Rec_18

60 21_Sep_Rec_12

61 21_Sep_Rec_8

Description: Operationally Representative Air-to-Air Tracking Tasks, VEST Data and Handling Qualities

Test Point:

62 18_Sep_Rec_12

63 18_Sep_Rec_17

64 21_Sep_Rec_11

65 21_Sep_Rec_7

66 18_Sep_Rec_14

67 18_Sep_Rec_19

68 21_Sep_Rec_13

69 21_Sep_Rec_10

Description: Operationally Representative Air-to-Ground Tracking Tasks, VEST Data and Handling Qualities

Test Point:

70 19_Sep_Rec_8

71 19_Sep_Rec_17a

72 19_Sep_Rec_14

73 19_Sep_Rec_17b

Description: Operationally Representative Air-to-Ground Tracking, VEST Data and Handling Qualities

Test Point:

74 19_Sep_Rec_6

75 19_Sep_Rec_18a

76 19_Sep_Rec_13

77 19_Sep_Rec_19a

78 19_Sep_Rec_11

79 19_Sep_Rec_18b

80 19_Sep_Rec_15

81 19_Sep_Rec_19b

Description: Visual Straight-In or ILS to Low Approach, VEST Data and Handling Qualities

Test Point:

82 11_Sep_Rec_20

83 13_Sep_Rec_19

84 17_Sep_Rec_25

85 18_Sep_Rec_23

86 19_Sep_Rec_24

87 21_Sep_Rec_19

Appendix F. Airspeed Flight Test Data Plots

The error time history plots in this appendix are arranged according to the following maneuvers (sections F.1 – F.6): J-Hook flight test technique (FTT), Sliceback FTT, Operational Maneuvers, Long Shot FTT, Container FTT, and Landing Approaches. Heading, calibrated and true airspeed time histories are included for each test point. Each plot is labeled as follows: conditions for the maneuver at the top, and test matrix test point and date at the bottom [McLaren 2007].

F.1. J-Hook Flight Test Technique

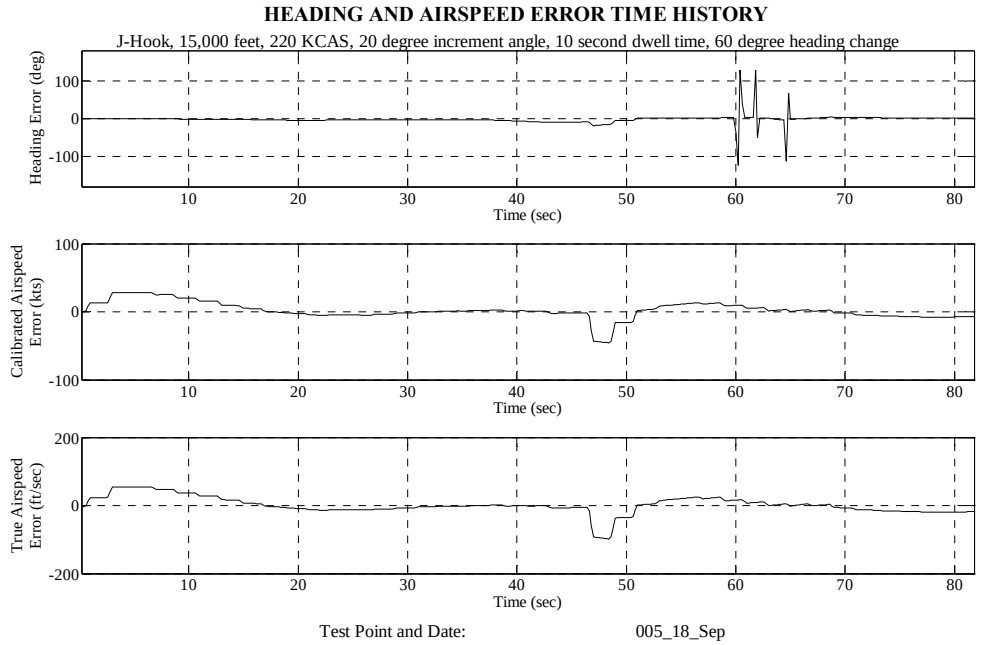

HEADING AND AIRSPEED ERROR TIME HISTORY

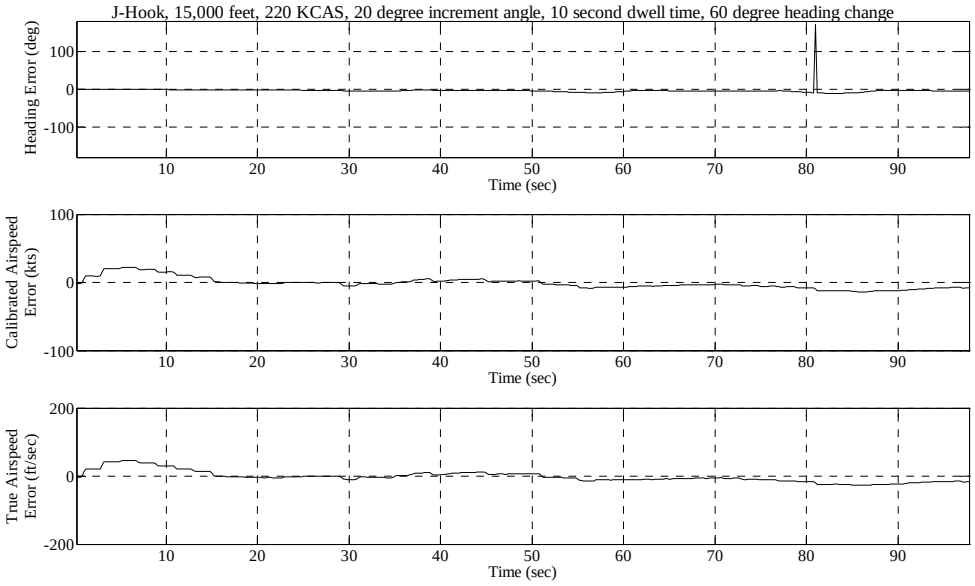

Test Point and Date: 005_21_Sep

HEADING AND AIRSPEED ERROR TIME HISTORY

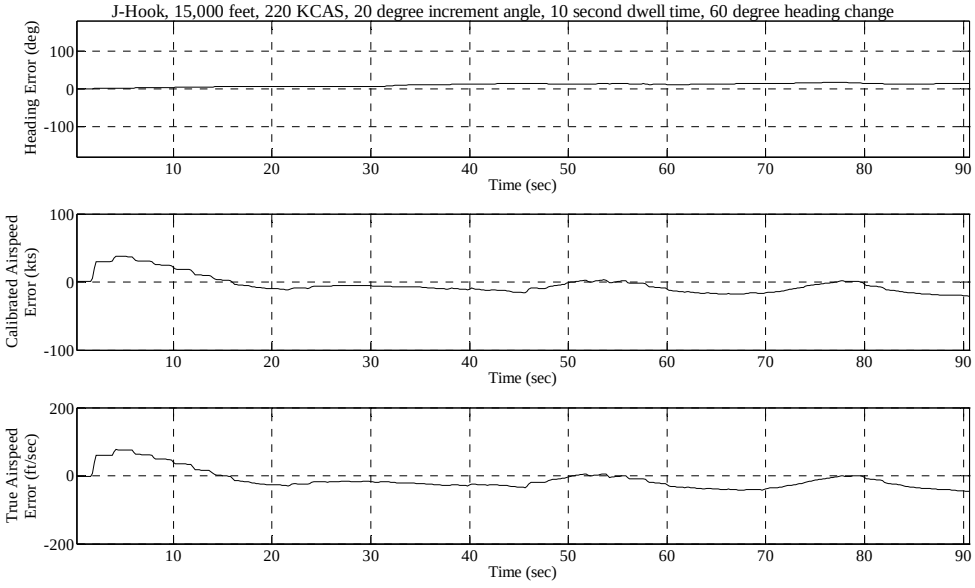

Test Point and Date: 006_13_Sep

HEADING AND AIRSPEED ERROR TIME HISTORY

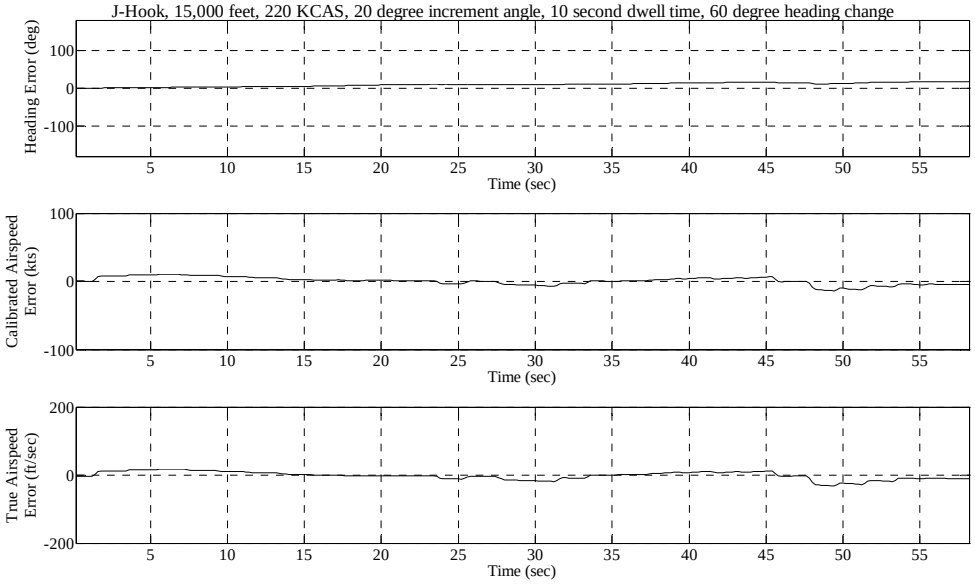

Test Point and Date: 007_13_Sep

HEADING AND AIRSPEED ERROR TIME HISTORY

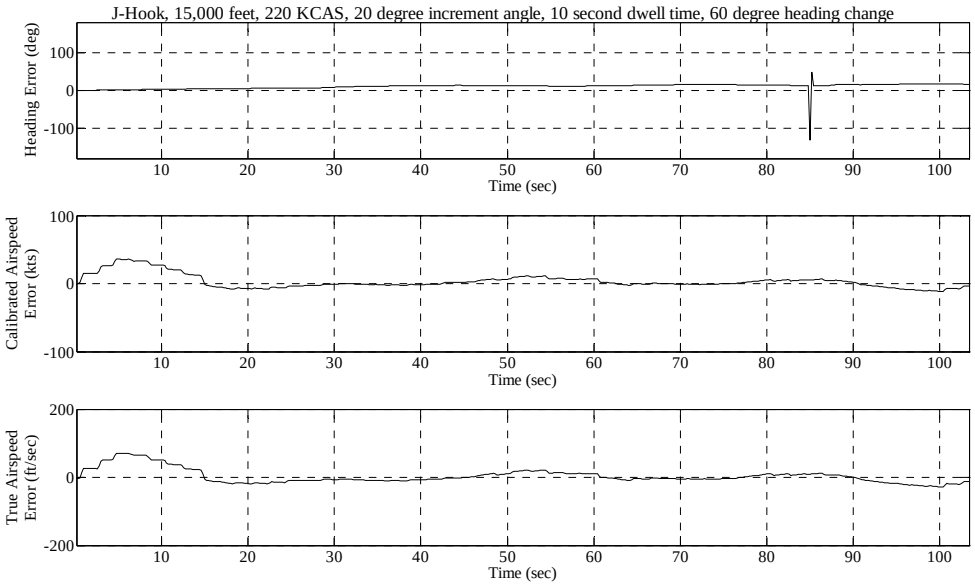

Test Point and Date: 008_13_Sep

HEADING AND AIRSPEED ERROR TIME HISTORY

J-Hook, 15,000 feet, 280 KCAS, 20 degree increment angle, 10 second dwell time, 150 degree heading change

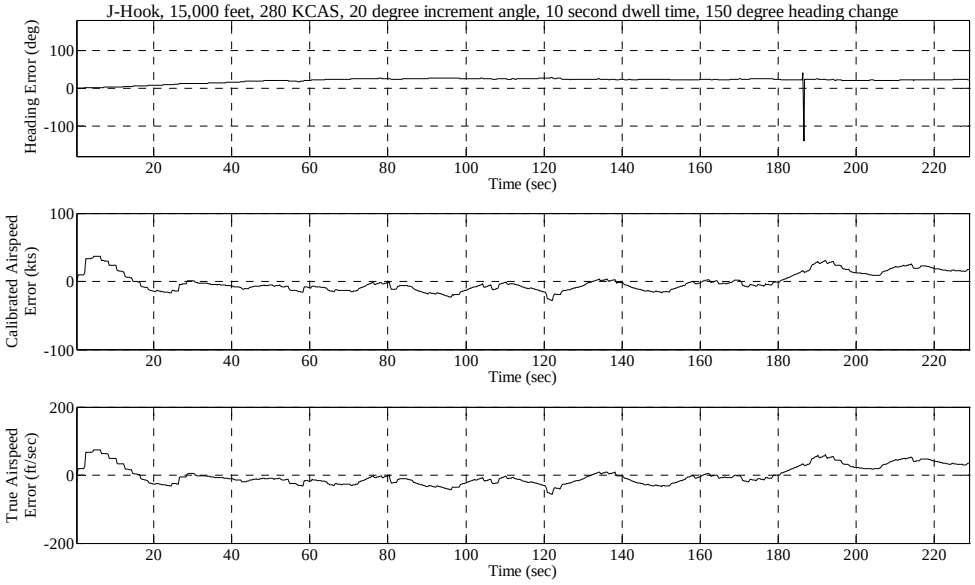

Test Point and Date: 009_17_Sep

HEADING AND AIRSPEED ERROR TIME HISTORY

J-Hook, 15,000 feet, 280 KCAS, 20 degree increment angle, 10 second dwell time, 150 degree heading change

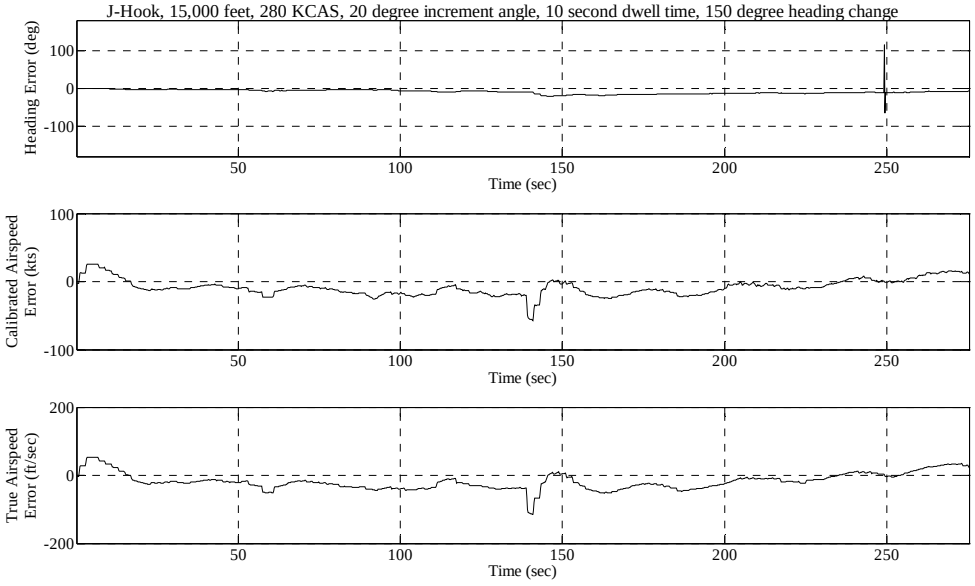

Test Point and Date: 010_19_Sep

HEADING AND AIRSPEED ERROR TIME HISTORY

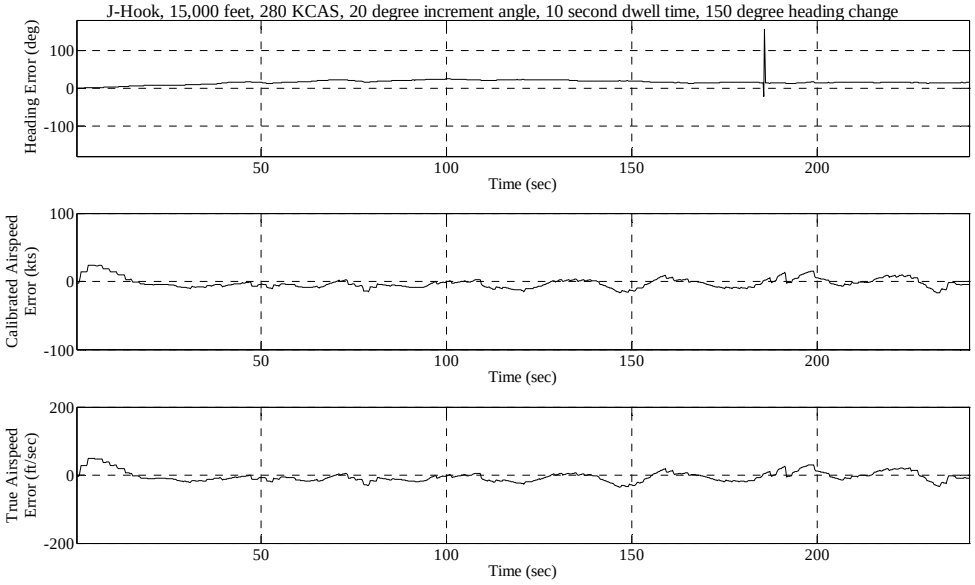

Test Point and Date: 011_17_Sep

HEADING AND AIRSPEED ERROR TIME HISTORY

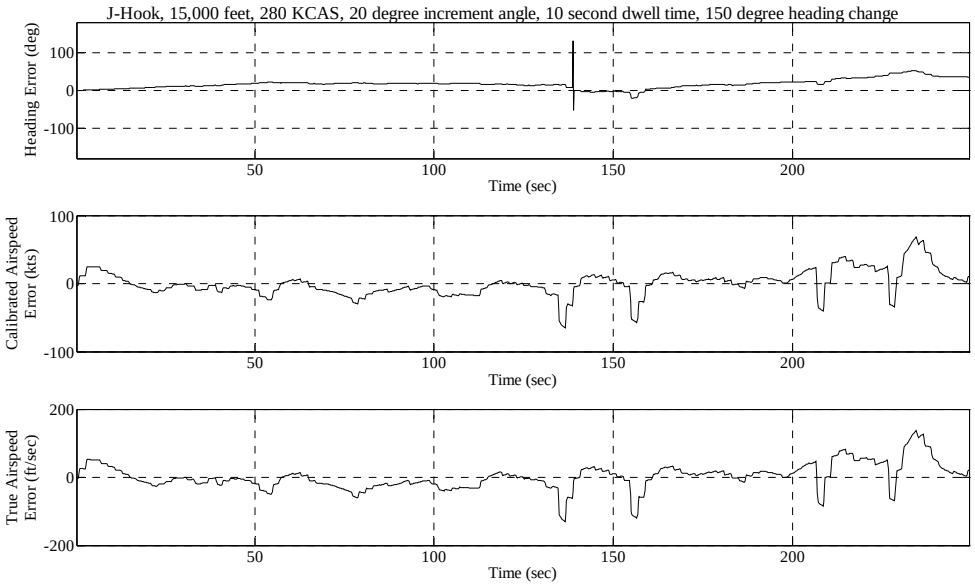

Test Point and Date: 012_17_Sep

HEADING AND AIRSPEED ERROR TIME HISTORY

J-Hook, 15,000 feet, 220 KCAS, 20 degree increment angle, 30 second dwell time, 150 degree heading change

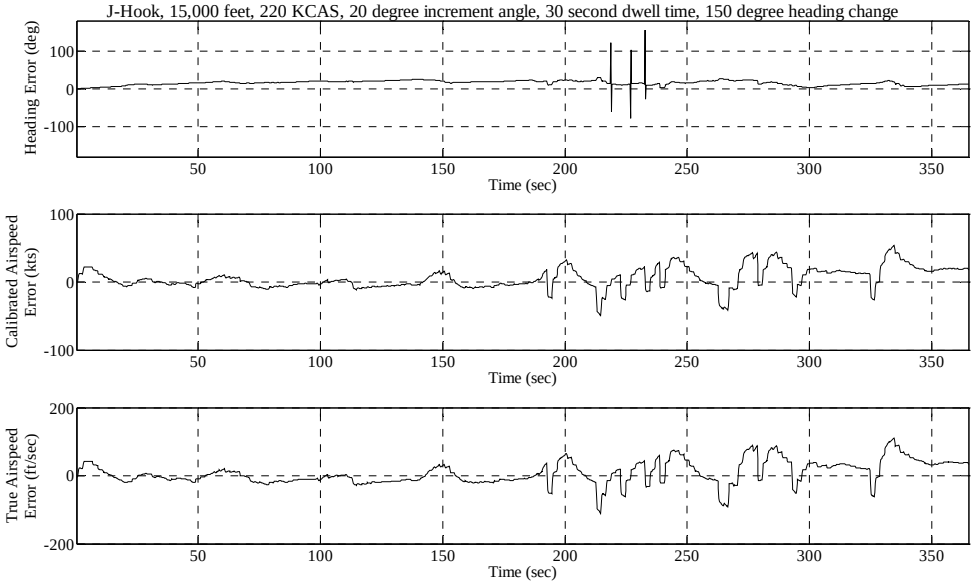

Test Point and Date: 013_13_Sep

HEADING AND AIRSPEED ERROR TIME HISTORY

J-Hook, 15,000 feet, 220 KCAS, 20 degree increment angle, 30 second dwell time, 150 degree heading change

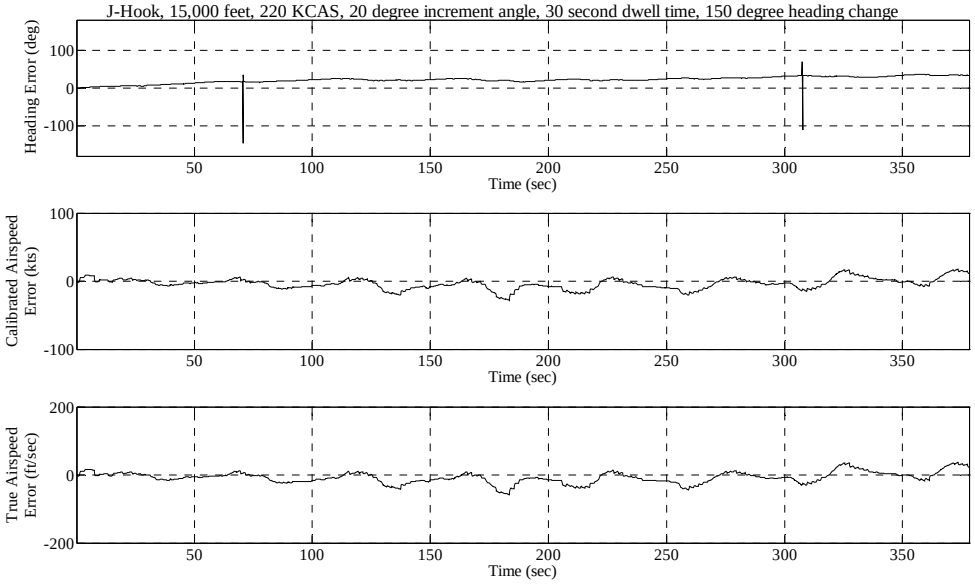

Test Point and Date: 014_17_Sep

HEADING AND AIRSPEED ERROR TIME HISTORY

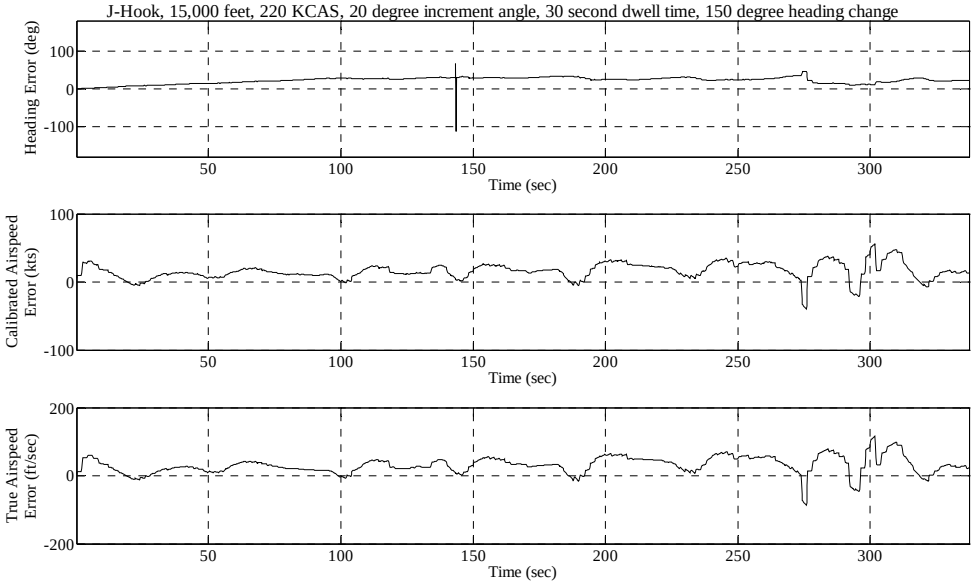

Test Point and Date: 015_13_Sep

HEADING AND AIRSPEED ERROR TIME HISTORY

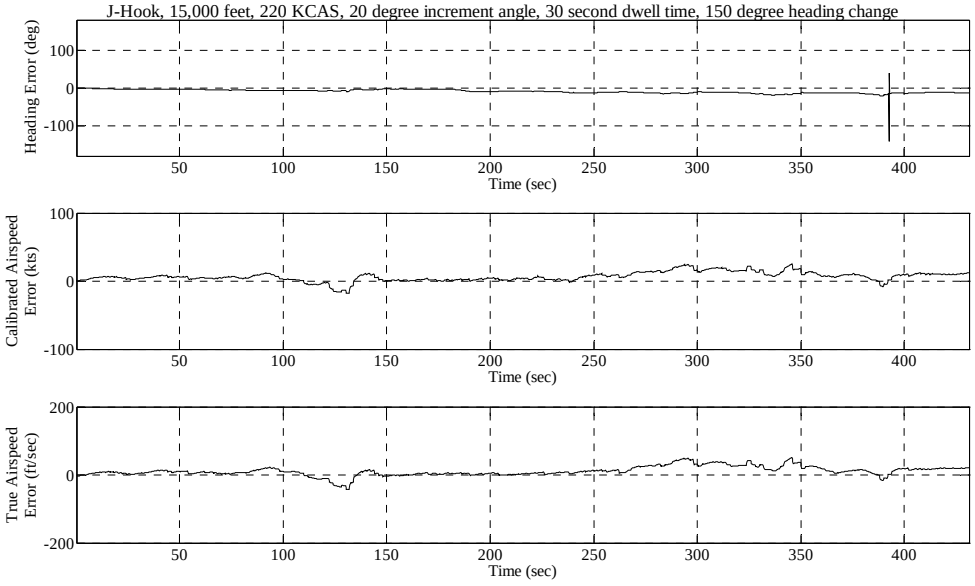

Test Point and Date: 016_19_Sep

HEADING AND AIRSPEED ERROR TIME HISTORY

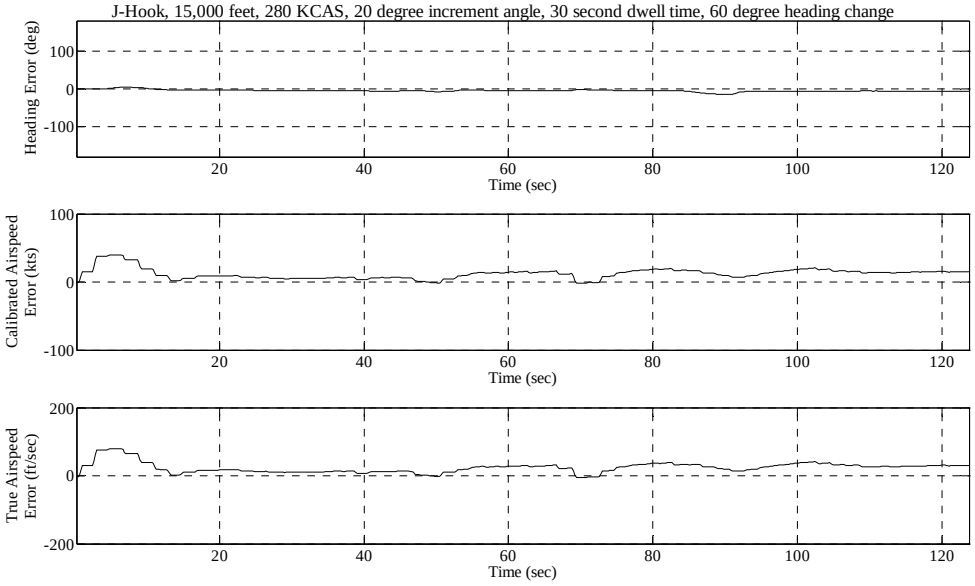

Test Point and Date: 017_18_Sep

HEADING AND AIRSPEED ERROR TIME HISTORY

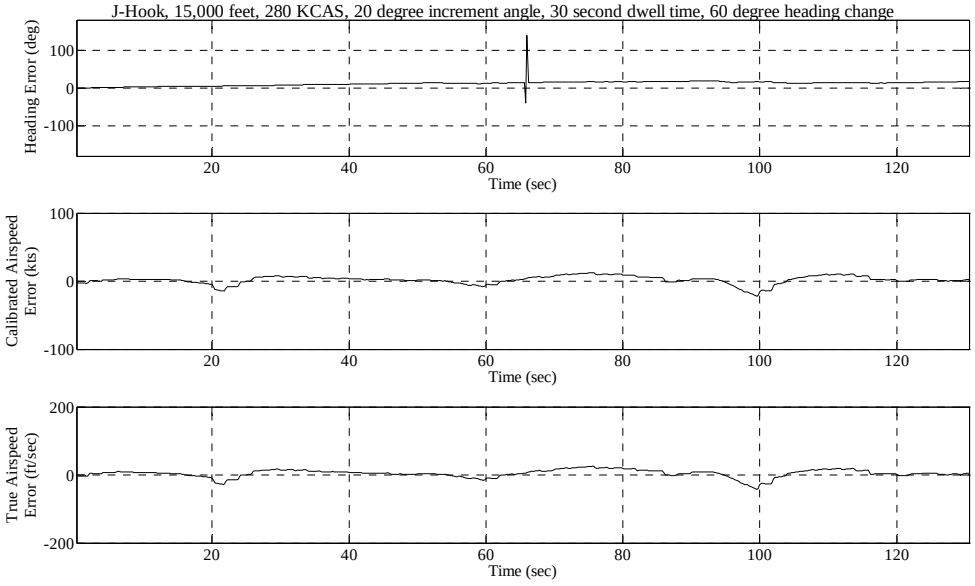

Test Point and Date: 018_13_Sep

HEADING AND AIRSPEED ERROR TIME HISTORY

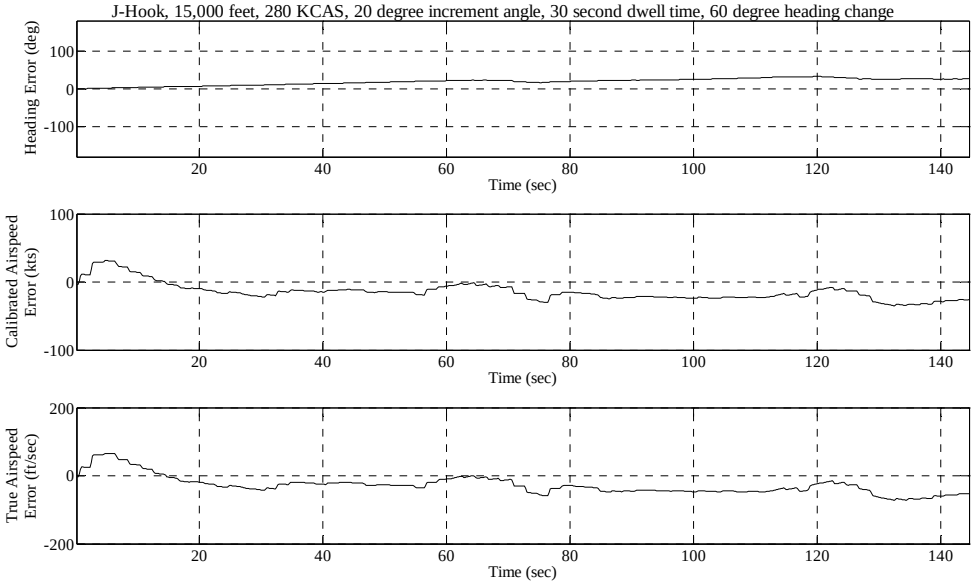

Test Point and Date: 019_17_Sep

HEADING AND AIRSPEED ERROR TIME HISTORY

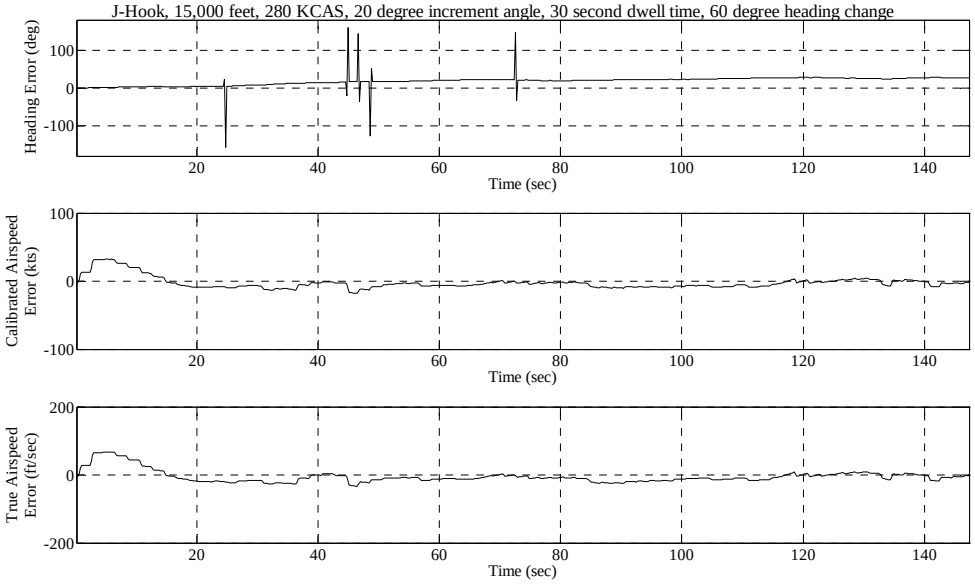

Test Point and Date: 020_17_Sep

HEADING AND AIRSPEED ERROR TIME HISTORY

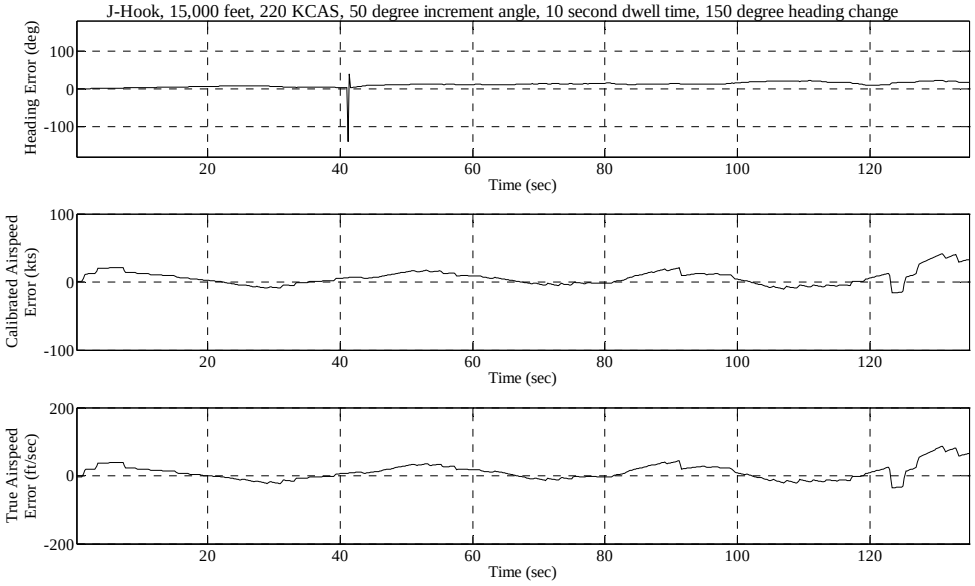

Test Point and Date: 021_13_Sep

HEADING AND AIRSPEED ERROR TIME HISTORY

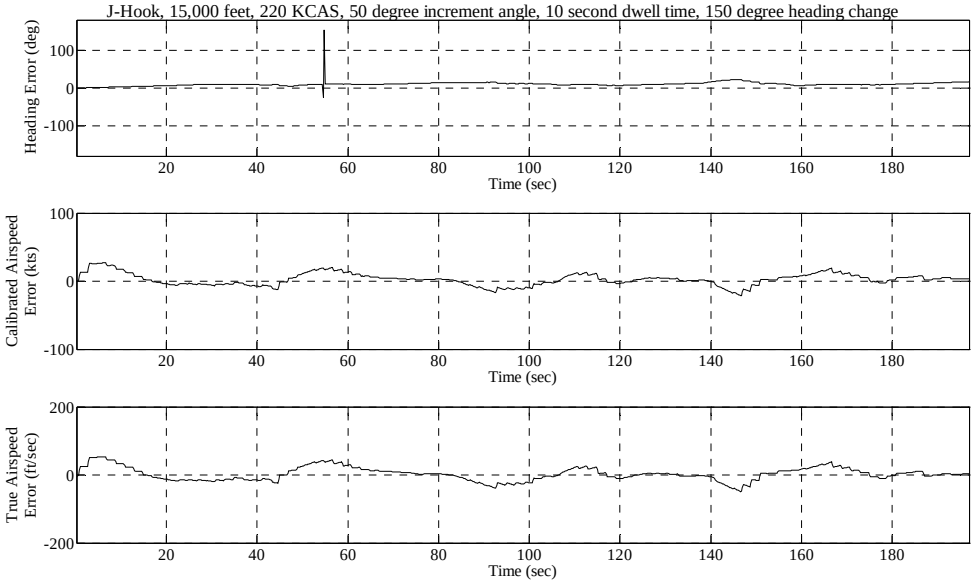

Test Point and Date: 022_13_Sep

HEADING AND AIRSPEED ERROR TIME HISTORY

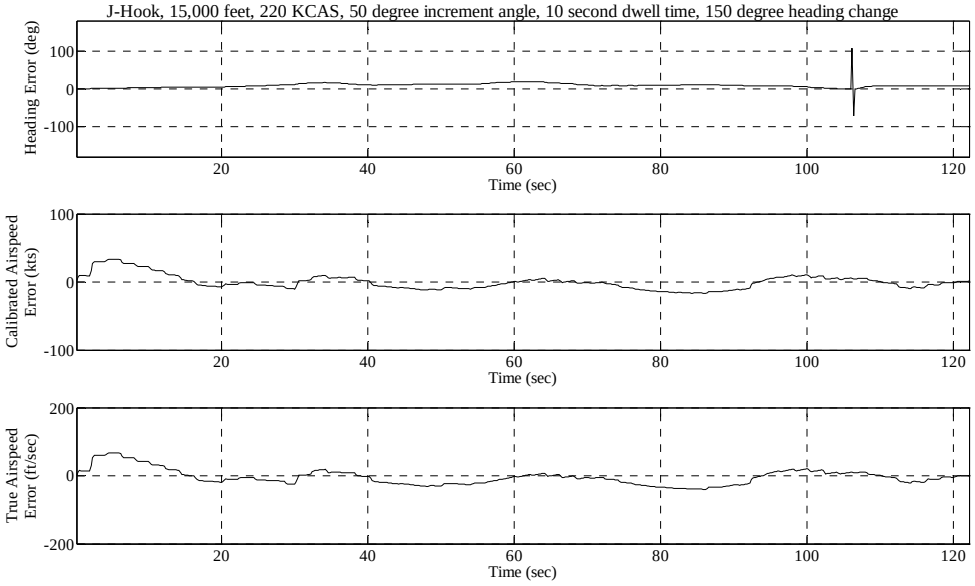

Test Point and Date: 023_13_Sep

HEADING AND AIRSPEED ERROR TIME HISTORY

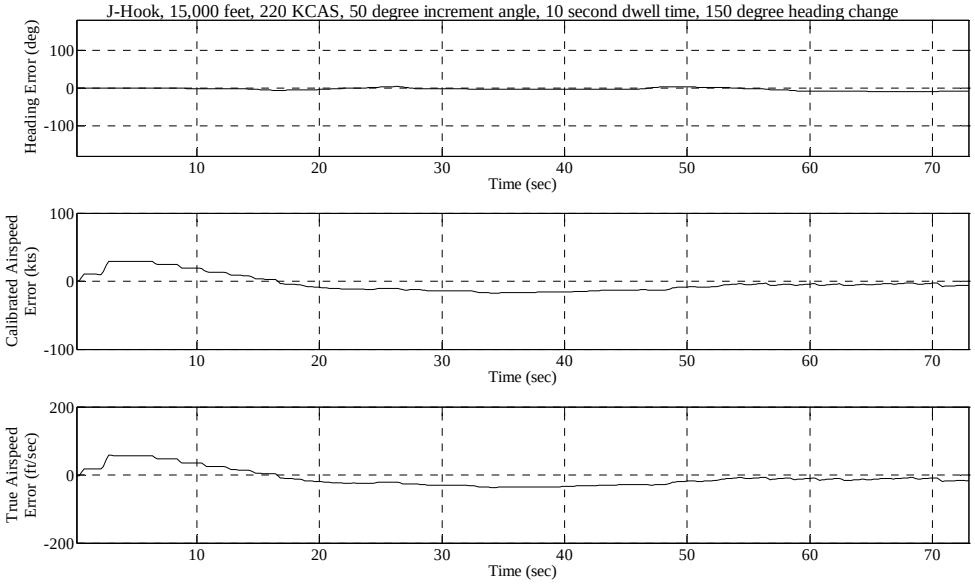

Test Point and Date: 024_18_Sep

HEADING AND AIRSPEED ERROR TIME HISTORY

J-Hook, 15,000 feet, 280 KCAS, 50 degree increment angle, 10 second dwell time, 60 degree heading change

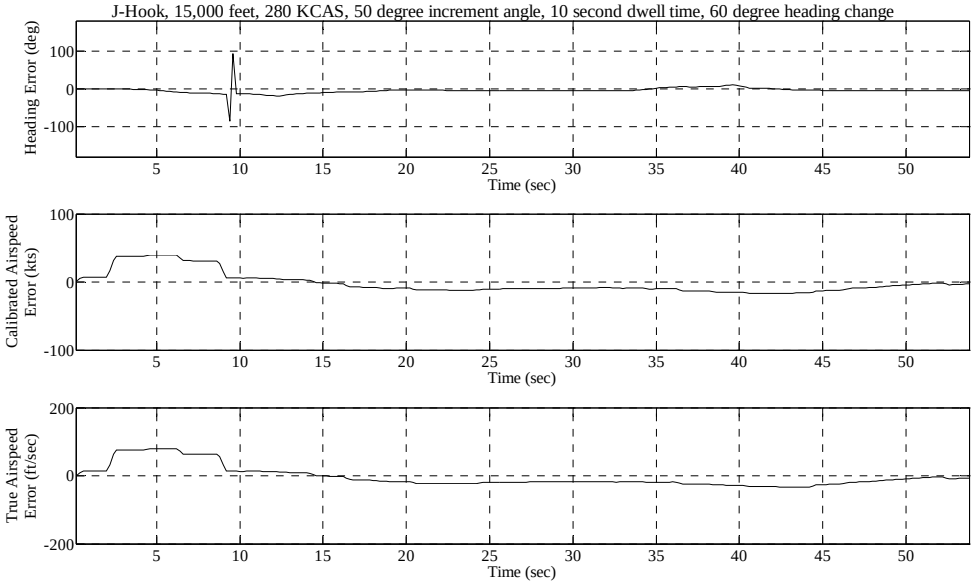

Test Point and Date: 025_18_Sep

HEADING AND AIRSPEED ERROR TIME HISTORY

J-Hook, 15,000 feet, 280 KCAS, 50 degree increment angle, 10 second dwell time, 60 degree heading change

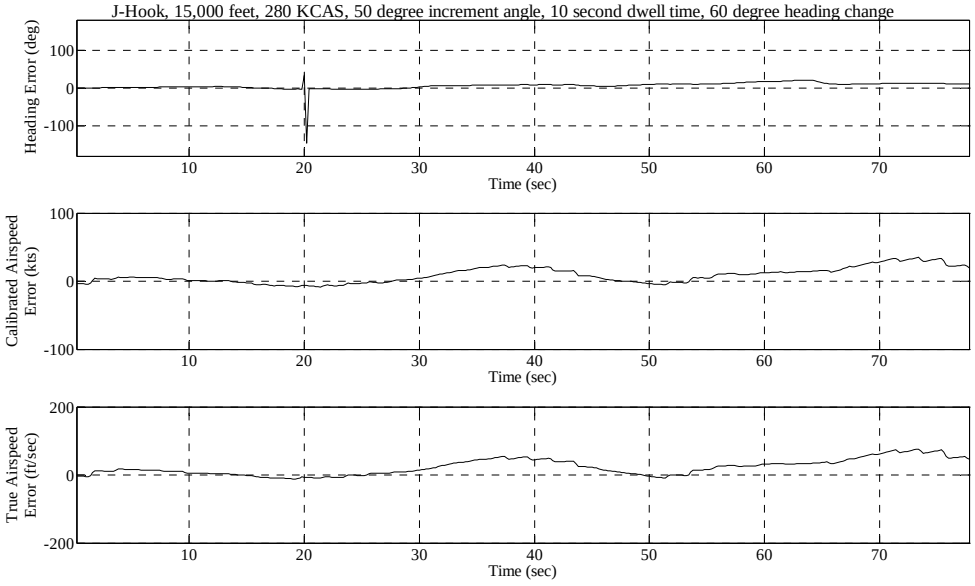

Test Point and Date: 026_17_Sep

HEADING AND AIRSPEED ERROR TIME HISTORY

J-Hook, 15,000 feet, 280 KCAS, 50 degree increment angle, 10 second dwell time, 60 degree heading change

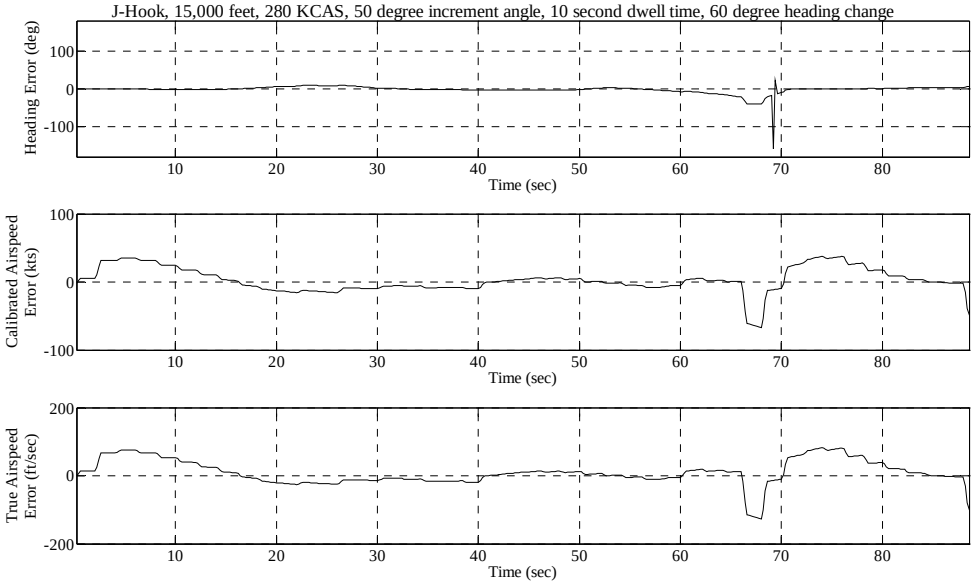

Test Point and Date: 026_21_Sep

HEADING AND AIRSPEED ERROR TIME HISTORY

J-Hook, 15,000 feet, 280 KCAS, 50 degree increment angle, 10 second dwell time, 60 degree heading change

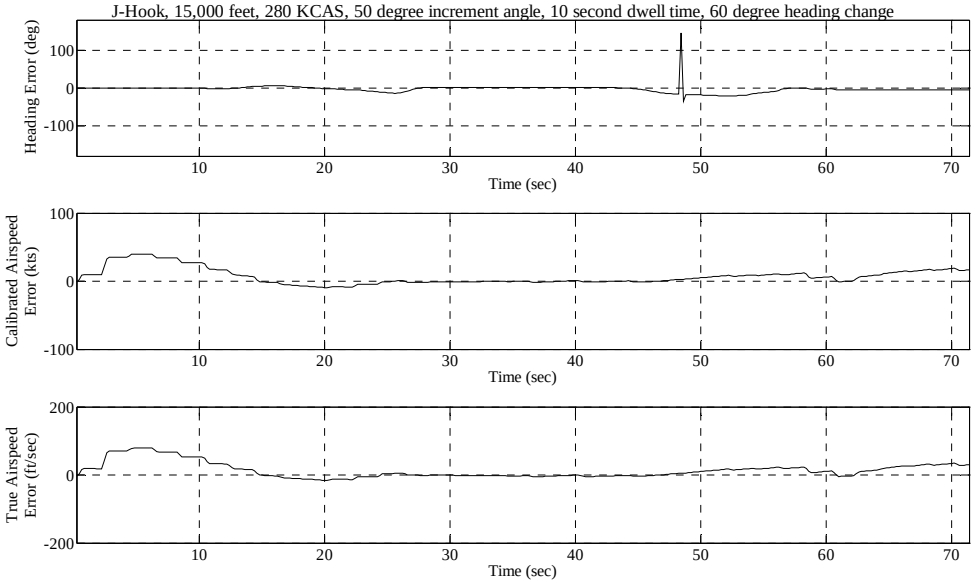

Test Point and Date: 027_18_Sep

HEADING AND AIRSPEED ERROR TIME HISTORY

J-Hook, 15,000 feet, 280 KCAS, 50 degree increment angle, 10 second dwell time, 60 degree heading change

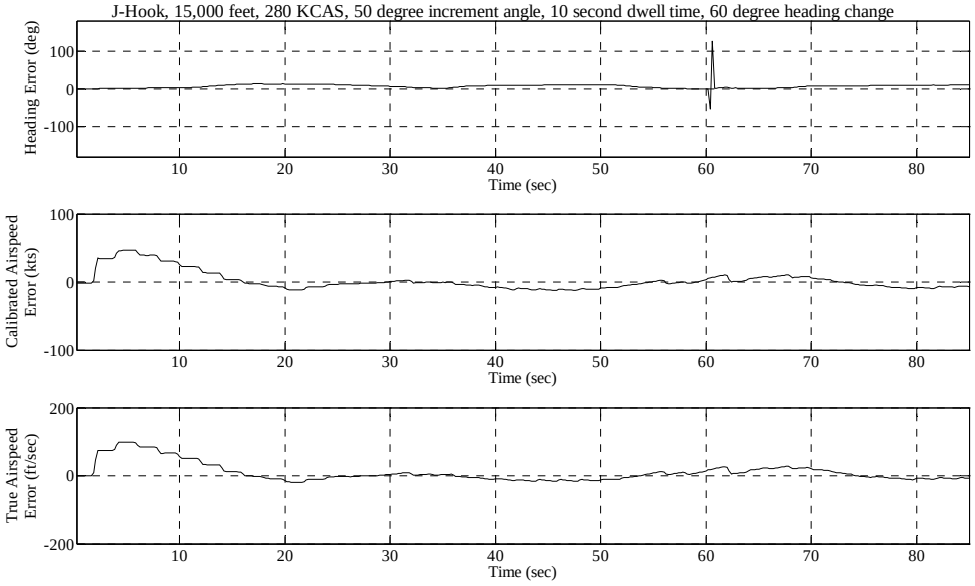

Test Point and Date: 028_17_Sep

HEADING AND AIRSPEED ERROR TIME HISTORY

J-Hook, 15,000 feet, 220 KCAS, 50 degree increment angle, 30 second dwell time, 60 degree heading change

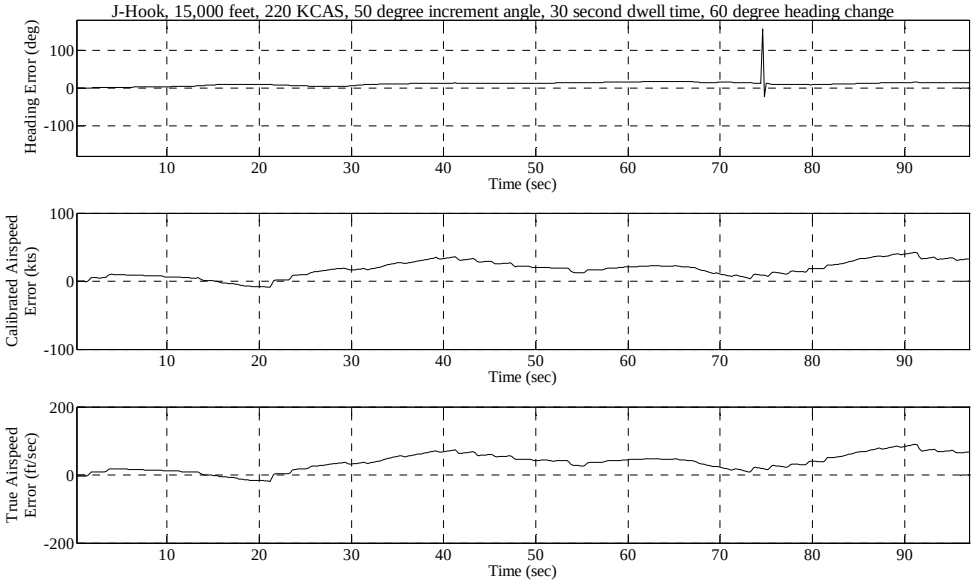

Test Point and Date: 029_17_Sep

HEADING AND AIRSPEED ERROR TIME HISTORY

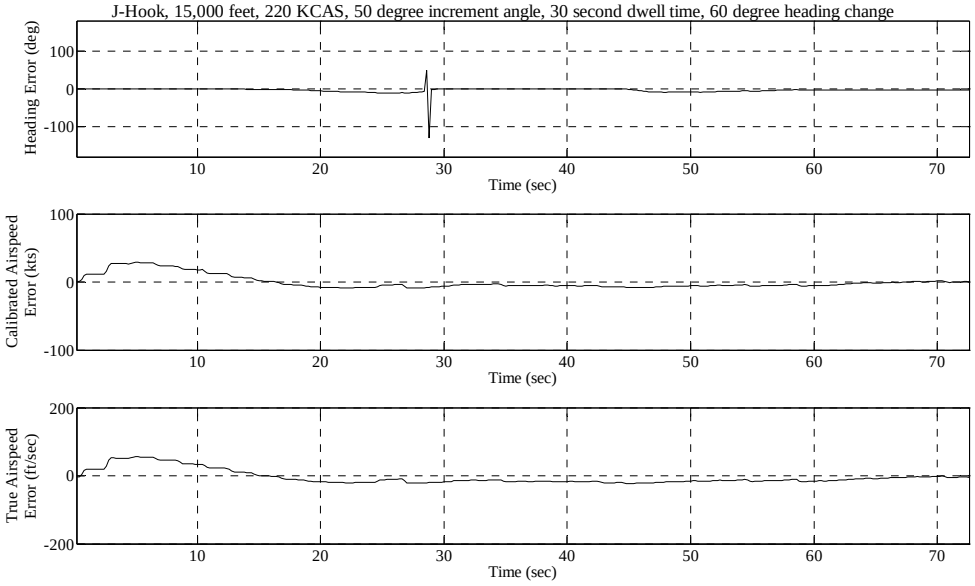

Test Point and Date: 030_18_Sep

HEADING AND AIRSPEED ERROR TIME HISTORY

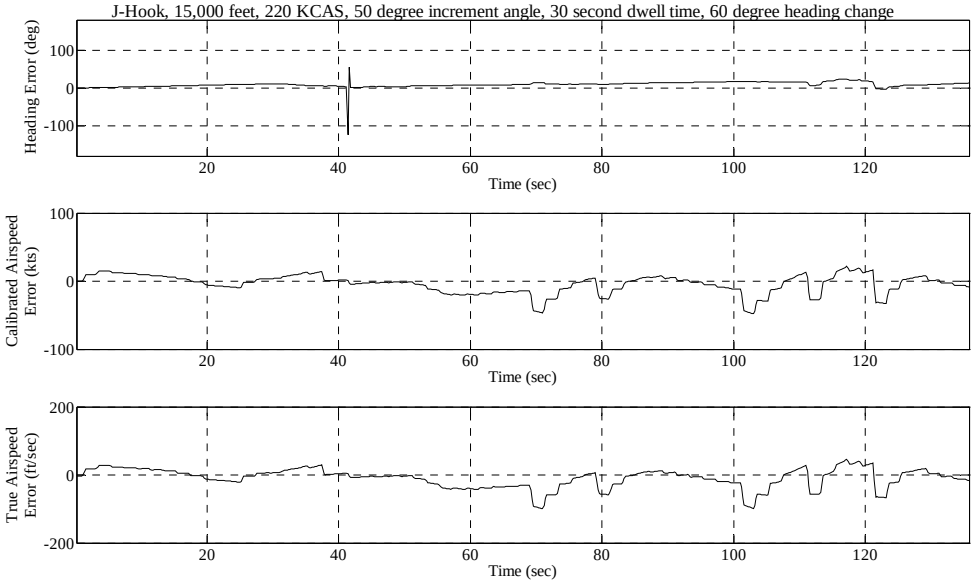

Test Point and Date: 031_17_Sep

HEADING AND AIRSPEED ERROR TIME HISTORY

J-Hook, 15,000 feet, 220 KCAS, 50 degree increment angle, 30 second dwell time, 60 degree heading change

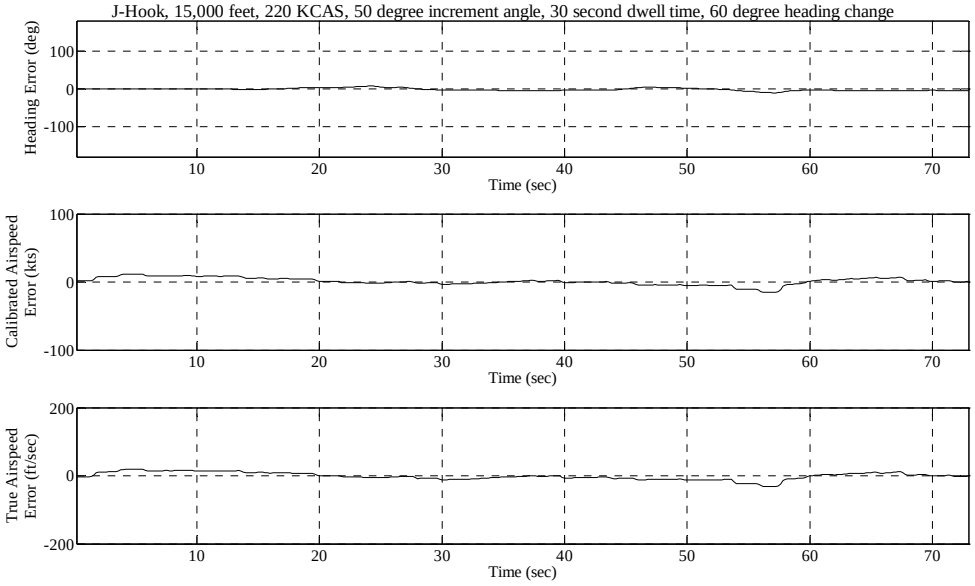

Test Point and Date: 032_18_Sep

HEADING AND AIRSPEED ERROR TIME HISTORY

J-Hook, 15,000 feet, 280 KCAS, 50 degree increment angle, 30 second dwell time, 150 degree heading change

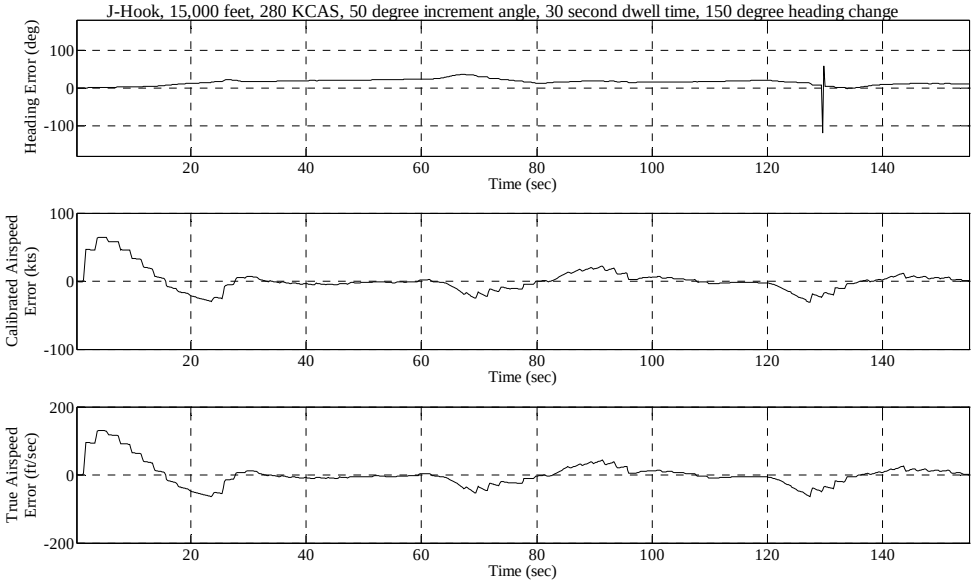

Test Point and Date: 033_17_Sep

HEADING AND AIRSPEED ERROR TIME HISTORY

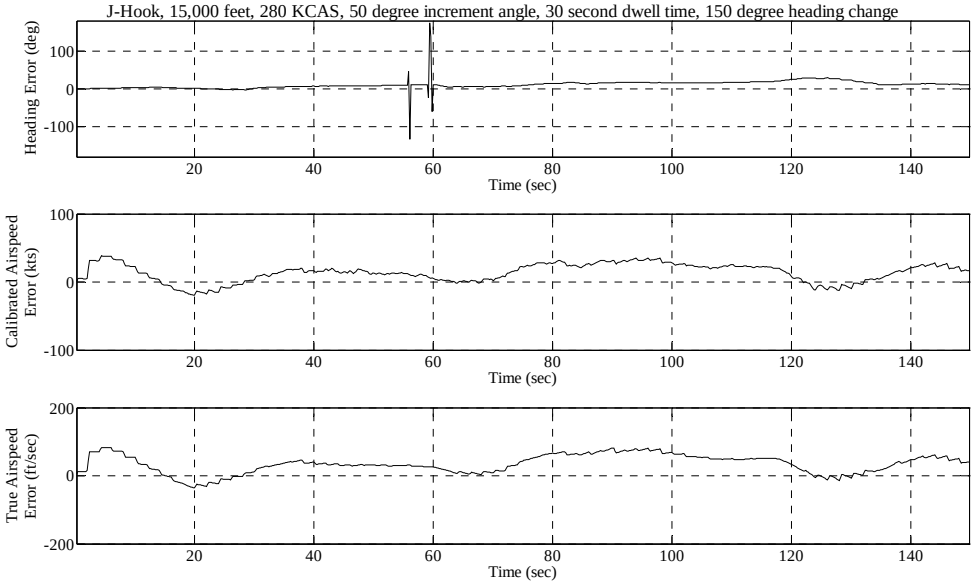

Test Point and Date: 034_17_Sep

HEADING AND AIRSPEED ERROR TIME HISTORY

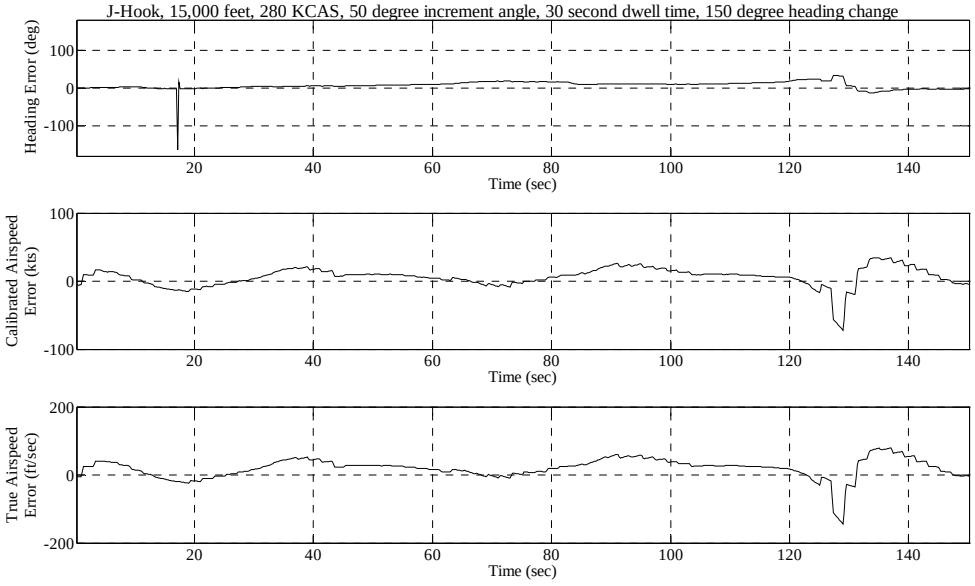

Test Point and Date: 035_17_Sep

HEADING AND AIRSPEED ERROR TIME HISTORY

J-Hook, 15,000 feet, 280 KCAS, 50 degree increment angle, 30 second dwell time, 150 degree heading change

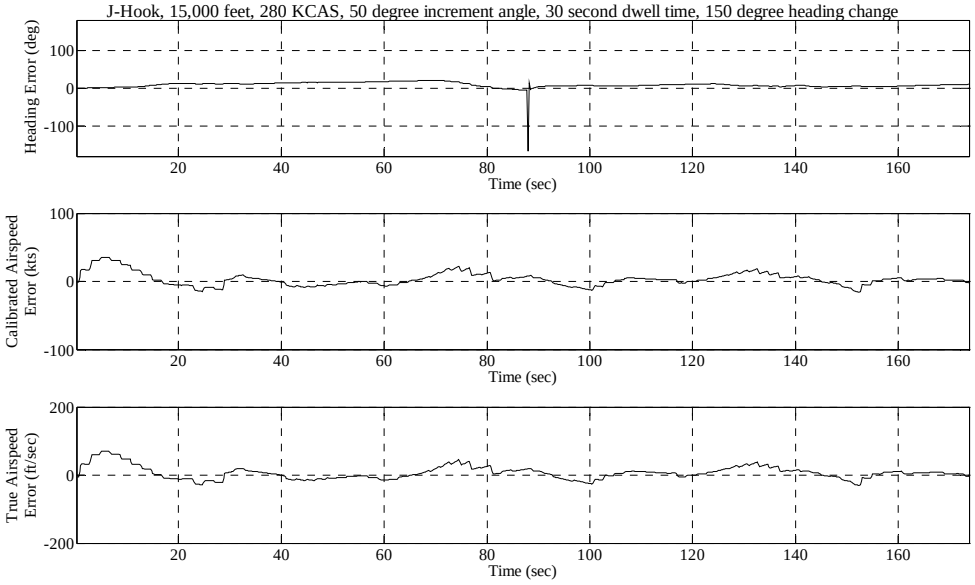

Test Point and Date: 036_17_Sep

F.2. Sliceback Flight Test Technique

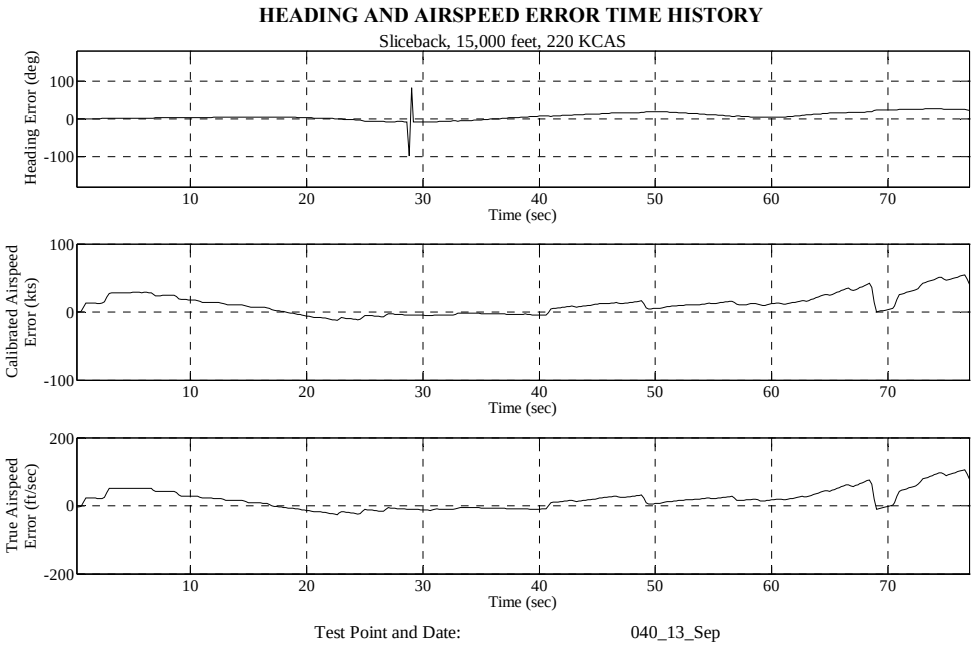

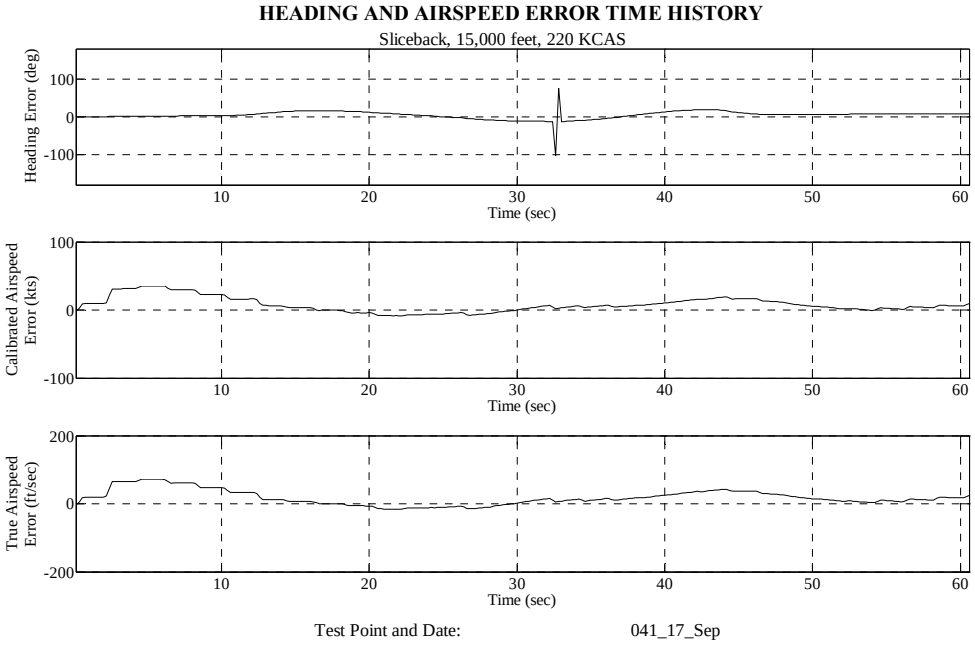

HEADING AND AIRSPEED ERROR TIME HISTORY

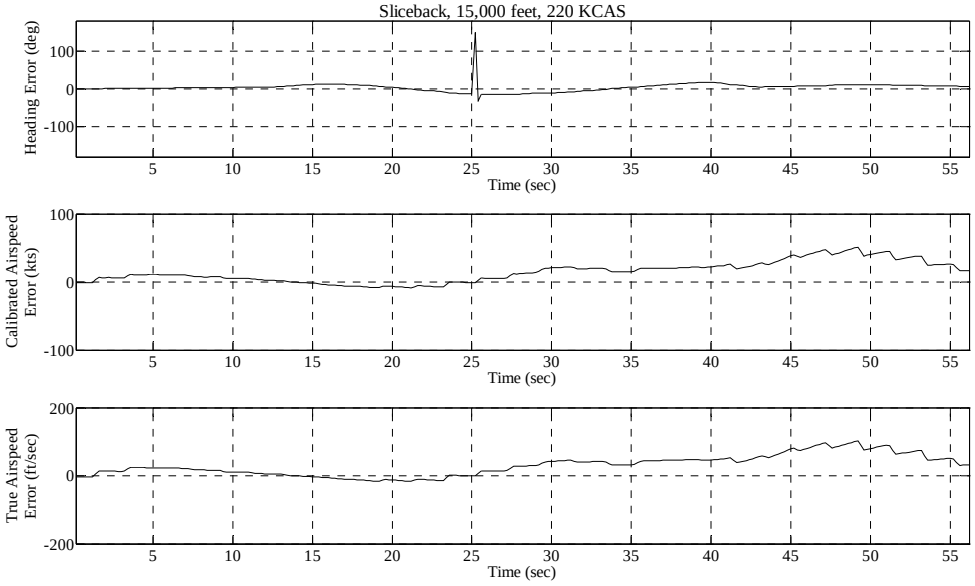

Test Point and Date: 042_17_Sep

HEADING AND AIRSPEED ERROR TIME HISTORY

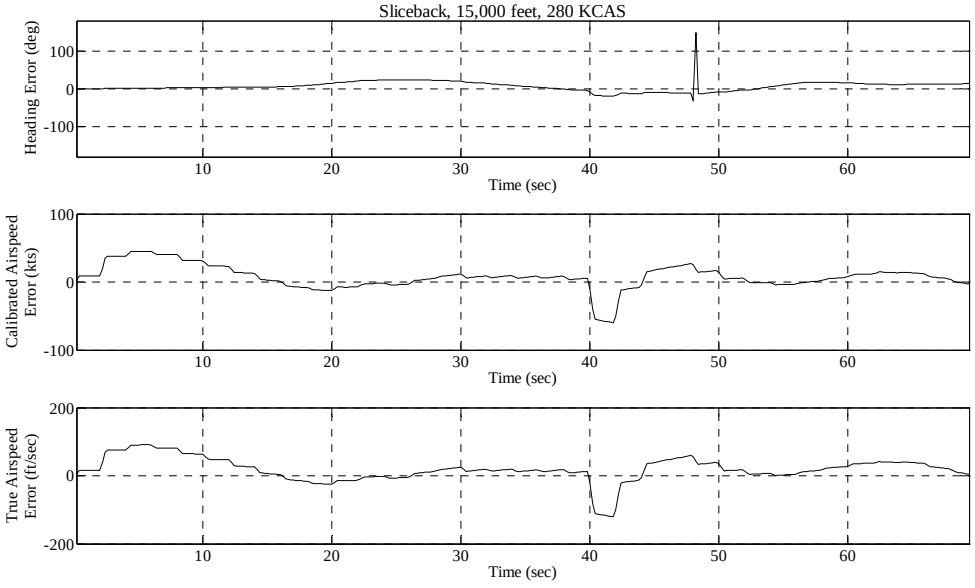

Test Point and Date: 043_13_Sep

HEADING AND AIRSPEED ERROR TIME HISTORY

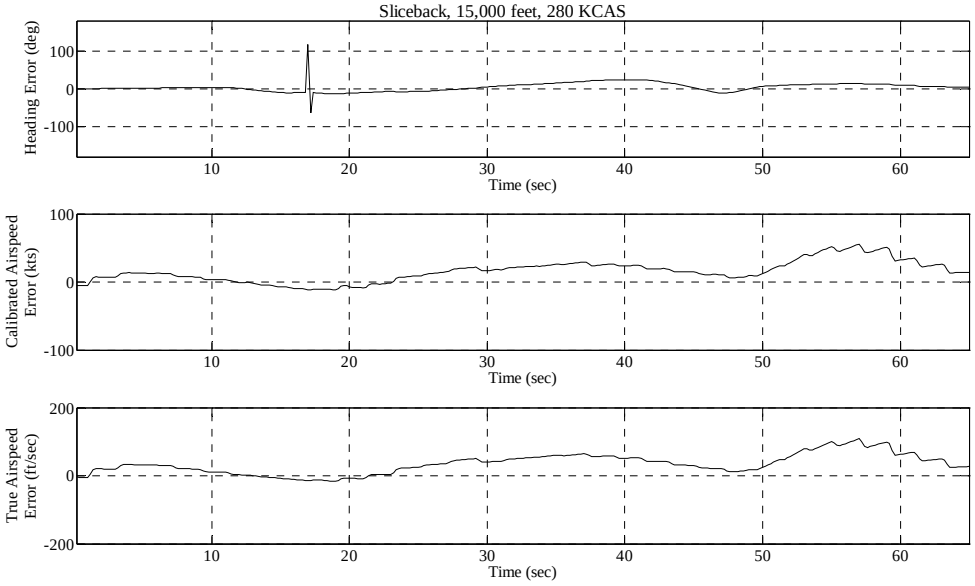

Test Point and Date: 044_17_Sep

HEADING AND AIRSPEED ERROR TIME HISTORY

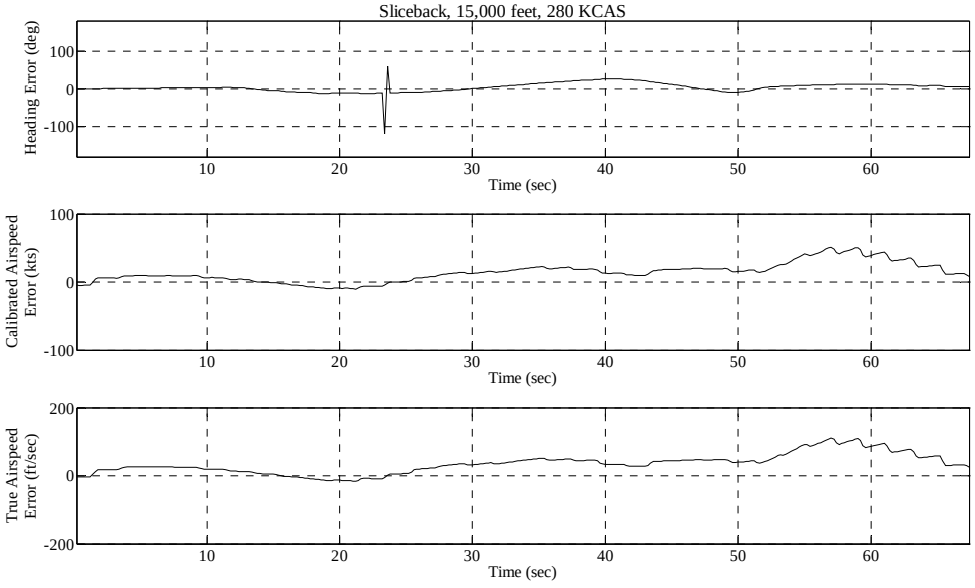

Test Point and Date: 045_17_Sep

F.3. Operational Maneuvers

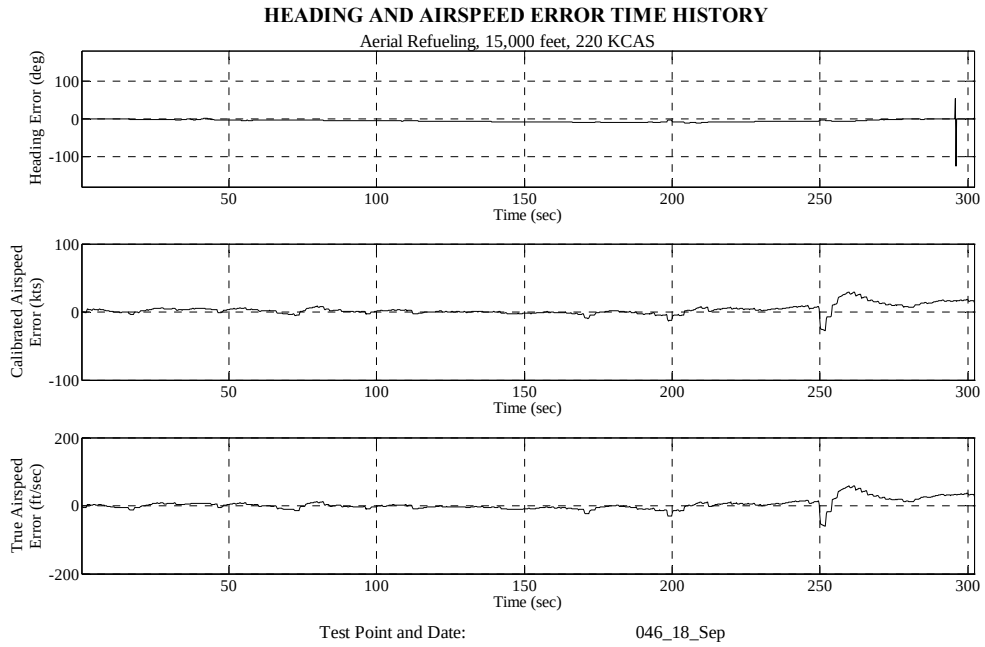

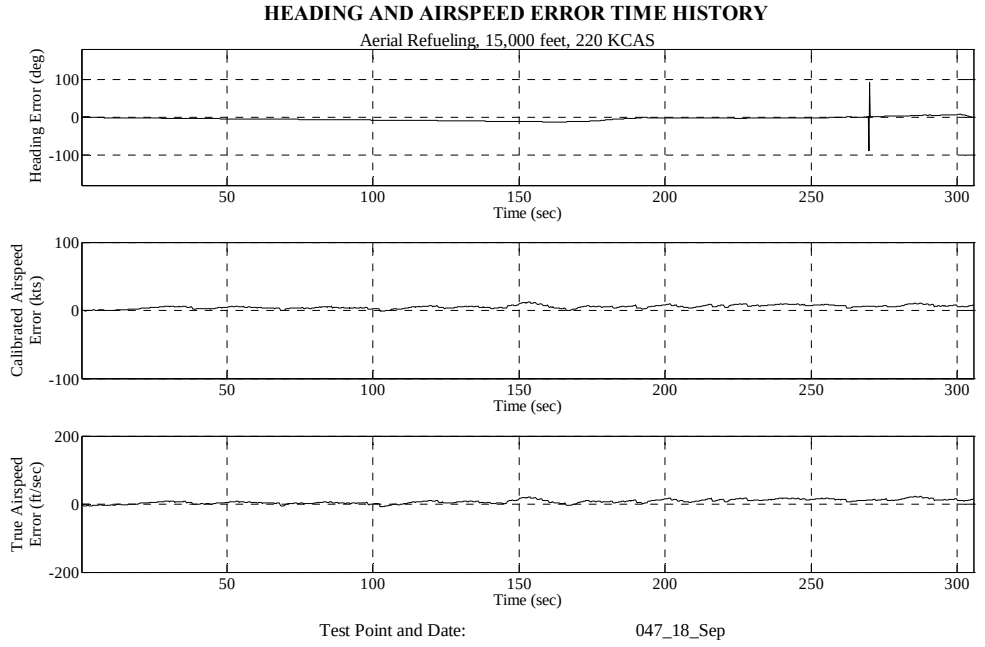

HEADING AND AIRSPEED ERROR TIME HISTORY

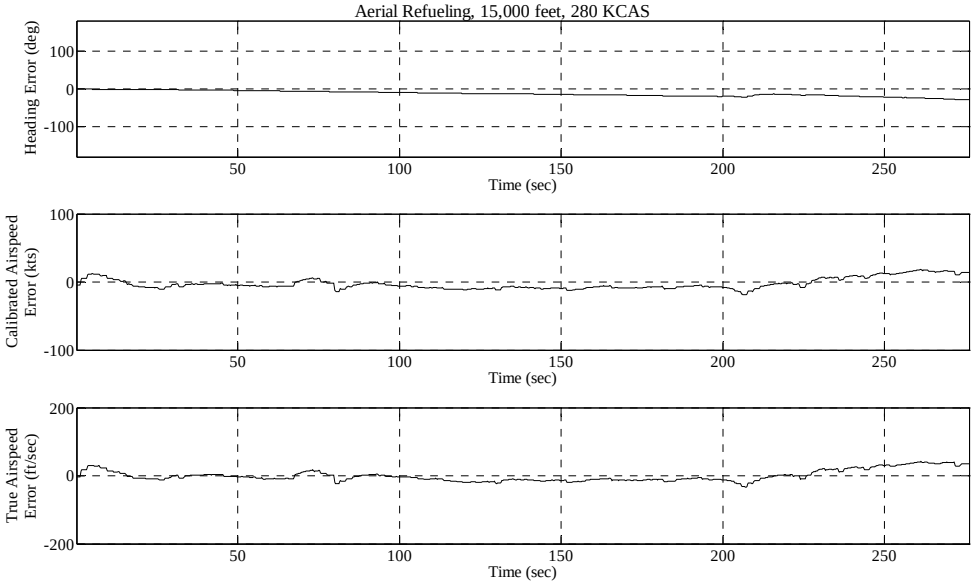

Test Point and Date: 048_21_Sep

HEADING AND AIRSPEED ERROR TIME HISTORY

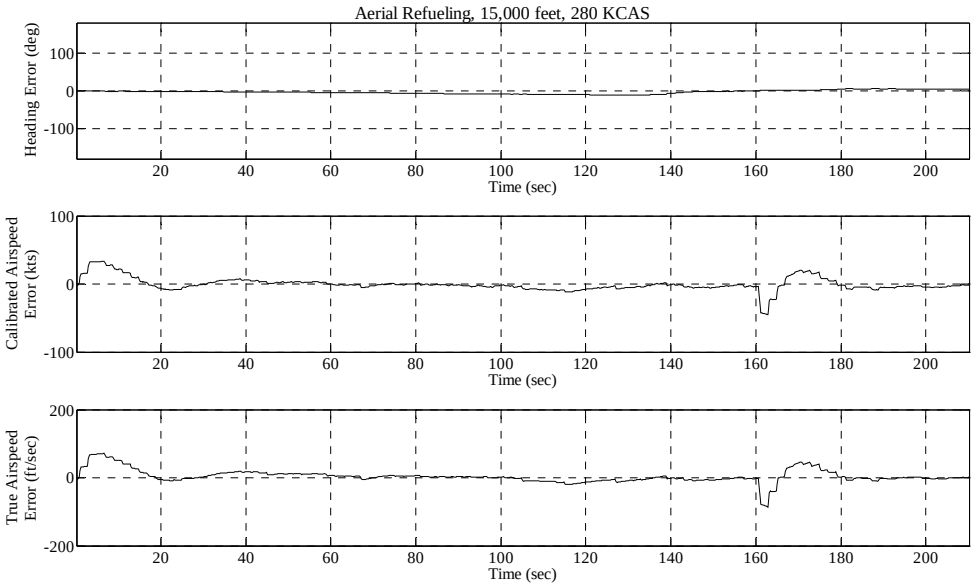

Test Point and Date: 049_21_Sep

HEADING AND AIRSPEED ERROR TIME HISTORY

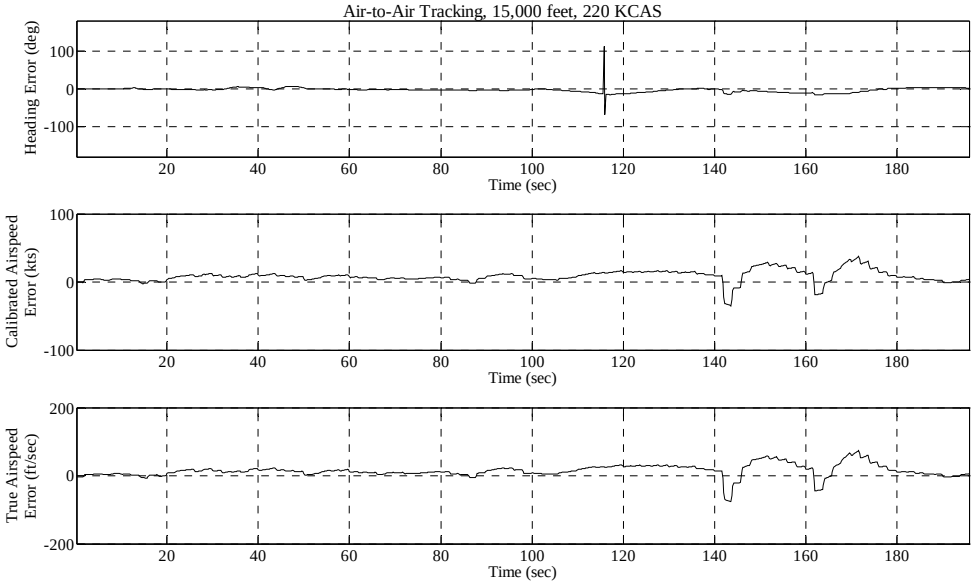

Test Point and Date: 058_18_Sep

HEADING AND AIRSPEED ERROR TIME HISTORY

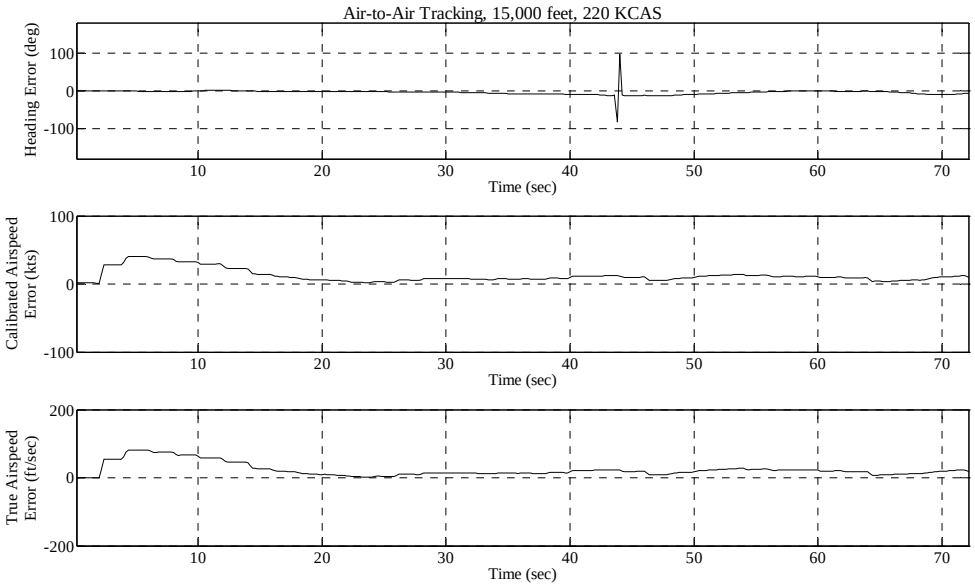

Test Point and Date: 059_18_Sep

HEADING AND AIRSPEED ERROR TIME HISTORY

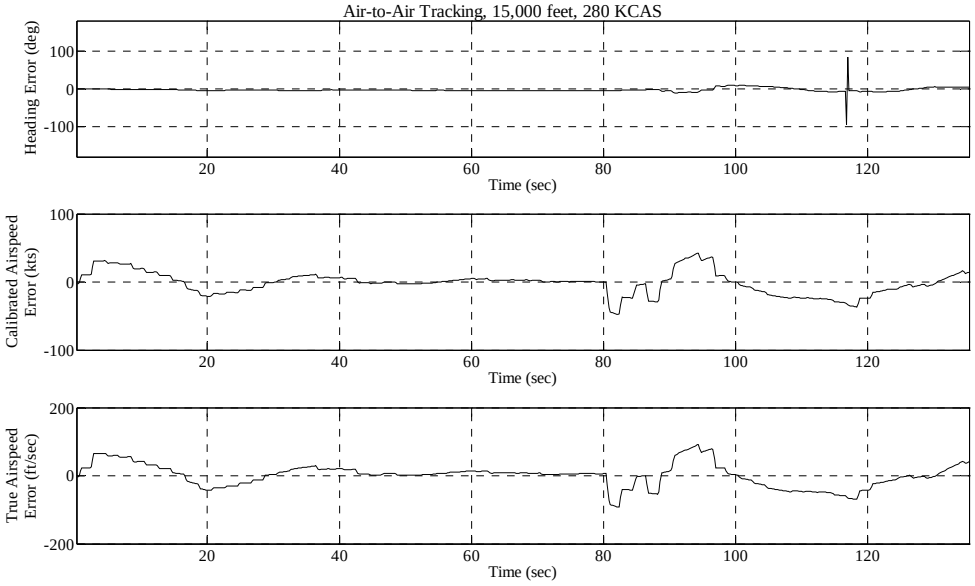

Test Point and Date: 060_21_Sep

HEADING AND AIRSPEED ERROR TIME HISTORY

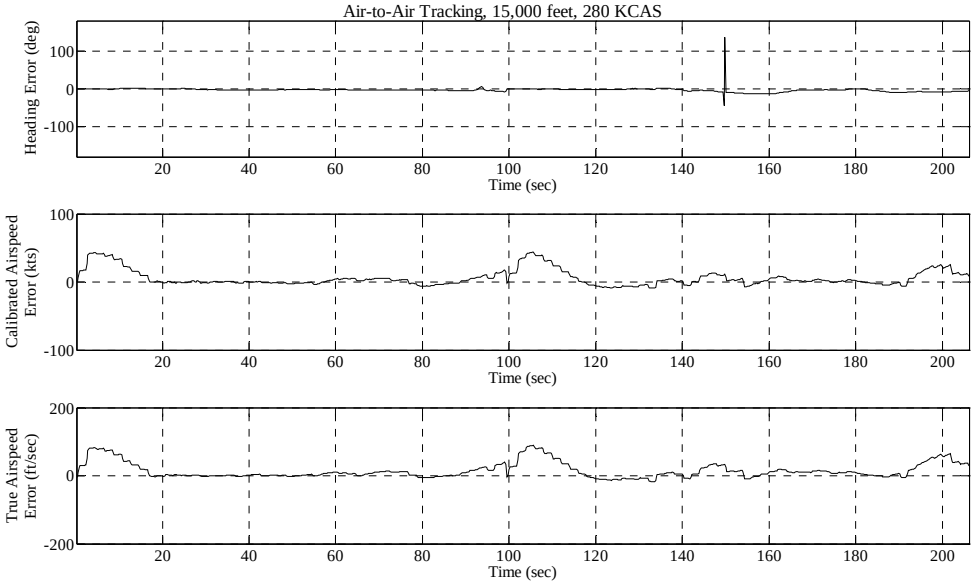

Test Point and Date: 061_21_Sep

HEADING AND AIRSPEED ERROR TIME HISTORY

Ground Attack, 17-13,000 feet, 220 KCAS

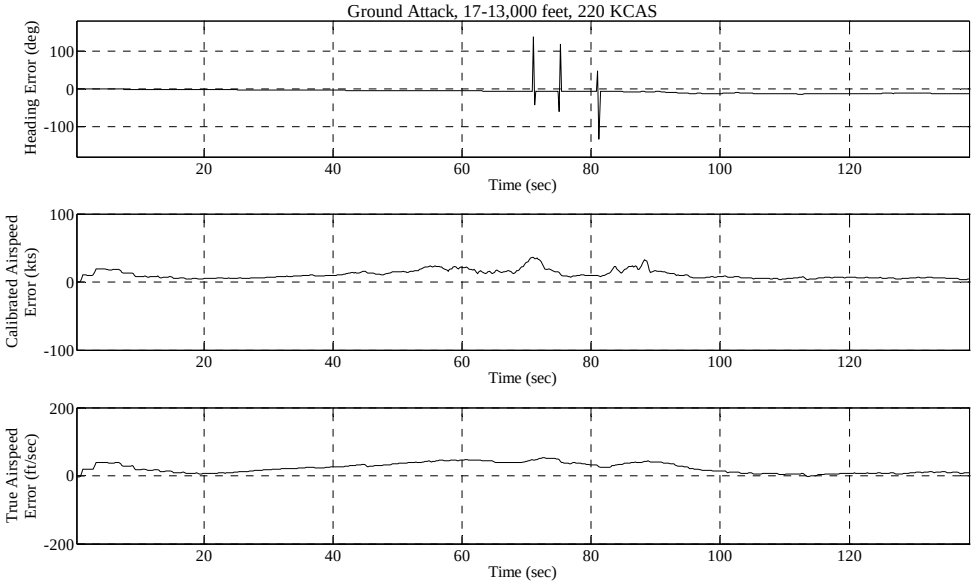

Test Point and Date: 070_19_Sep

HEADING AND AIRSPEED ERROR TIME HISTORY

Ground Attack, 17-13,000 feet, 220 KCAS

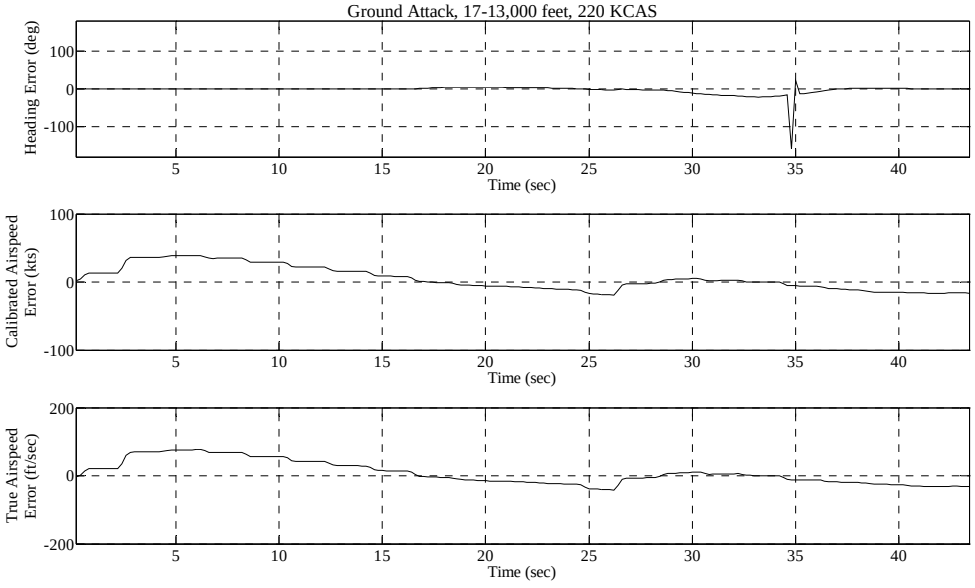

Test Point and Date: 071_19_Sep

HEADING AND AIRSPEED ERROR TIME HISTORY

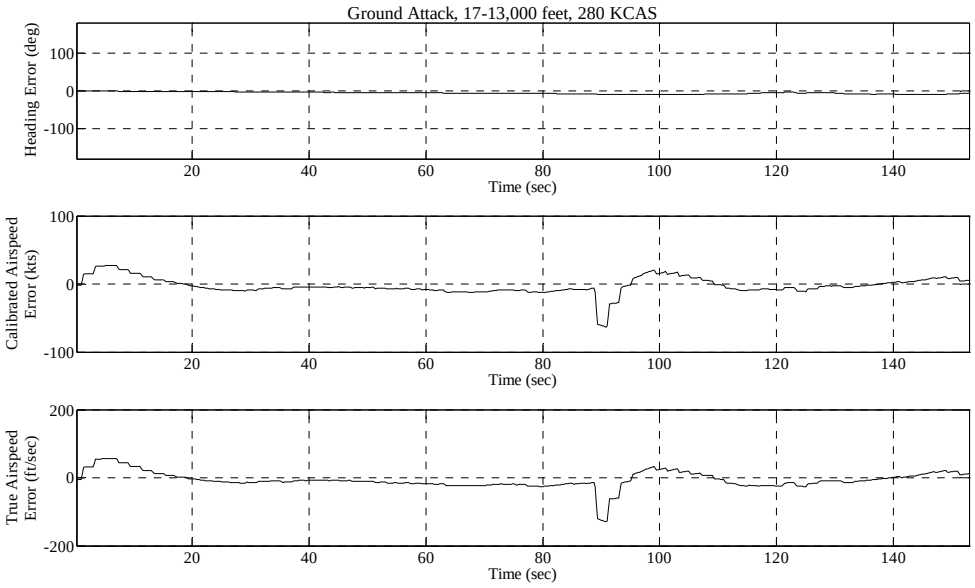

Test Point and Date: 072_19_Sep

HEADING AND AIRSPEED ERROR TIME HISTORY

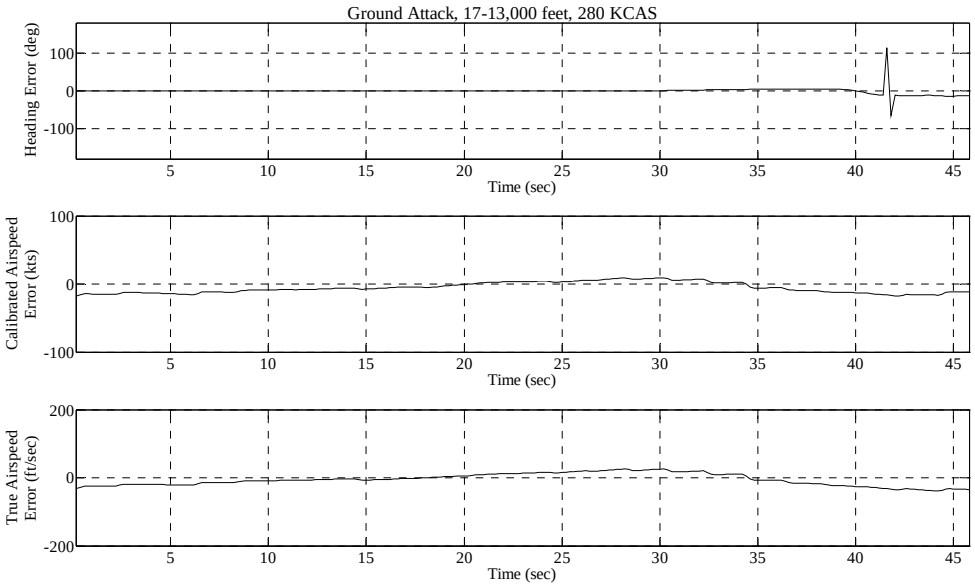

Test Point and Date: 073_19_Sep

F.4. Long Shot Flight Test Technique

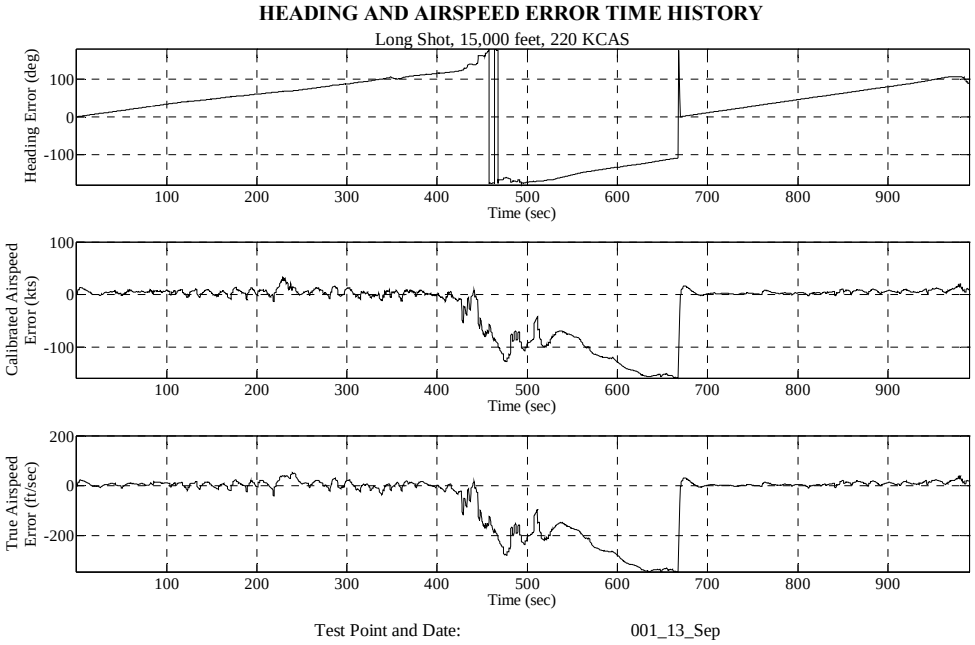

Test Point and Date: 001_13_Sep

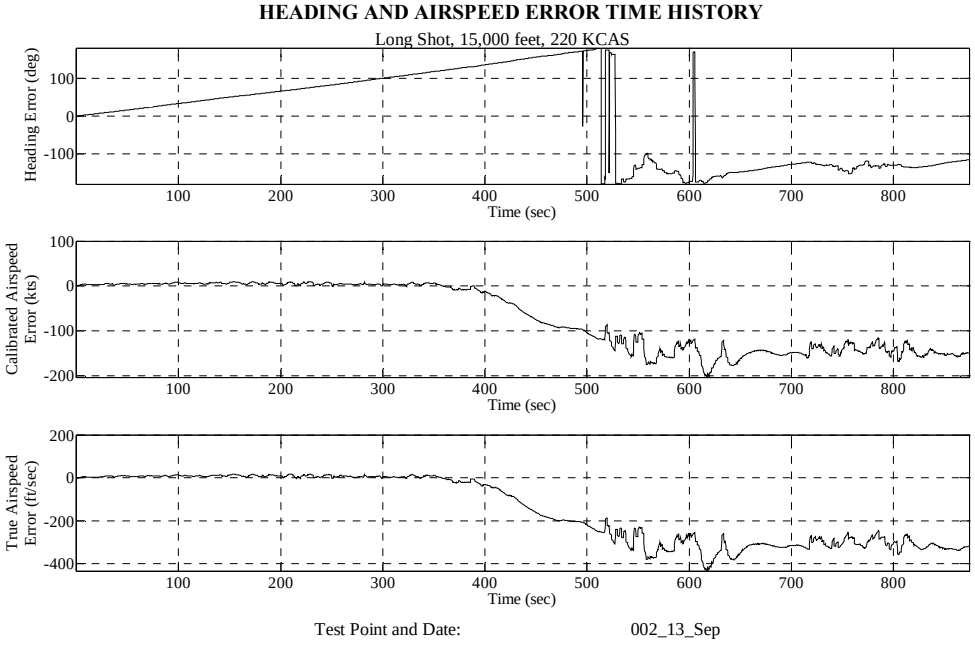

Test Point and Date: 002_13_Sep

HEADING AND AIRSPEED ERROR TIME HISTORY

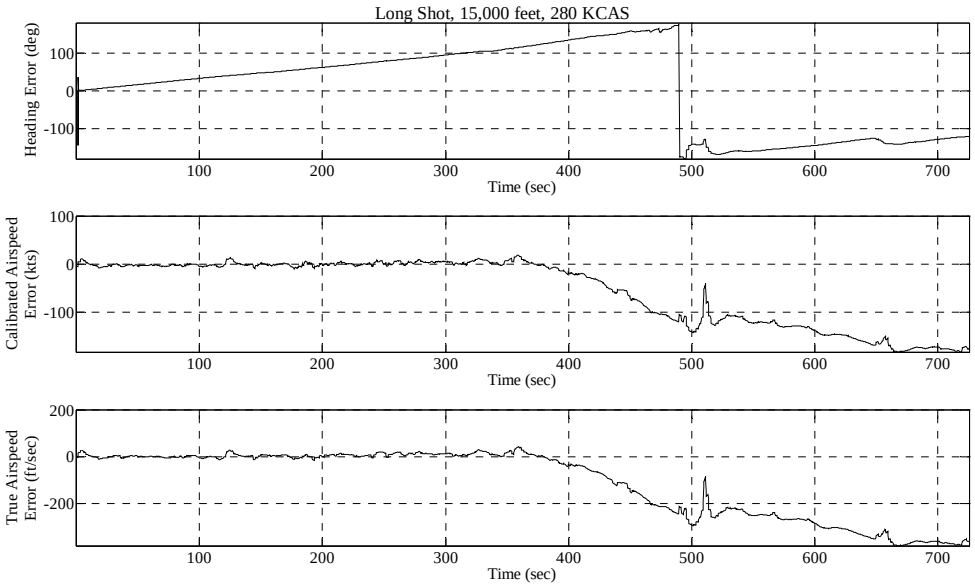

Test Point and Date: 003_17_Sep

HEADING AND AIRSPEED ERROR TIME HISTORY

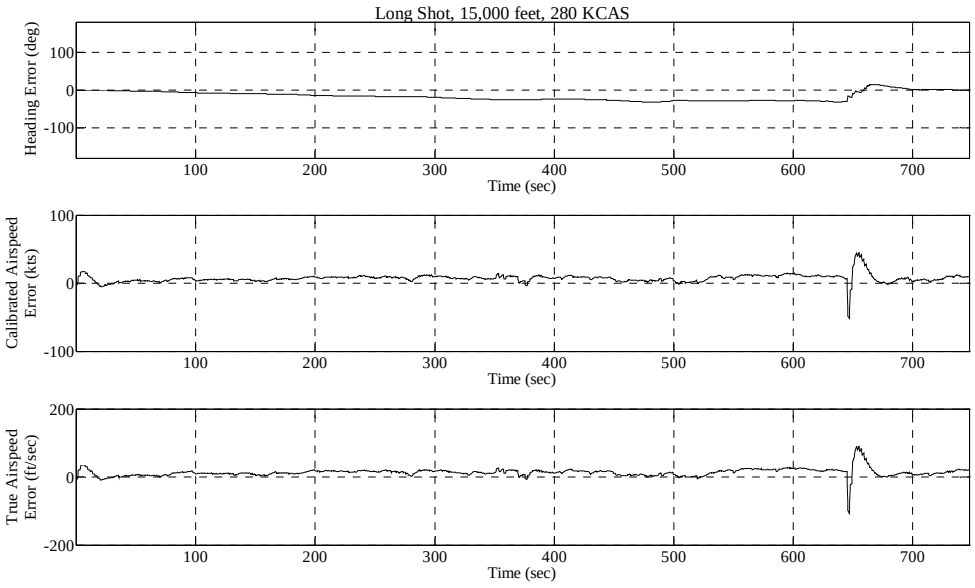

Test Point and Date: 004_19_Sep

F.5. Container Flight Test Technique

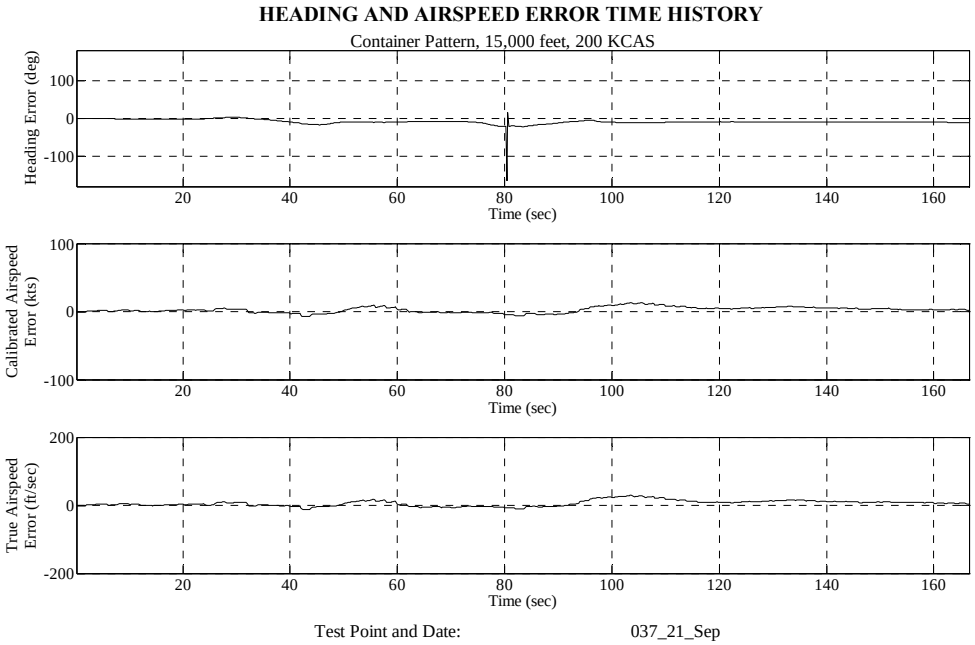

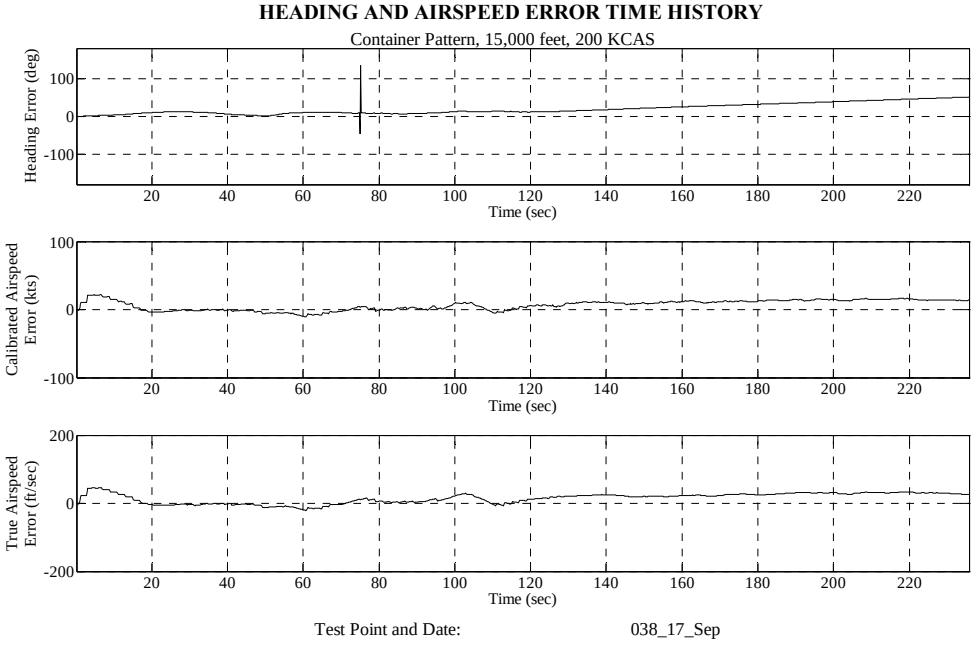

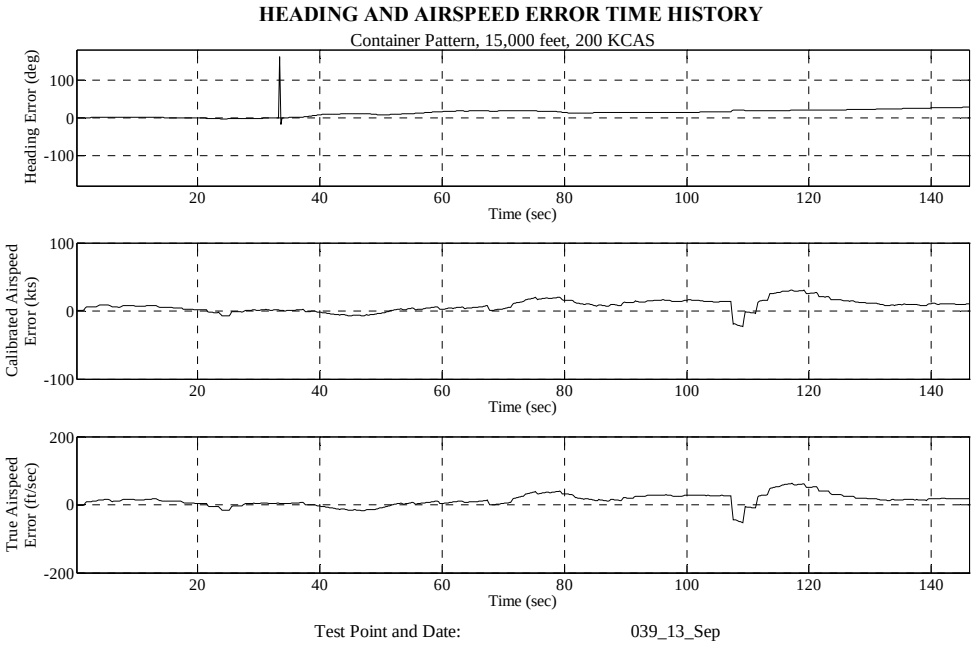

F.6. Landing Approaches

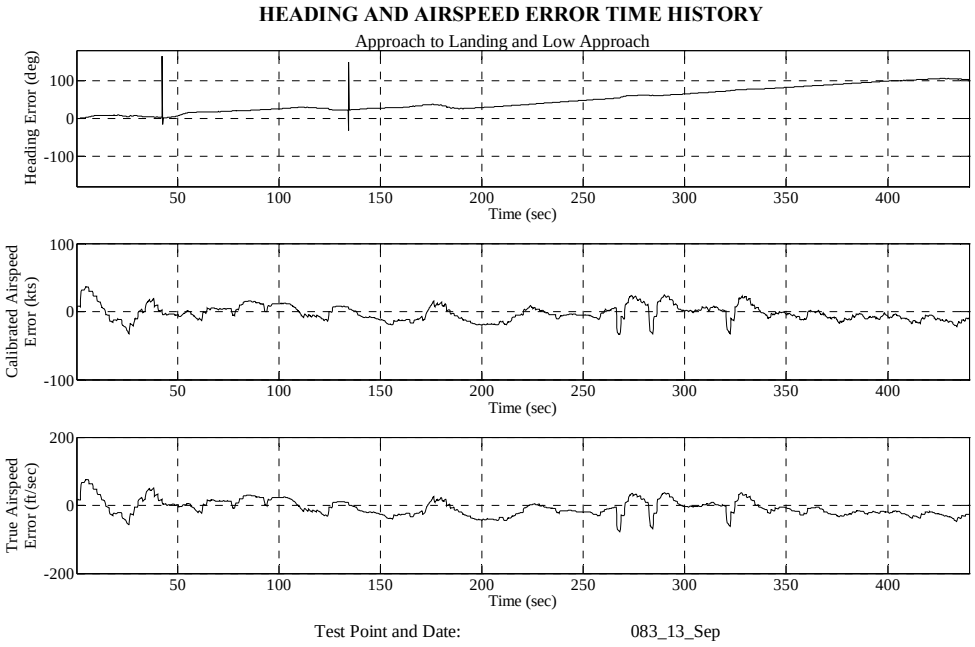

HEADING AND AIRSPEED ERROR TIME HISTORY

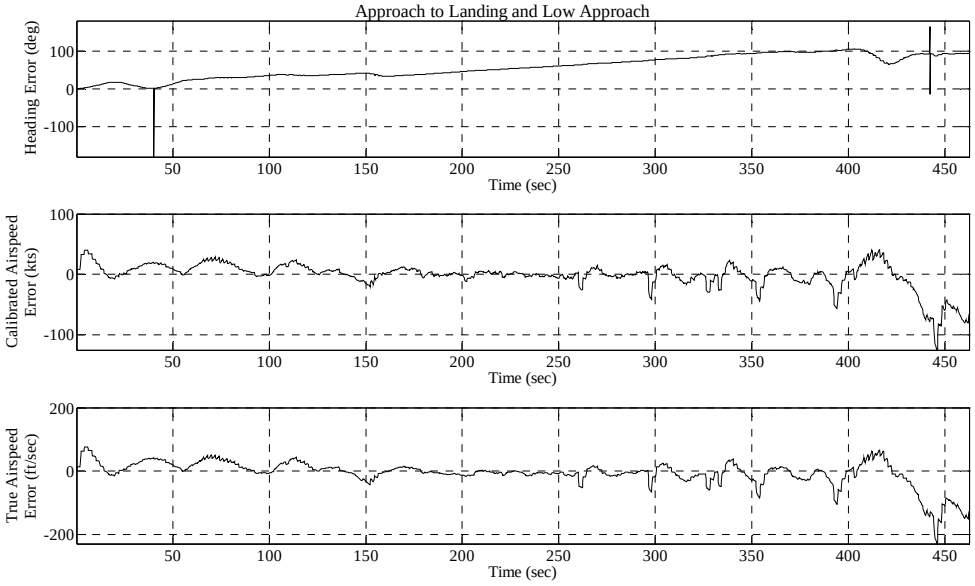

Test Point and Date: 084_17_Sep

HEADING AND AIRSPEED ERROR TIME HISTORY

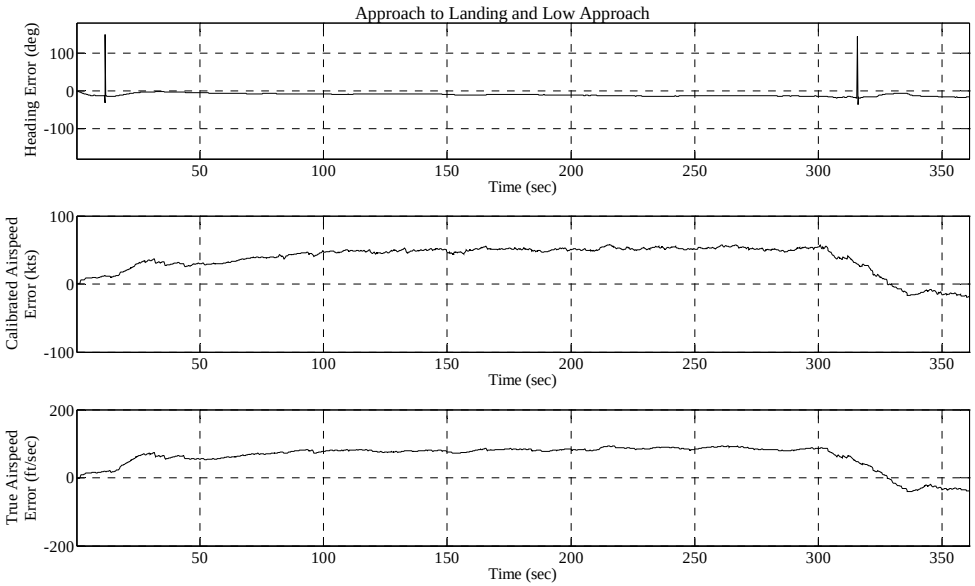

Test Point and Date: 085_18_Sep

HEADING AND AIRSPEED ERROR TIME HISTORY

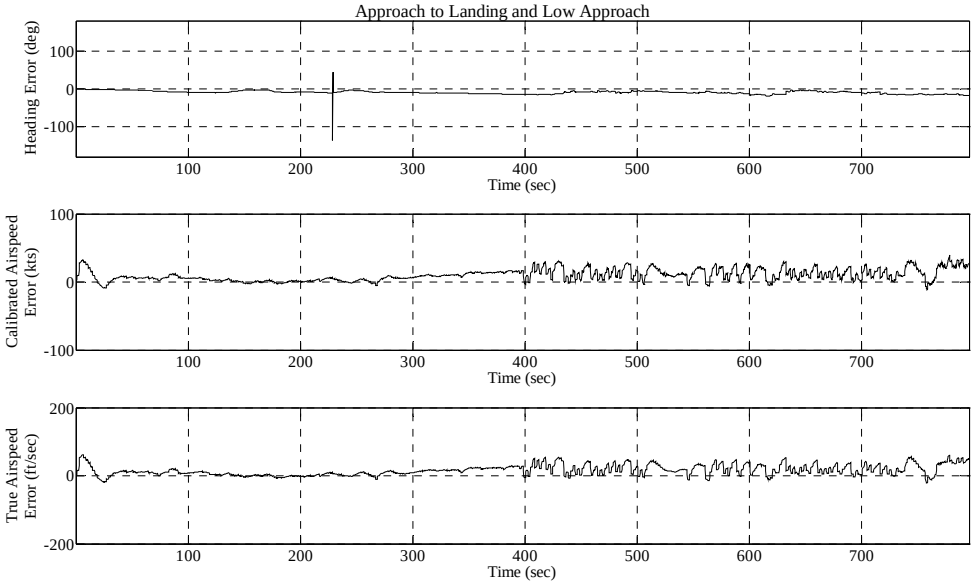

Test Point and Date: 086_19_Sep

HEADING AND AIRSPEED ERROR TIME HISTORY

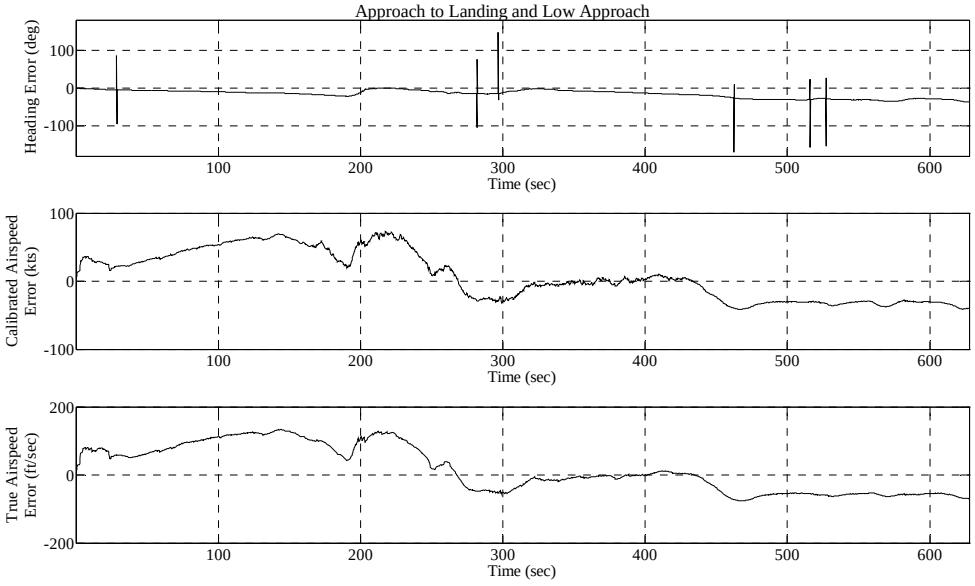

Test Point and Date: 087_21_Sep

Appendix G. Secondary Flight Test Data Plots

The error time history plots in this appendix are arranged according to the following maneuvers (sections G.1 – G.7): Ground Taxi, J-Hook FTT, Sliceback FTT, Operational Maneuvers, Long Shot FTT, Container FTT, and Landing Approaches. The section for Ground Taxi is further divided into Ground Taxi without GPS Updates (section G.1.1), and Ground Taxi with GPS Updates (section G.1.2),. The sections for J-Hook, Sliceback, and Operational maneuvers are further divided into position (for example section G.2.1 for J-Hook plots, G.3.1 for Slicebacks, etc.), velocity (G.2.2, G.3.2, etc.), and wind (G.2.3, G.3.3, etc.). Each plot is labeled as follows: conditions for the maneuver at the top, and test matrix test point and date at the bottom [McLaren 2007].

G.1. Ground Taxi

G.1.1. Ground Taxi without GPS Updates

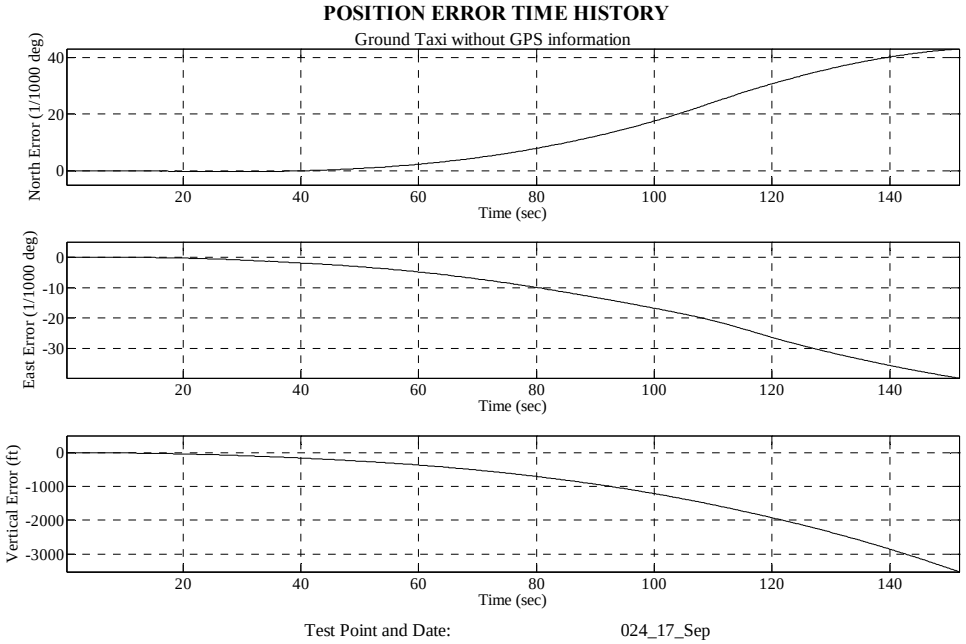

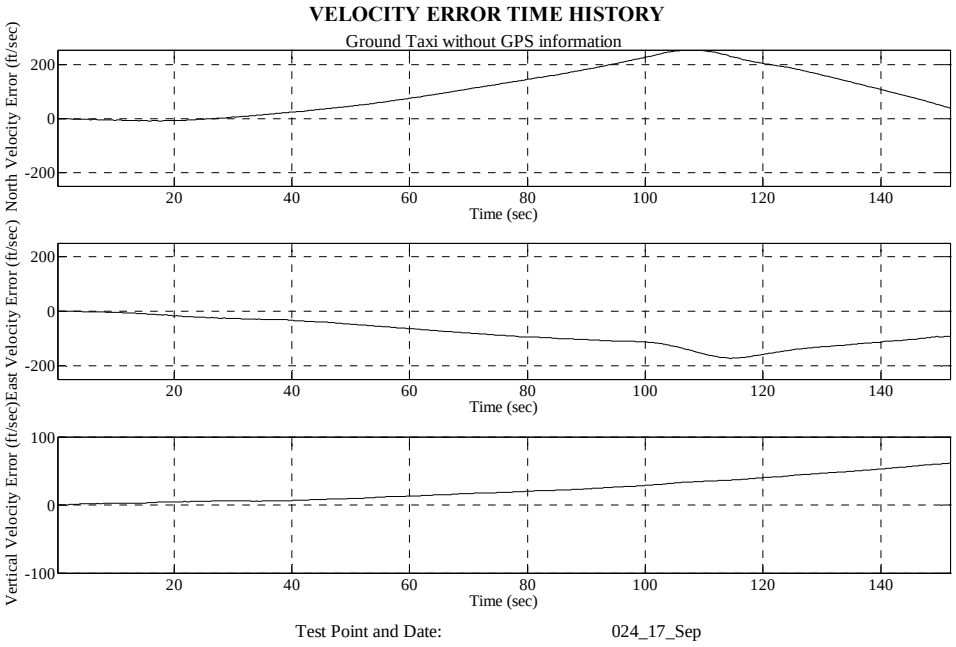
VELOCITY ERROR TIME HISTORY
Ground Taxi without GPS information
North Velocity Error (ft/sec)
East Velocity Error (ft/sec)
Vertical Velocity Error (ft/sec)
Time (sec)
Test Point and Date: 024_17_Sep

POSITION ERROR TIME HISTORY

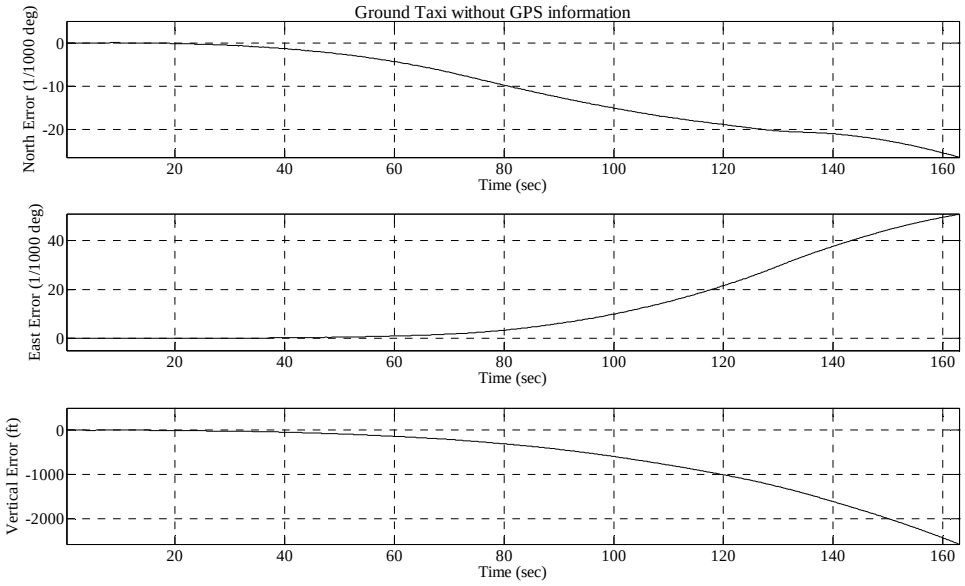

Test Point and Date: 025_21_Sep

VELOCITY ERROR TIME HISTORY

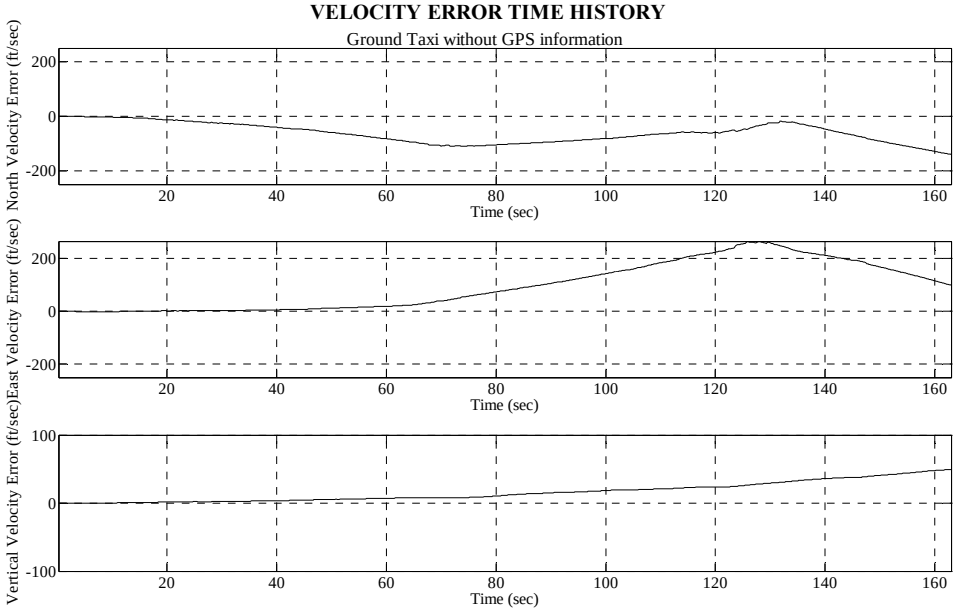

Test Point and Date: 025_21_Sep

POSITION ERROR TIME HISTORY

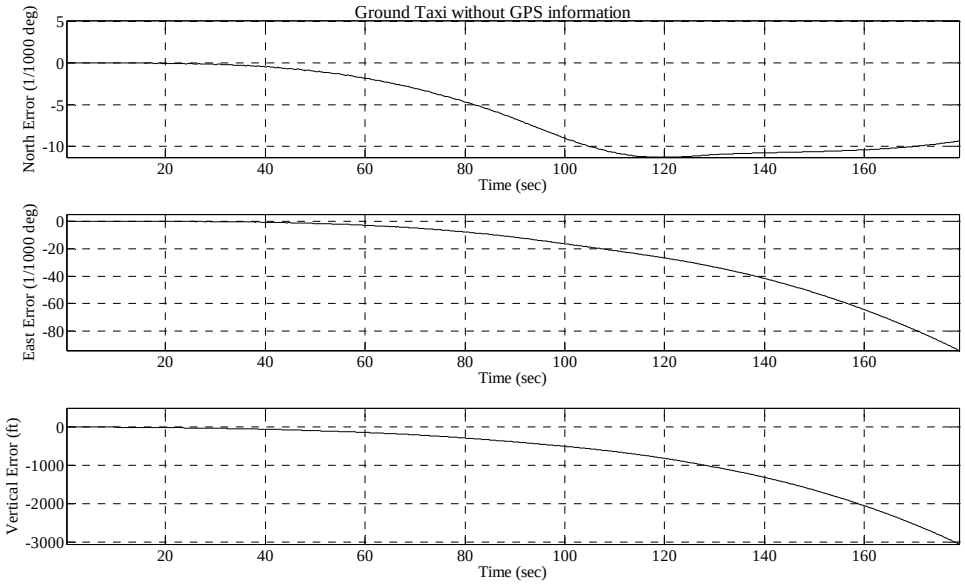

Test Point and Date: 026_21_Sep

VELOCITY ERROR TIME HISTORY

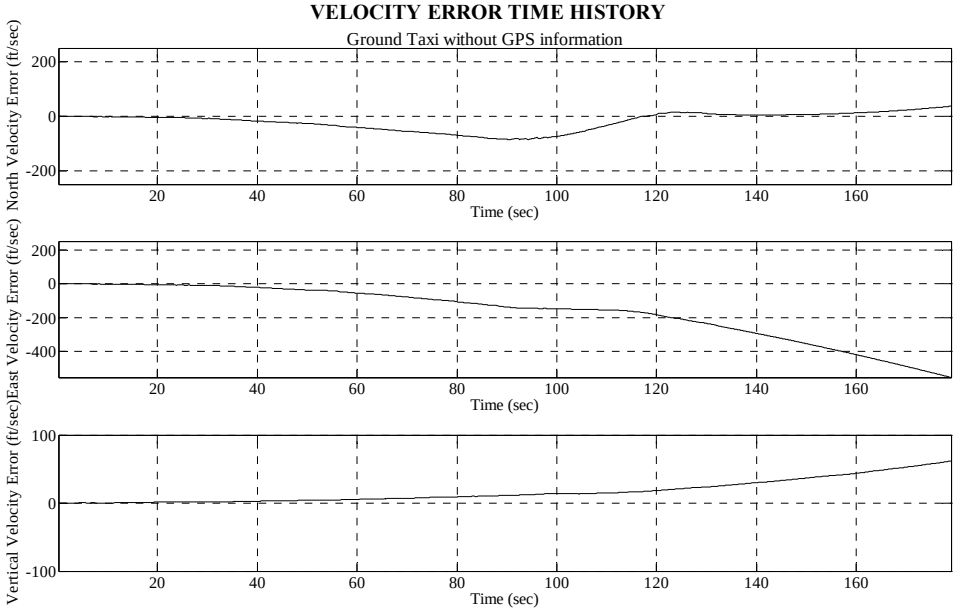

Test Point and Date: 026_21_Sep

POSITION ERROR TIME HISTORY

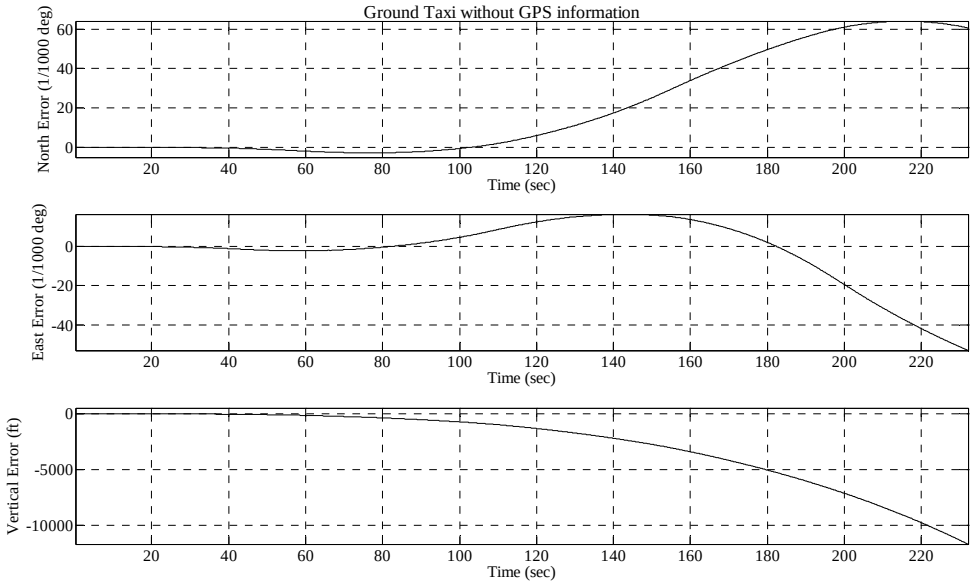

Test Point and Date: 027_21_Sep

VELOCITY ERROR TIME HISTORY

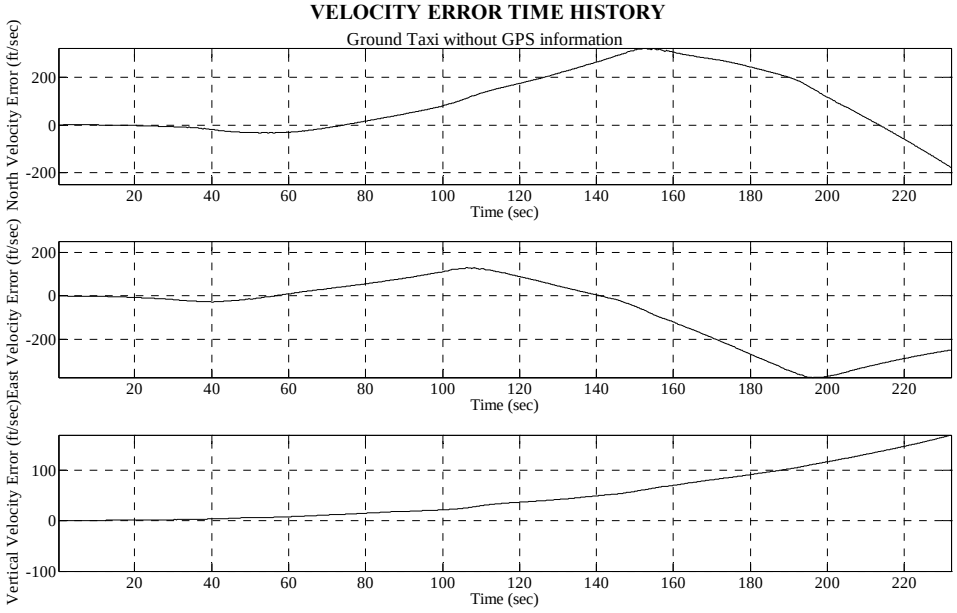

Test Point and Date: 027_21_Sep

G.1.2. Ground Taxi with GPS Updates

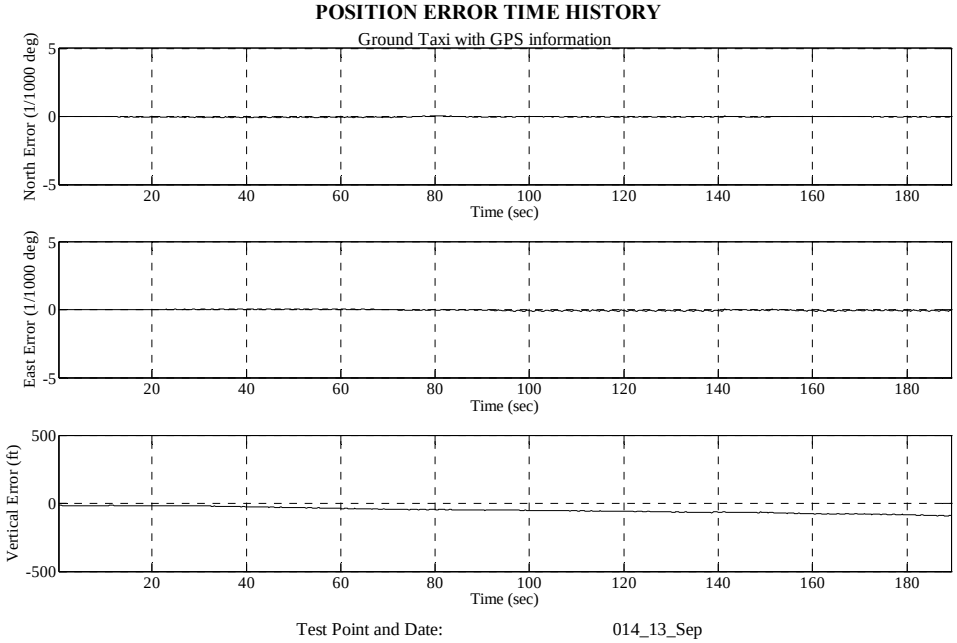

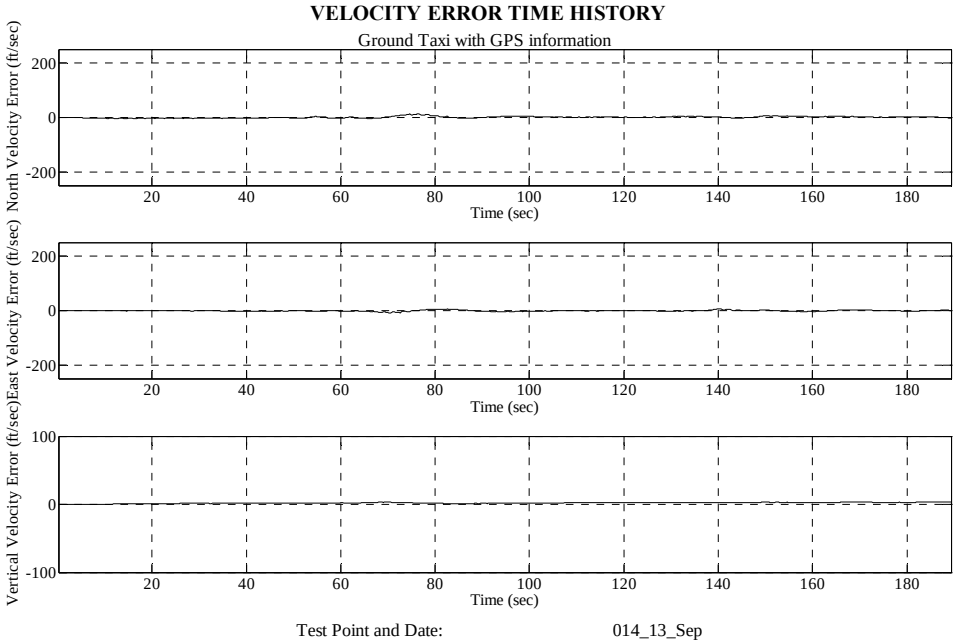

POSITION ERROR TIME HISTORY

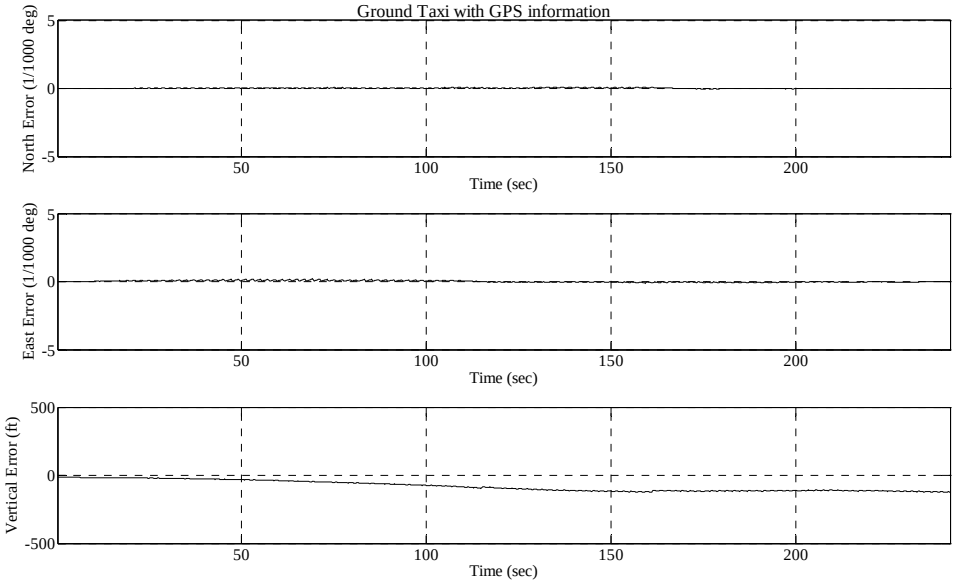

Test Point and Date: 015_13_Sep

VELOCITY ERROR TIME HISTORY

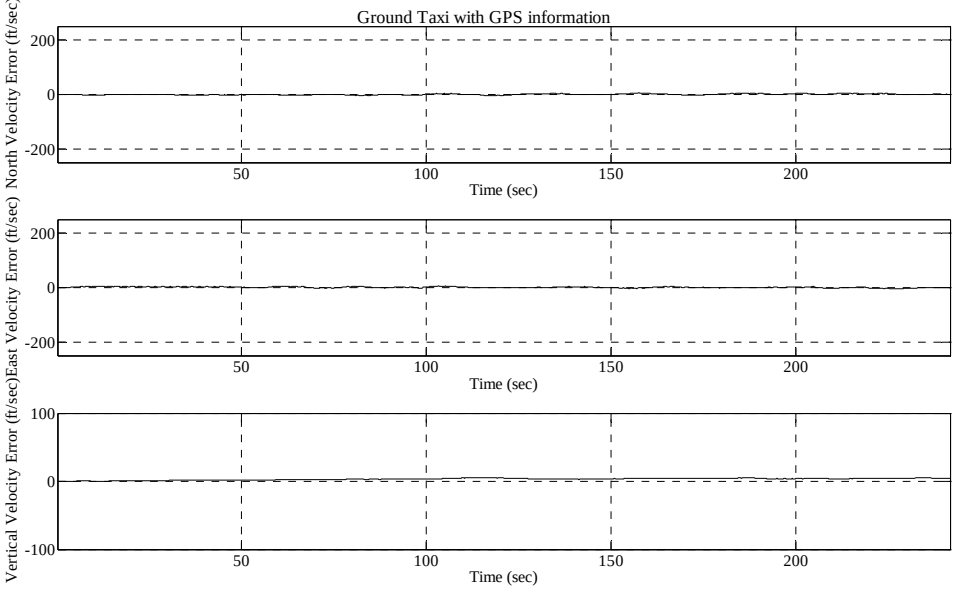

Test Point and Date: 015_13_Sep

POSITION ERROR TIME HISTORY

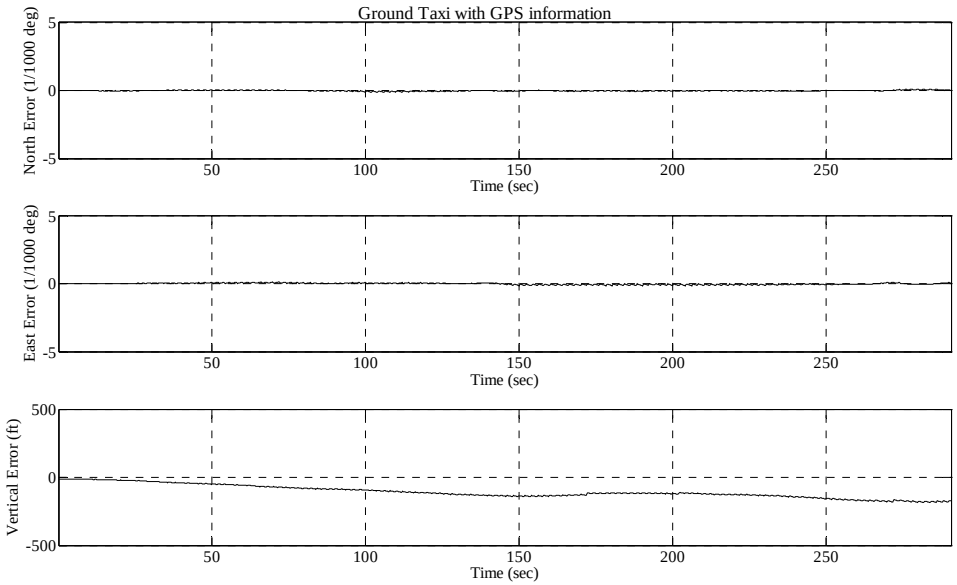

Test Point and Date: 016_17_Sep

VELOCITY ERROR TIME HISTORY

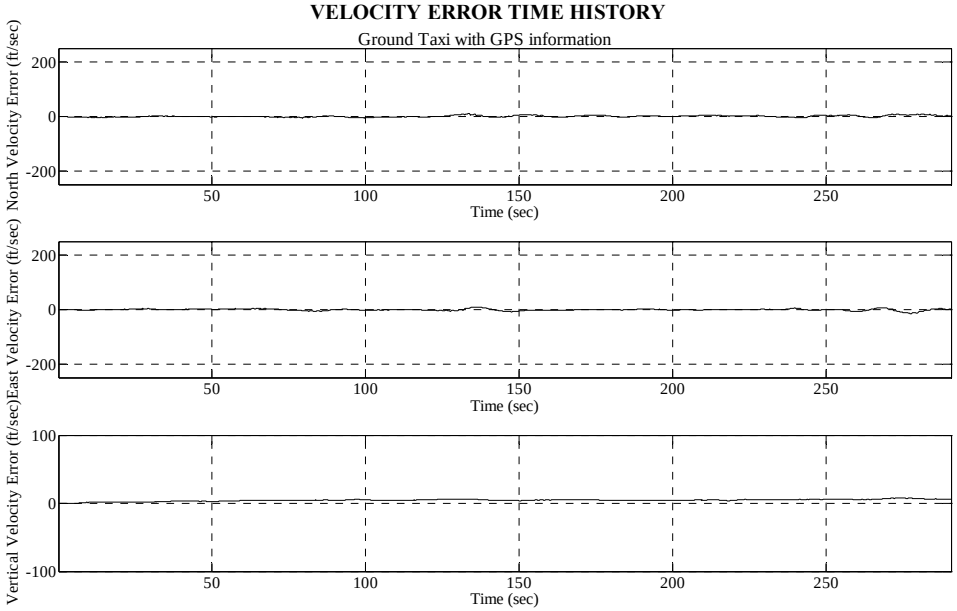

Test Point and Date: 016_17_Sep

POSITION ERROR TIME HISTORY

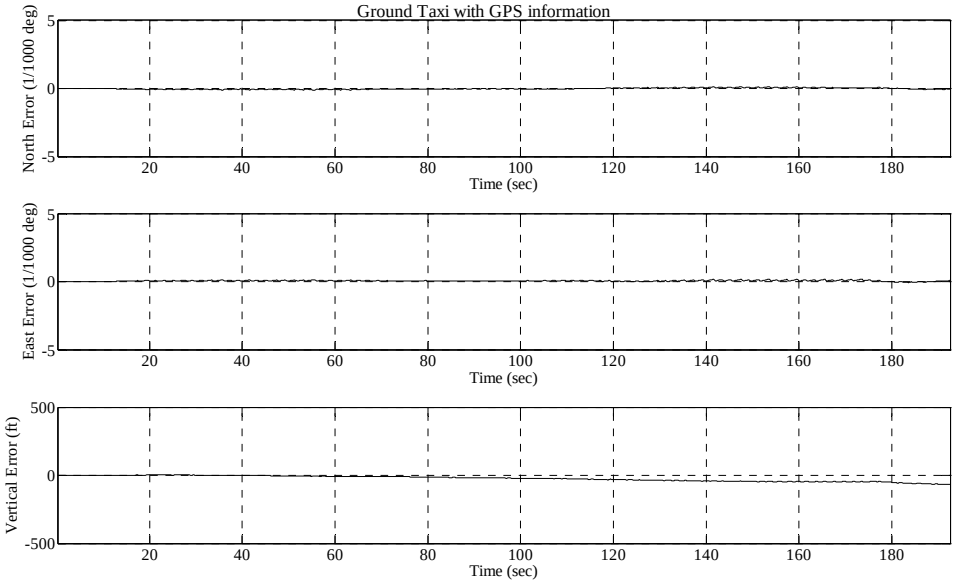

Test Point and Date: 017_21_Sep

VELOCITY ERROR TIME HISTORY

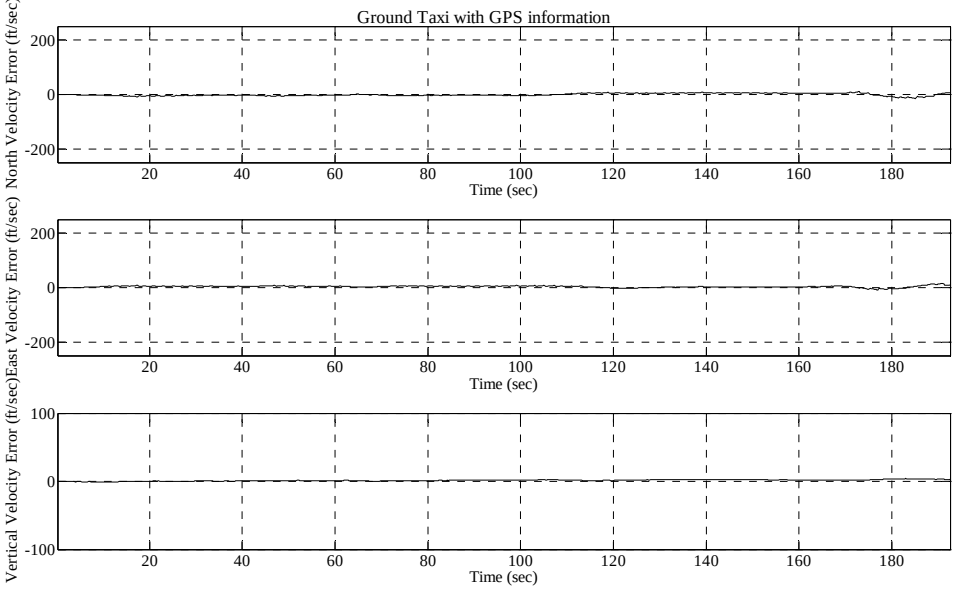

Test Point and Date: 017_21_Sep

POSITION ERROR TIME HISTORY

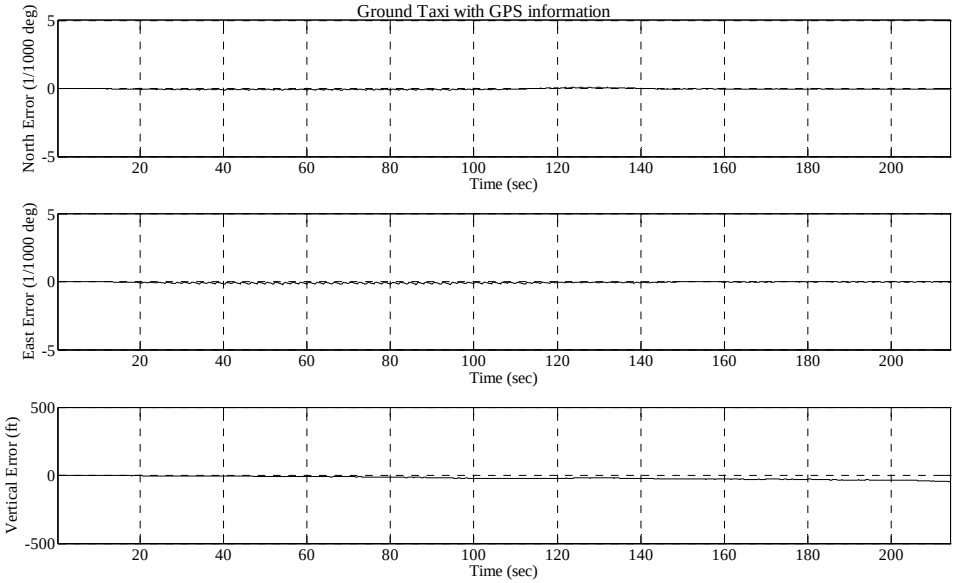

Test Point and Date: 018_21_Sep

VELOCITY ERROR TIME HISTORY

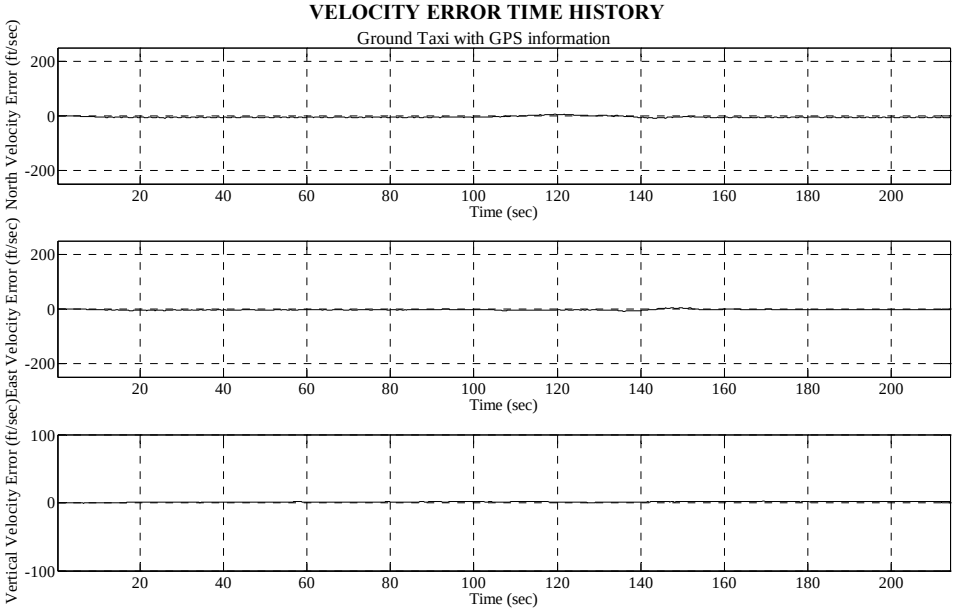

Test Point and Date: 018_21_Sep

POSITION ERROR TIME HISTORY

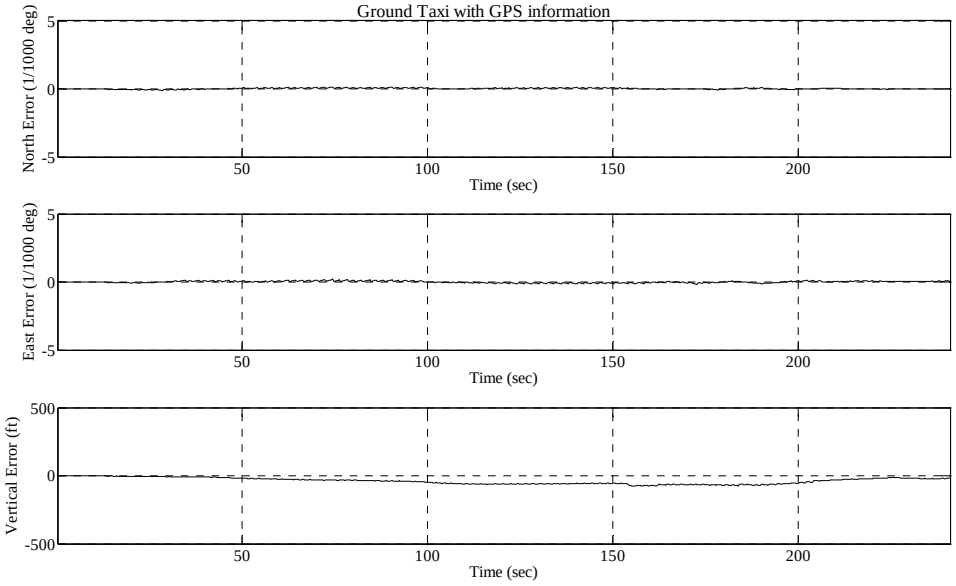

Test Point and Date: 019_21_Sep

VELOCITY ERROR TIME HISTORY

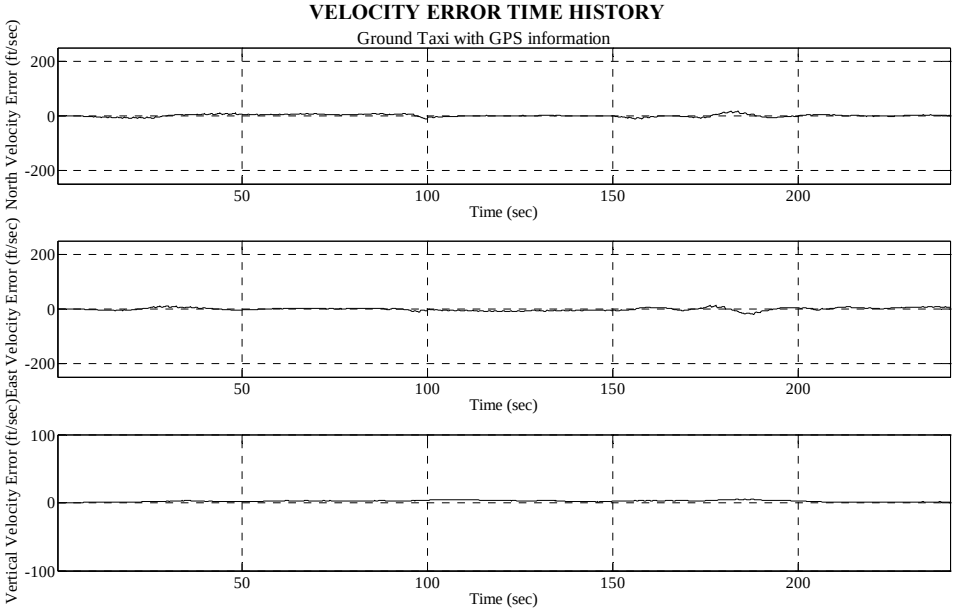

Test Point and Date: 019_21_Sep

G.2. J-Hook Flight Test Technique

G.2.1. J-Hook Position Plots

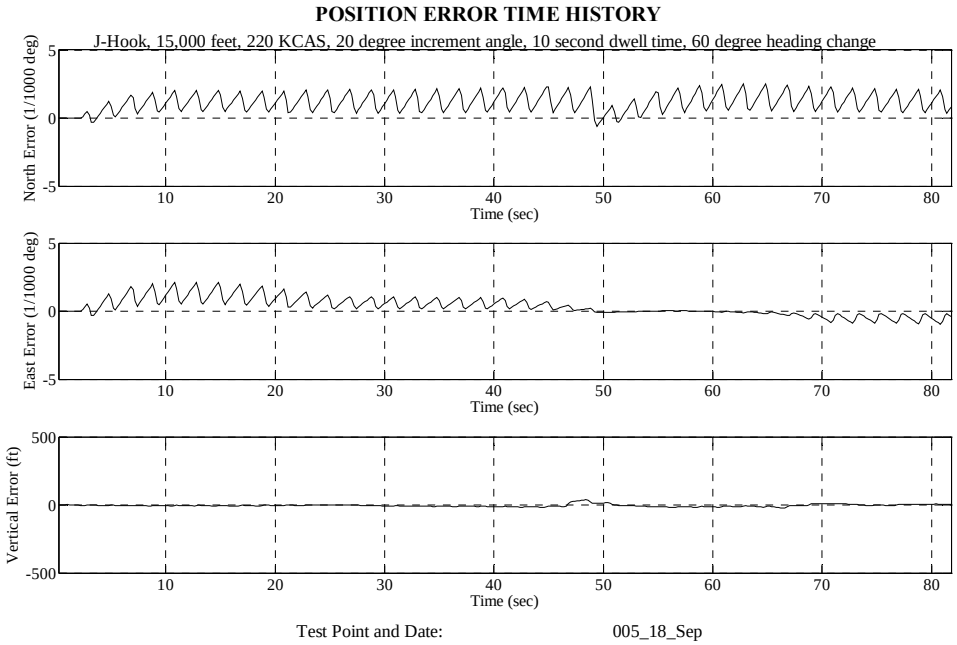

POSITION ERROR TIME HISTORY

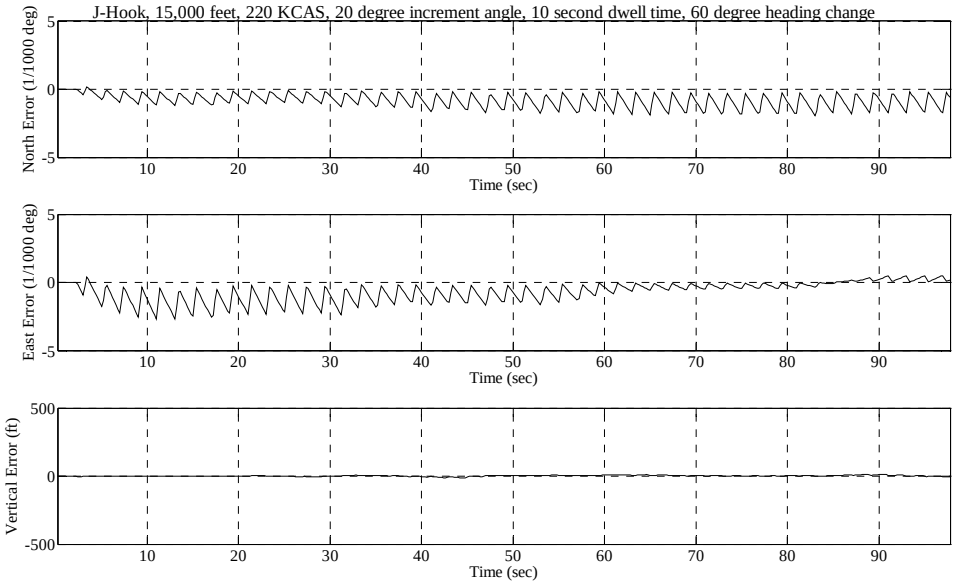

Test Point and Date: 005_21_Sep

POSITION ERROR TIME HISTORY

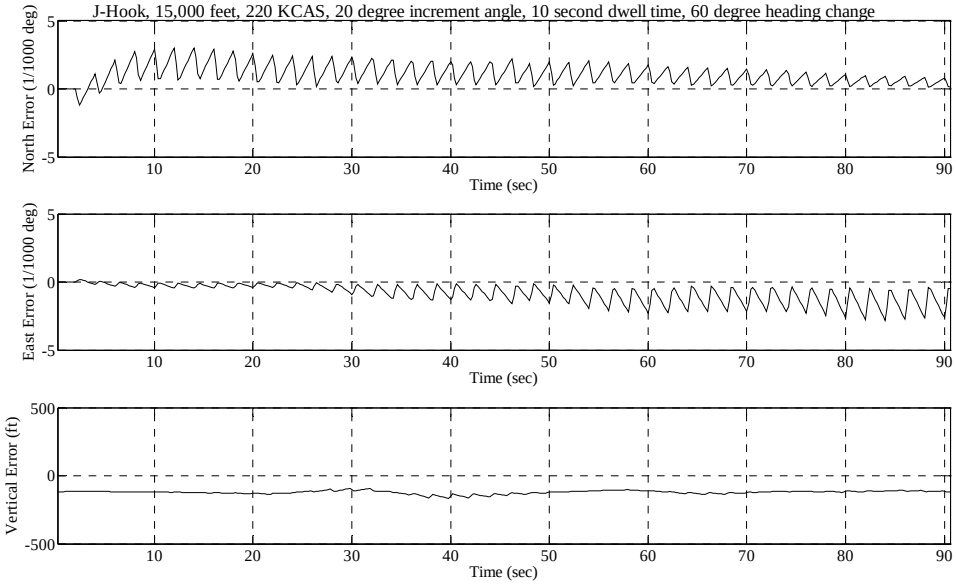

Test Point and Date: 006_13_Sep

POSITION ERROR TIME HISTORY

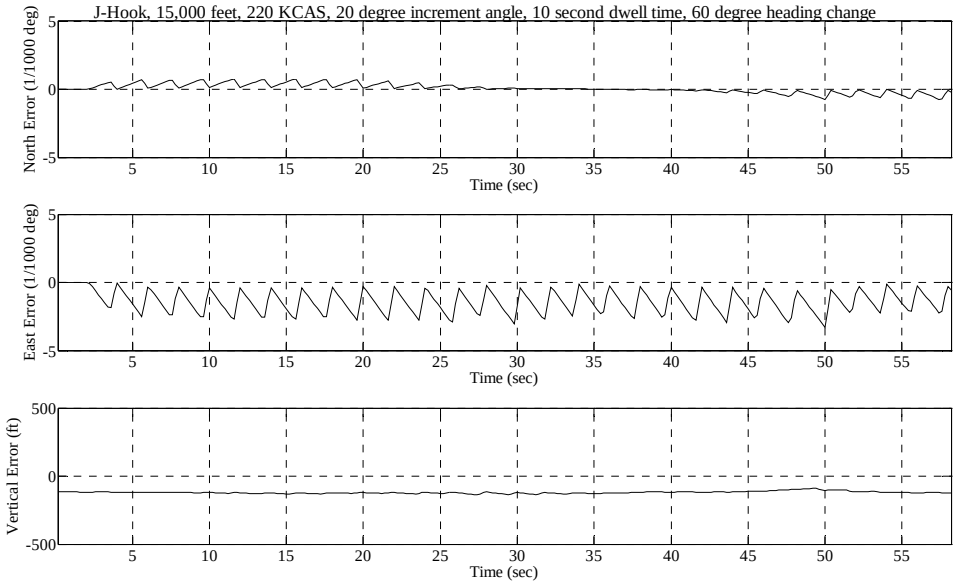

Test Point and Date: 007_13_Sep

POSITION ERROR TIME HISTORY

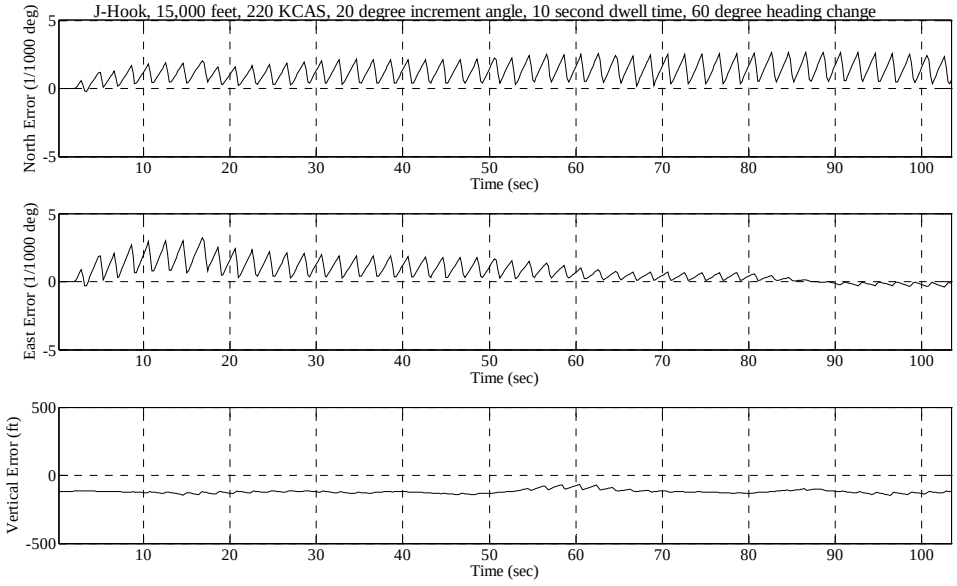

Test Point and Date: 008_13_Sep

POSITION ERROR TIME HISTORY

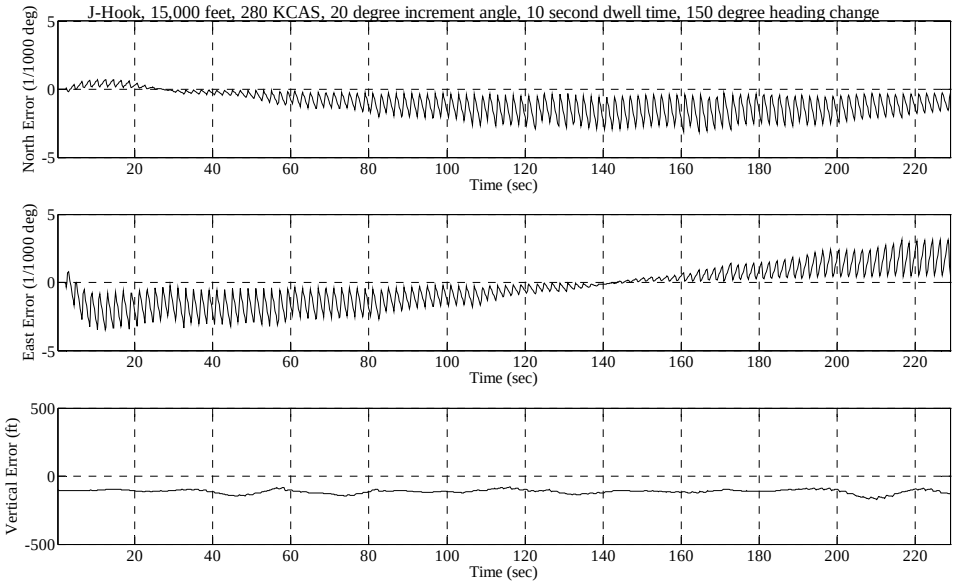

Test Point and Date: 009_17_Sep

POSITION ERROR TIME HISTORY

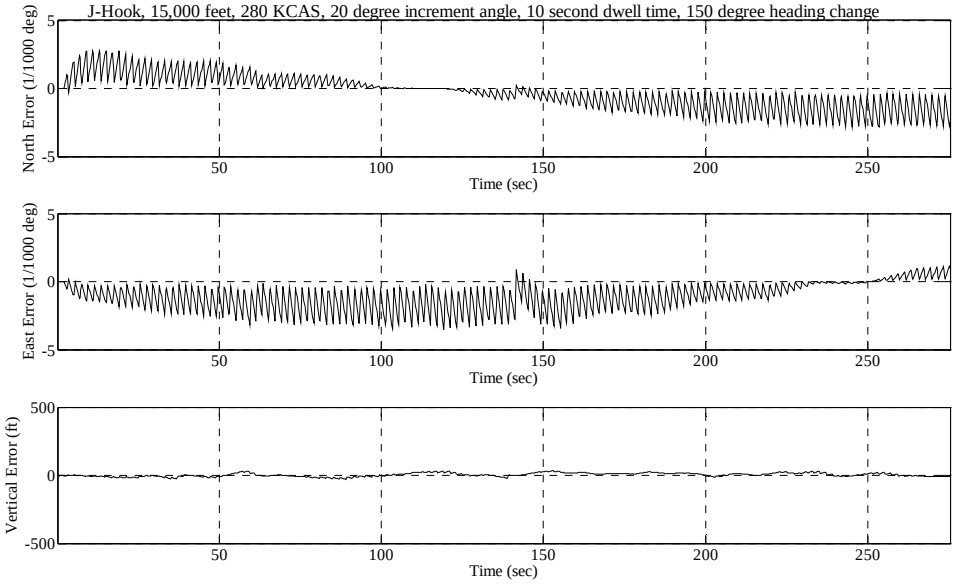

Test Point and Date: 010_19_Sep

POSITION ERROR TIME HISTORY

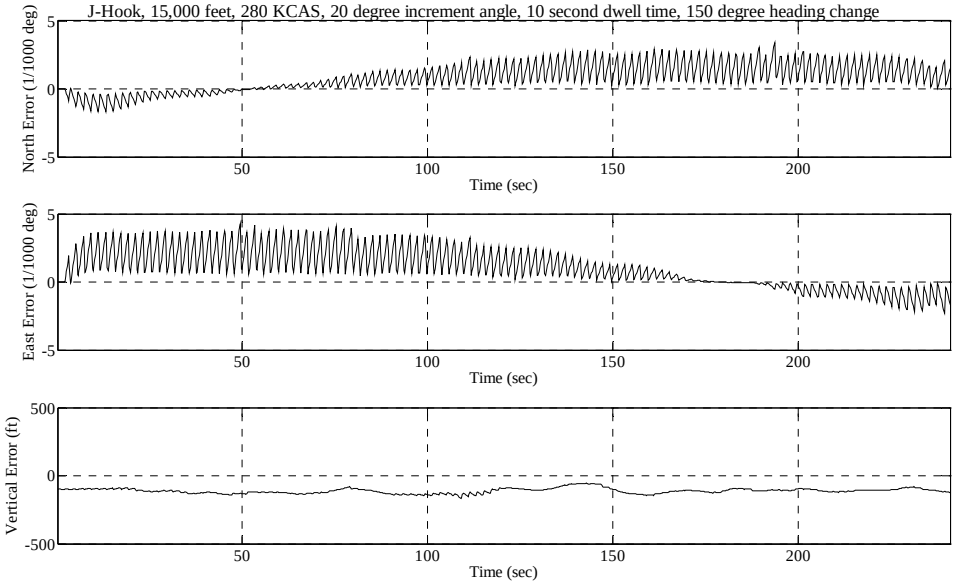

Test Point and Date: 011_17_Sep

POSITION ERROR TIME HISTORY

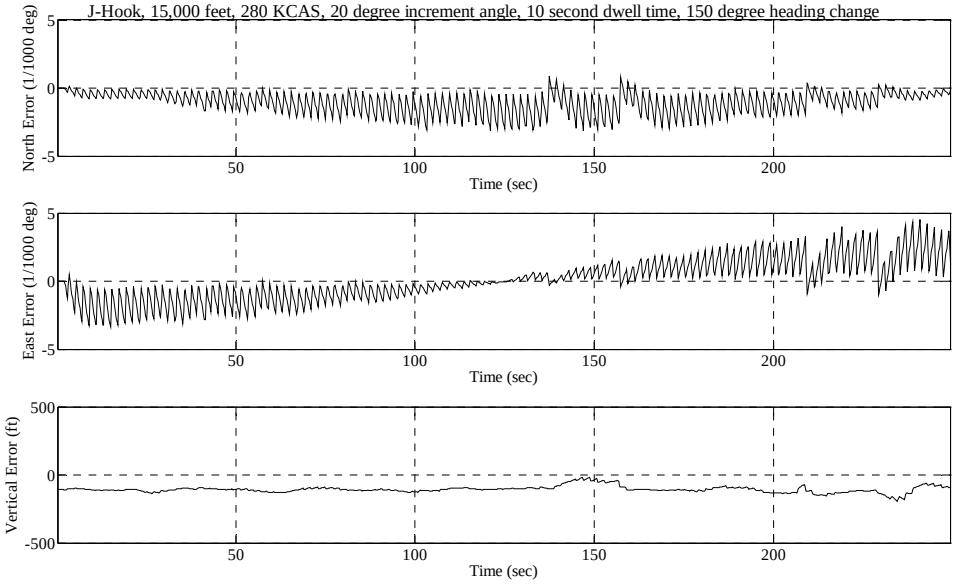

Test Point and Date: 012_17_Sep

POSITION ERROR TIME HISTORY

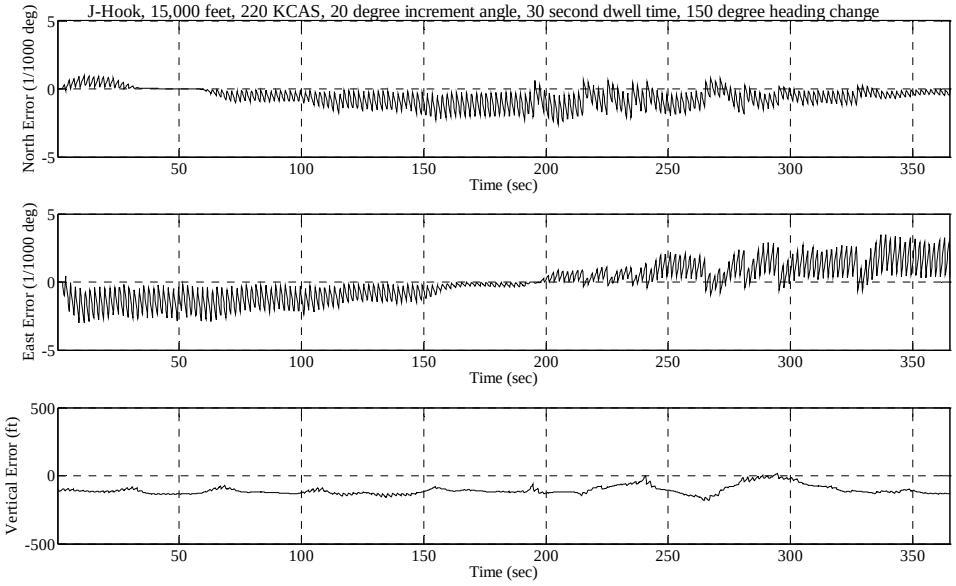

Test Point and Date: 013_13_Sep

POSITION ERROR TIME HISTORY

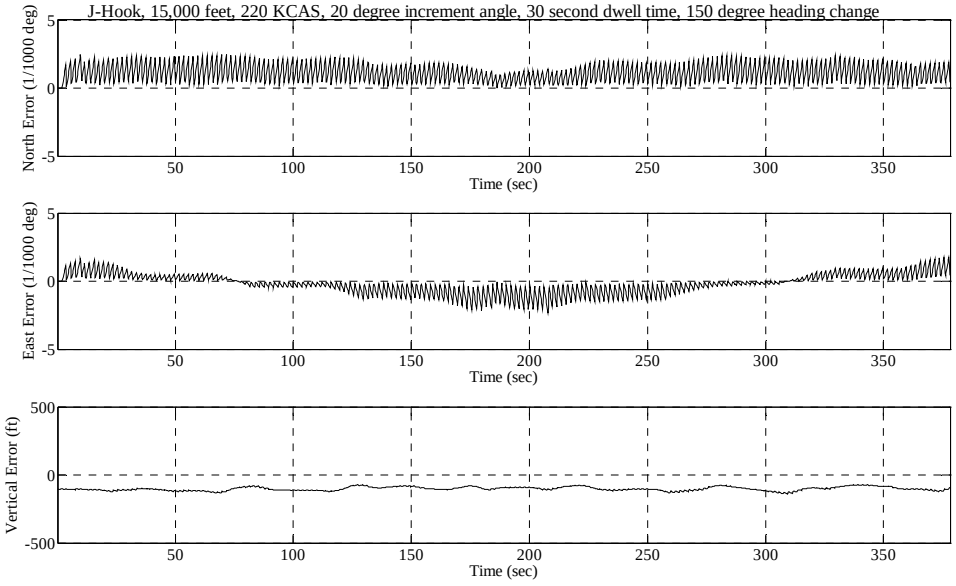

Test Point and Date: 014_17_Sep

POSITION ERROR TIME HISTORY

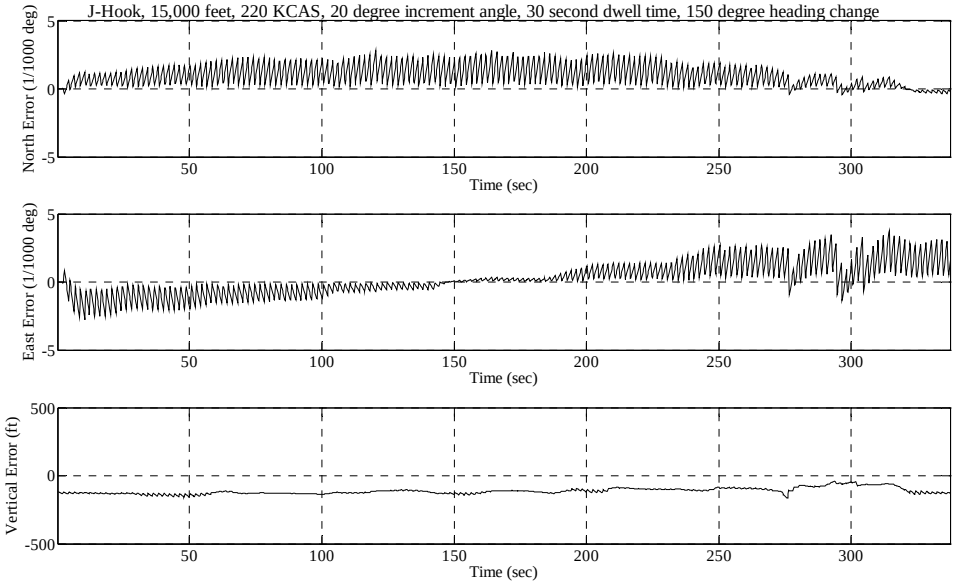

Test Point and Date: 015_13_Sep

POSITION ERROR TIME HISTORY

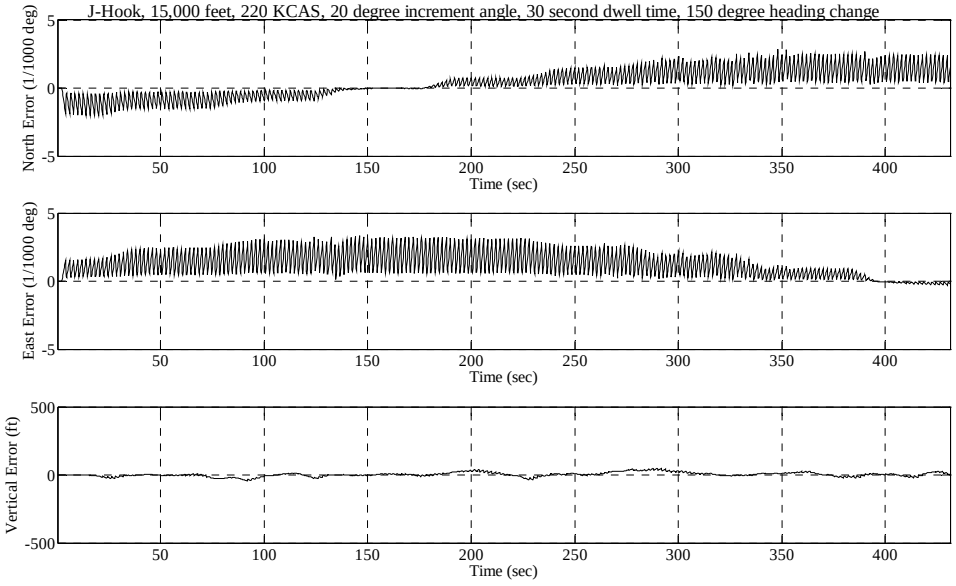

Test Point and Date: 016_19_Sep

POSITION ERROR TIME HISTORY

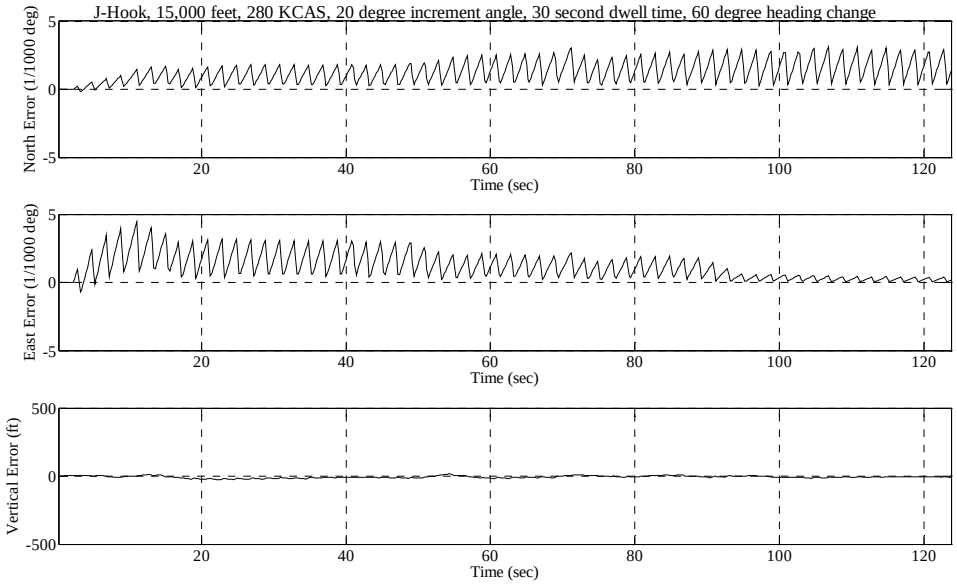

Test Point and Date: 017_18_Sep

POSITION ERROR TIME HISTORY

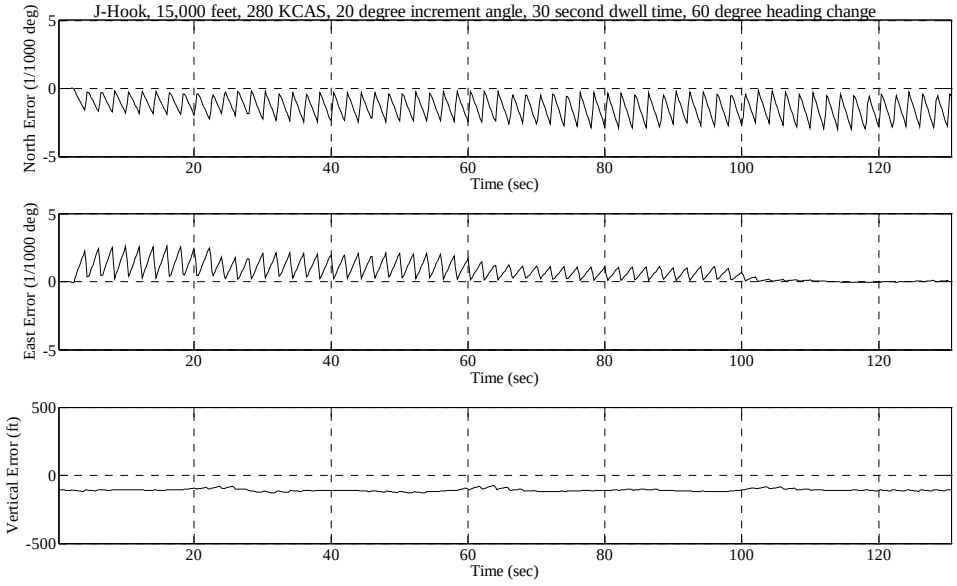

Test Point and Date: 018_13_Sep

POSITION ERROR TIME HISTORY

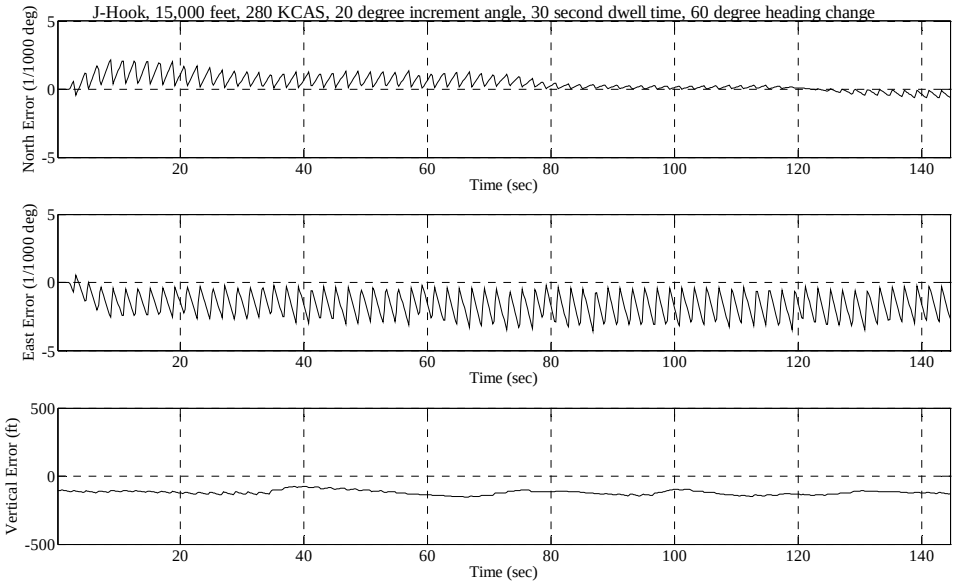

Test Point and Date: 019_17_Sep

POSITION ERROR TIME HISTORY

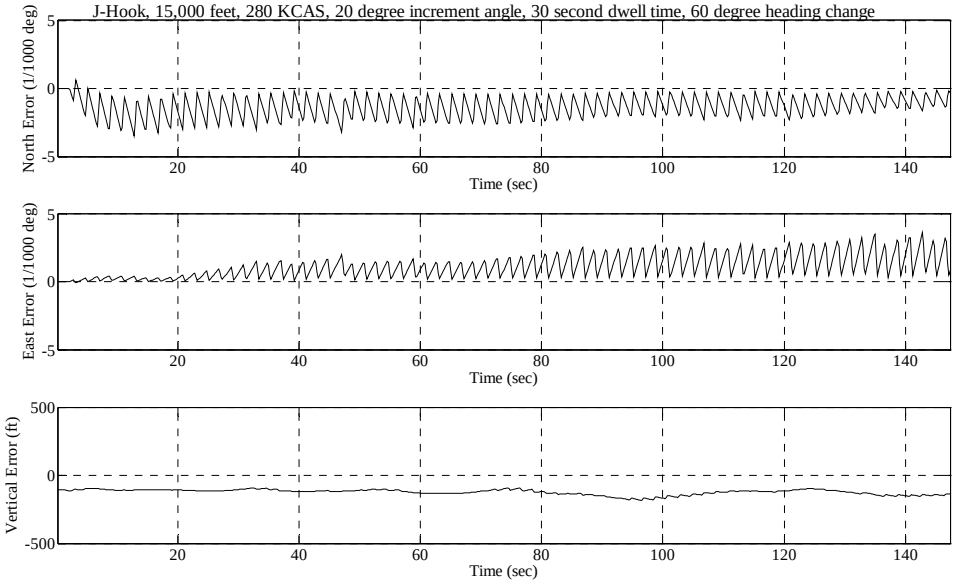

Test Point and Date: 020_17_Sep

POSITION ERROR TIME HISTORY

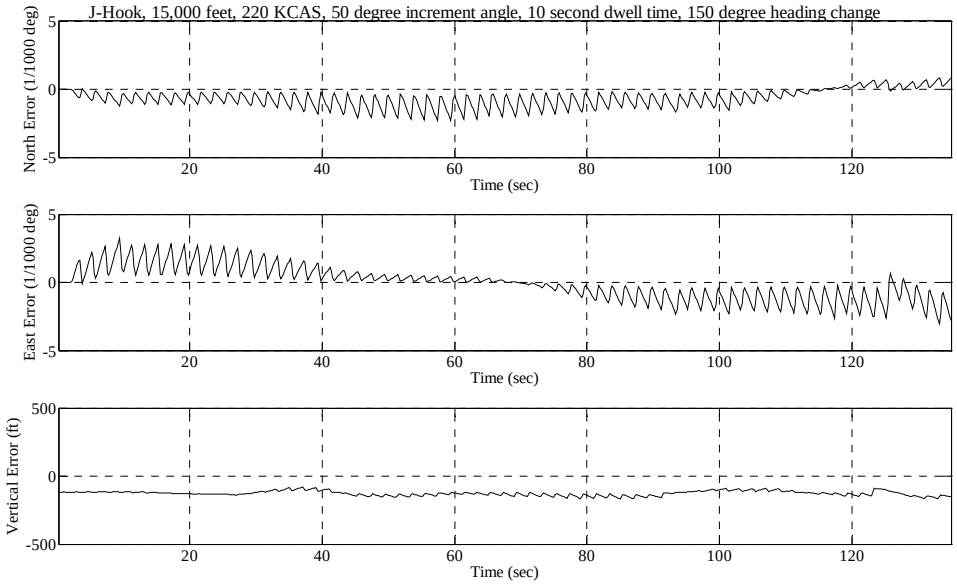

Test Point and Date: 021_13_Sep

POSITION ERROR TIME HISTORY

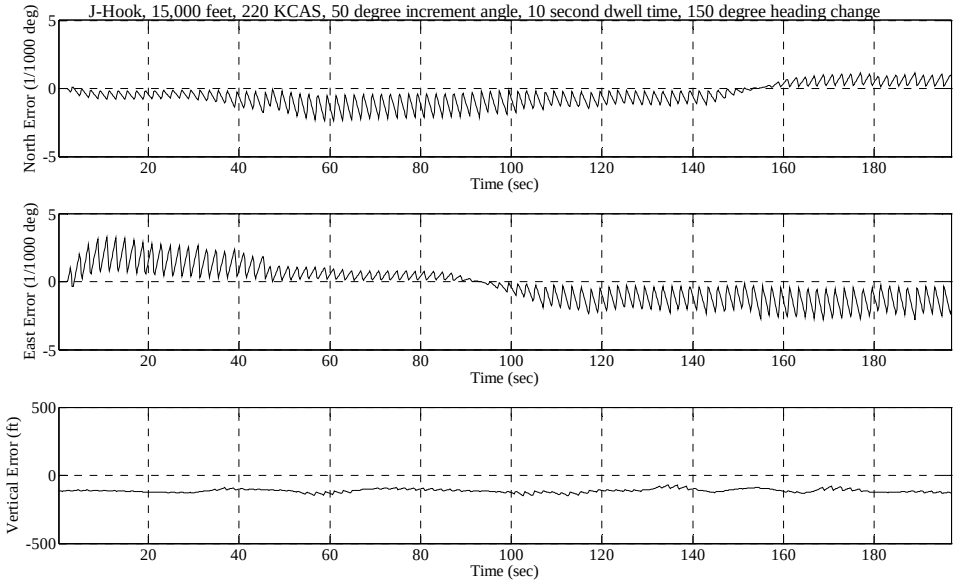

Test Point and Date: 022_13_Sep

POSITION ERROR TIME HISTORY

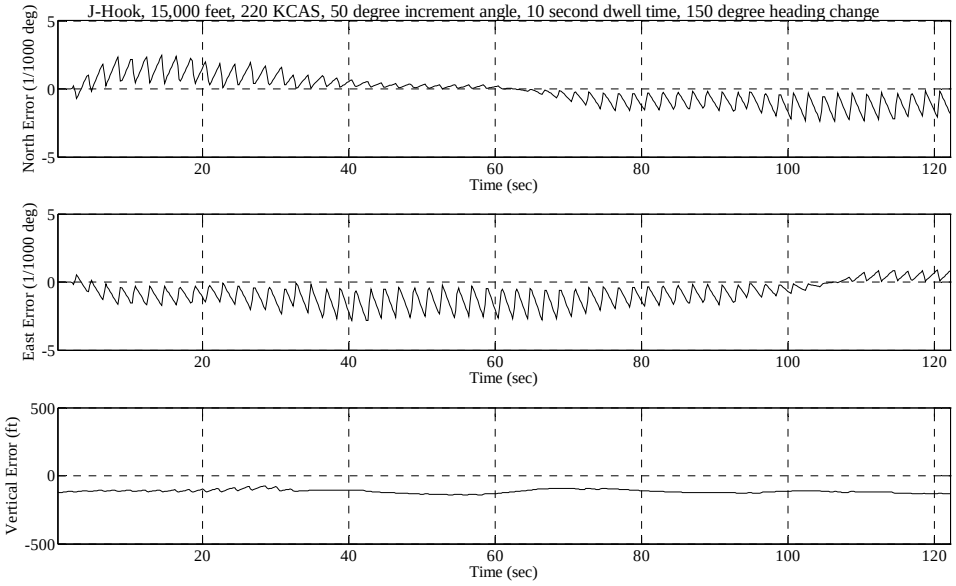

Test Point and Date: 023_13_Sep

POSITION ERROR TIME HISTORY

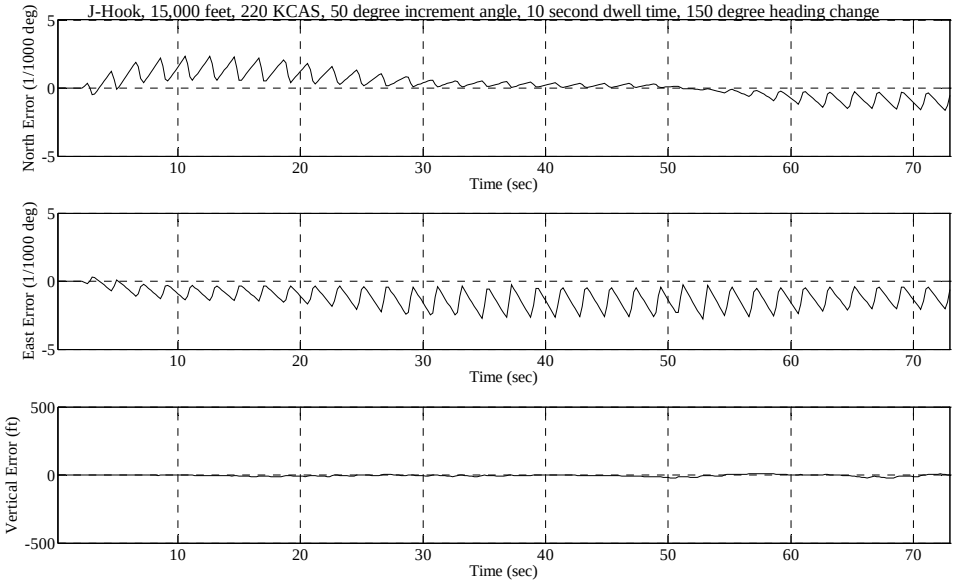

Test Point and Date: 024_18_Sep

POSITION ERROR TIME HISTORY

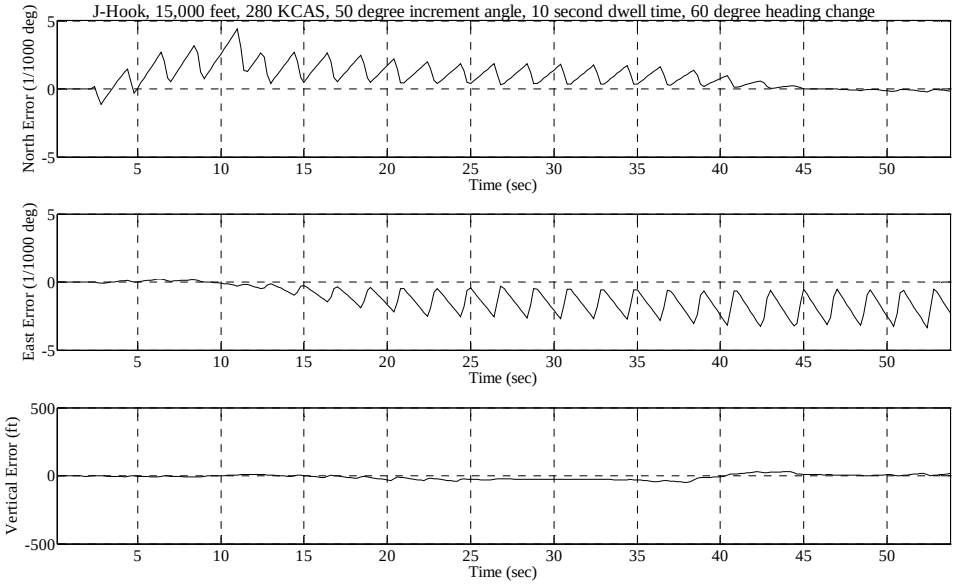

Test Point and Date: 025_18_Sep

POSITION ERROR TIME HISTORY

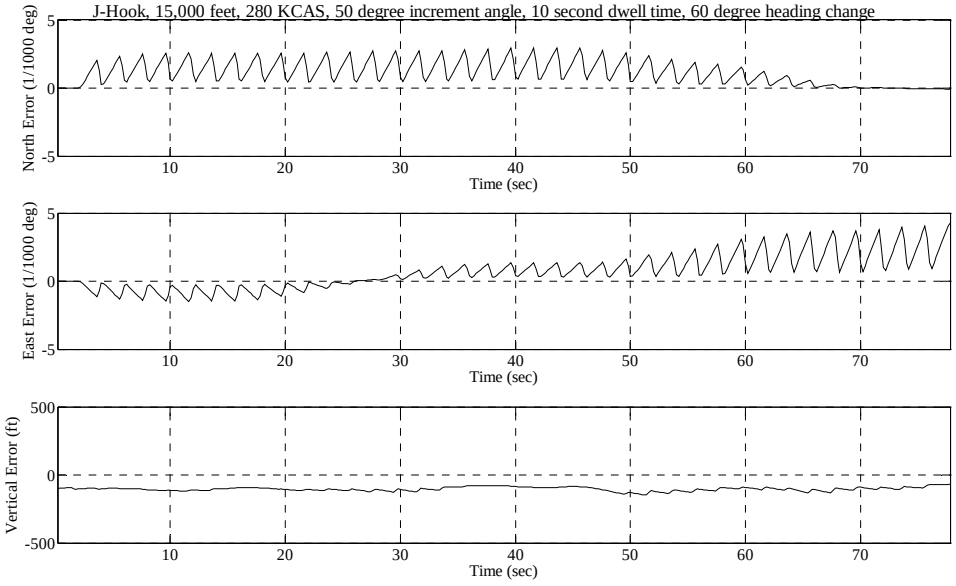

Test Point and Date: 026_17_Sep

POSITION ERROR TIME HISTORY

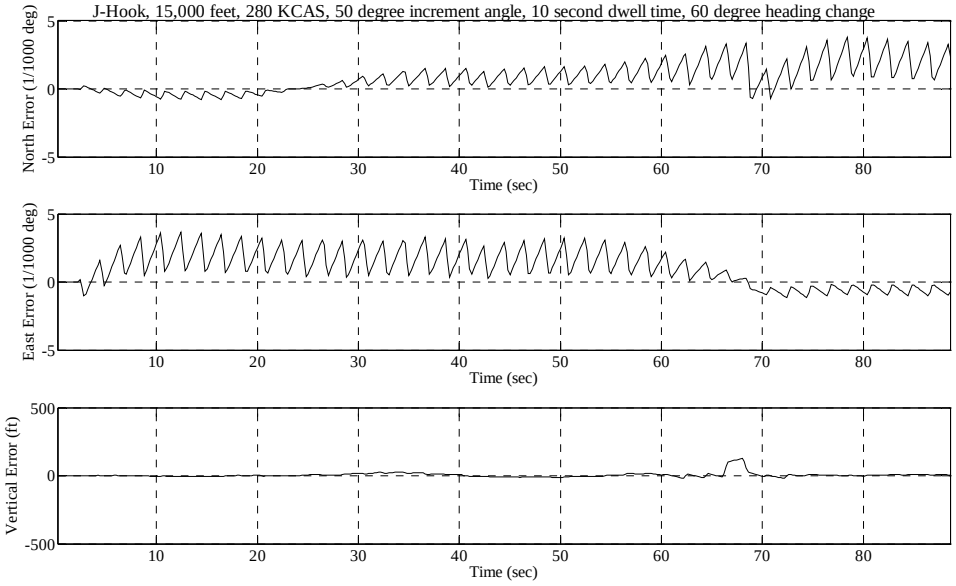

Test Point and Date: 026_21_Sep

POSITION ERROR TIME HISTORY

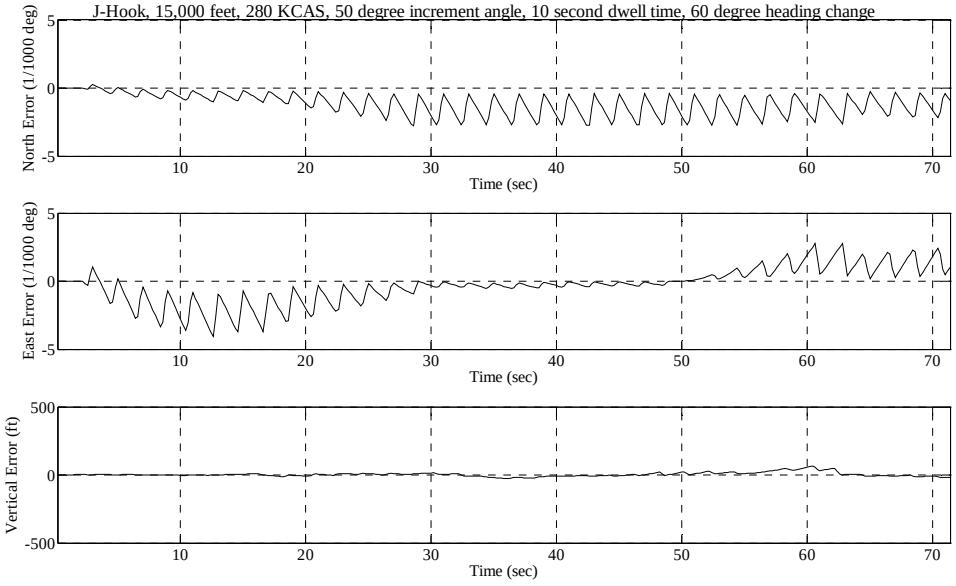

Test Point and Date: 027_18_Sep

POSITION ERROR TIME HISTORY

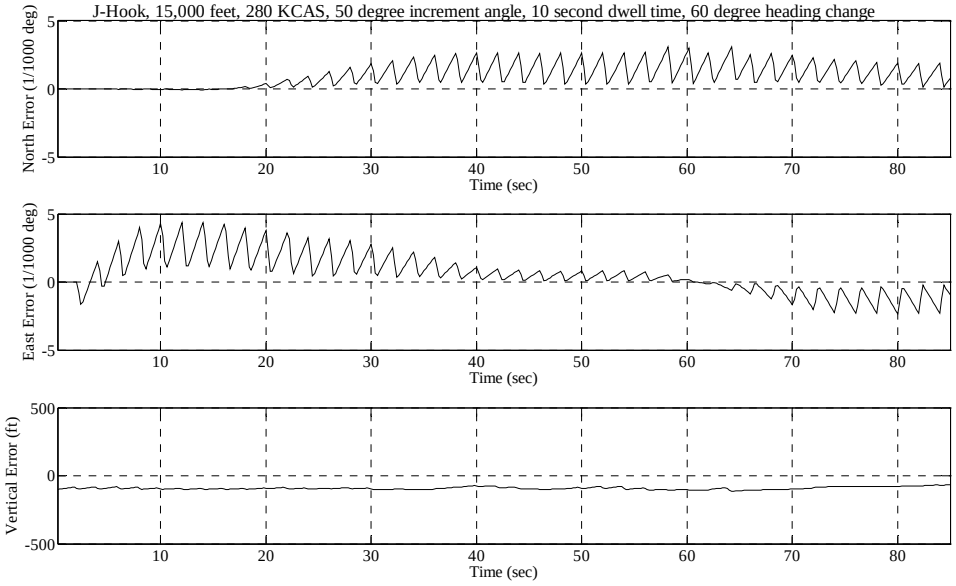

Test Point and Date: 028_17_Sep

POSITION ERROR TIME HISTORY

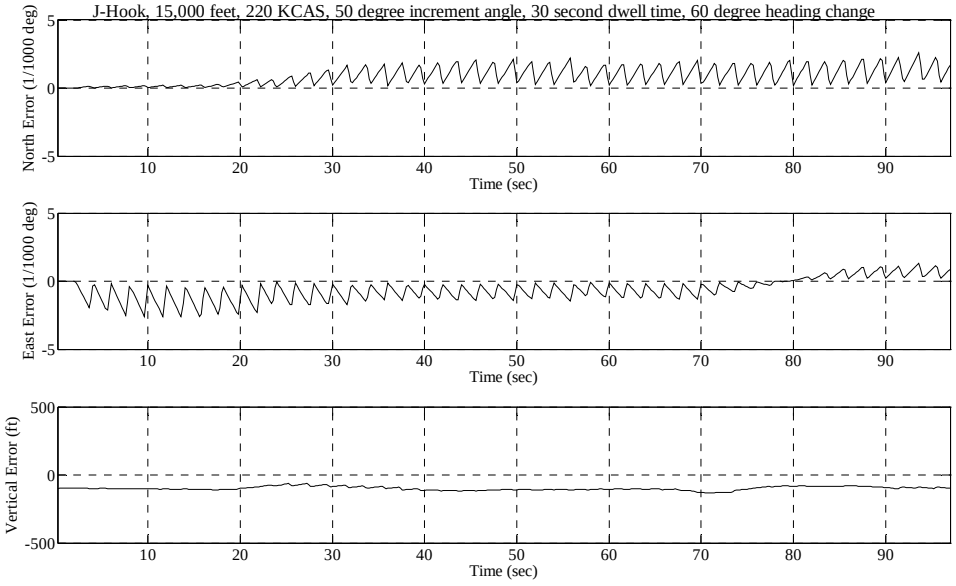

Test Point and Date: 029_17_Sep

POSITION ERROR TIME HISTORY

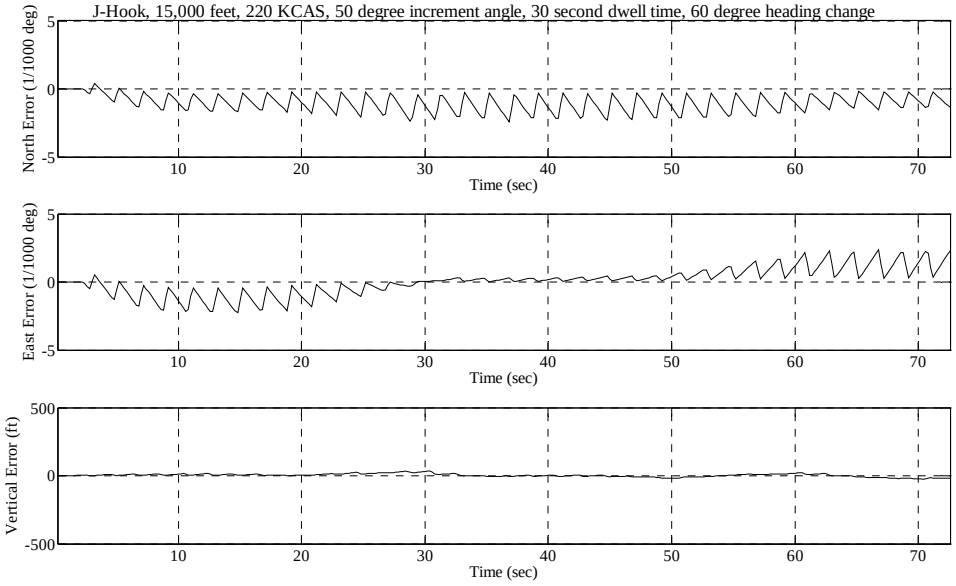

Test Point and Date: 030_18_Sep

POSITION ERROR TIME HISTORY

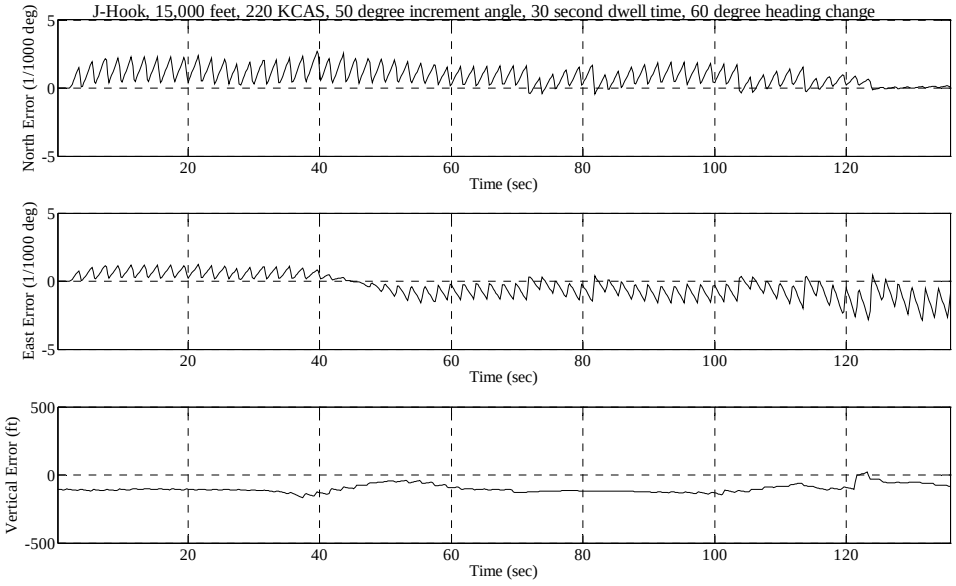

Test Point and Date: 031_17_Sep

POSITION ERROR TIME HISTORY

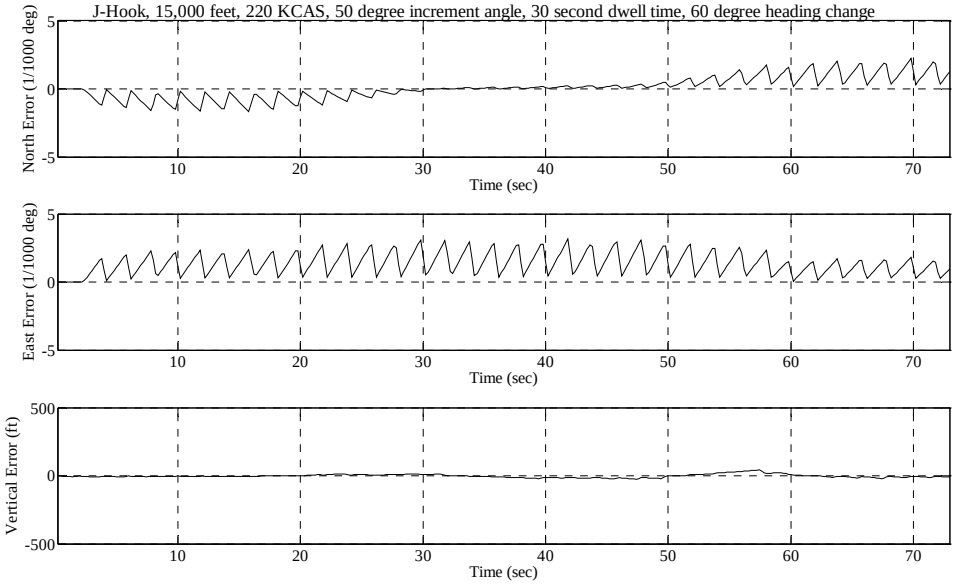

Test Point and Date: 032_18_Sep

POSITION ERROR TIME HISTORY

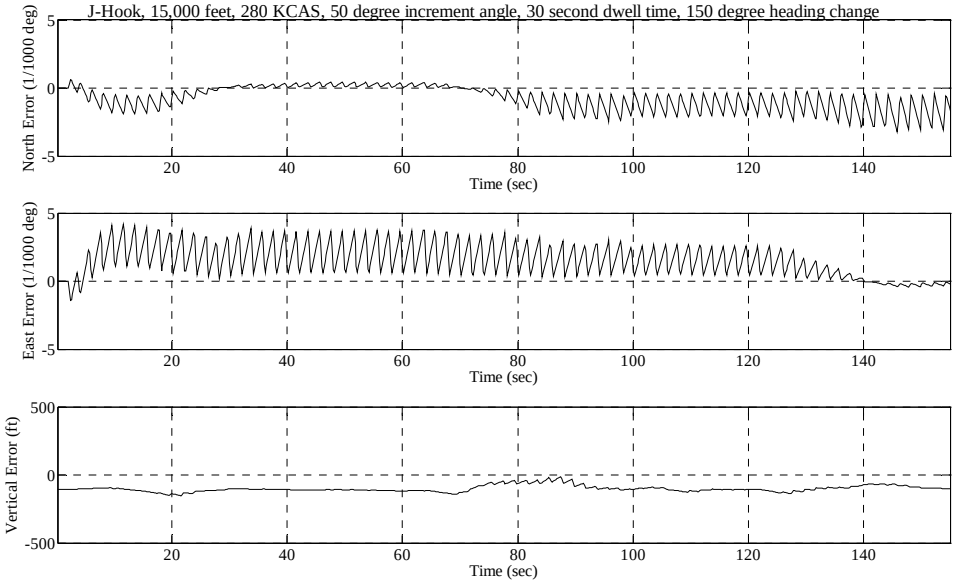

Test Point and Date: 033_17_Sep

POSITION ERROR TIME HISTORY

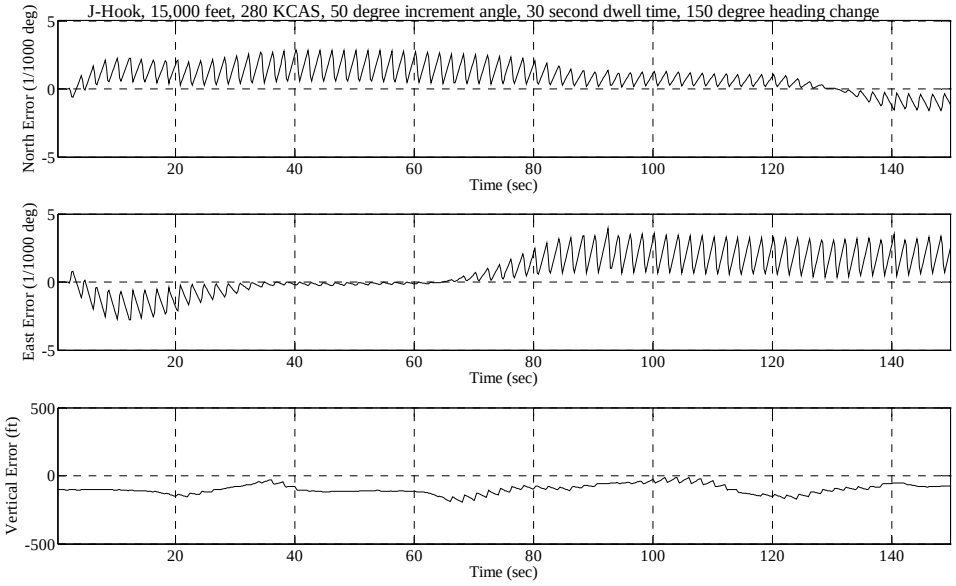

Test Point and Date: 034_17_Sep

POSITION ERROR TIME HISTORY

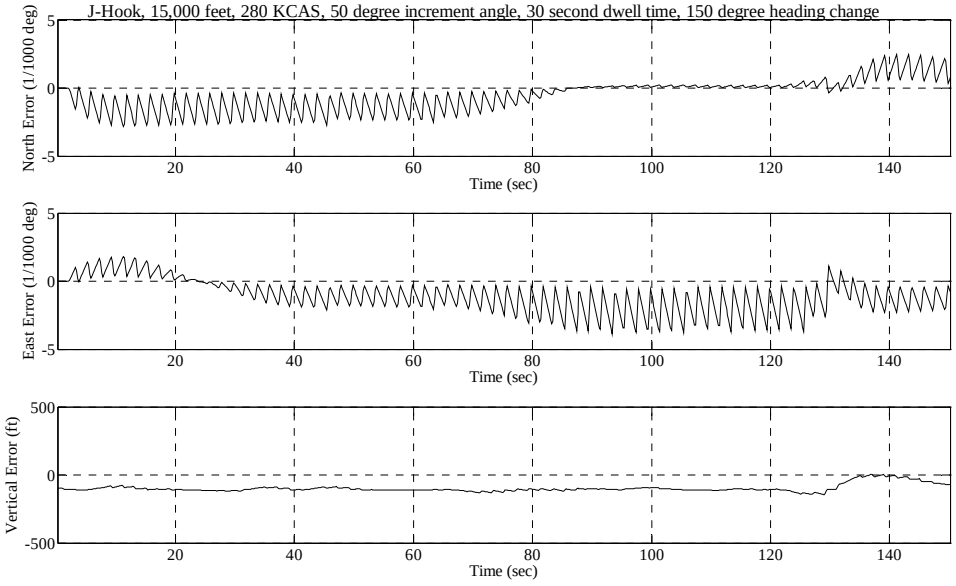

Test Point and Date: 035_17_Sep

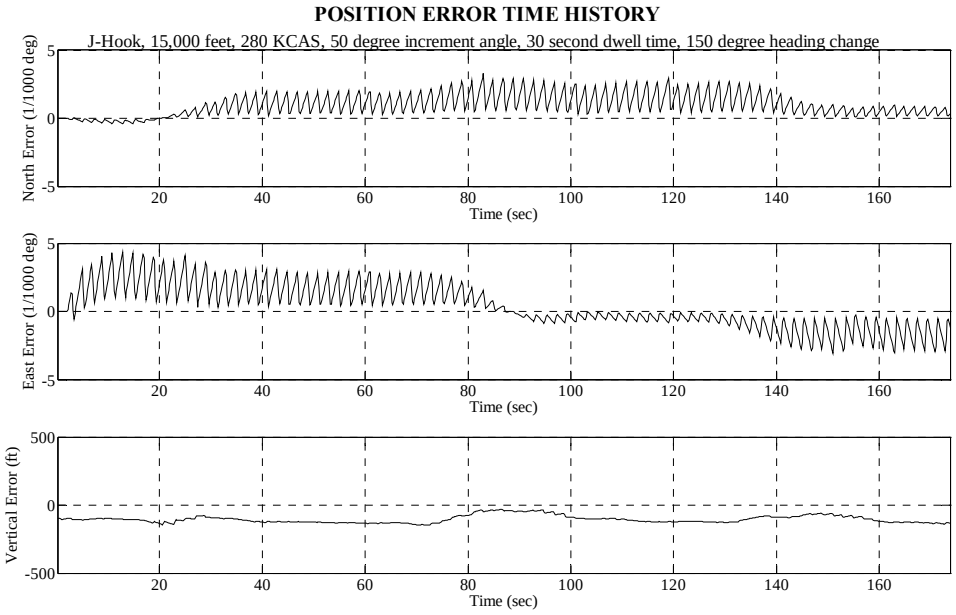

Test Point and Date: 036_17_Sep

G.2.2. J-Hook Velocity Plots

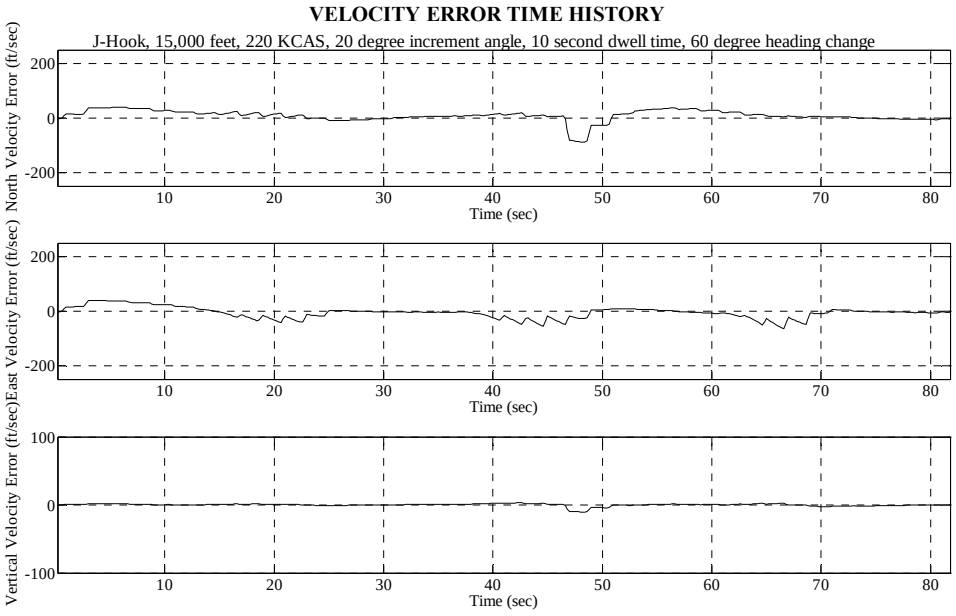

Test Point and Date: 005_18_Sep

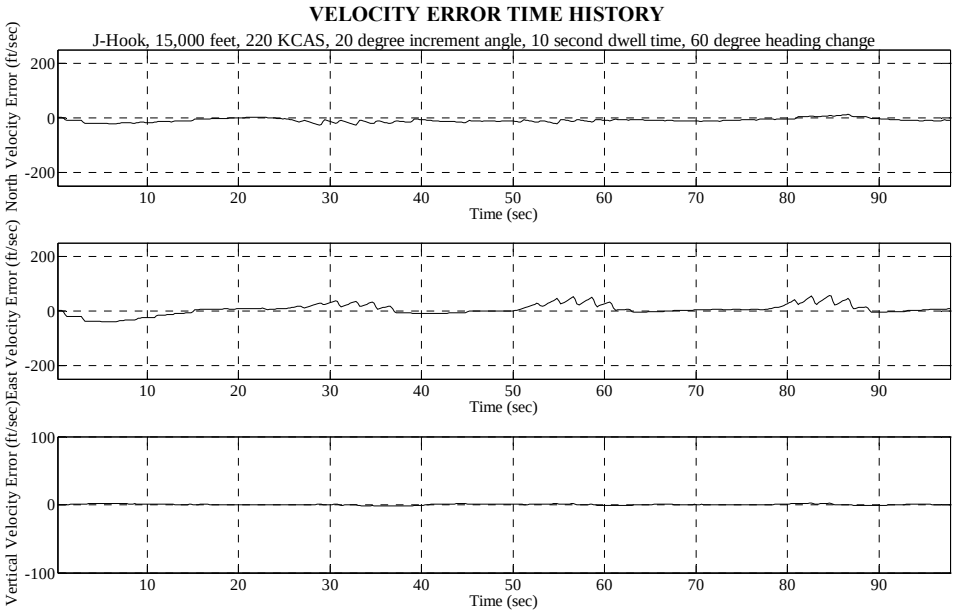
VELOCITY ERROR TIME HISTORY
J-Hook, 15,000 feet, 220 KCAS, 20 degree increment angle, 10 second dwell time, 60 degree heading change
North Velocity Error (ft/sec)
East Velocity Error (ft/sec)
Vertical Velocity Error (ft/sec)
Time (sec)
Test Point and Date: 005_21_Sep

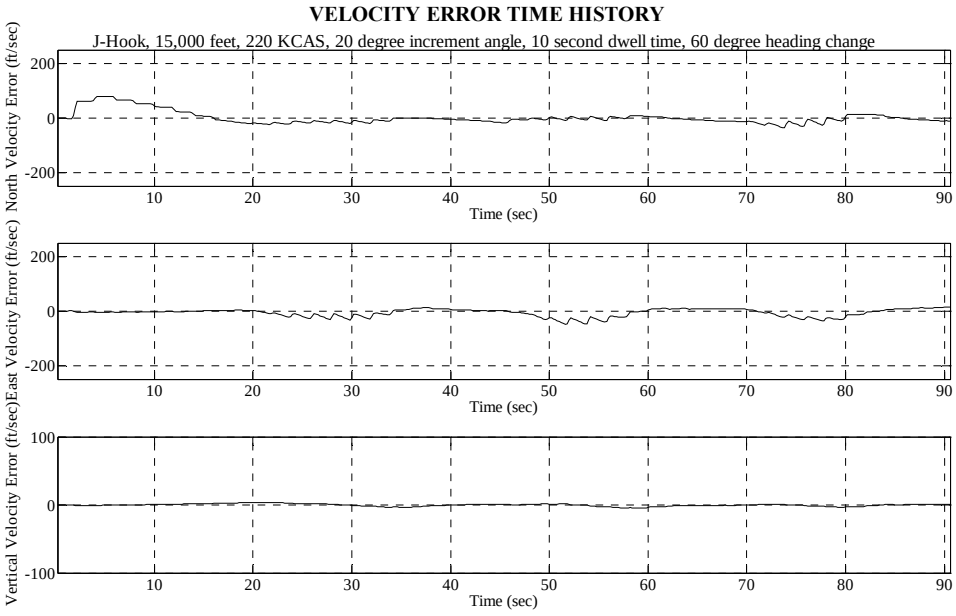
VELOCITY ERROR TIME HISTORY
J-Hook, 15,000 feet, 220 KCAS, 20 degree increment angle, 10 second dwell time, 60 degree heading change
North Velocity Error (ft/sec)
East Velocity Error (ft/sec)
Vertical Velocity Error (ft/sec)
Time (sec)
Test Point and Date: 006_13_Sep

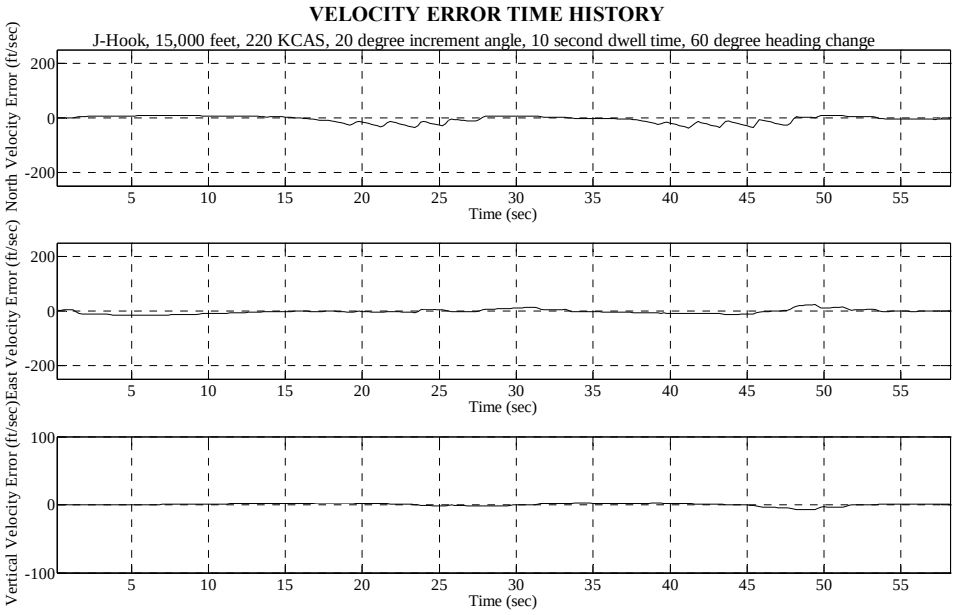

Test Point and Date: 007_13_Sep

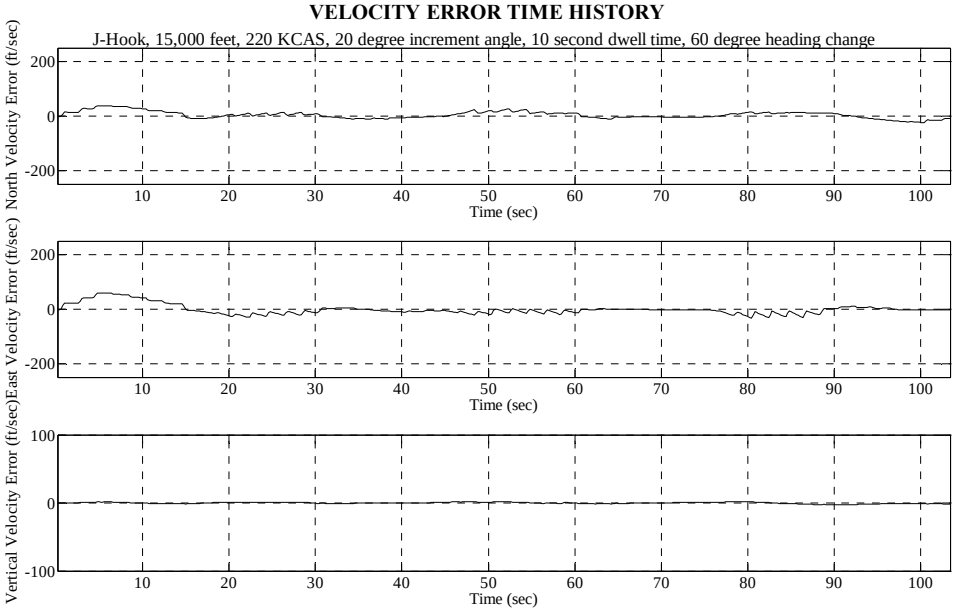

Test Point and Date: 008_13_Sep

VELOCITY ERROR TIME HISTORY

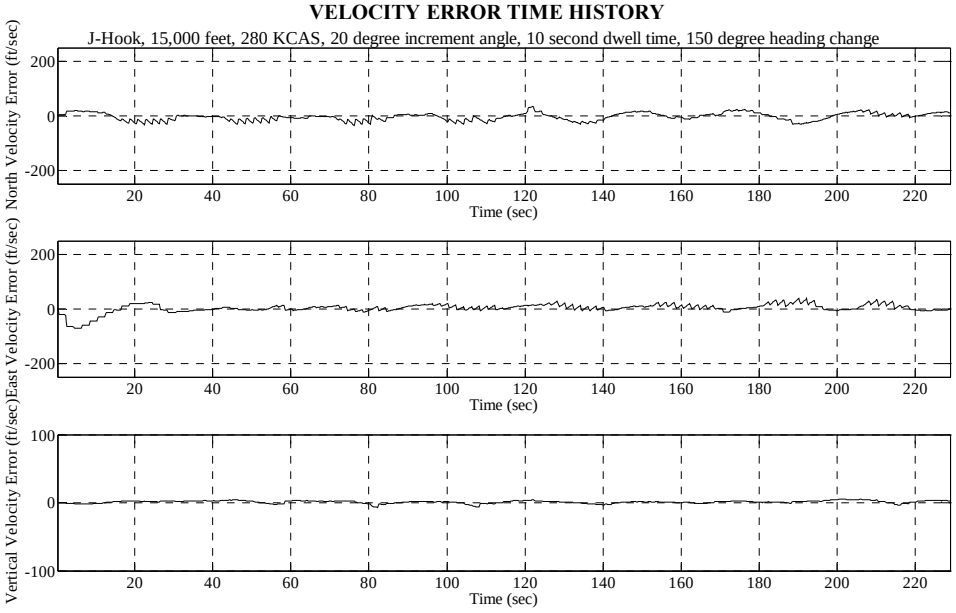

Test Point and Date: 009_17_Sep

VELOCITY ERROR TIME HISTORY

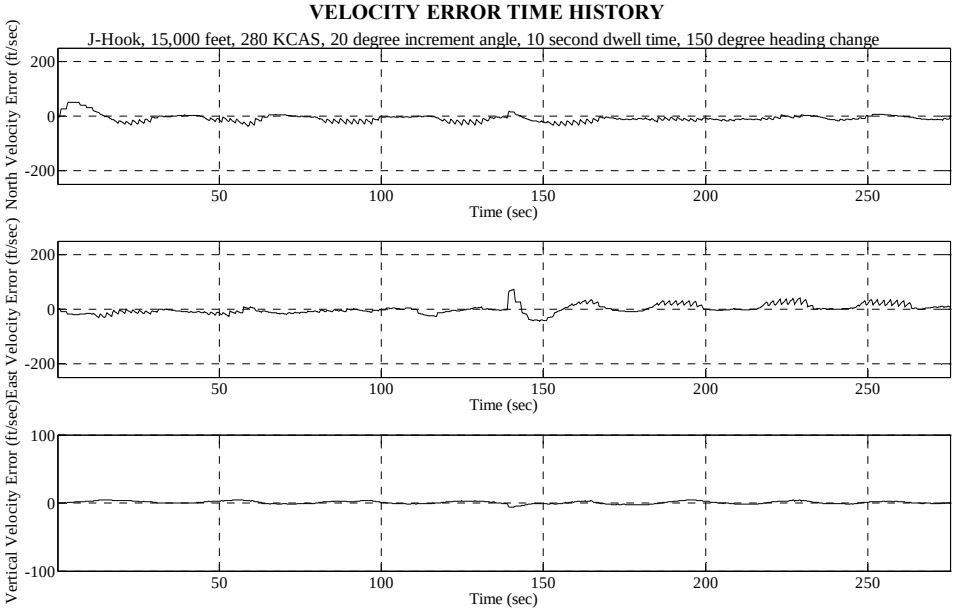

Test Point and Date: 010_19_Sep

VELOCITY ERROR TIME HISTORY

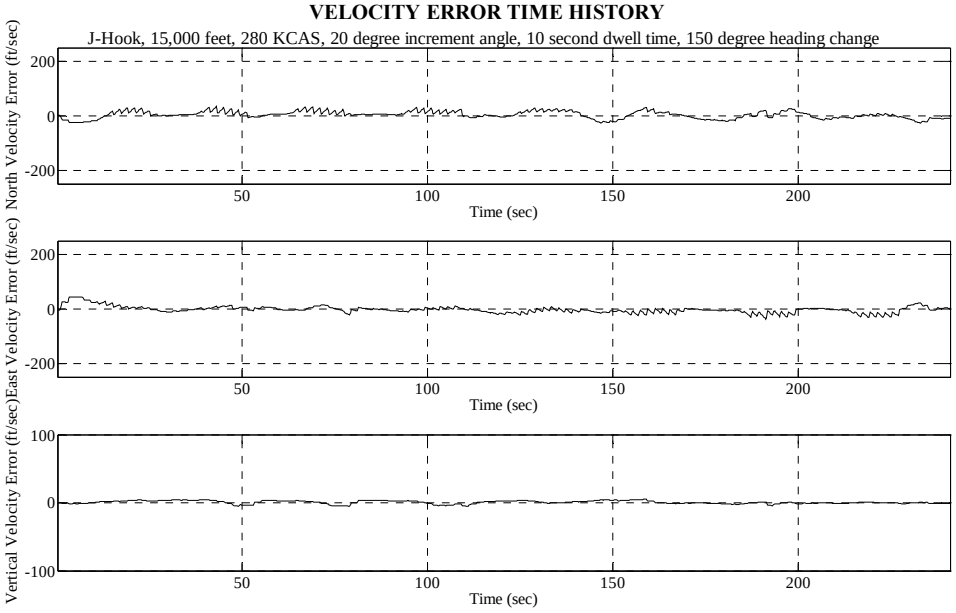

Test Point and Date: 011_17_Sep

VELOCITY ERROR TIME HISTORY

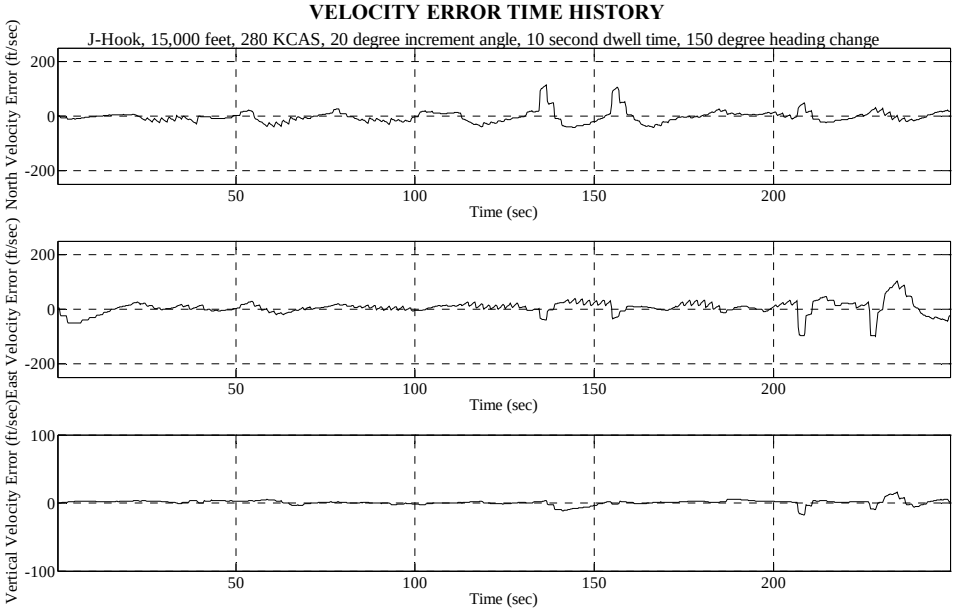

Test Point and Date: 012_17_Sep

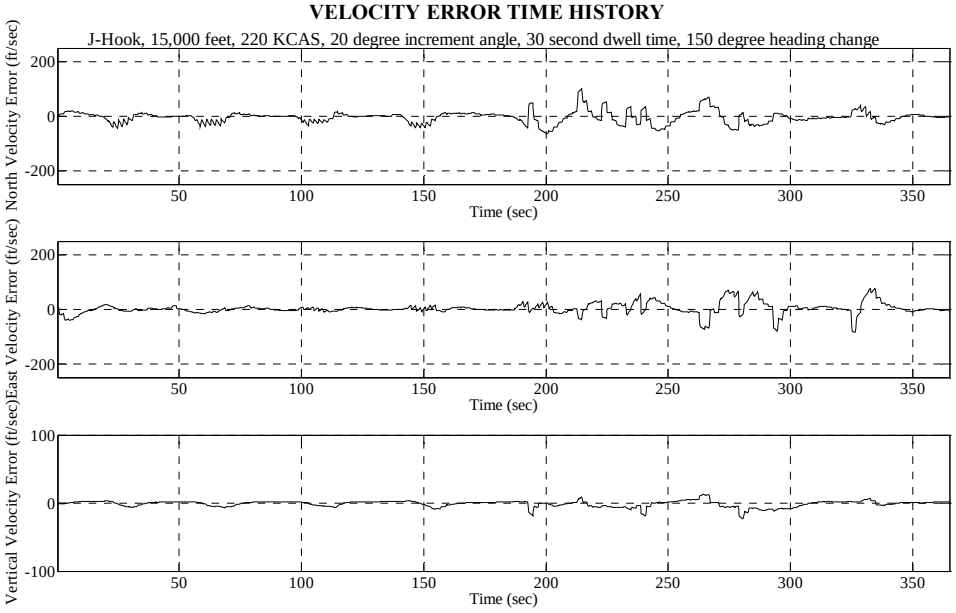

Test Point and Date: 013_13_Sep

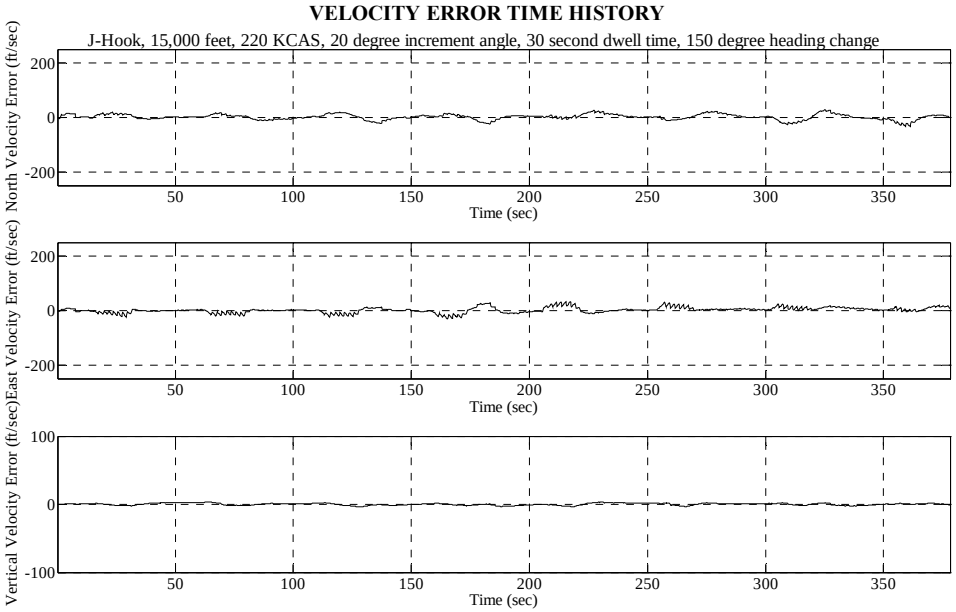

Test Point and Date: 014_17_Sep

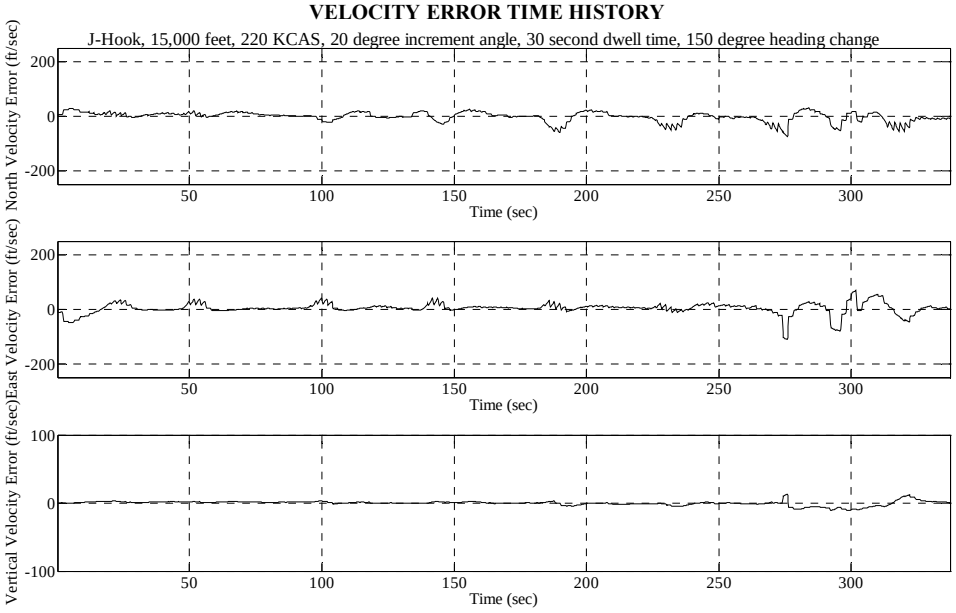

Test Point and Date: 015_13_Sep

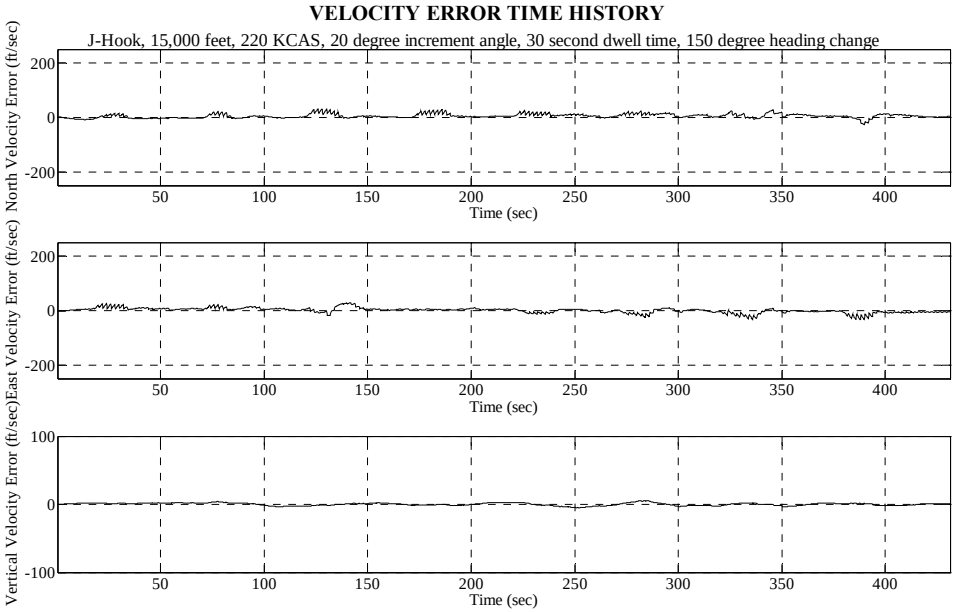

Test Point and Date: 016_19_Sep

VELOCITY ERROR TIME HISTORY

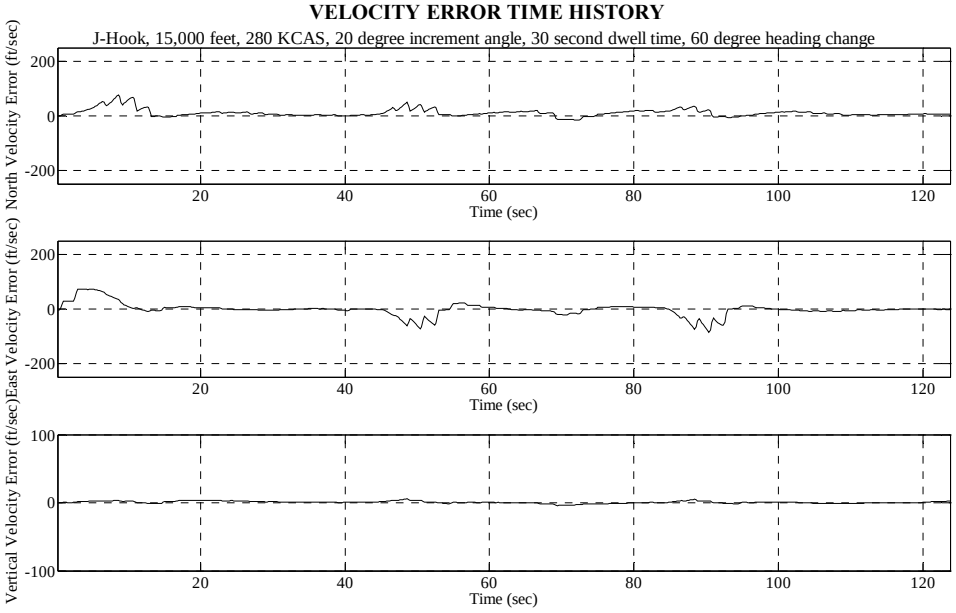

Test Point and Date: 017_18_Sep

VELOCITY ERROR TIME HISTORY

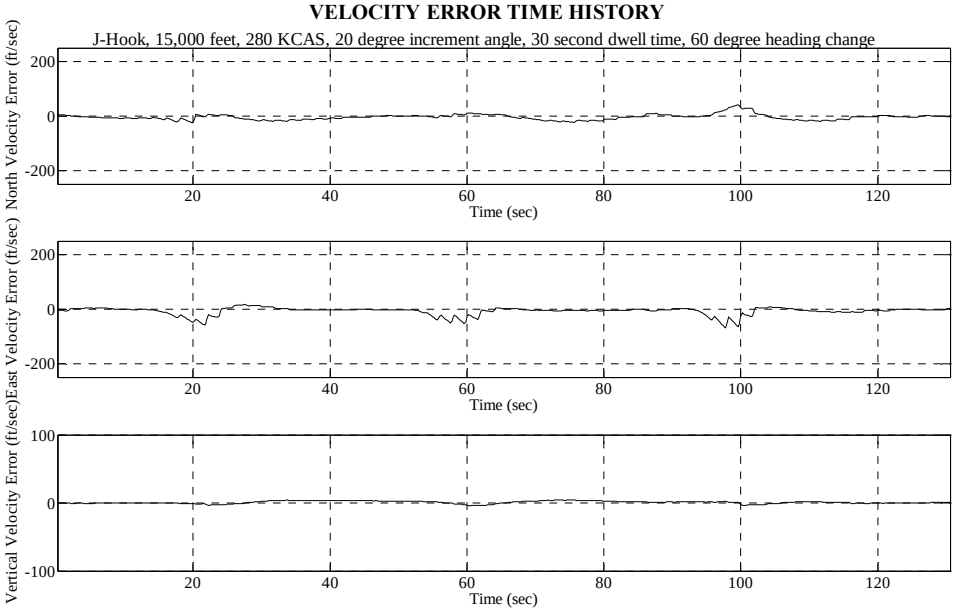

Test Point and Date: 018_13_Sep

VELOCITY ERROR TIME HISTORY

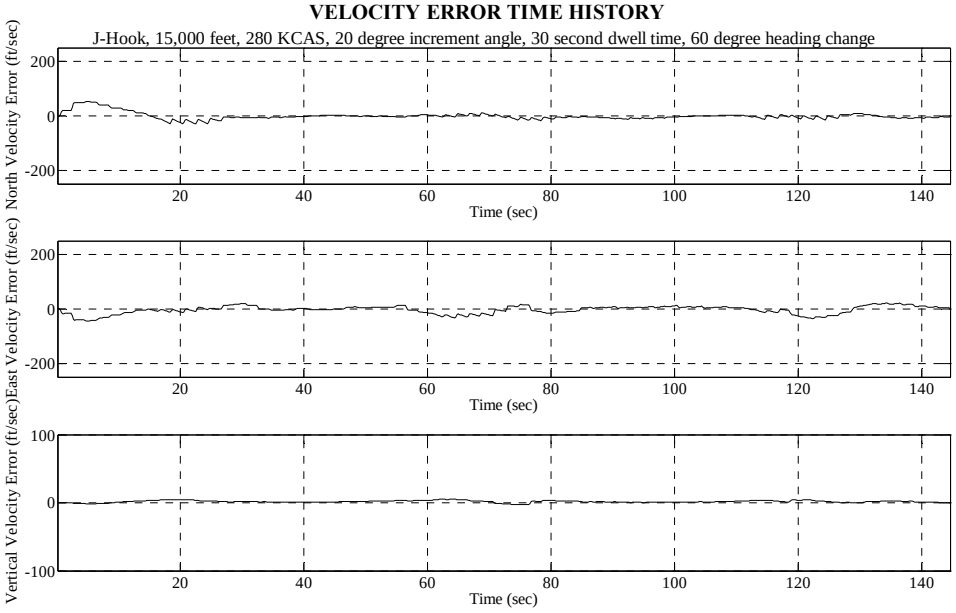

Test Point and Date: 019_17_Sep

VELOCITY ERROR TIME HISTORY

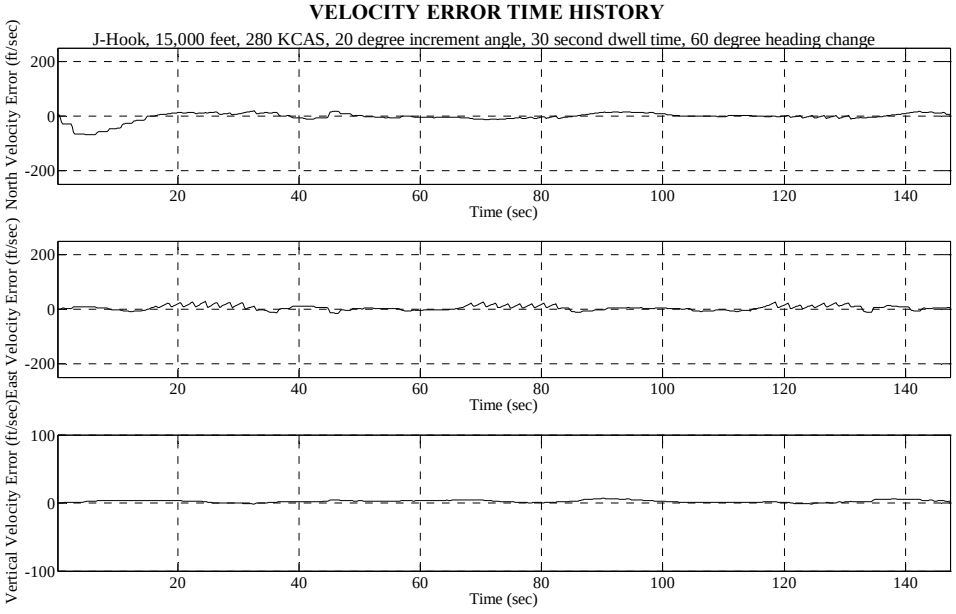

Test Point and Date: 020_17_Sep

VELOCITY ERROR TIME HISTORY

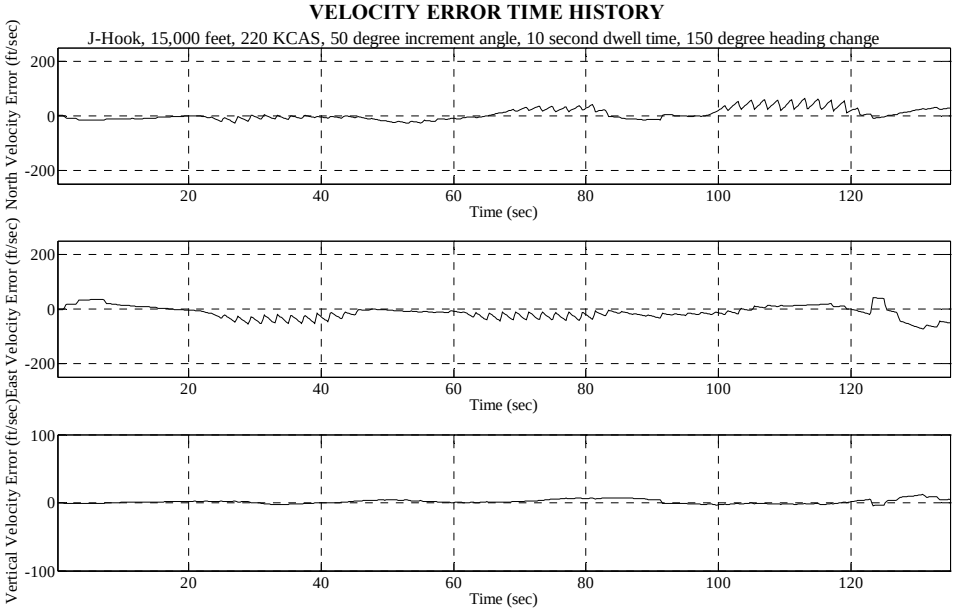

Test Point and Date: 021_13_Sep

VELOCITY ERROR TIME HISTORY

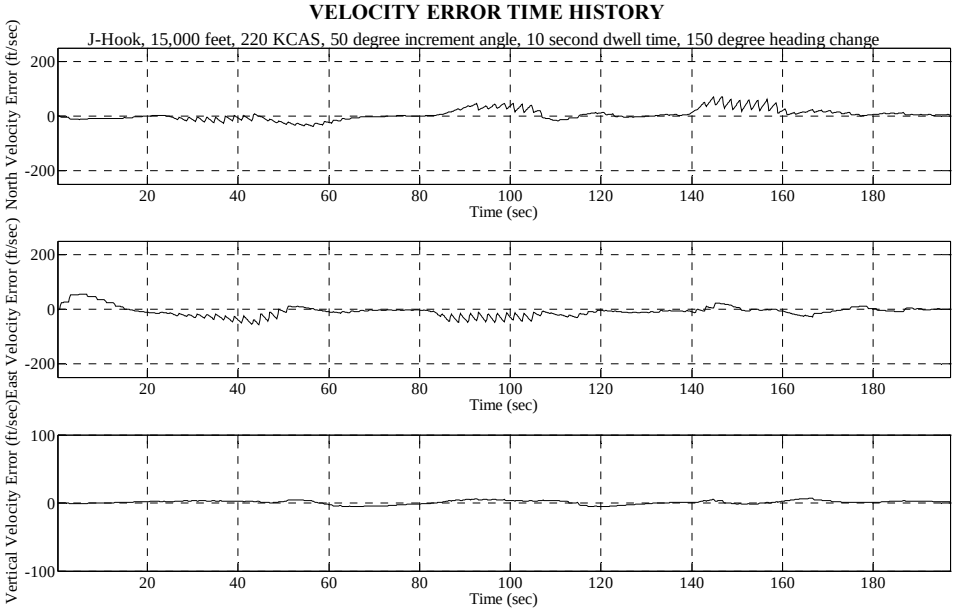

Test Point and Date: 022_13_Sep

VELOCITY ERROR TIME HISTORY

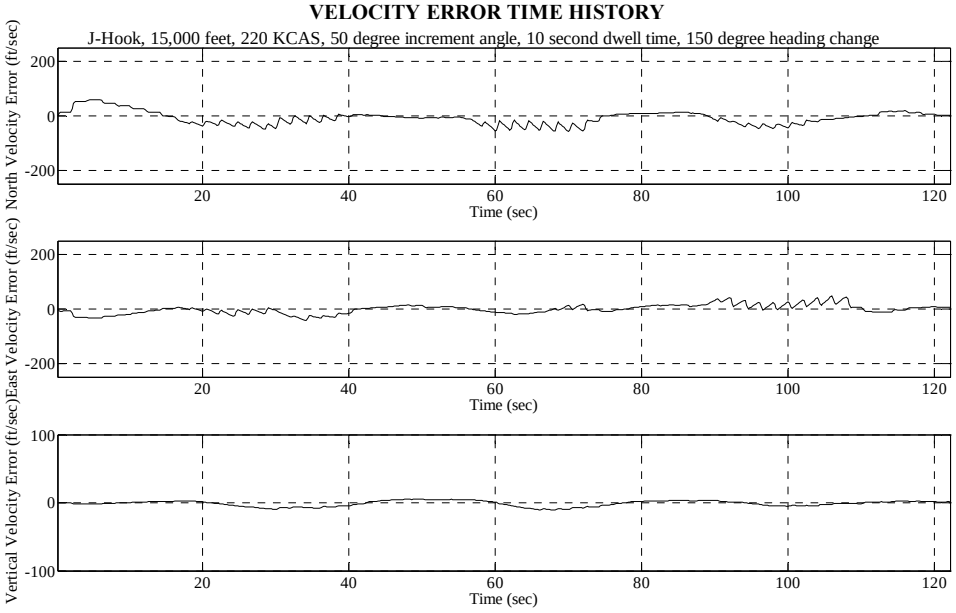

Test Point and Date: 023_13_Sep

VELOCITY ERROR TIME HISTORY

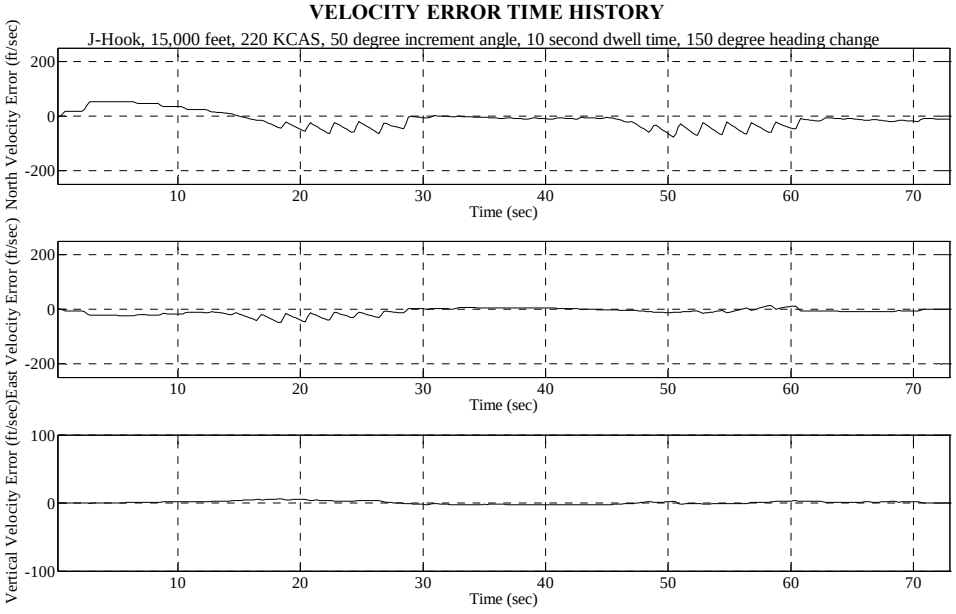

Test Point and Date: 024_18_Sep

VELOCITY ERROR TIME HISTORY

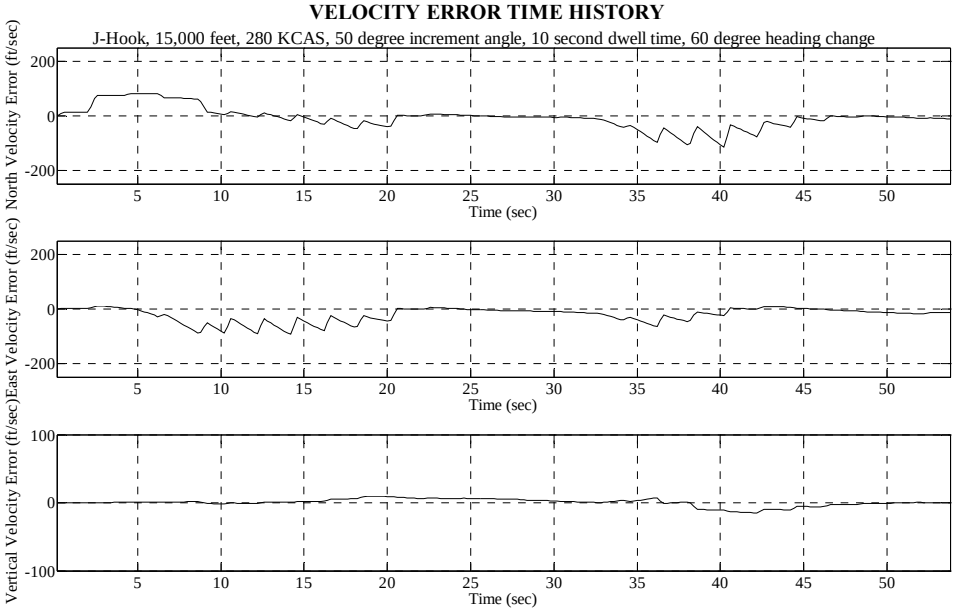

Test Point and Date: 025_18_Sep

VELOCITY ERROR TIME HISTORY

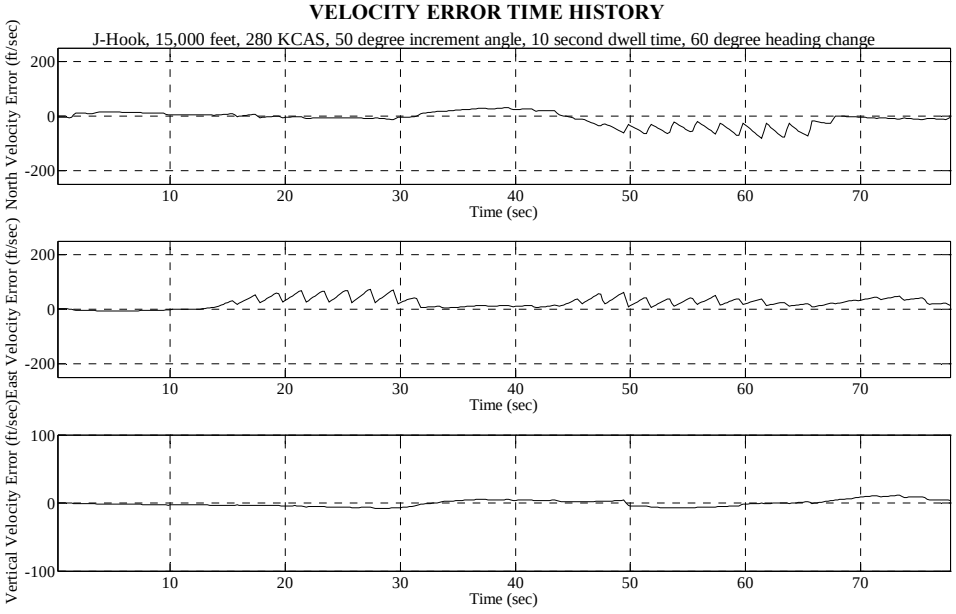

Test Point and Date: 026_17_Sep

VELOCITY ERROR TIME HISTORY

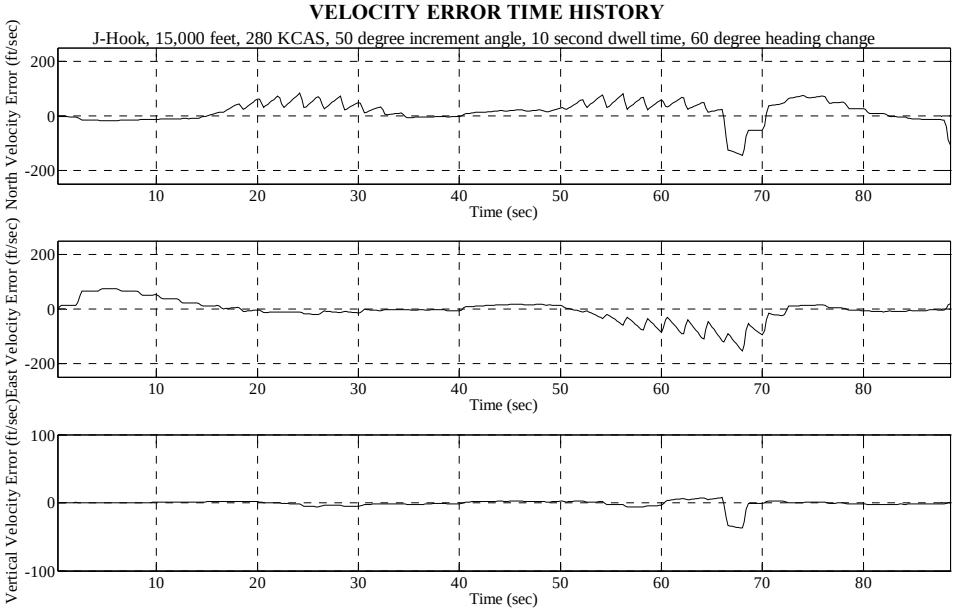

Test Point and Date: 026_21_Sep

VELOCITY ERROR TIME HISTORY

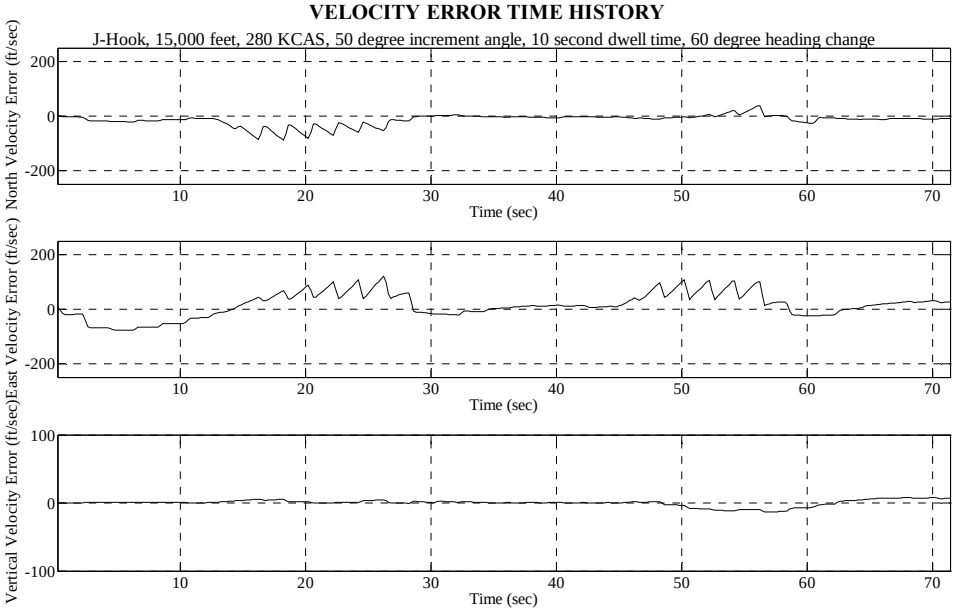

Test Point and Date: 027_18_Sep

VELOCITY ERROR TIME HISTORY

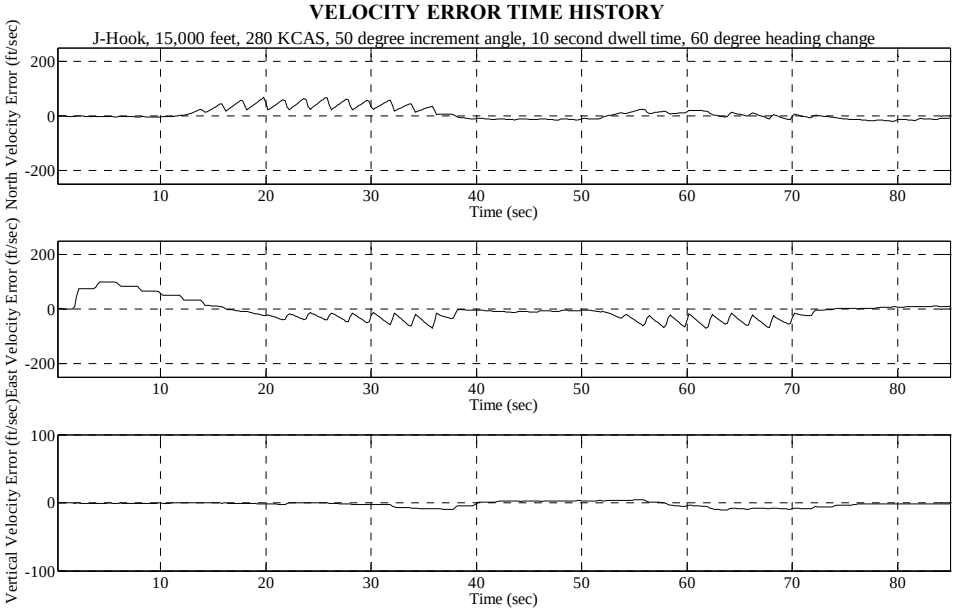

Test Point and Date: 028_17_Sep

VELOCITY ERROR TIME HISTORY

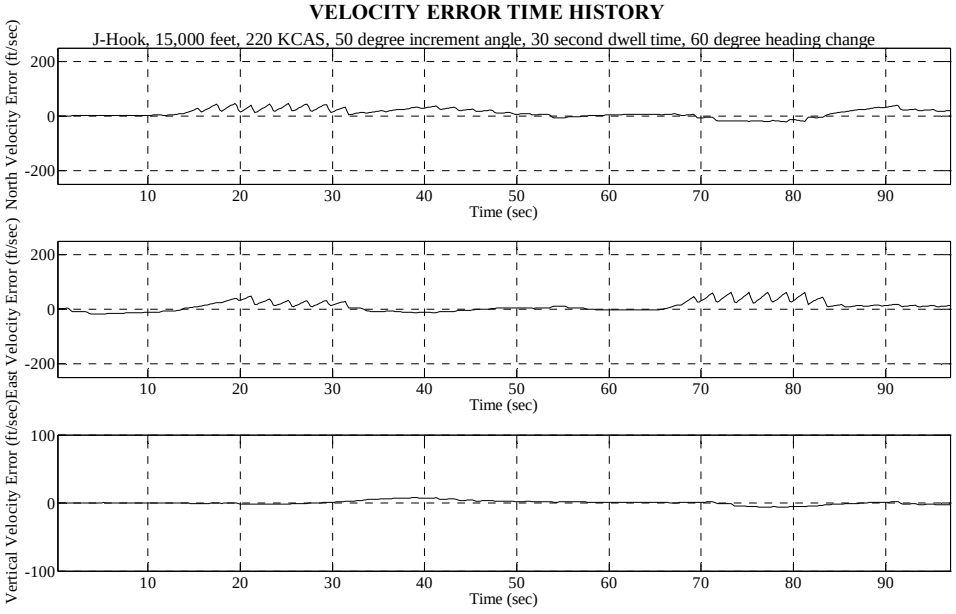

Test Point and Date: 029_17_Sep

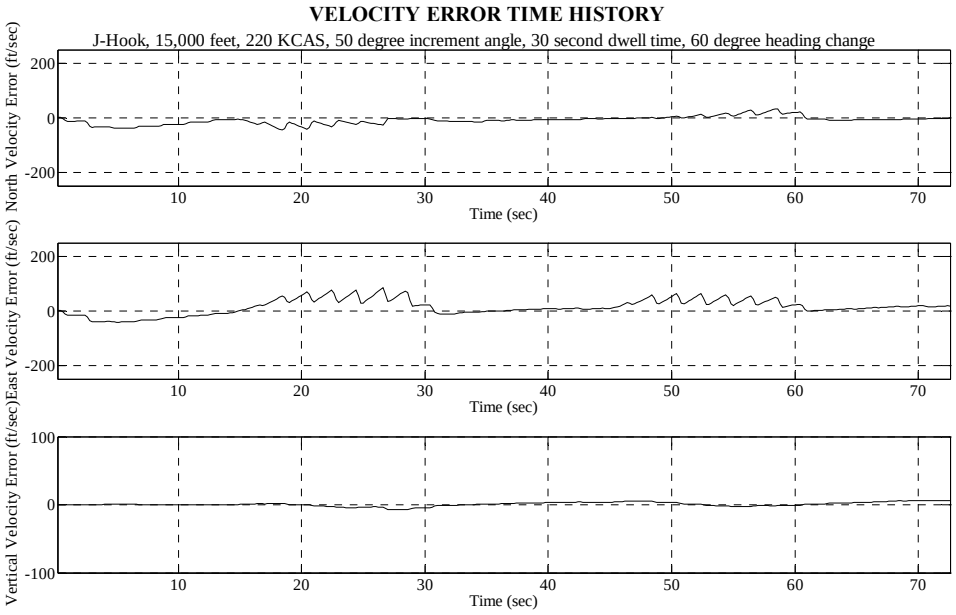

Test Point and Date: 030_18_Sep

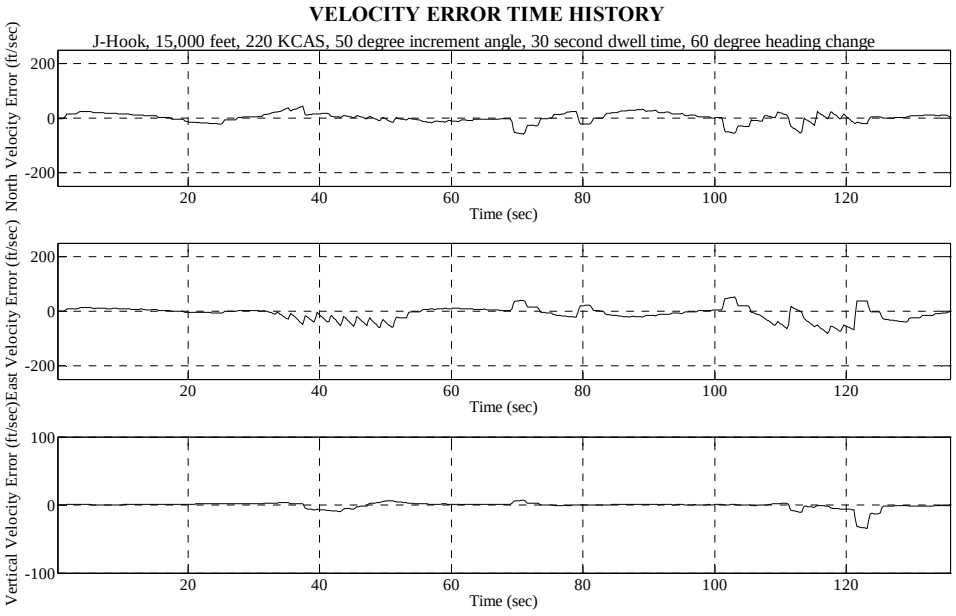

Test Point and Date: 031_17_Sep

VELOCITY ERROR TIME HISTORY

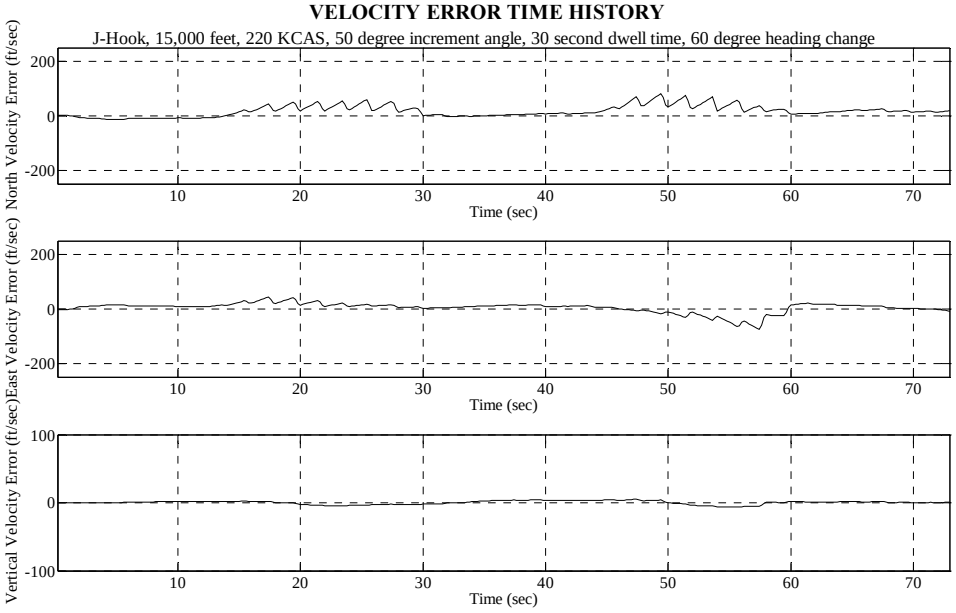

Test Point and Date: 032_18_Sep

VELOCITY ERROR TIME HISTORY

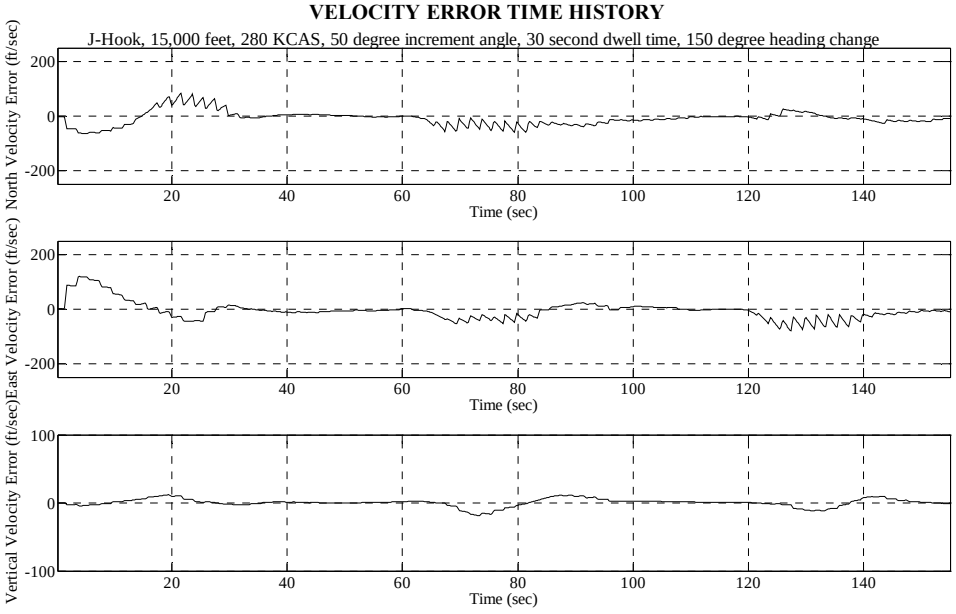

Test Point and Date: 033_17_Sep

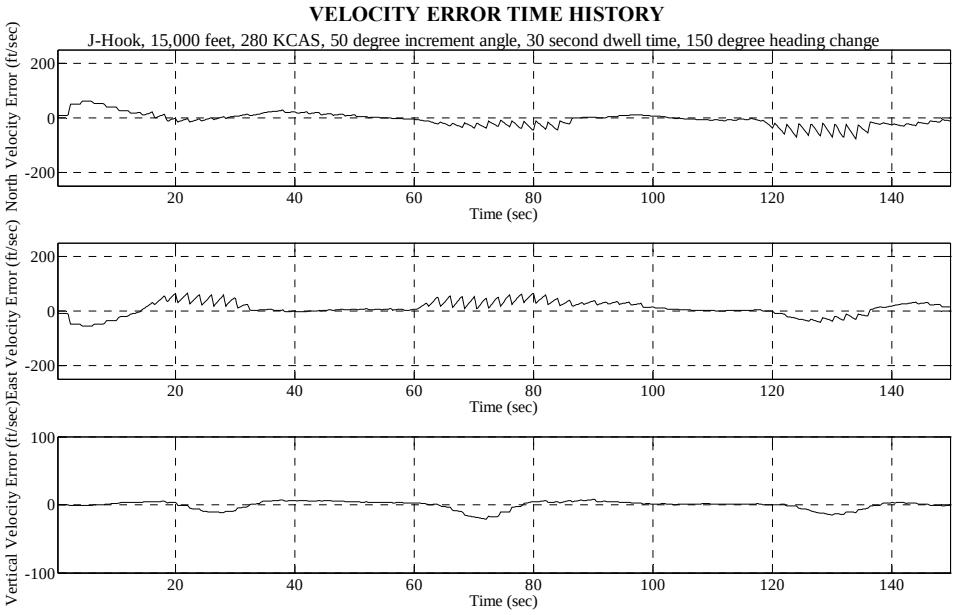

Test Point and Date: 034_17_Sep

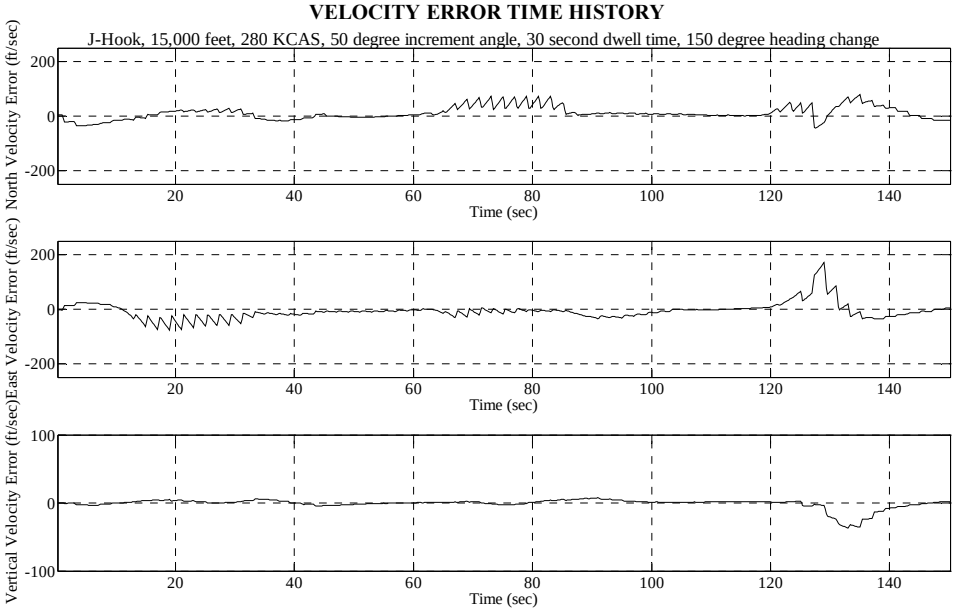

Test Point and Date: 035_17_Sep

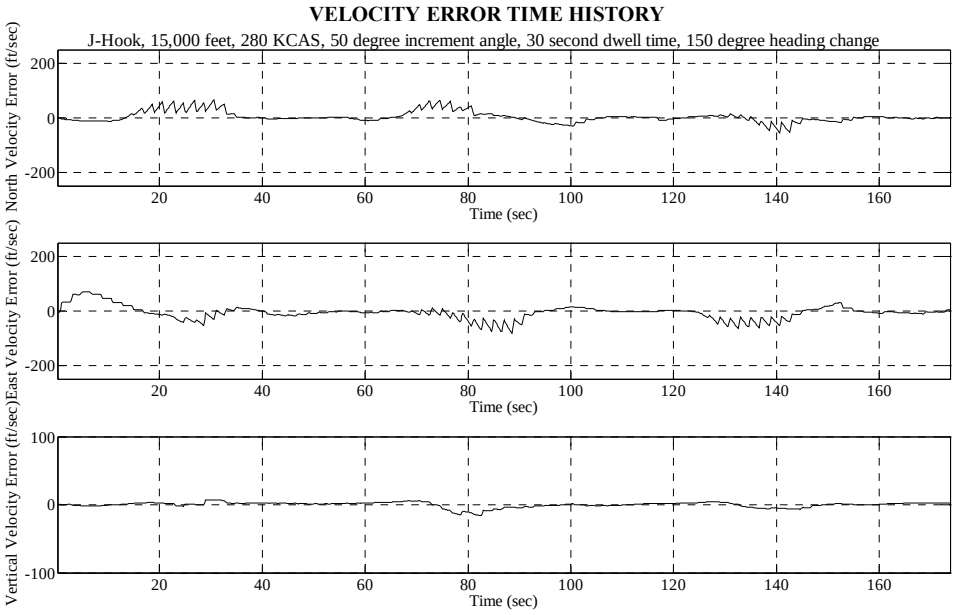

Test Point and Date: 036_17_Sep

G.2.3. J-Hook Wind Plots

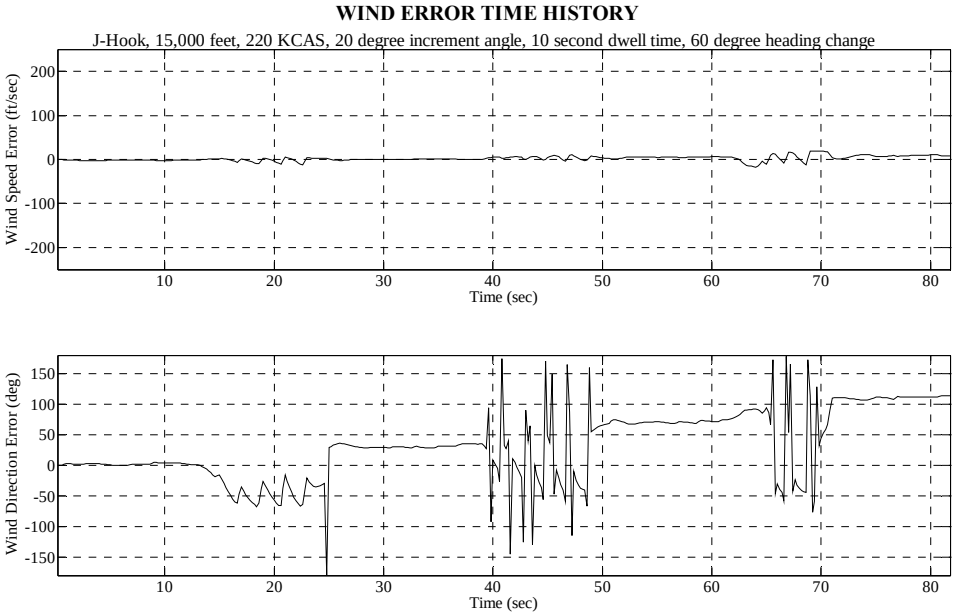

Test Point and Date: 005_18_Sep

WIND ERROR TIME HISTORY

J-Hook, 15,000 feet, 220 KCAS, 20 degree increment angle, 10 second dwell time, 60 degree heading change

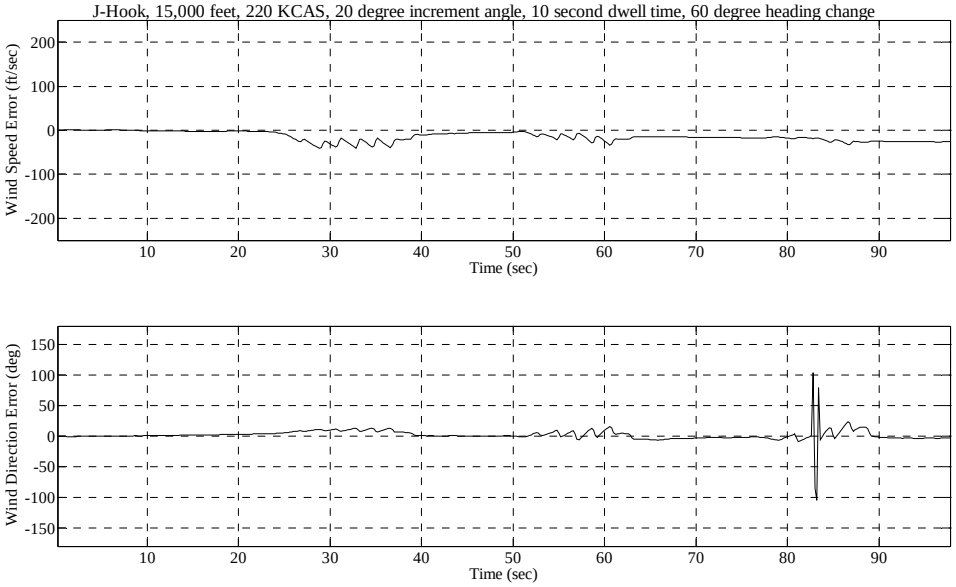

Test Point and Date: 005_21_Sep

WIND ERROR TIME HISTORY

J-Hook, 15,000 feet, 220 KCAS, 20 degree increment angle, 10 second dwell time, 60 degree heading change

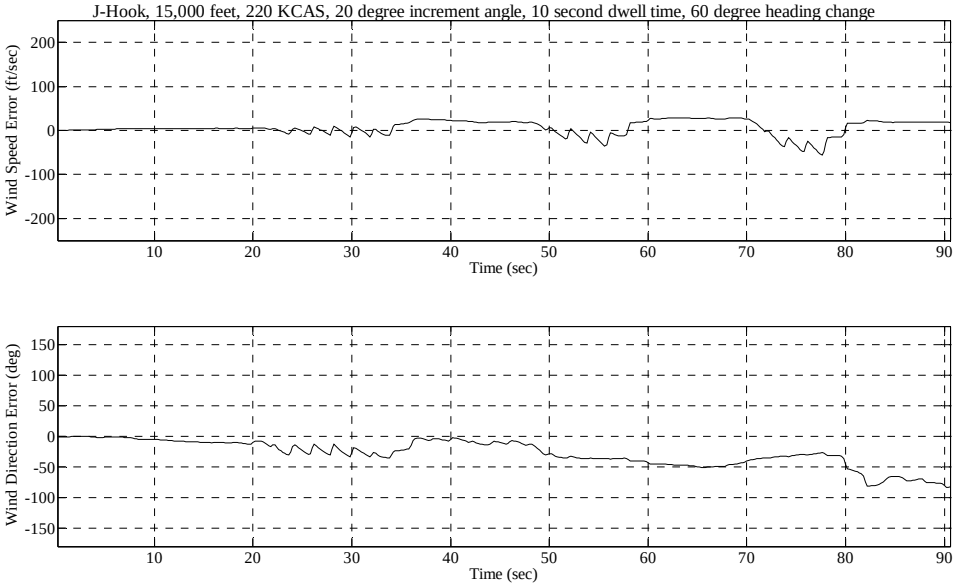

Test Point and Date: 006_13_Sep

WIND ERROR TIME HISTORY

J-Hook, 15,000 feet, 220 KCAS, 20 degree increment angle, 10 second dwell time, 60 degree heading change

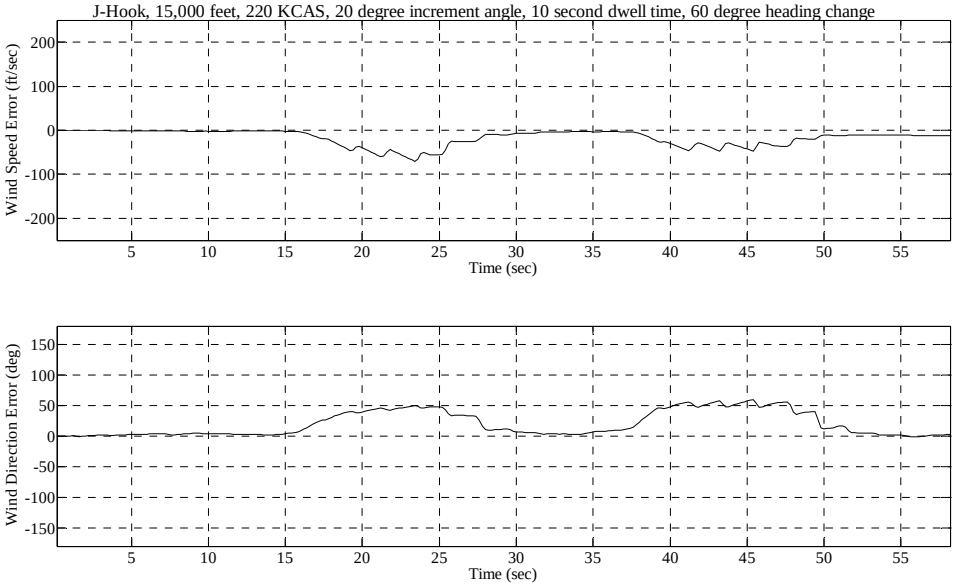

Test Point and Date: 007_13_Sep

WIND ERROR TIME HISTORY

J-Hook, 15,000 feet, 220 KCAS, 20 degree increment angle, 10 second dwell time, 60 degree heading change

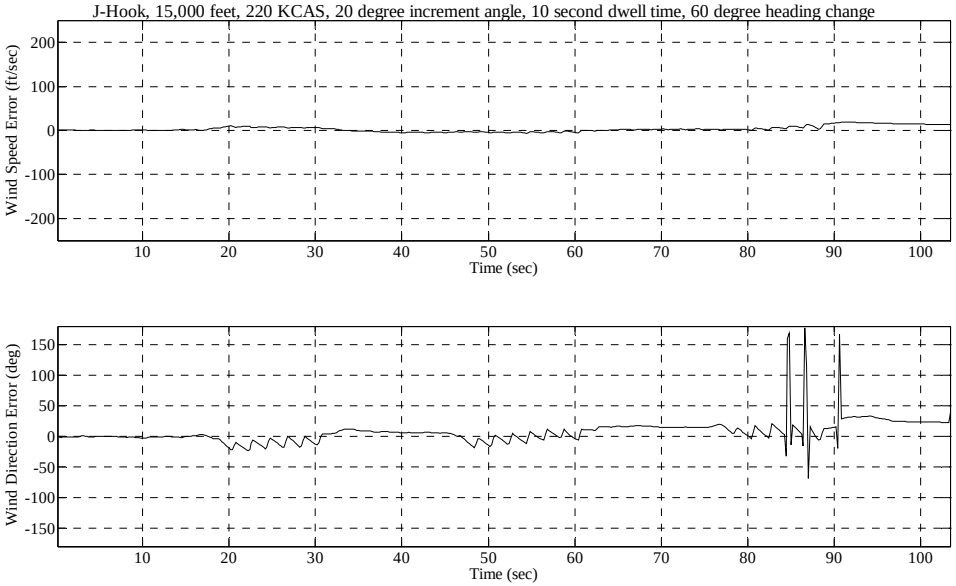

Test Point and Date: 008_13_Sep

WIND ERROR TIME HISTORY

J-Hook, 15,000 feet, 280 KCAS, 20 degree increment angle, 10 second dwell time, 150 degree heading change

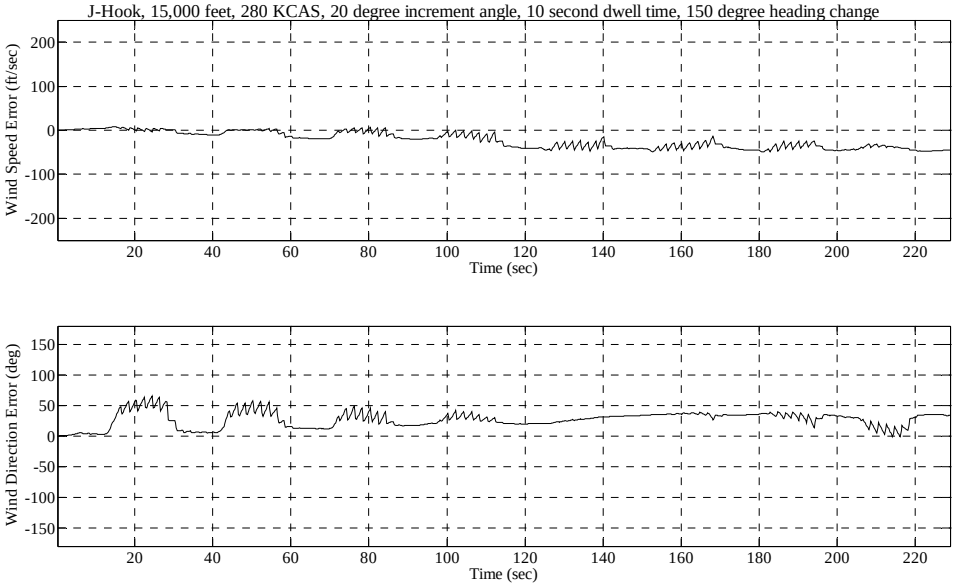

Test Point and Date: 009_17_Sep

WIND ERROR TIME HISTORY

J-Hook, 15,000 feet, 280 KCAS, 20 degree increment angle, 10 second dwell time, 150 degree heading change

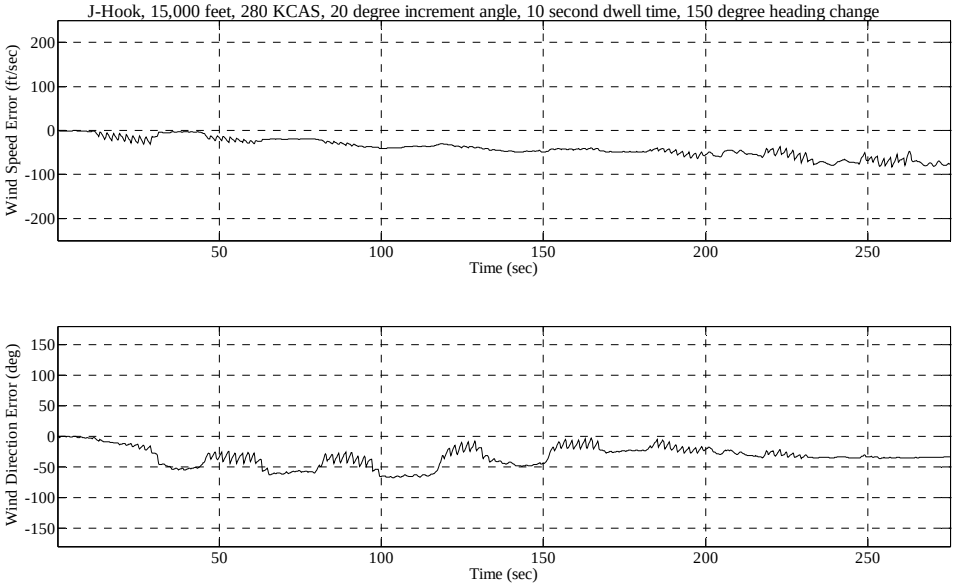

Test Point and Date: 010_19_Sep

WIND ERROR TIME HISTORY

J-Hook, 15,000 feet, 280 KCAS, 20 degree increment angle, 10 second dwell time, 150 degree heading change

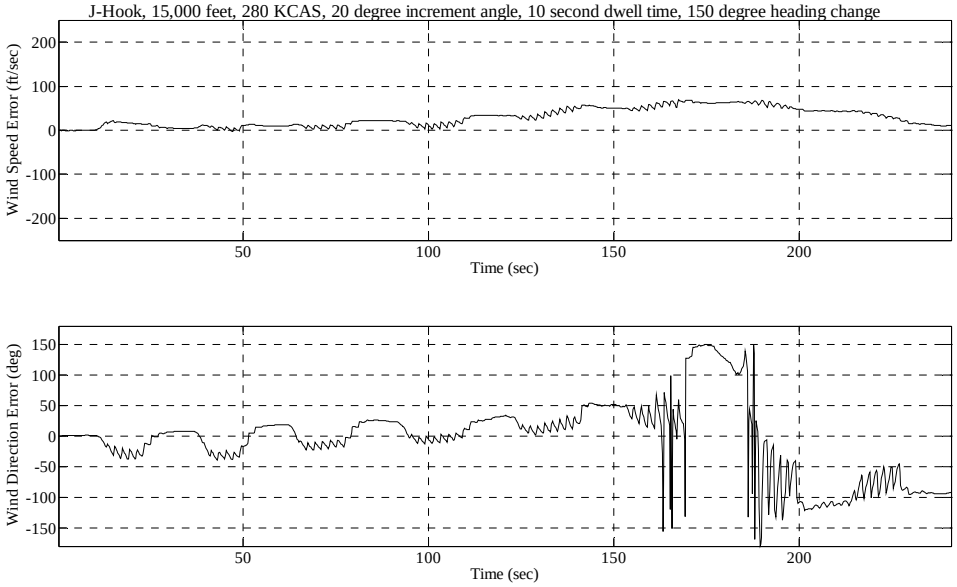

Test Point and Date: 011_17_Sep

WIND ERROR TIME HISTORY

J-Hook, 15,000 feet, 280 KCAS, 20 degree increment angle, 10 second dwell time, 150 degree heading change

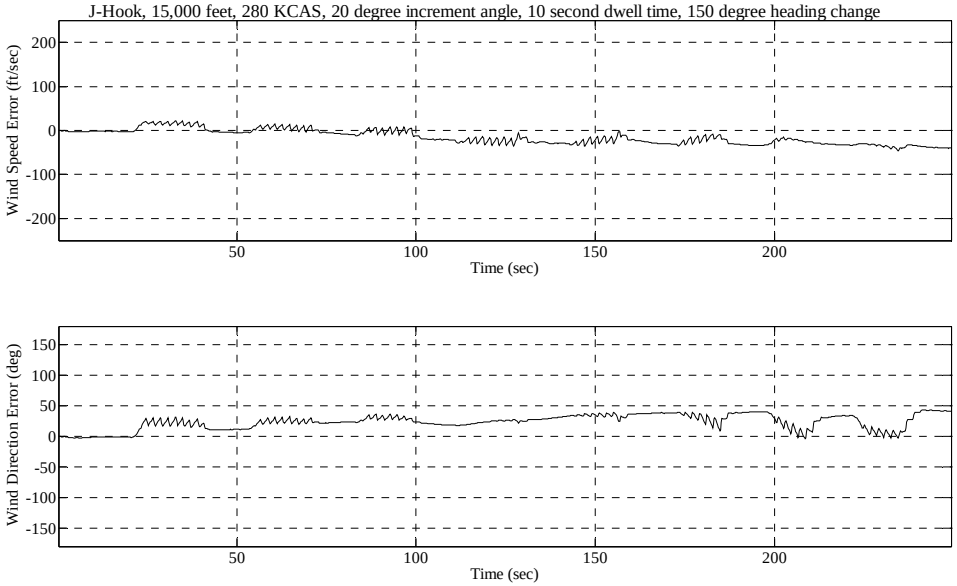

Test Point and Date: 012_17_Sep

WIND ERROR TIME HISTORY

J-Hook, 15,000 feet, 220 KCAS, 20 degree increment angle, 30 second dwell time, 150 degree heading change

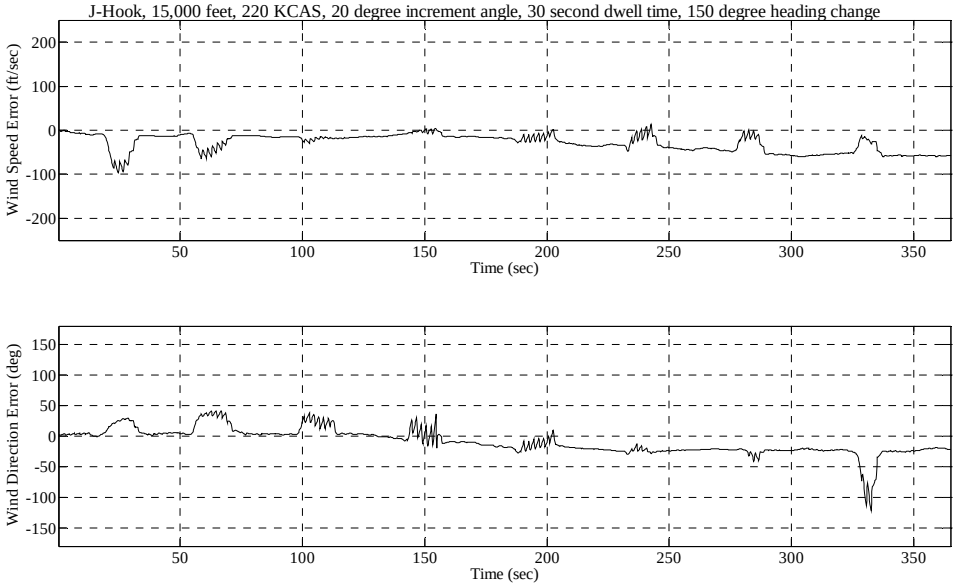

Test Point and Date: 013_13_Sep

WIND ERROR TIME HISTORY

J-Hook, 15,000 feet, 220 KCAS, 20 degree increment angle, 30 second dwell time, 150 degree heading change

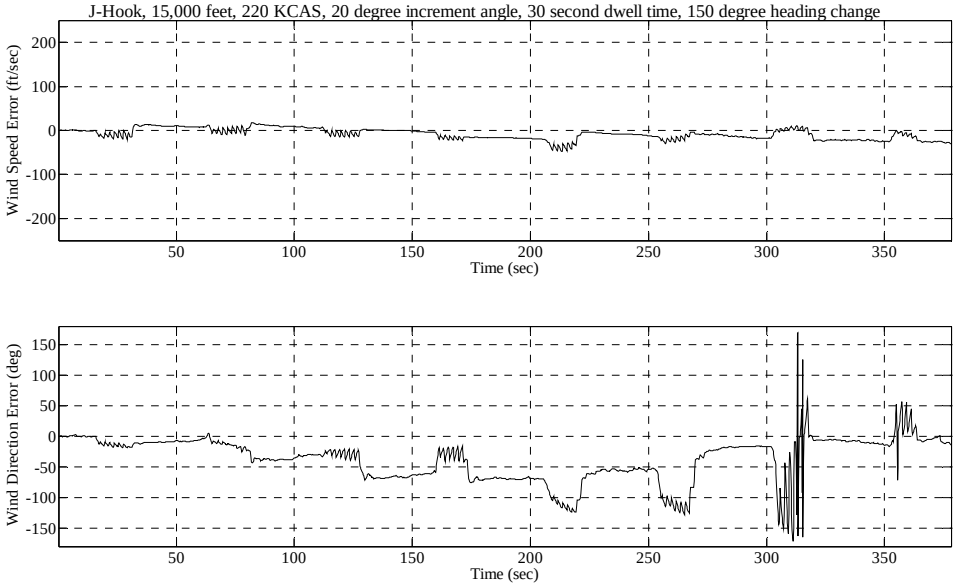

Test Point and Date: 014_17_Sep

WIND ERROR TIME HISTORY

J-Hook, 15,000 feet, 220 KCAS, 20 degree increment angle, 30 second dwell time, 150 degree heading change

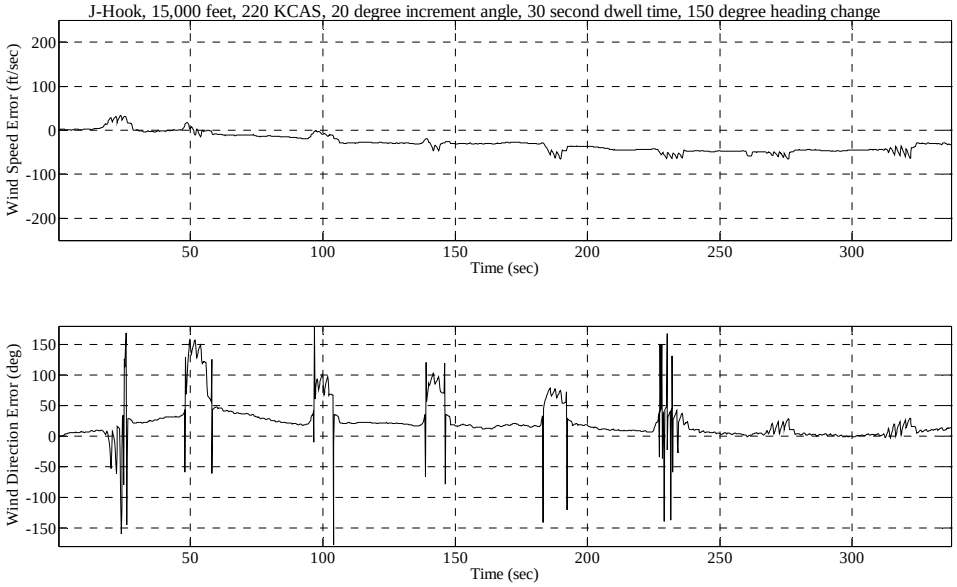

Test Point and Date: 015_13_Sep

WIND ERROR TIME HISTORY

J-Hook, 15,000 feet, 220 KCAS, 20 degree increment angle, 30 second dwell time, 150 degree heading change

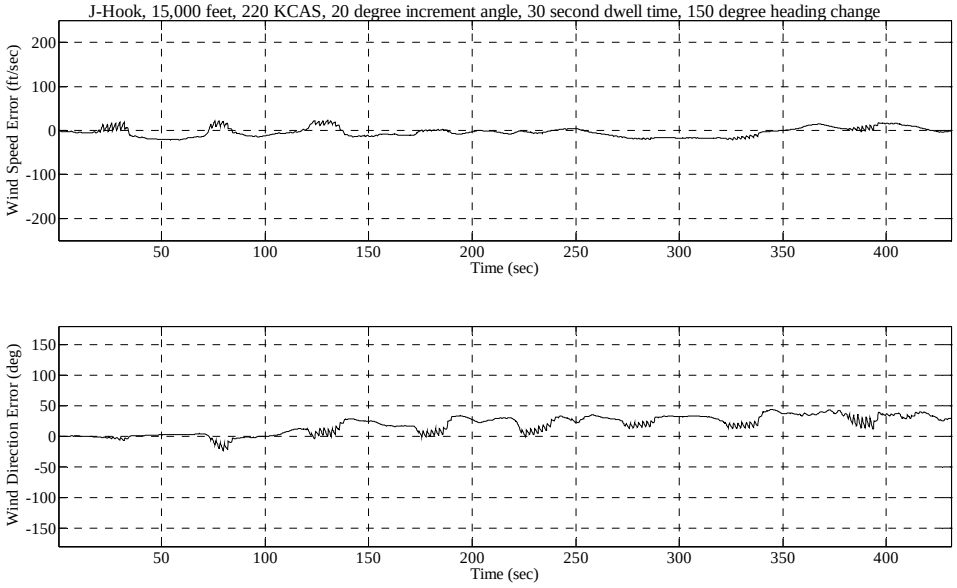

Test Point and Date: 016_19_Sep

WIND ERROR TIME HISTORY

J-Hook, 15,000 feet, 280 KCAS, 20 degree increment angle, 30 second dwell time, 60 degree heading change

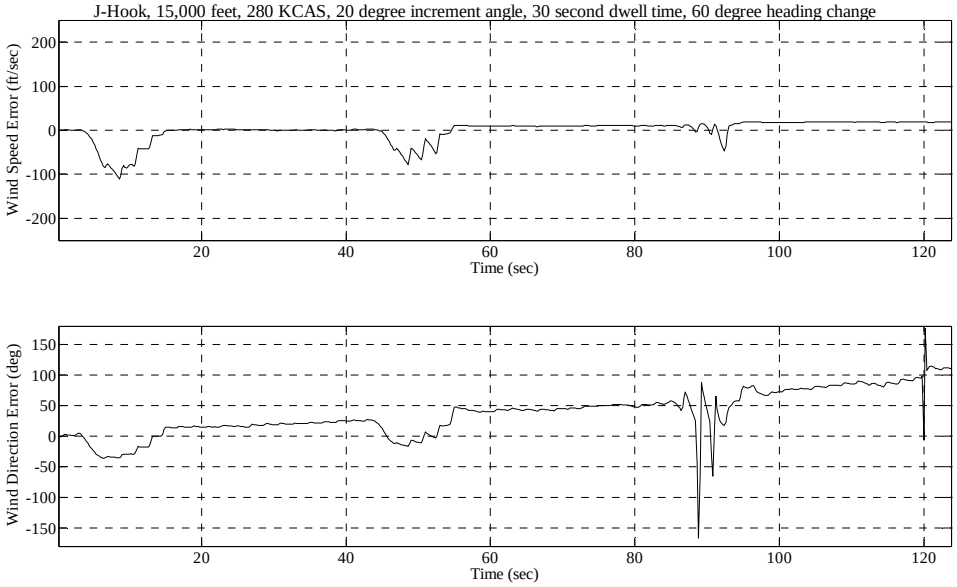

Test Point and Date: 017_18_Sep

WIND ERROR TIME HISTORY

J-Hook, 15,000 feet, 280 KCAS, 20 degree increment angle, 30 second dwell time, 60 degree heading change

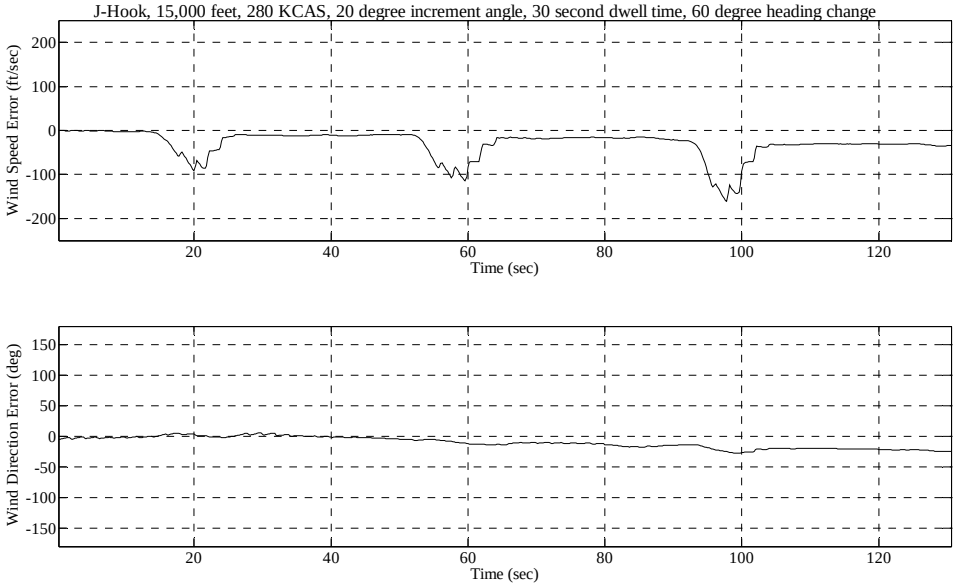

Test Point and Date: 018_13_Sep

WIND ERROR TIME HISTORY

J-Hook, 15,000 feet, 280 KCAS, 20 degree increment angle, 30 second dwell time, 60 degree heading change

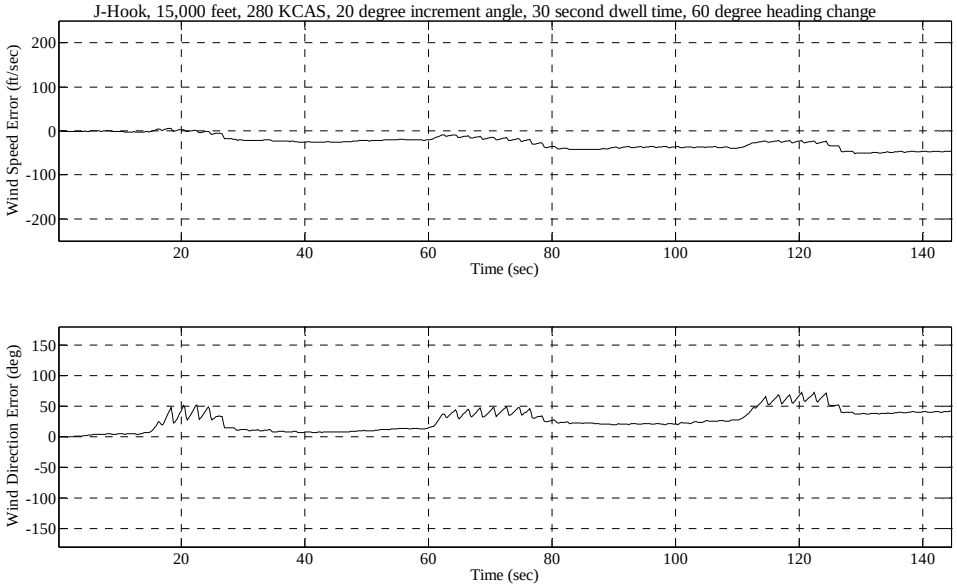

Test Point and Date: 019_17_Sep

WIND ERROR TIME HISTORY

J-Hook, 15,000 feet, 280 KCAS, 20 degree increment angle, 30 second dwell time, 60 degree heading change

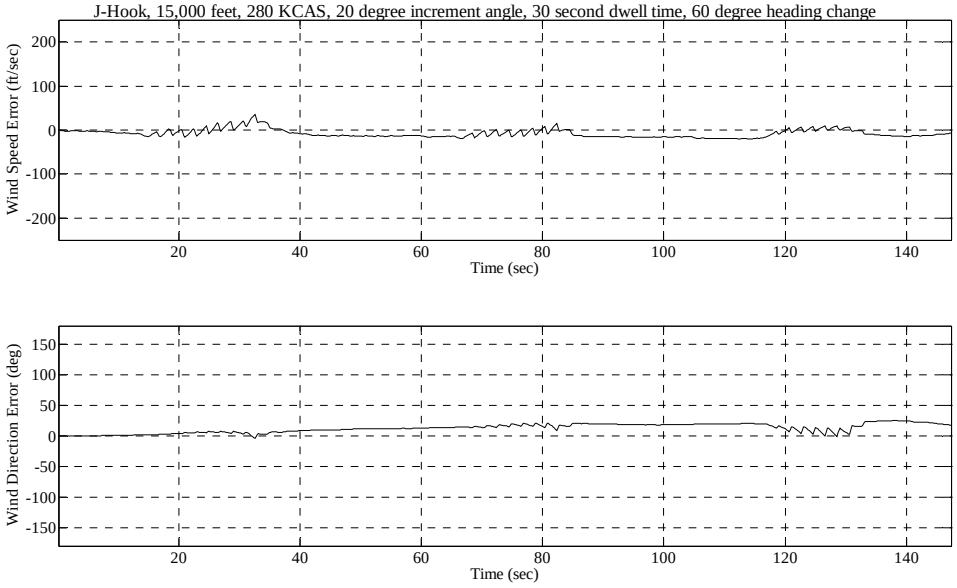

Test Point and Date: 020_17_Sep

WIND ERROR TIME HISTORY

J-Hook, 15,000 feet, 220 KCAS, 50 degree increment angle, 10 second dwell time, 150 degree heading change

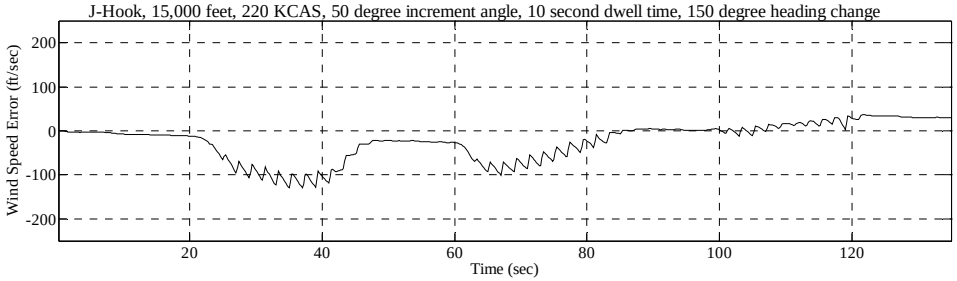

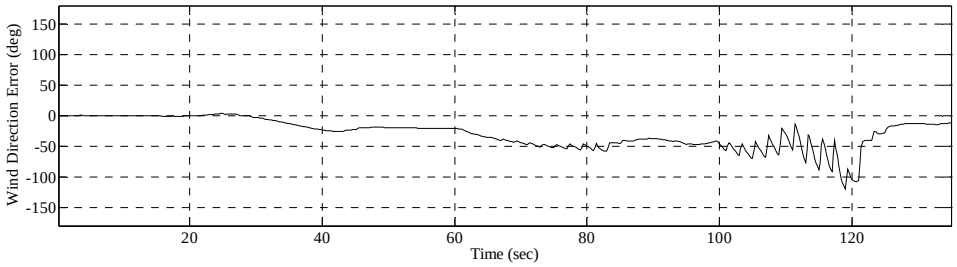

Test Point and Date: 021_13_Sep

WIND ERROR TIME HISTORY

J-Hook, 15,000 feet, 220 KCAS, 50 degree increment angle, 10 second dwell time, 150 degree heading change

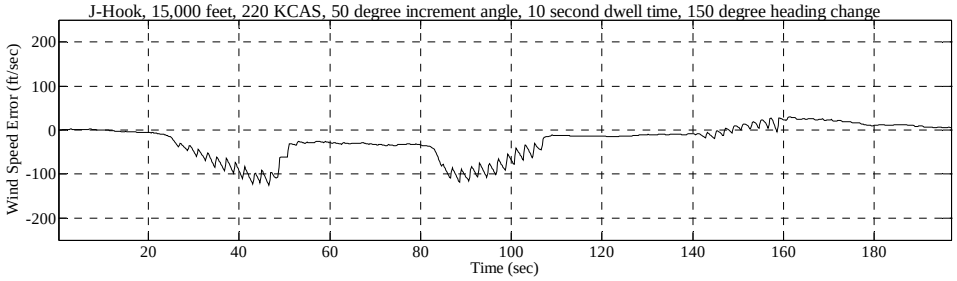

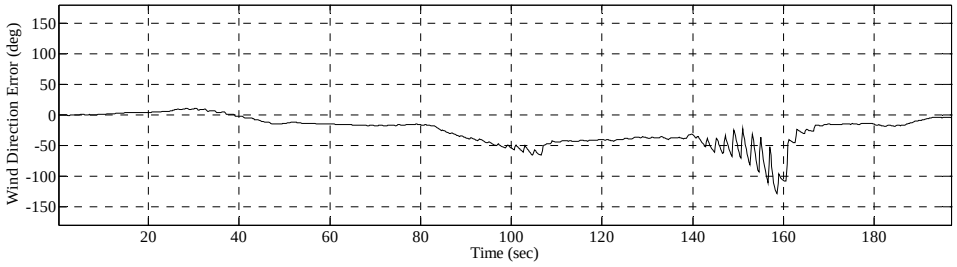

Test Point and Date: 022_13_Sep

WIND ERROR TIME HISTORY

J-Hook, 15,000 feet, 220 KCAS, 50 degree increment angle, 10 second dwell time, 150 degree heading change

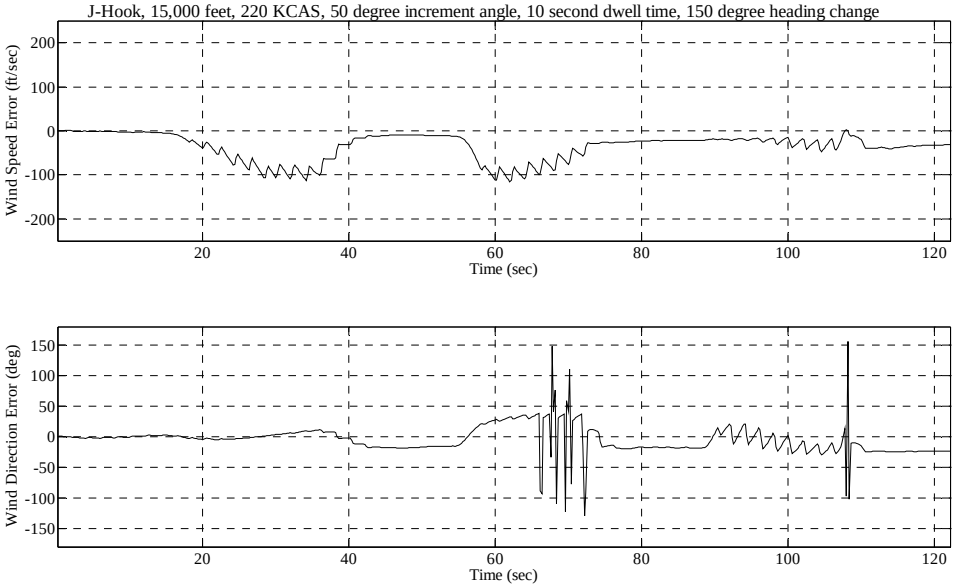

Test Point and Date: 023_13_Sep

WIND ERROR TIME HISTORY

J-Hook, 15,000 feet, 220 KCAS, 50 degree increment angle, 10 second dwell time, 150 degree heading change

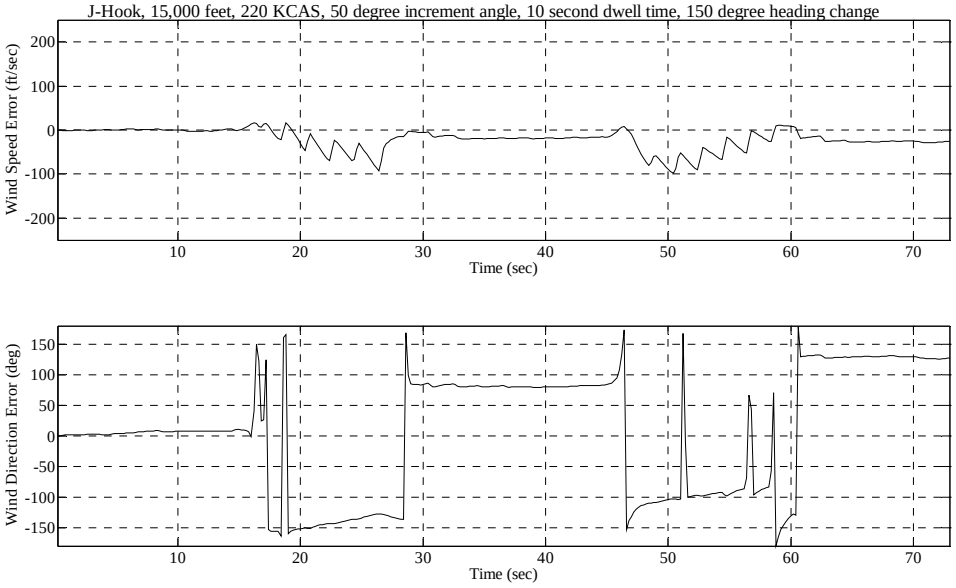

Test Point and Date: 024_18_Sep

WIND ERROR TIME HISTORY

J-Hook, 15,000 feet, 280 KCAS, 50 degree increment angle, 10 second dwell time, 60 degree heading change

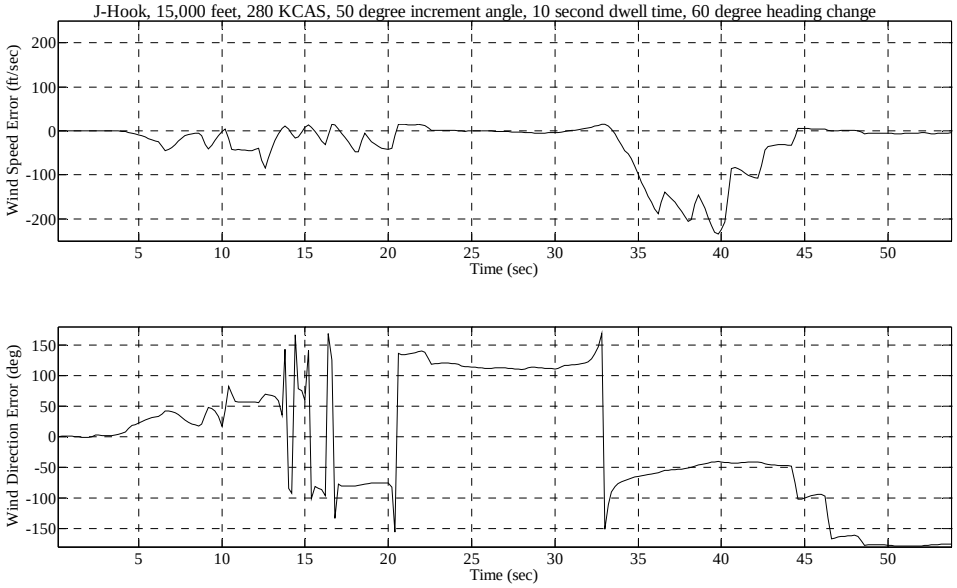

Test Point and Date: 025_18_Sep

WIND ERROR TIME HISTORY

J-Hook, 15,000 feet, 280 KCAS, 50 degree increment angle, 10 second dwell time, 60 degree heading change

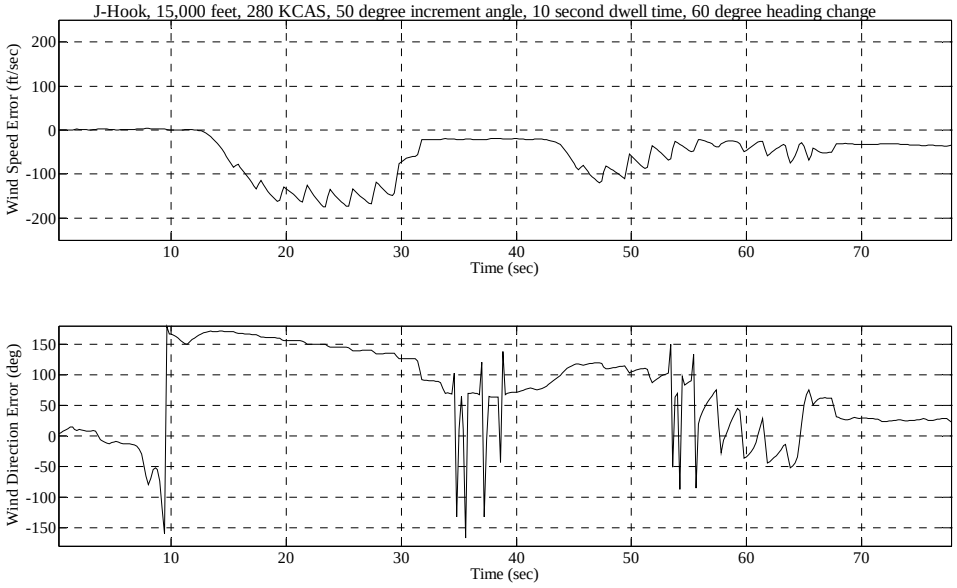

Test Point and Date: 026_17_Sep

WIND ERROR TIME HISTORY

J-Hook, 15,000 feet, 280 KCAS, 50 degree increment angle, 10 second dwell time, 60 degree heading change

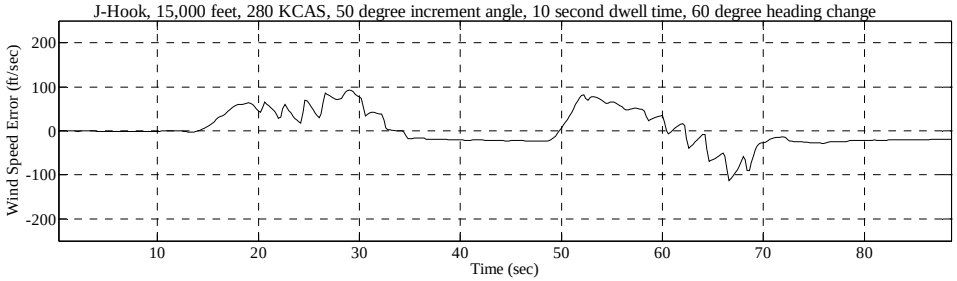

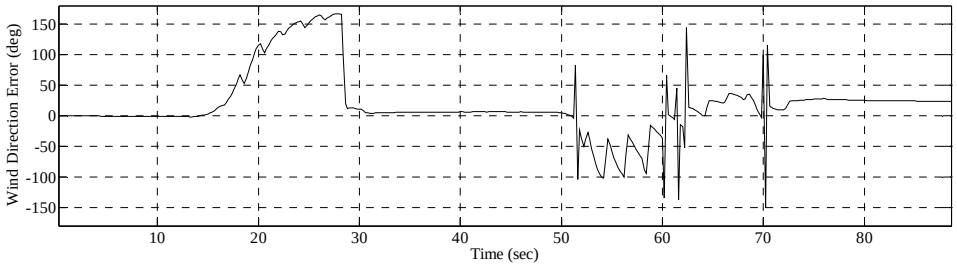

Test Point and Date: 026_21_Sep

WIND ERROR TIME HISTORY

J-Hook, 15,000 feet, 280 KCAS, 50 degree increment angle, 10 second dwell time, 60 degree heading change

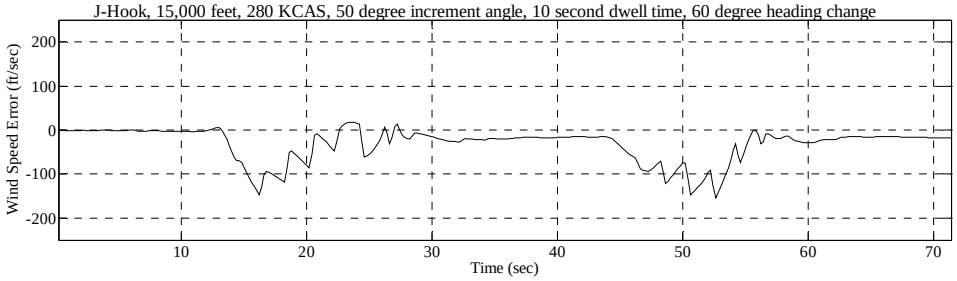

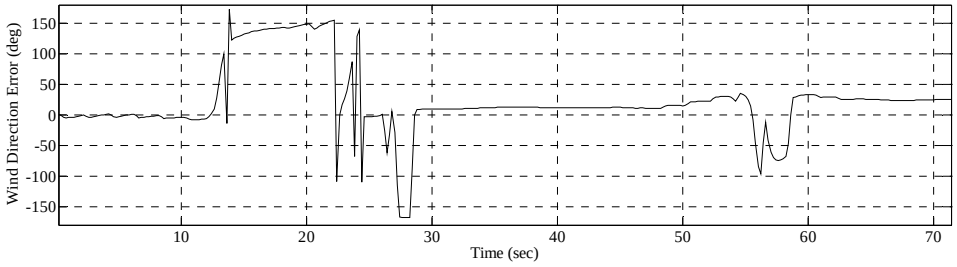

Test Point and Date: 027_18_Sep

WIND ERROR TIME HISTORY

J-Hook, 15,000 feet, 280 KCAS, 50 degree increment angle, 10 second dwell time, 60 degree heading change

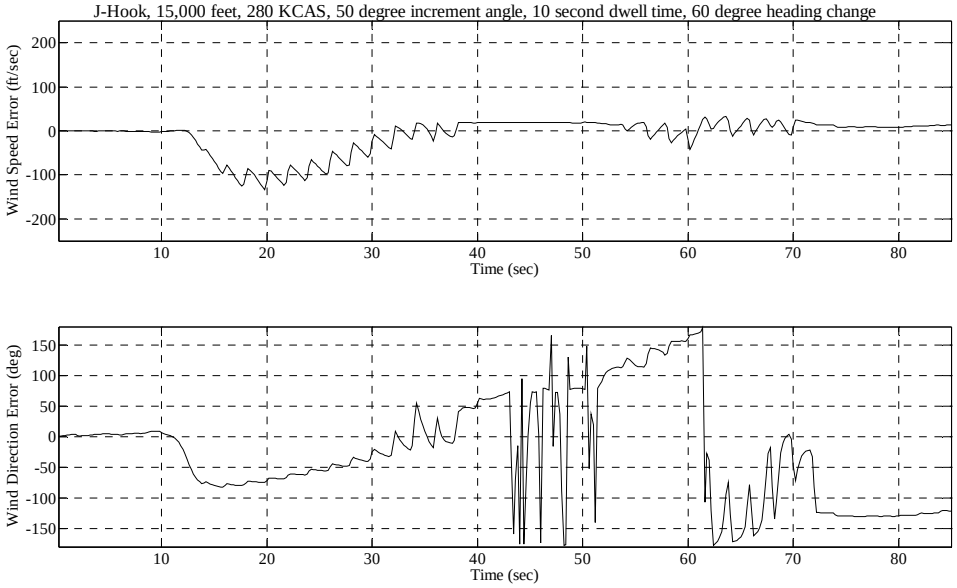

Test Point and Date: 028_17_Sep

WIND ERROR TIME HISTORY

J-Hook, 15,000 feet, 220 KCAS, 50 degree increment angle, 30 second dwell time, 60 degree heading change

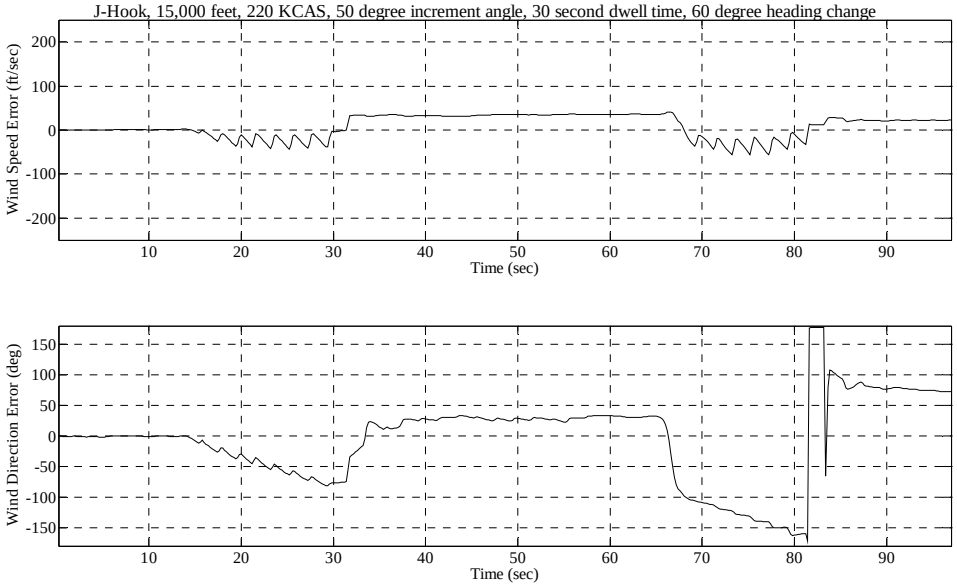

Test Point and Date: 029_17_Sep

WIND ERROR TIME HISTORY

J-Hook, 15,000 feet, 220 KCAS, 50 degree increment angle, 30 second dwell time, 60 degree heading change

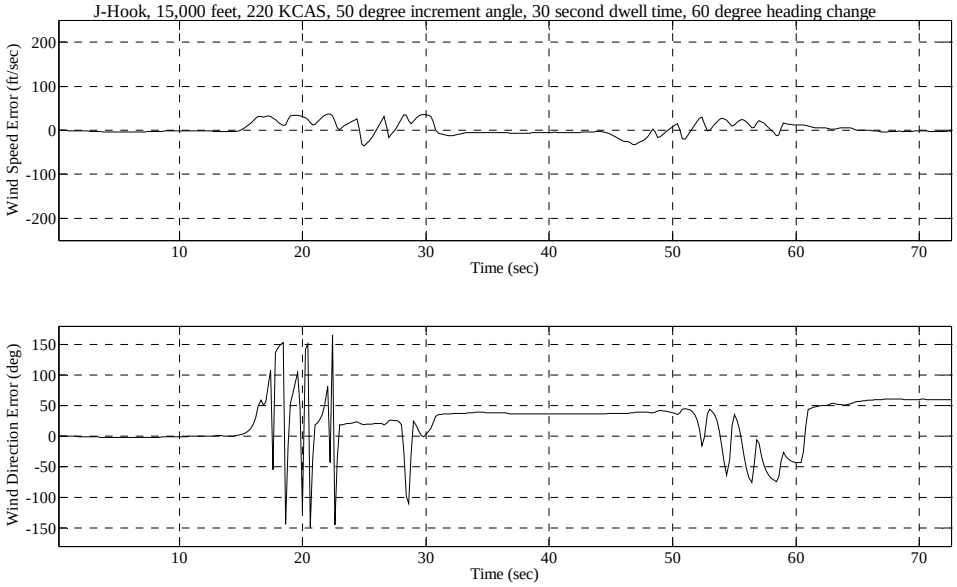

Test Point and Date: 030_18_Sep

WIND ERROR TIME HISTORY

J-Hook, 15,000 feet, 220 KCAS, 50 degree increment angle, 30 second dwell time, 60 degree heading change

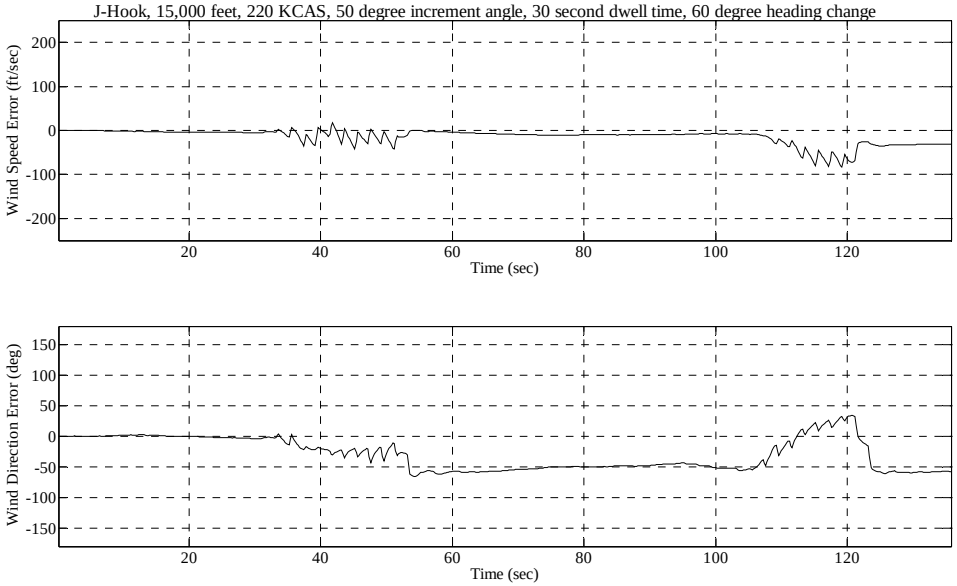

Test Point and Date: 031_17_Sep

WIND ERROR TIME HISTORY

J-Hook, 15,000 feet, 220 KCAS, 50 degree increment angle, 30 second dwell time, 60 degree heading change

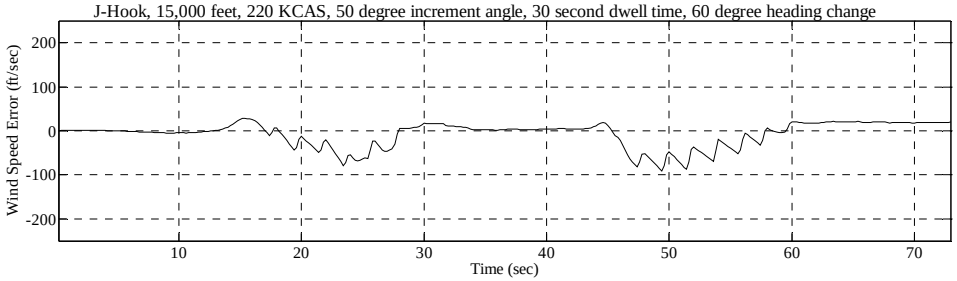

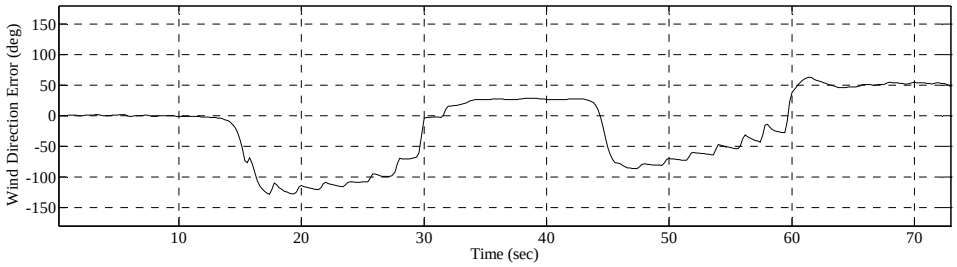

Test Point and Date: 032_18_Sep

WIND ERROR TIME HISTORY

J-Hook, 15,000 feet, 280 KCAS, 50 degree increment angle, 30 second dwell time, 150 degree heading change

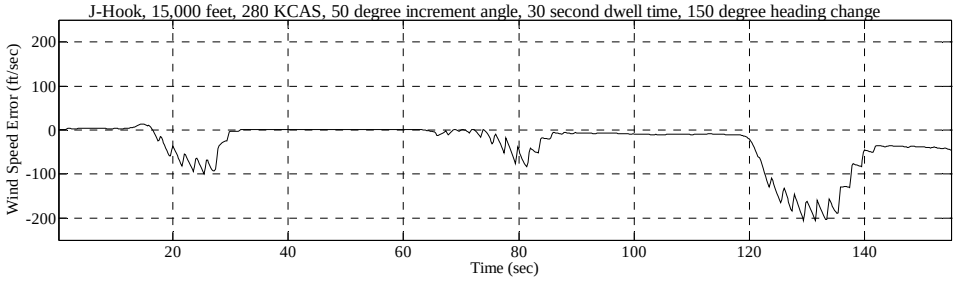

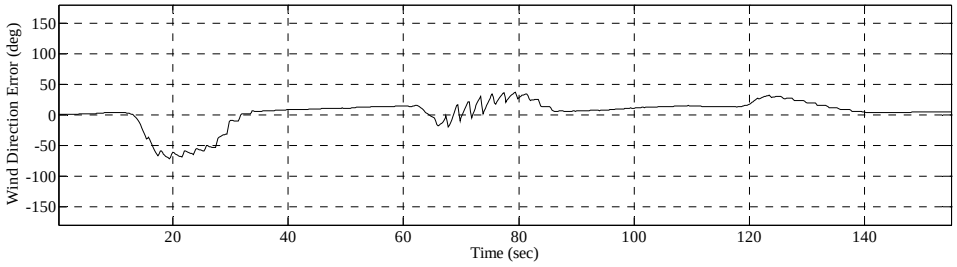

Test Point and Date: 033_17_Sep

WIND ERROR TIME HISTORY

J-Hook, 15,000 feet, 280 KCAS, 50 degree increment angle, 30 second dwell time, 150 degree heading change

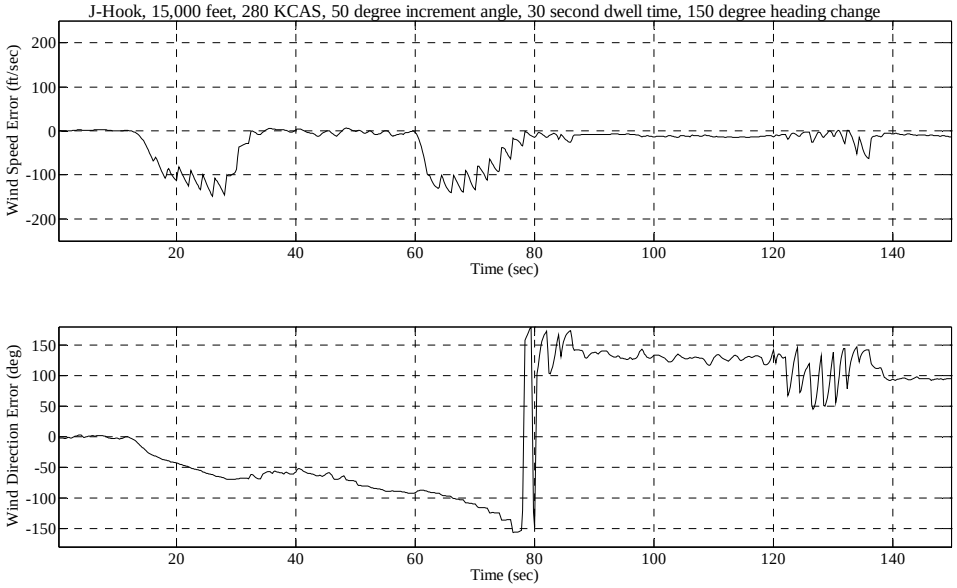

Test Point and Date: 034_17_Sep

WIND ERROR TIME HISTORY

J-Hook, 15,000 feet, 280 KCAS, 50 degree increment angle, 30 second dwell time, 150 degree heading change

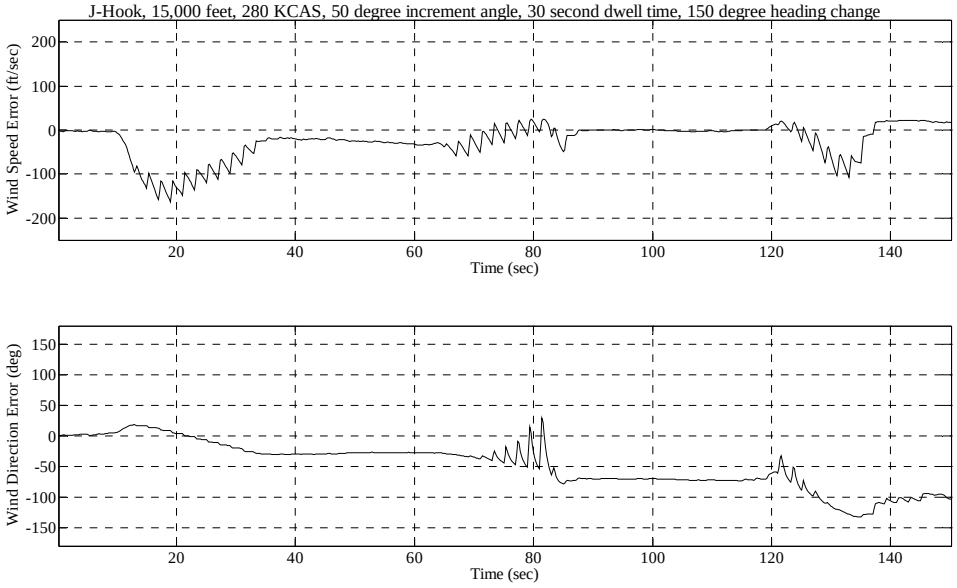

Test Point and Date: 035_17_Sep

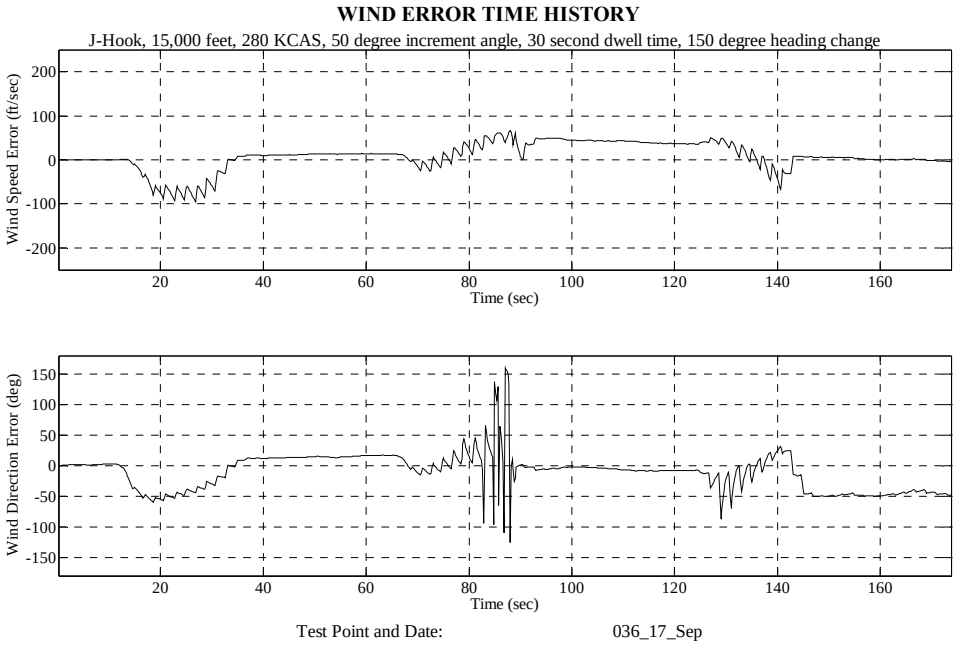

G.3. Sliceback Flight Test Technique

G.3.1. Sliceback Positon

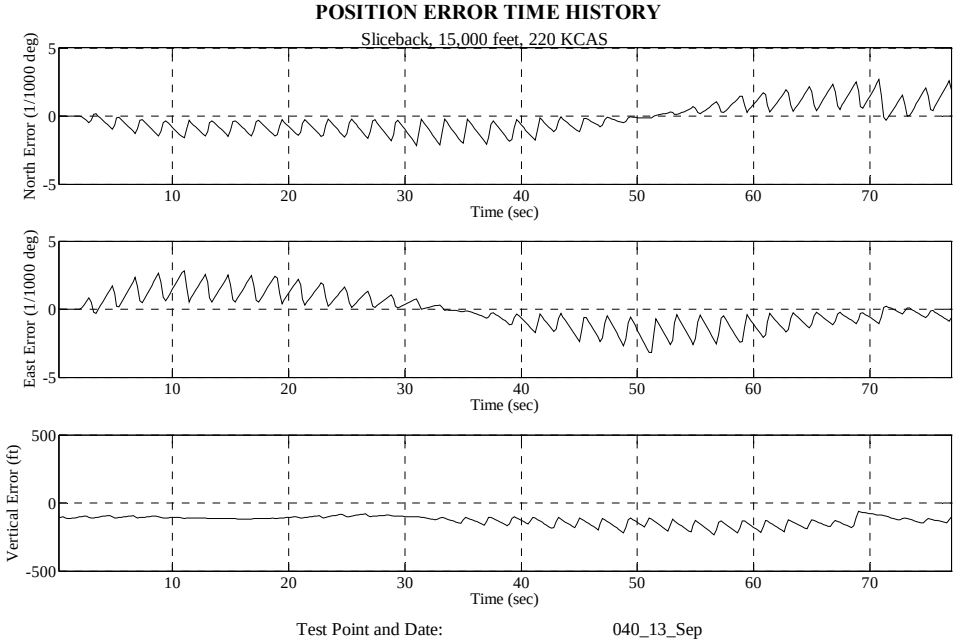

POSITION ERROR TIME HISTORY

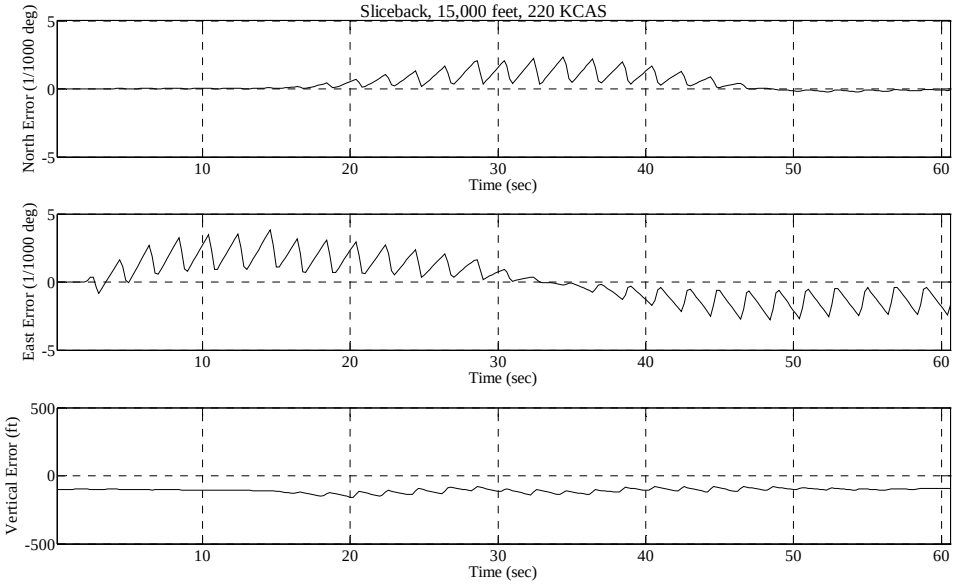

Test Point and Date: 041_17_Sep

POSITION ERROR TIME HISTORY

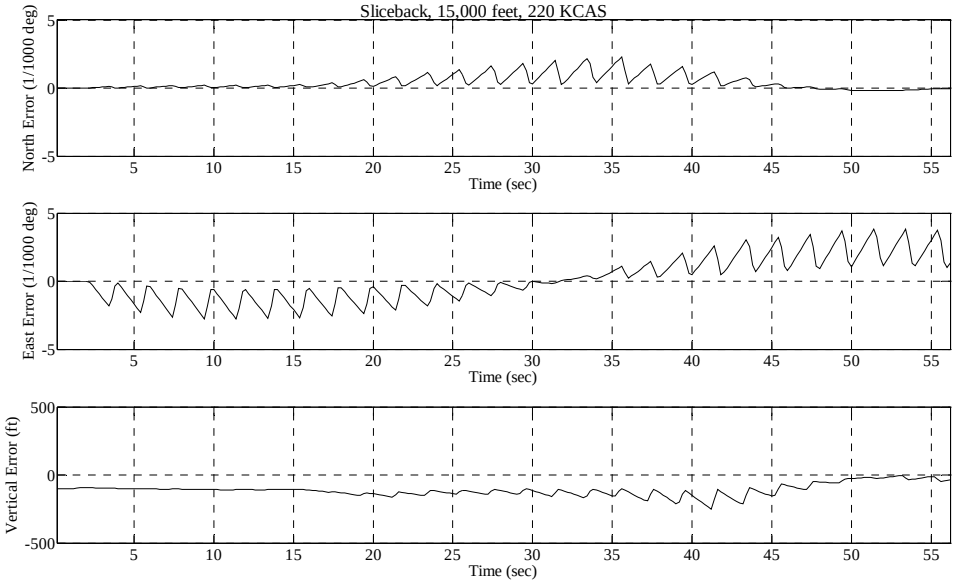

Test Point and Date: 042_17_Sep

POSITION ERROR TIME HISTORY

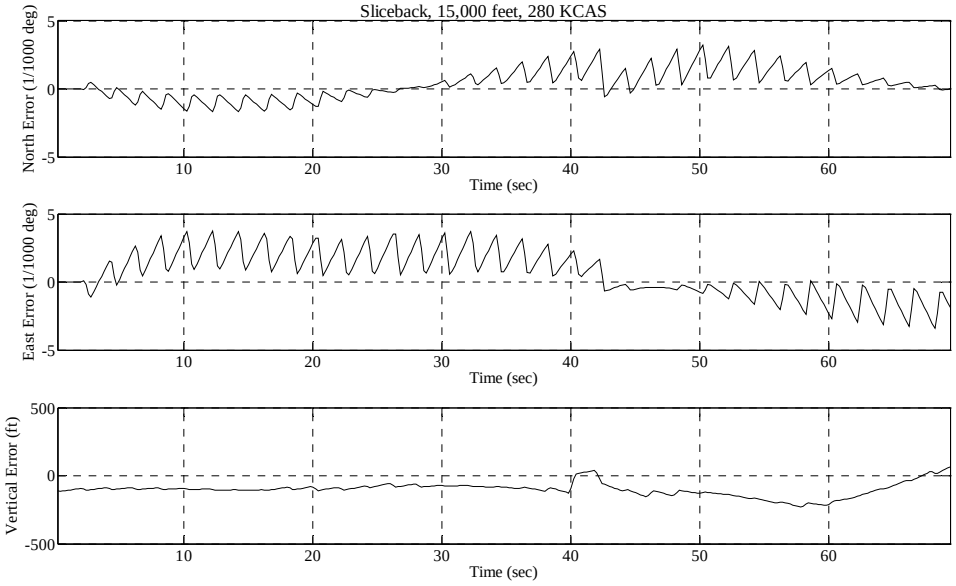

Test Point and Date: 043_13_Sep

POSITION ERROR TIME HISTORY

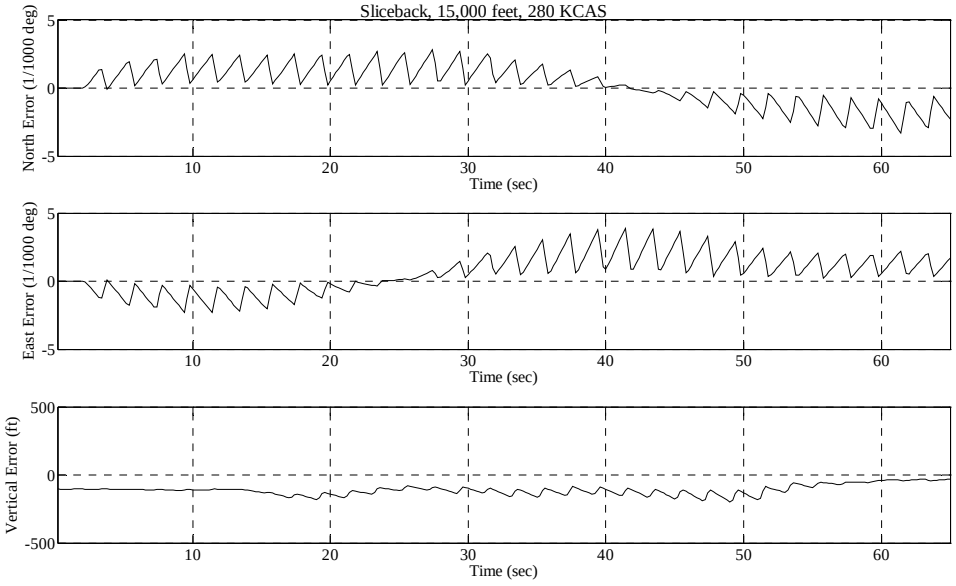

Test Point and Date: 044_17_Sep

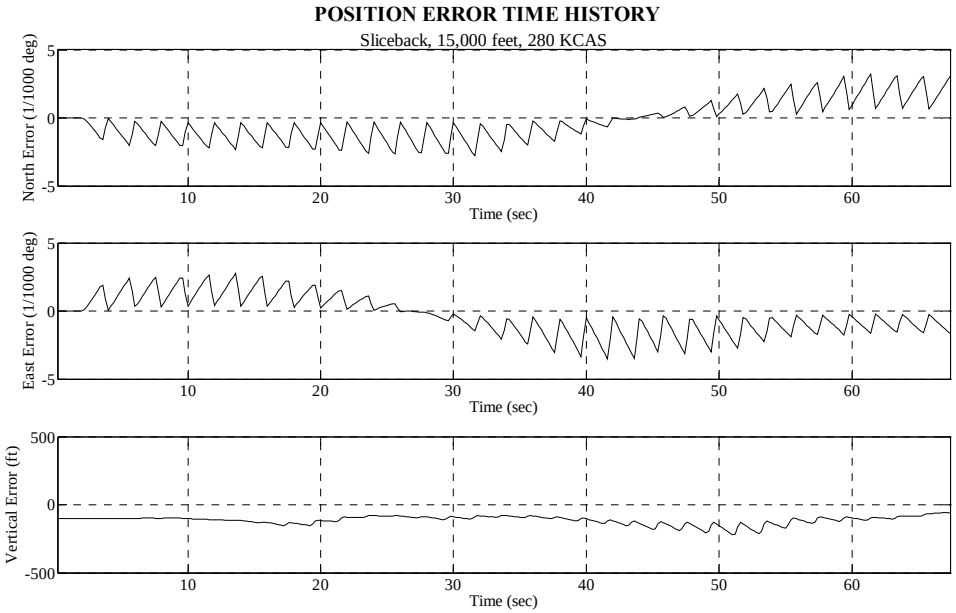

G.3.2. Sliceback Velocity

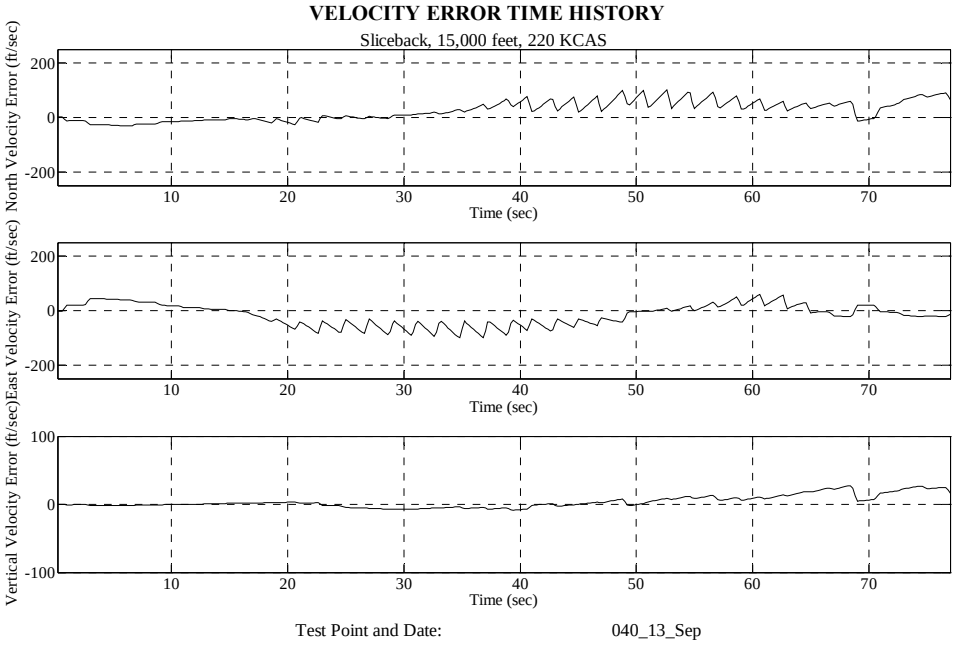

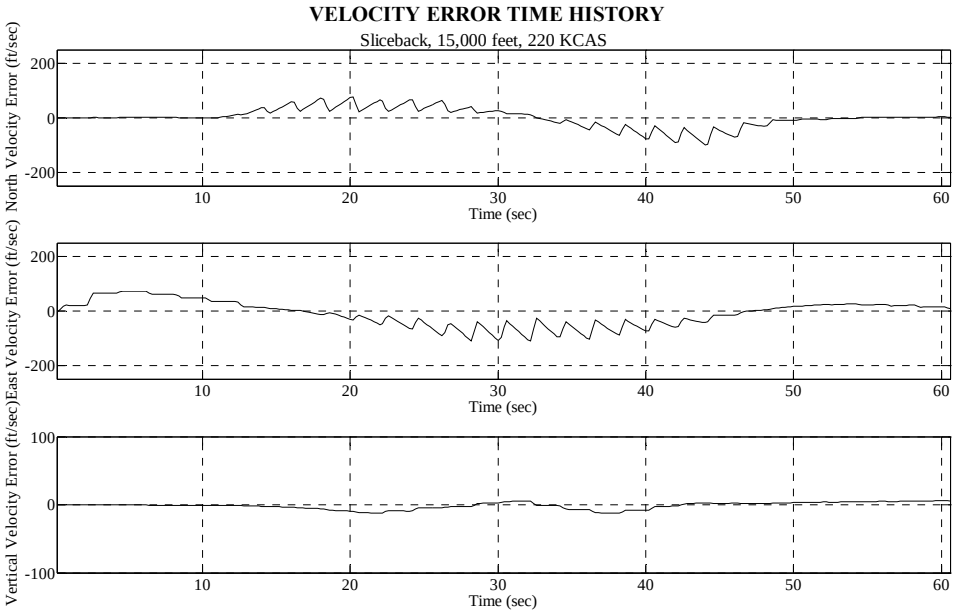

Test Point and Date: 041_17_Sep

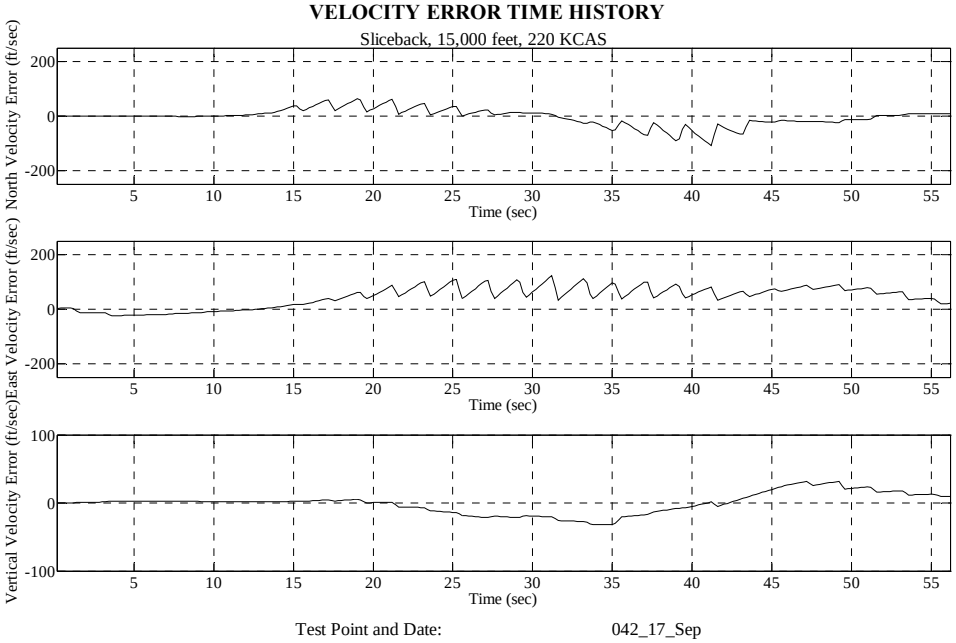

Test Point and Date: 042_17_Sep

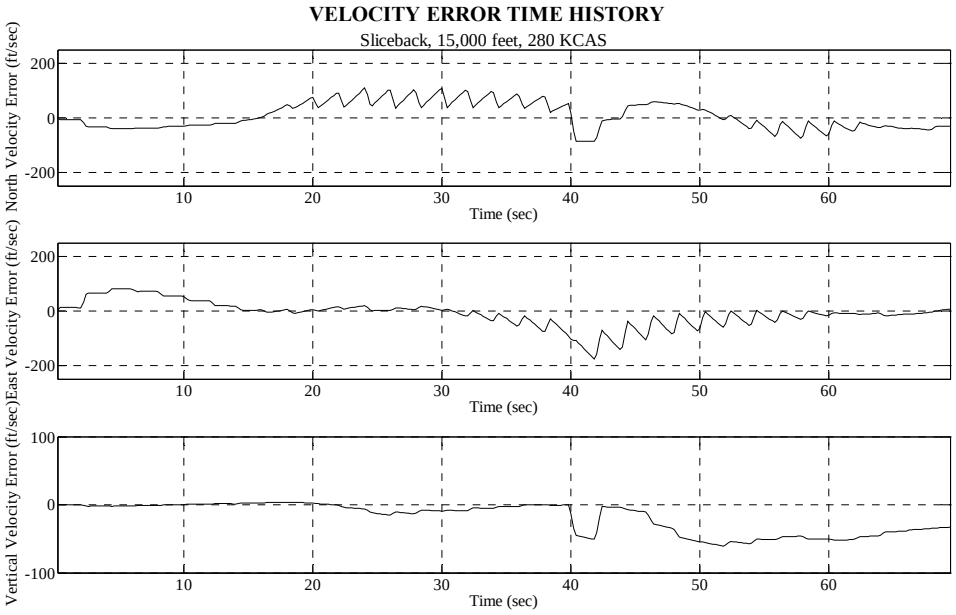

Test Point and Date: 043_13_Sep

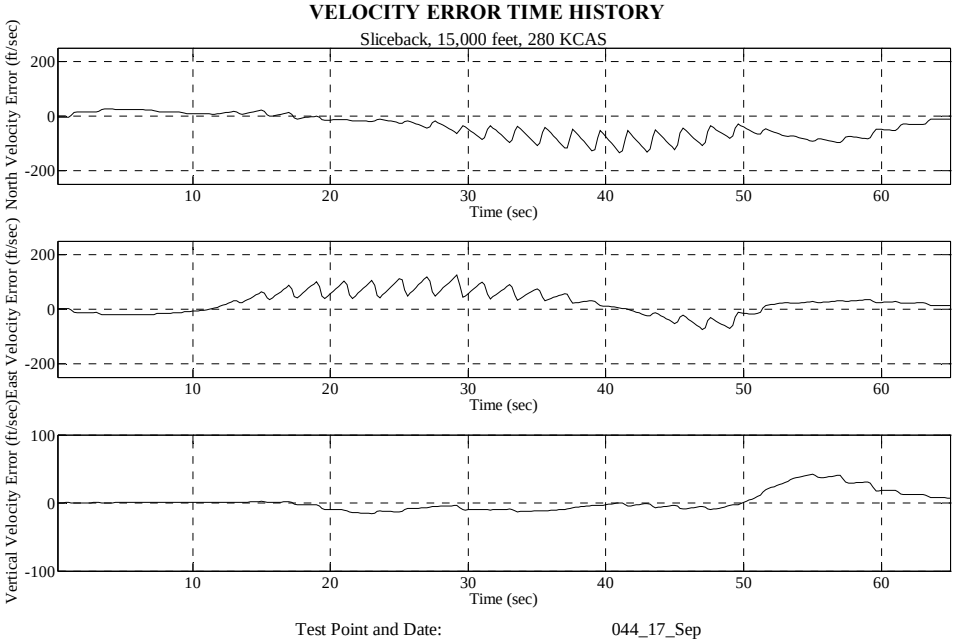

Test Point and Date: 044_17_Sep

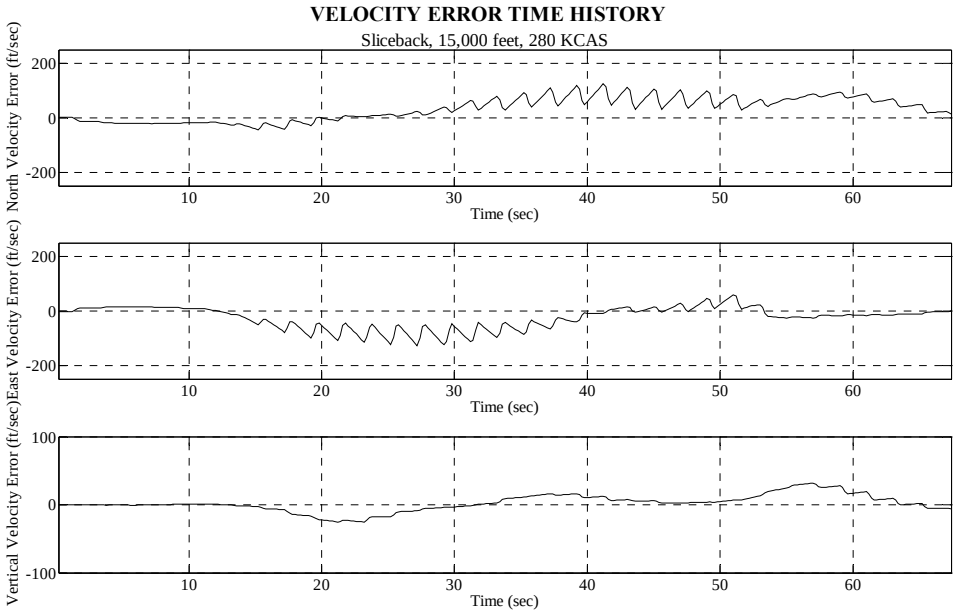

G.3.3. Sliceback Wind

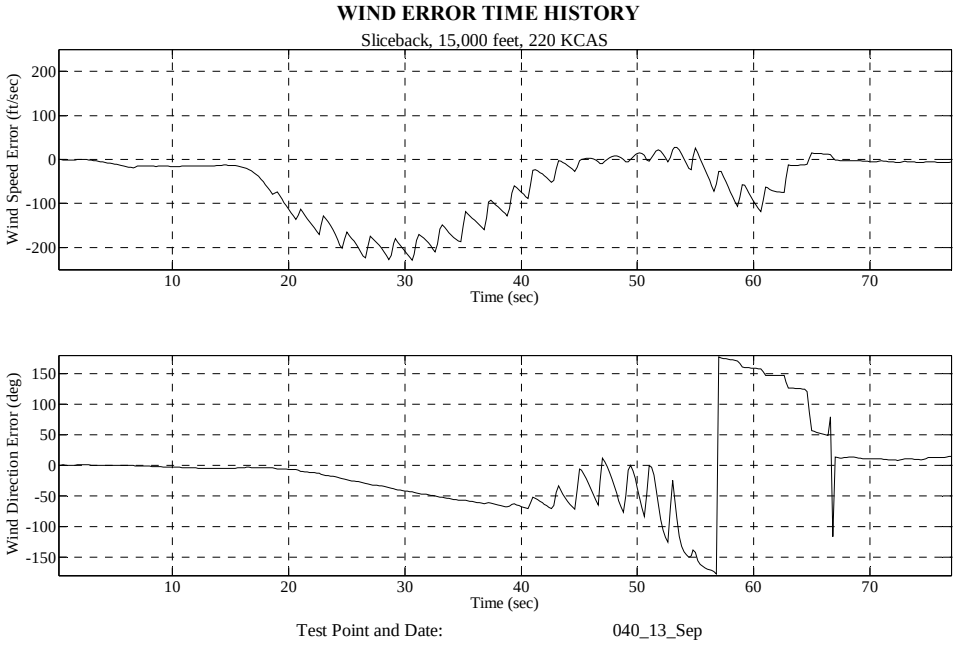

WIND ERROR TIME HISTORY

Sliceback, 15,000 feet, 220 KCAS

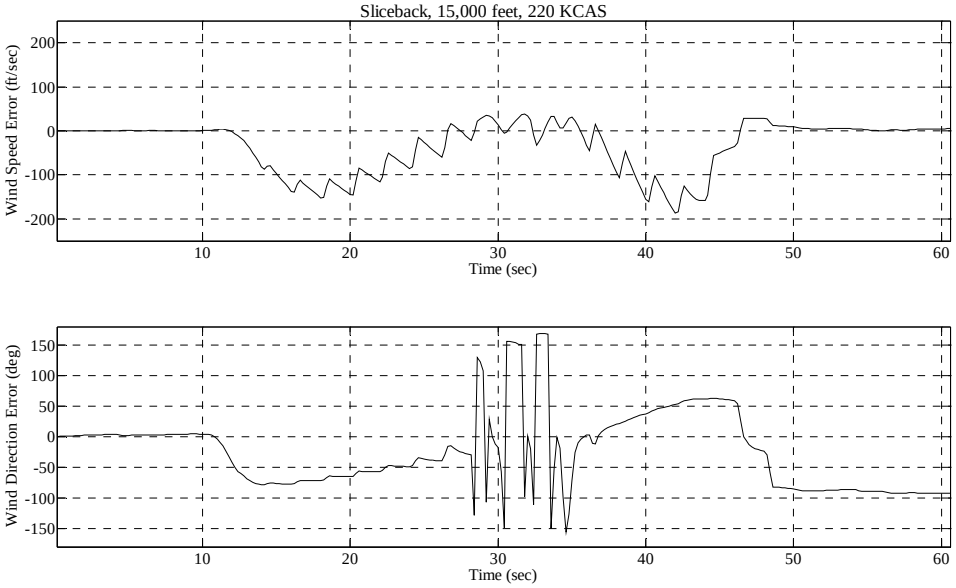

Test Point and Date: 041_17_Sep

WIND ERROR TIME HISTORY

Sliceback, 15,000 feet, 220 KCAS

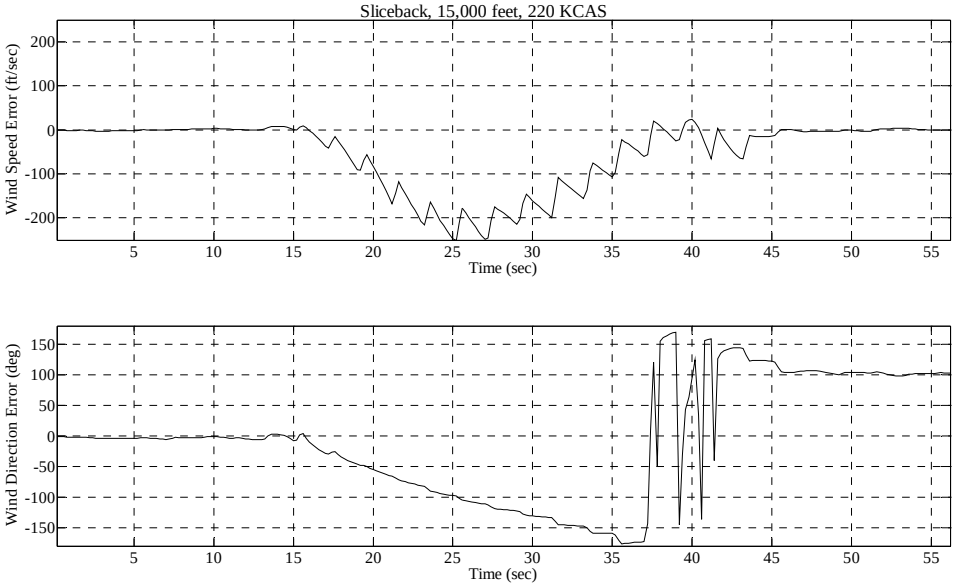

Test Point and Date: 042_17_Sep

WIND ERROR TIME HISTORY

Sliceback, 15,000 feet, 280 KCAS

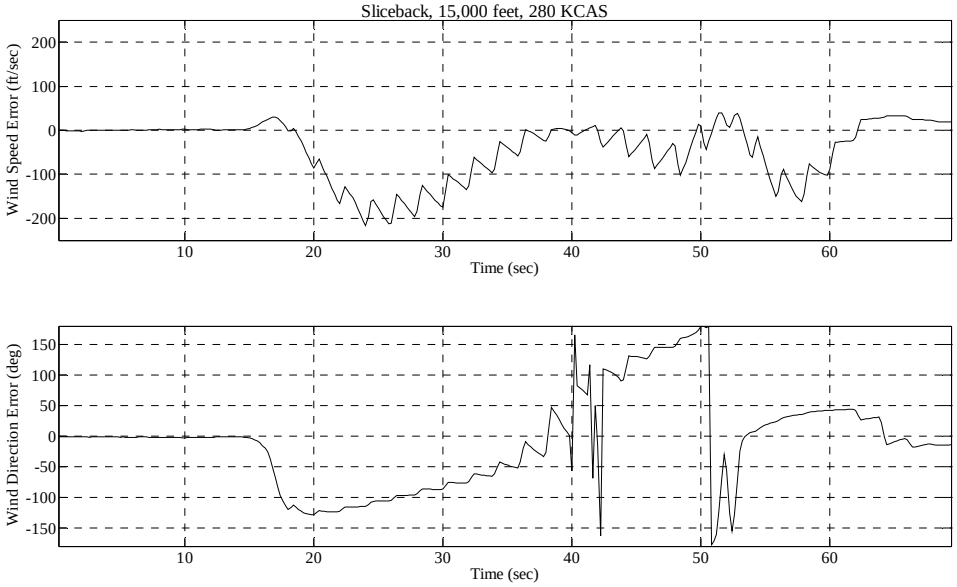

Test Point and Date: 043_13_Sep

WIND ERROR TIME HISTORY

Sliceback, 15,000 feet, 280 KCAS

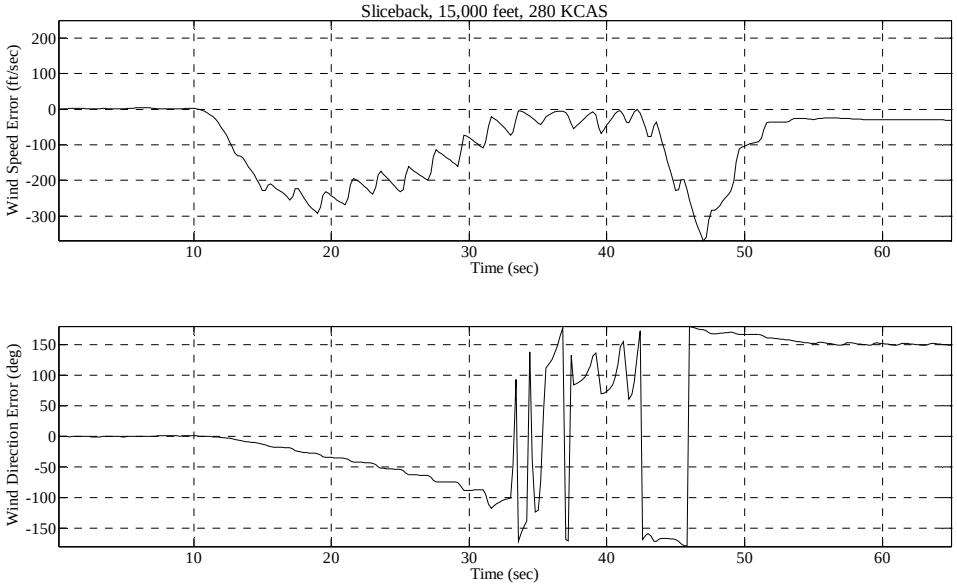

Test Point and Date: 044_17_Sep

WIND ERROR TIME HISTORY

Sliceback, 15,000 feet, 280 KCAS

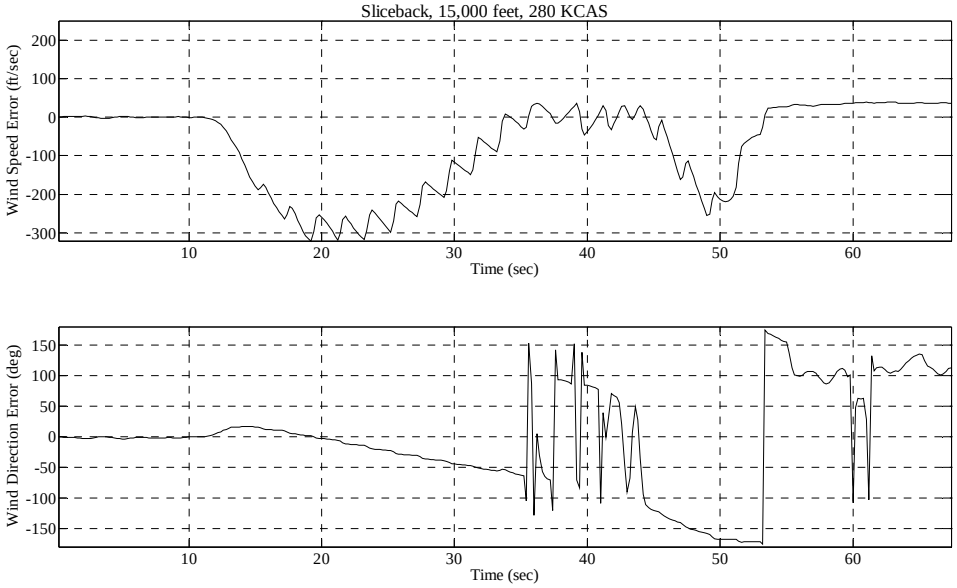

Test Point and Date: 045_17_Sep

G.4. Operational Maneuvers

G.4.1. Operational Maneuvers Positon

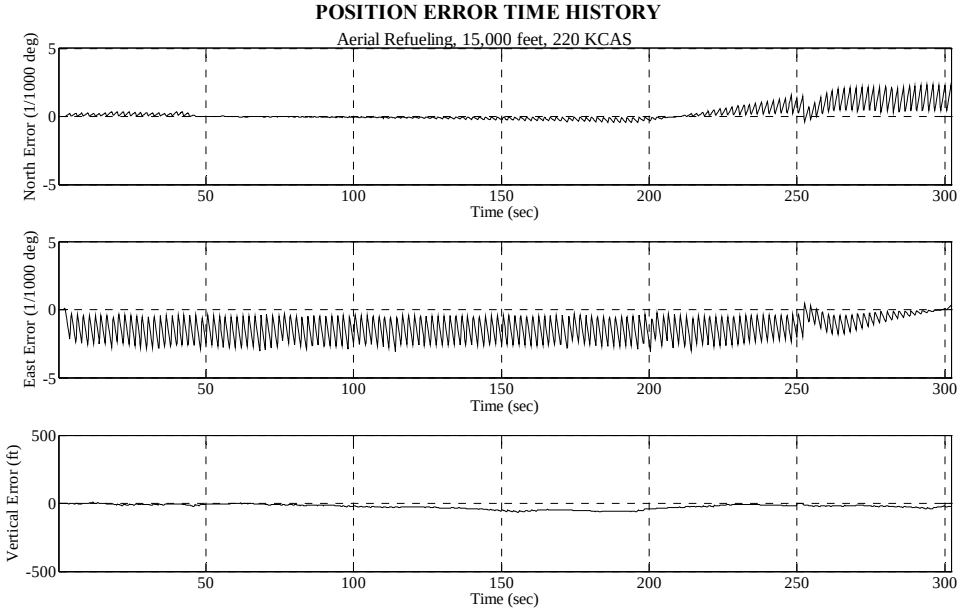

Test Point and Date: 046_18_Sep

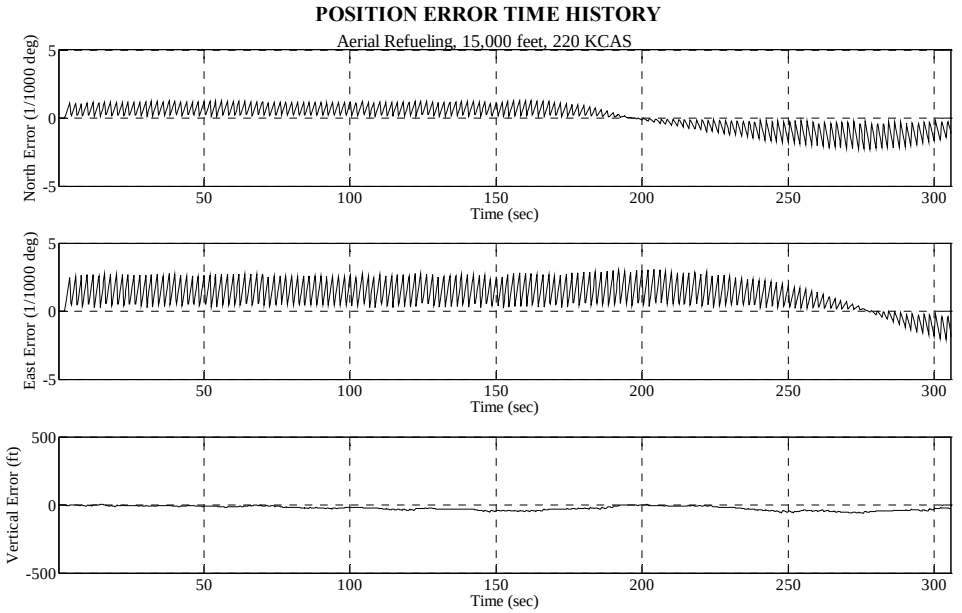

Test Point and Date: 047_18_Sep

POSITION ERROR TIME HISTORY

Aerial Refueling, 15,000 feet, 280 KCAS

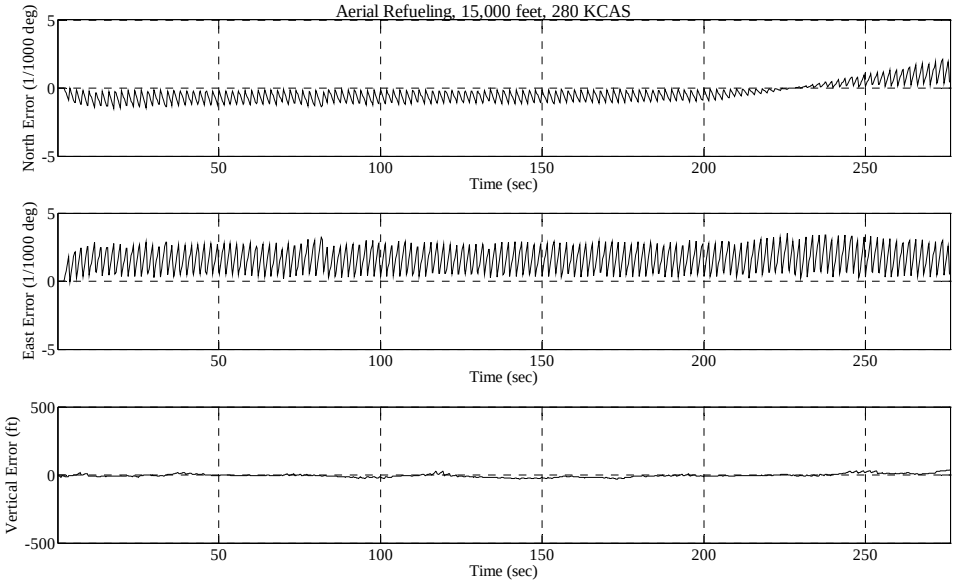

Test Point and Date: 048_21_Sep

POSITION ERROR TIME HISTORY

Aerial Refueling, 15,000 feet, 280 KCAS

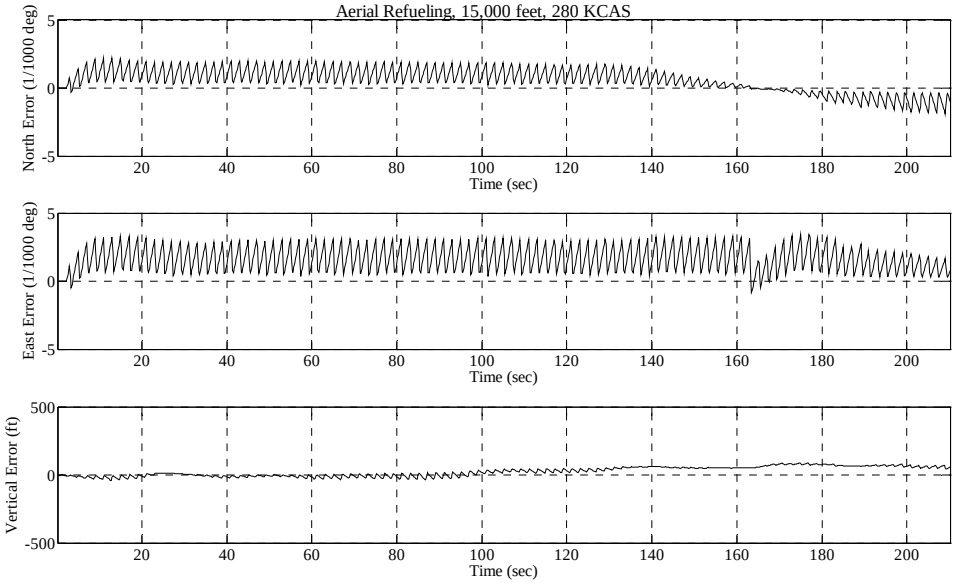

Test Point and Date: 049_21_Sep

POSITION ERROR TIME HISTORY

Air-to-Air Tracking, 15,000 feet, 220 KCAS

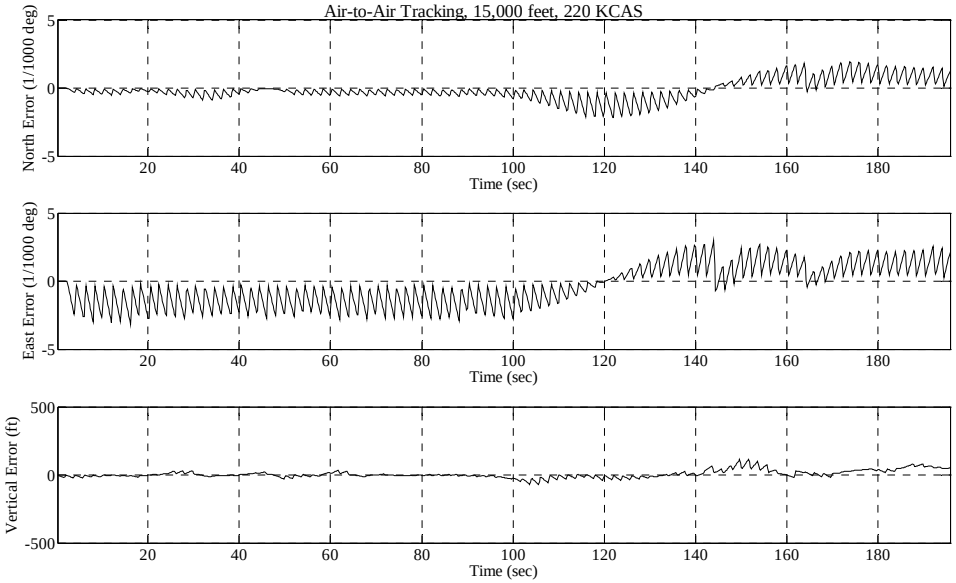

Test Point and Date: 058_18_Sep

POSITION ERROR TIME HISTORY

Air-to-Air Tracking, 15,000 feet, 220 KCAS

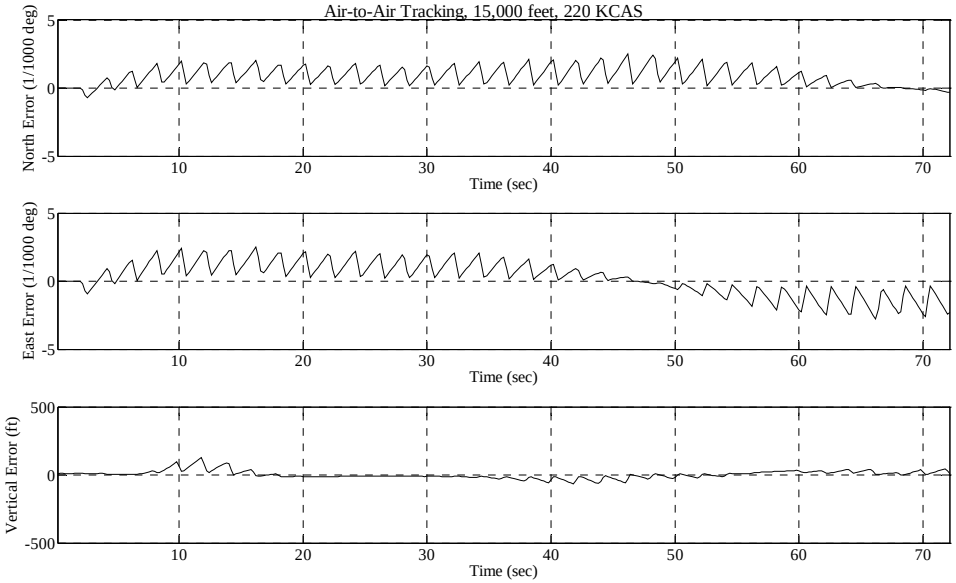

Test Point and Date: 059_18_Sep

POSITION ERROR TIME HISTORY

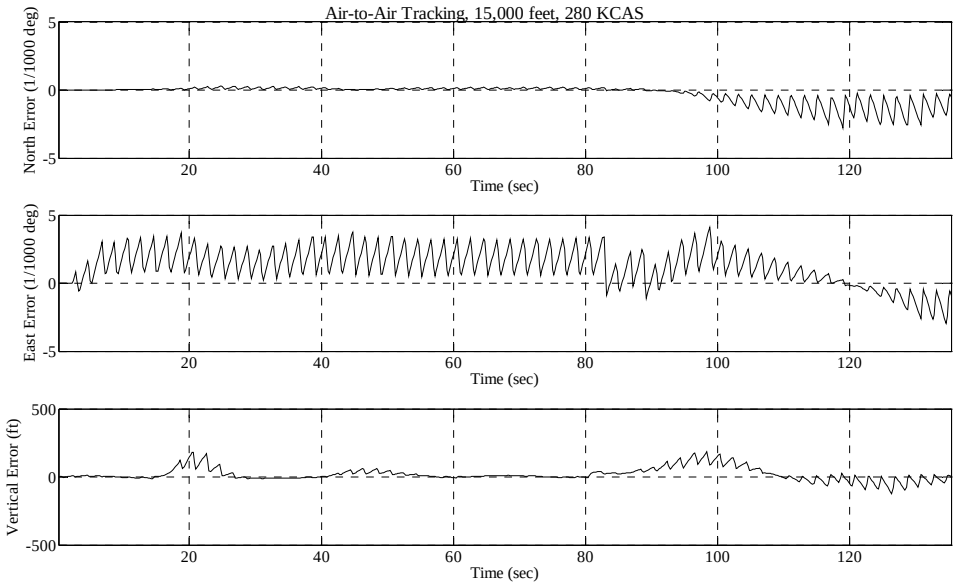

Test Point and Date: 060_21_Sep

POSITION ERROR TIME HISTORY

Air-to-Air Tracking, 15,000 feet, 280 KCAS

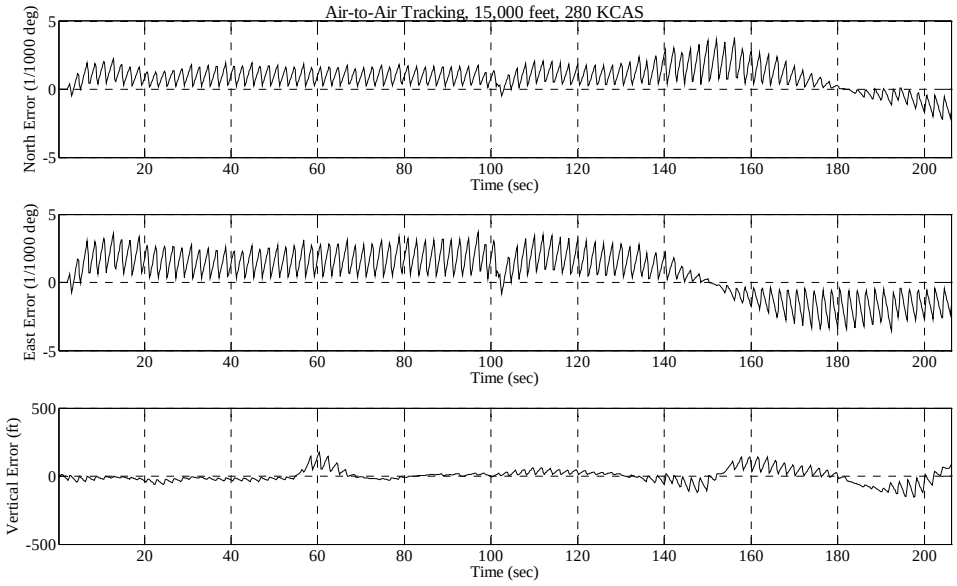

Test Point and Date: 061_21_Sep

POSITION ERROR TIME HISTORY

Ground Attack, 17-13,000 feet, 220 KCAS

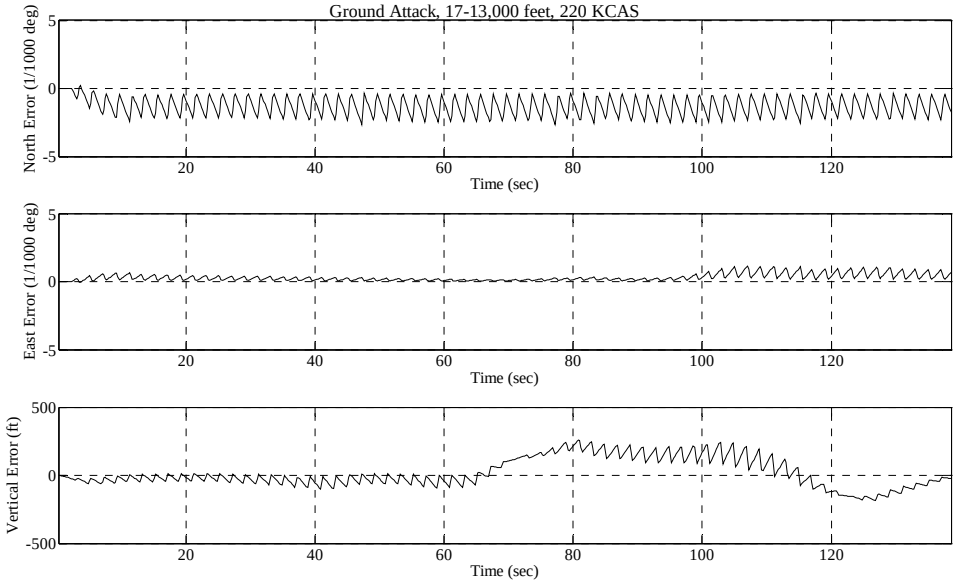

Test Point and Date: 070_19_Sep

POSITION ERROR TIME HISTORY

Ground Attack, 17-13,000 feet, 220 KCAS

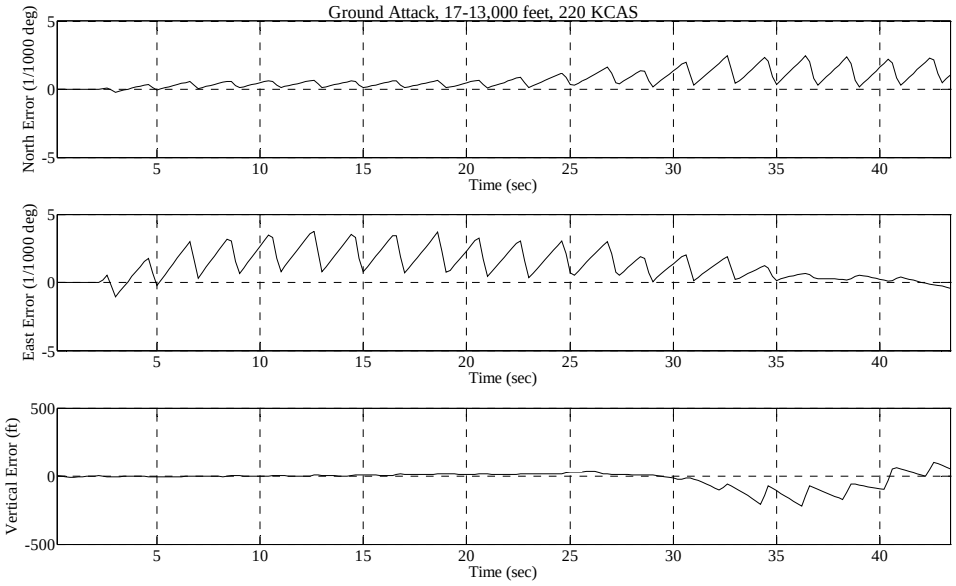

Test Point and Date: 071_19_Sep

POSITION ERROR TIME HISTORY

Ground Attack, 17-13,000 feet, 280 KCAS

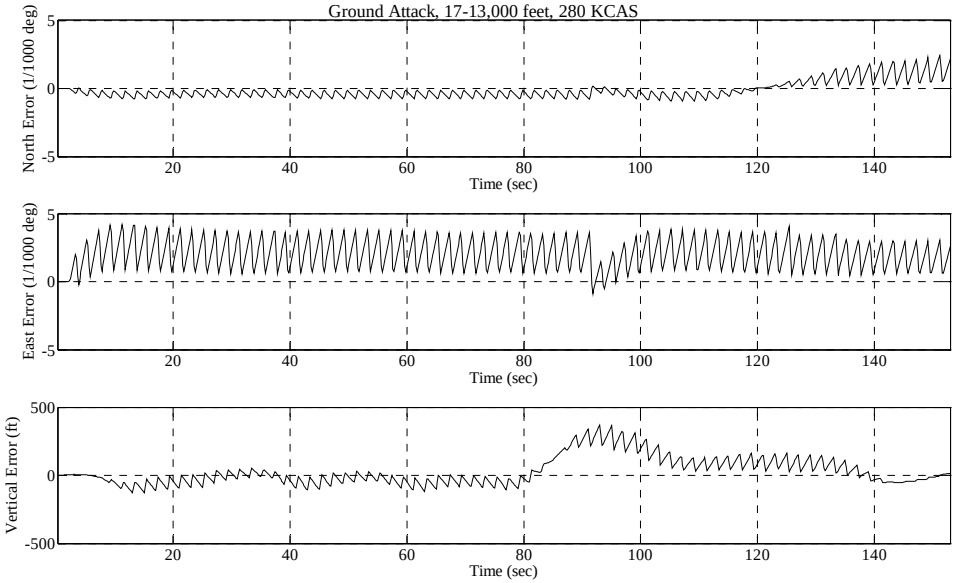

Test Point and Date: 072_19_Sep

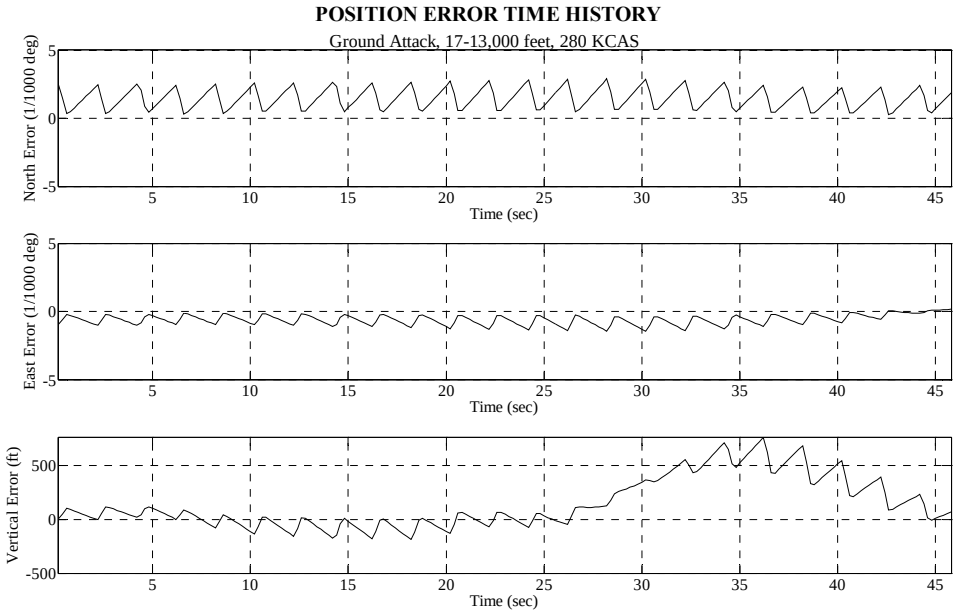

Test Point and Date: 073_19_Sep

G.4.2. Operational Maneuvers Velocity

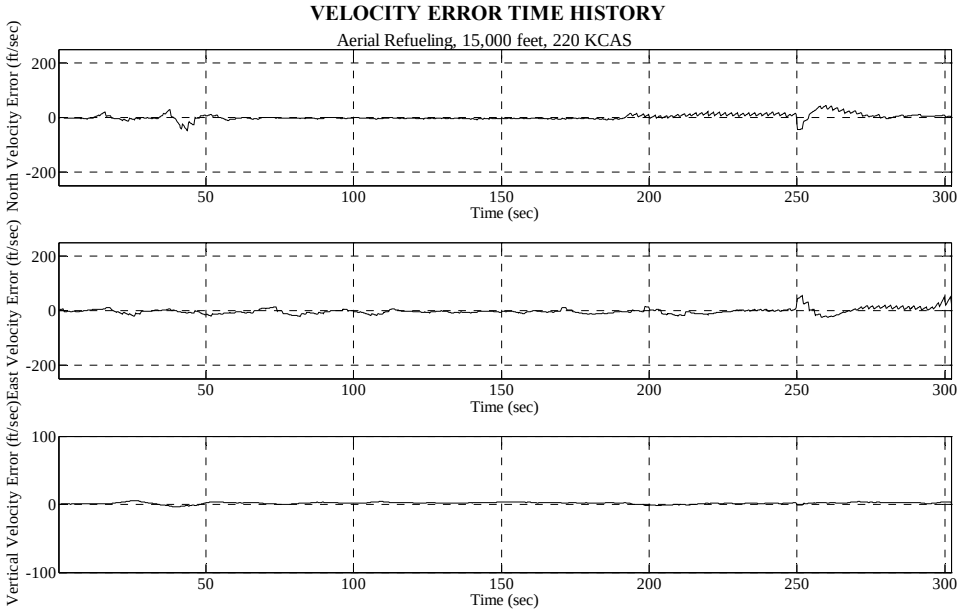

Test Point and Date: 046_18_Sep

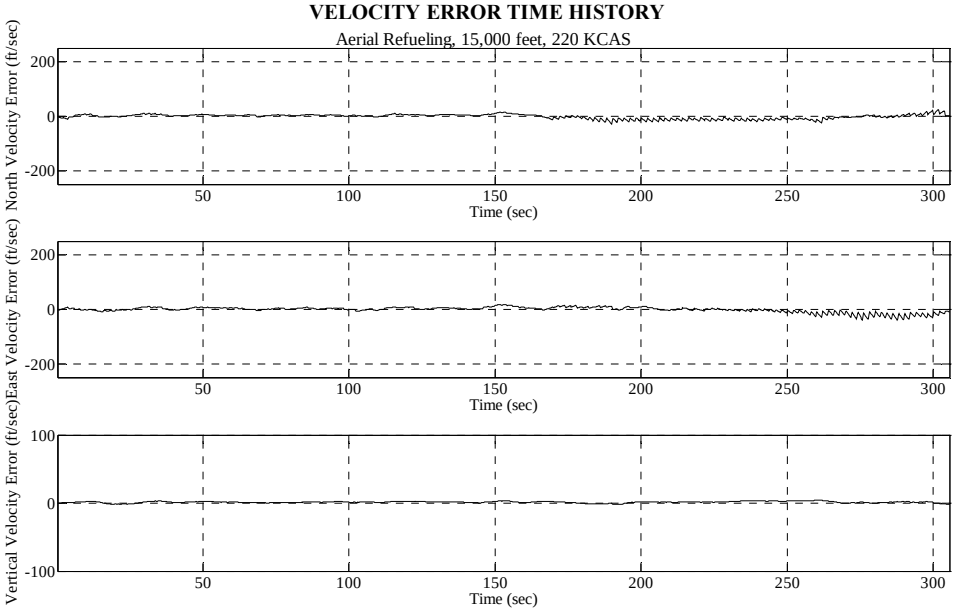

Test Point and Date: 047_18_Sep

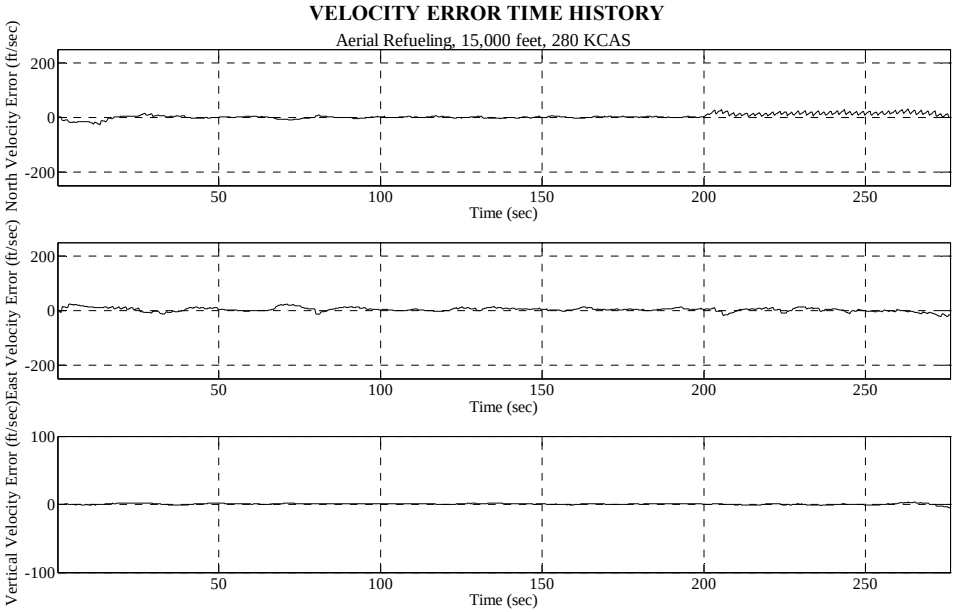

Test Point and Date: 048_21_Sep

VELOCITY ERROR TIME HISTORY

Aerial Refueling, 15,000 feet, 280 KCAS

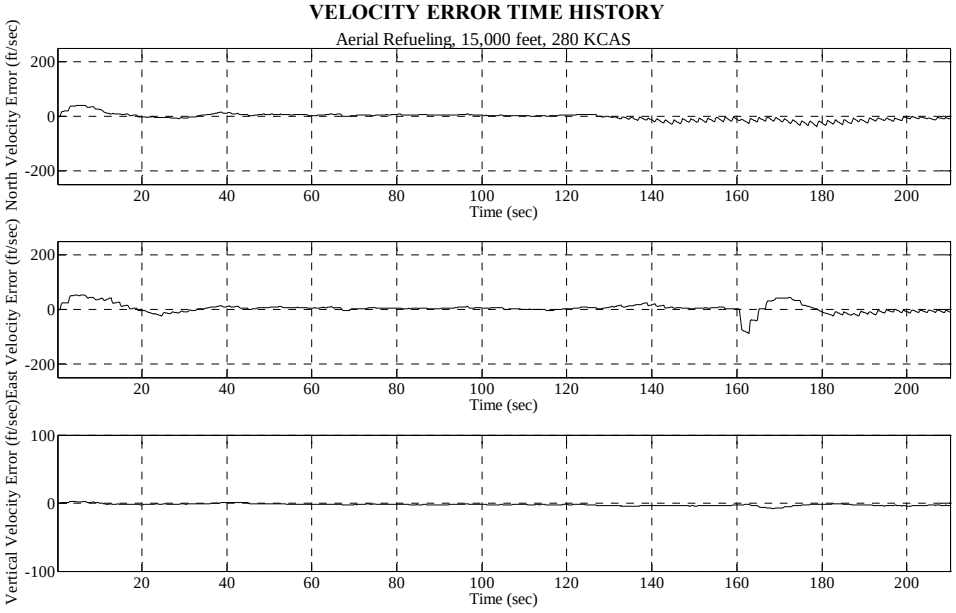

Test Point and Date: 049_21_Sep

VELOCITY ERROR TIME HISTORY

Air-to-Air Tracking, 15,000 feet, 220 KCAS

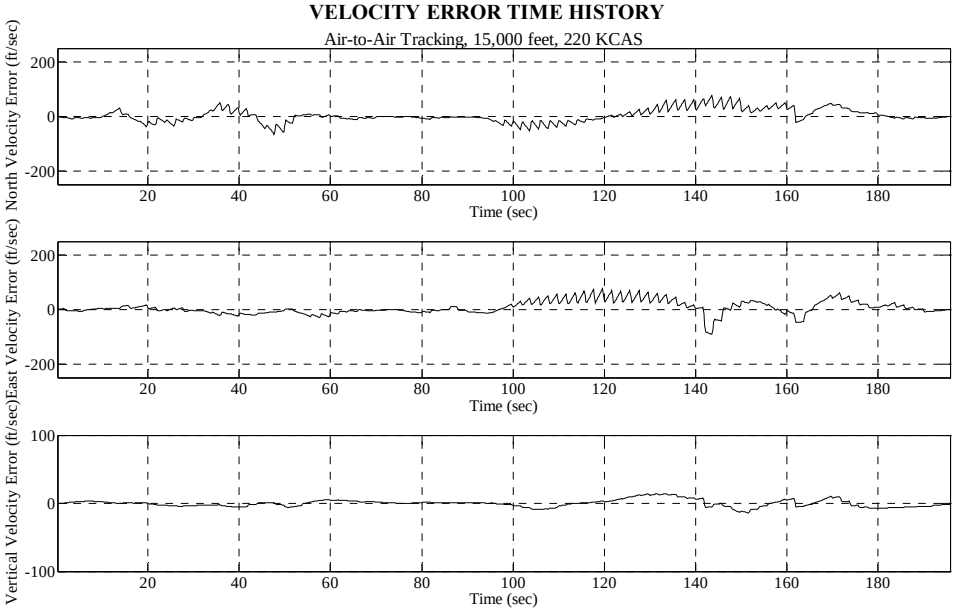

Test Point and Date: 058_18_Sep

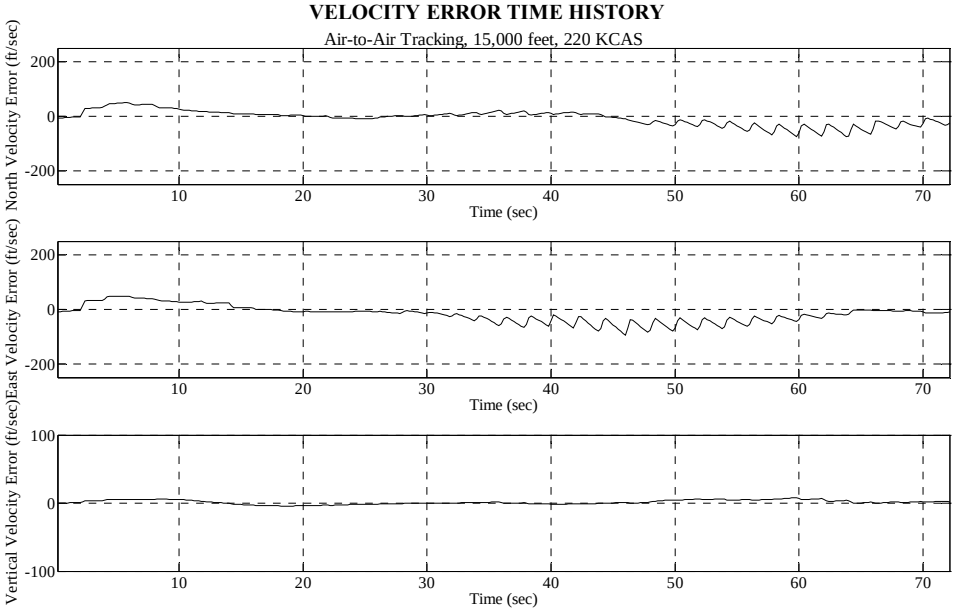

Test Point and Date: 059_18_Sep

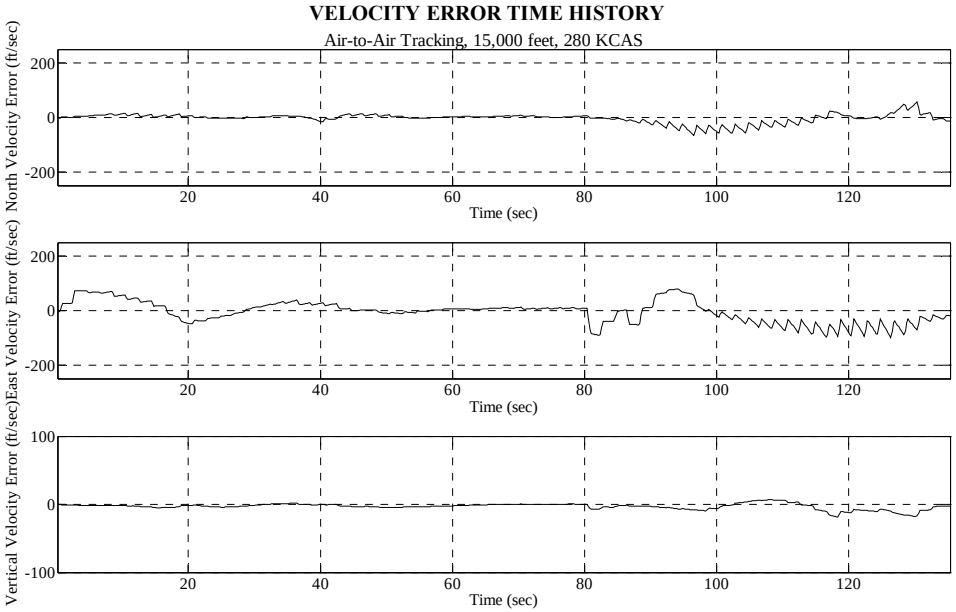

Test Point and Date: 060_21_Sep

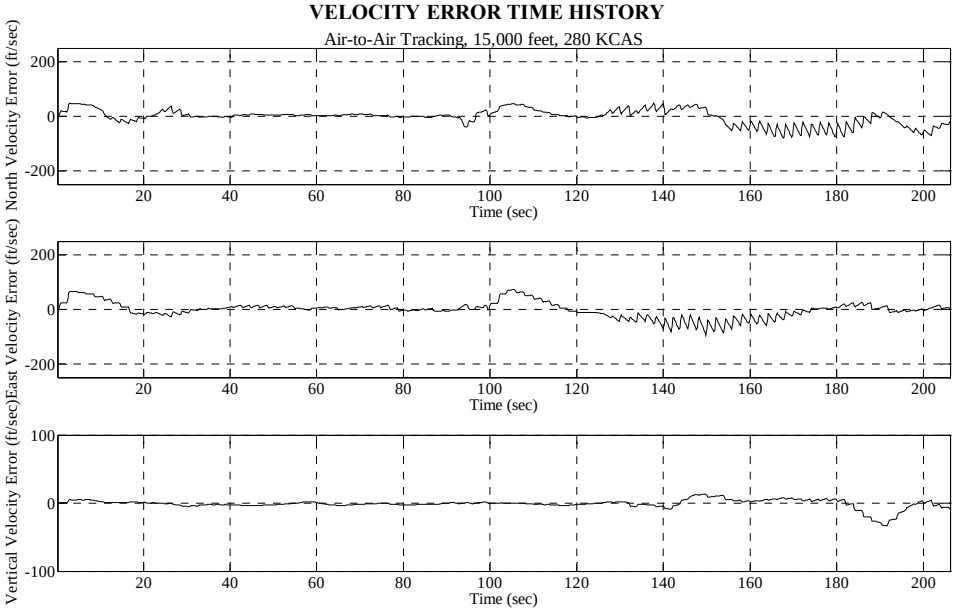

Test Point and Date: 061_21_Sep

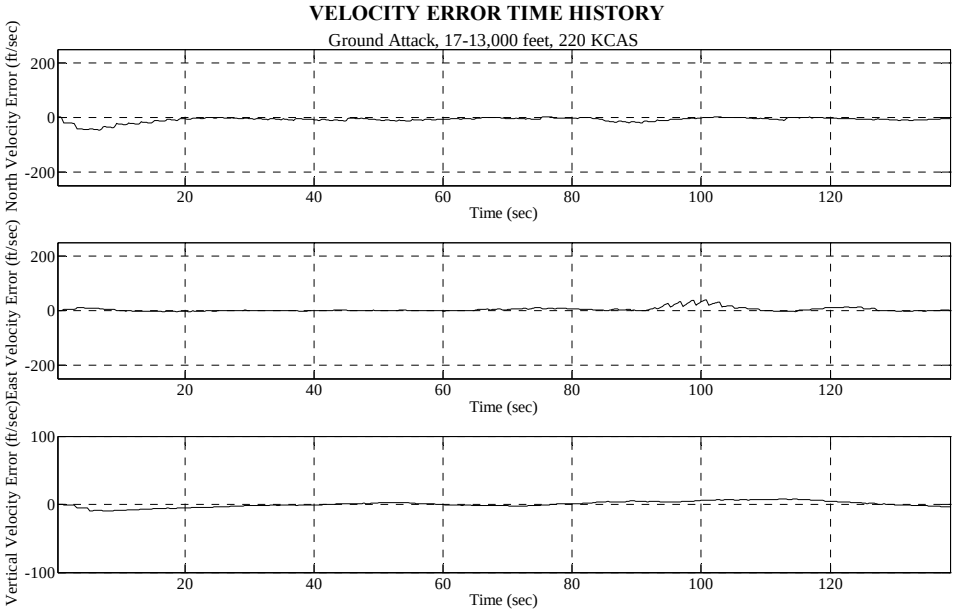

Test Point and Date: 070_19_Sep

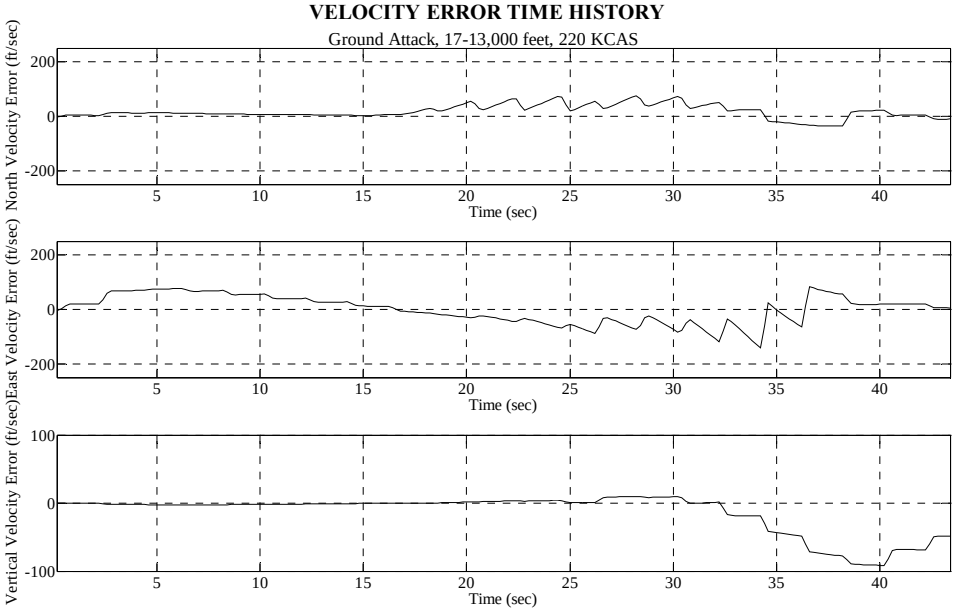

Test Point and Date: 071_19_Sep

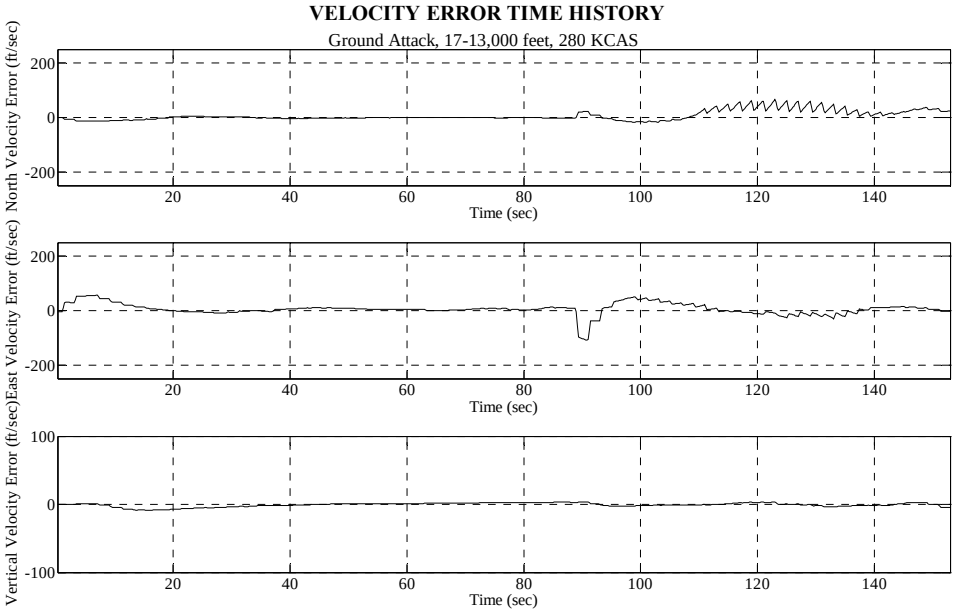

Test Point and Date: 072_19_Sep

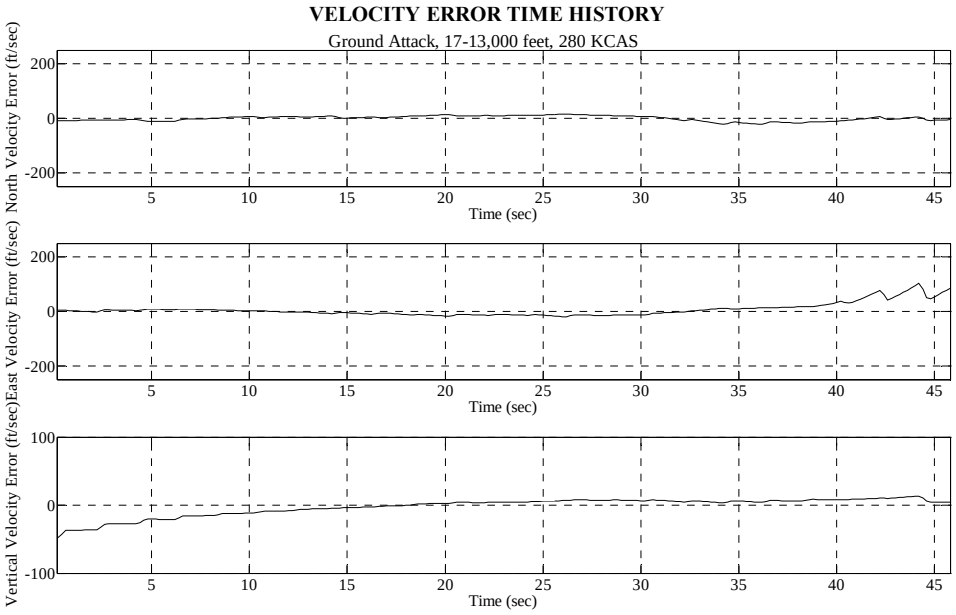

Test Point and Date: 073_19_Sep

G.4.3. Operational Maneuvers Wind

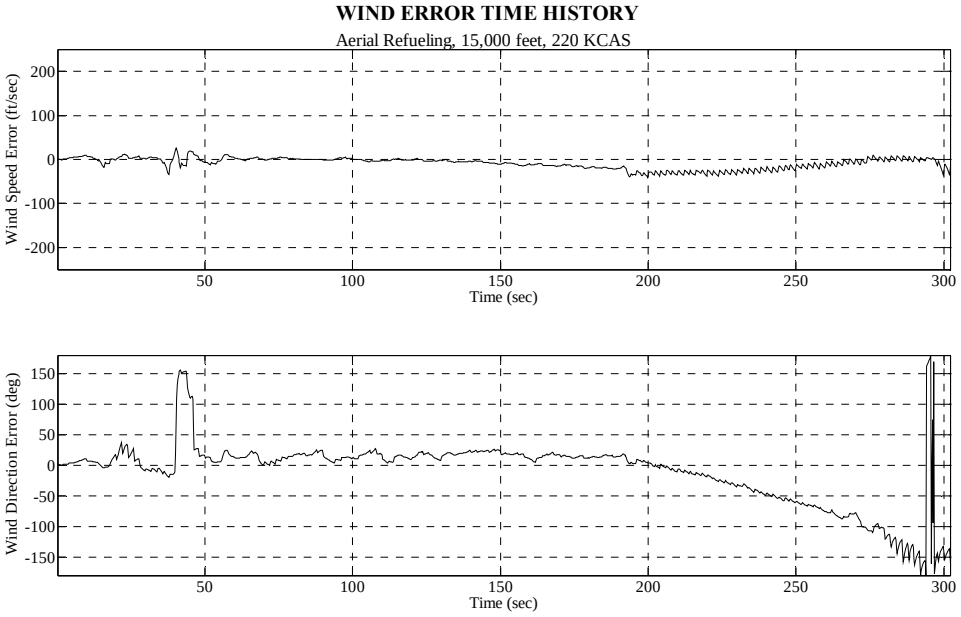

Test Point and Date: 046_18_Sep

WIND ERROR TIME HISTORY

Aerial Refueling, 15,000 feet, 220 KCAS

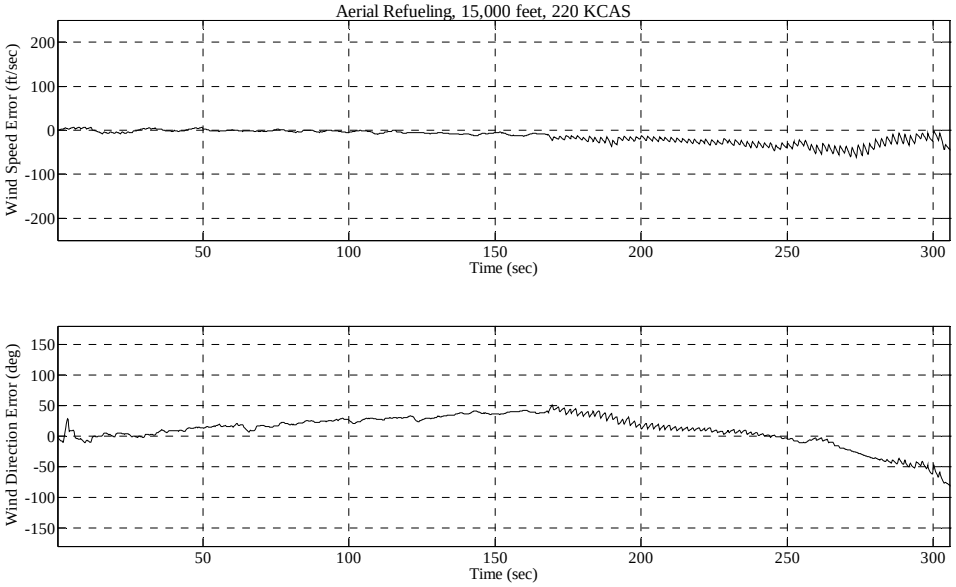

Test Point and Date: 047_18_Sep

WIND ERROR TIME HISTORY

Aerial Refueling, 15,000 feet, 280 KCAS

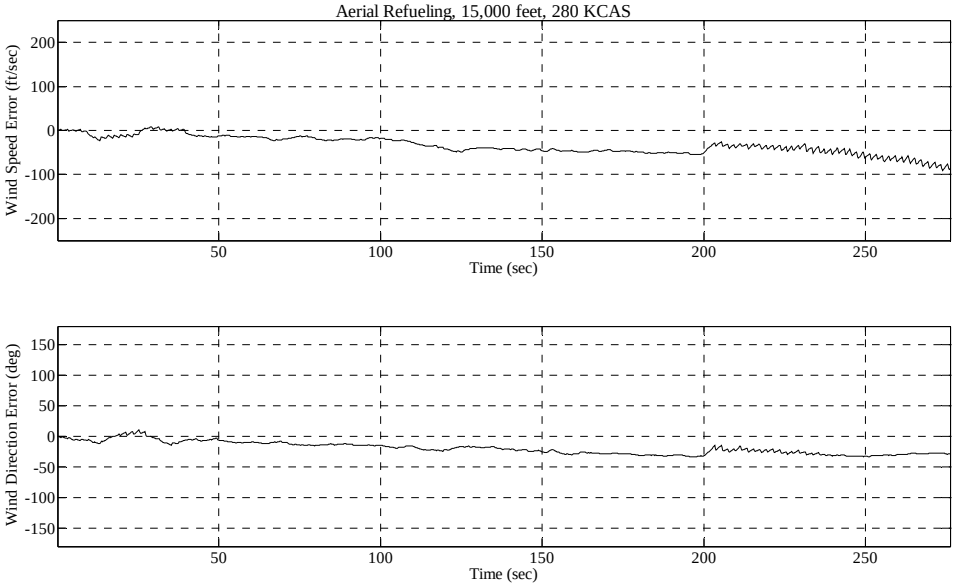

Test Point and Date: 048_21_Sep

WIND ERROR TIME HISTORY

Aerial Refueling, 15,000 feet, 280 KCAS

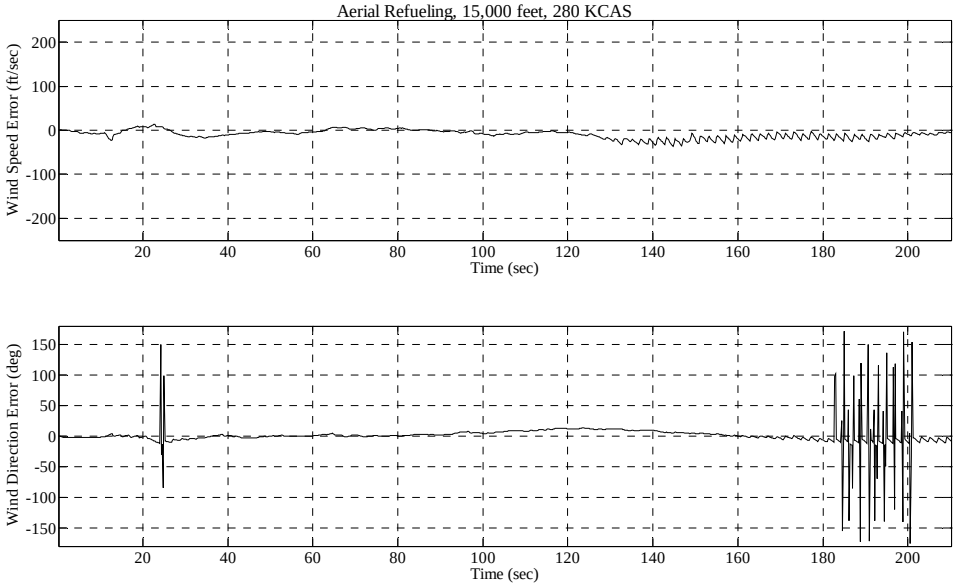

Test Point and Date: 049_21_Sep

WIND ERROR TIME HISTORY

Air-to-Air Tracking, 15,000 feet, 220 KCAS

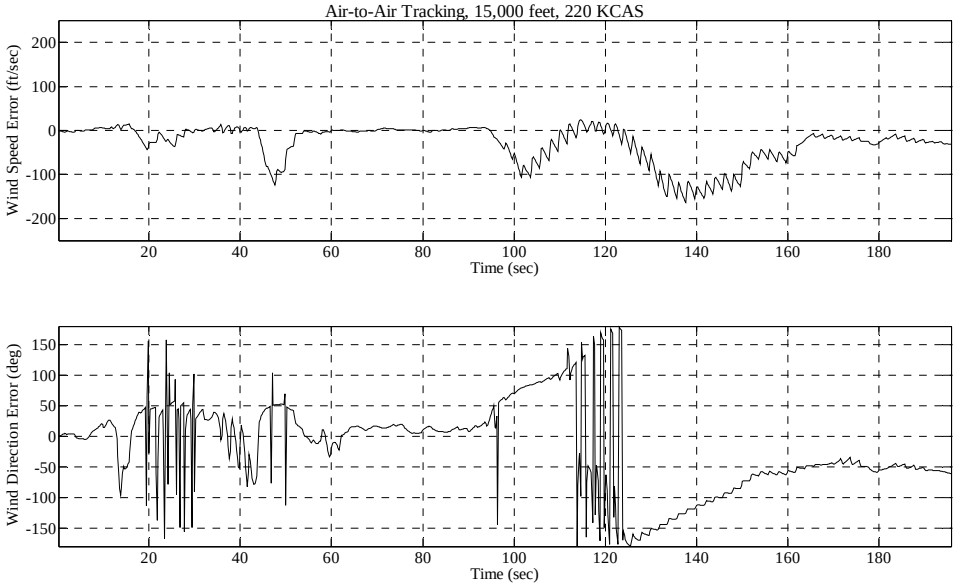

Test Point and Date: 058_18_Sep

WIND ERROR TIME HISTORY

Air-to-Air Tracking, 15,000 feet, 220 KCAS

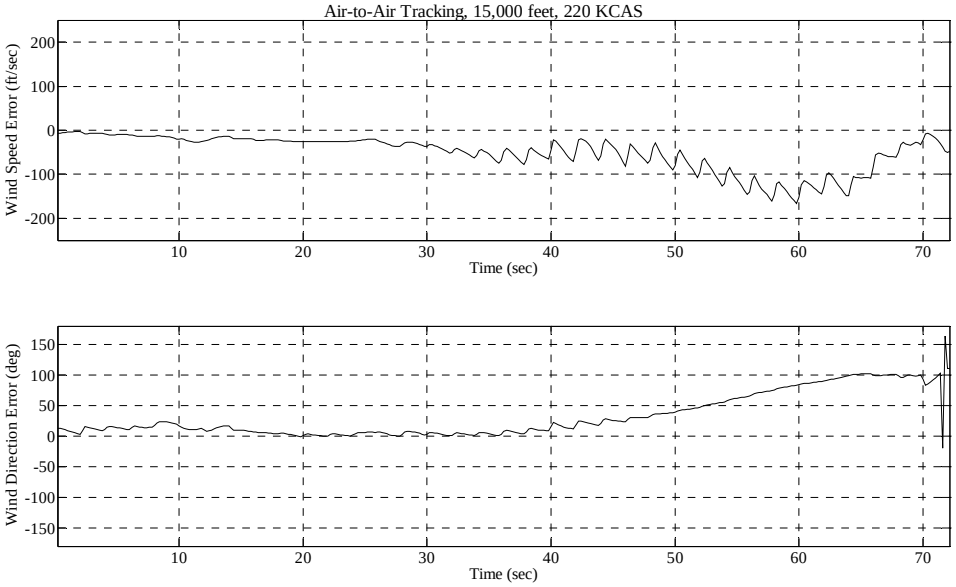

Test Point and Date: 059_18_Sep

WIND ERROR TIME HISTORY

Air-to-Air Tracking, 15,000 feet, 280 KCAS

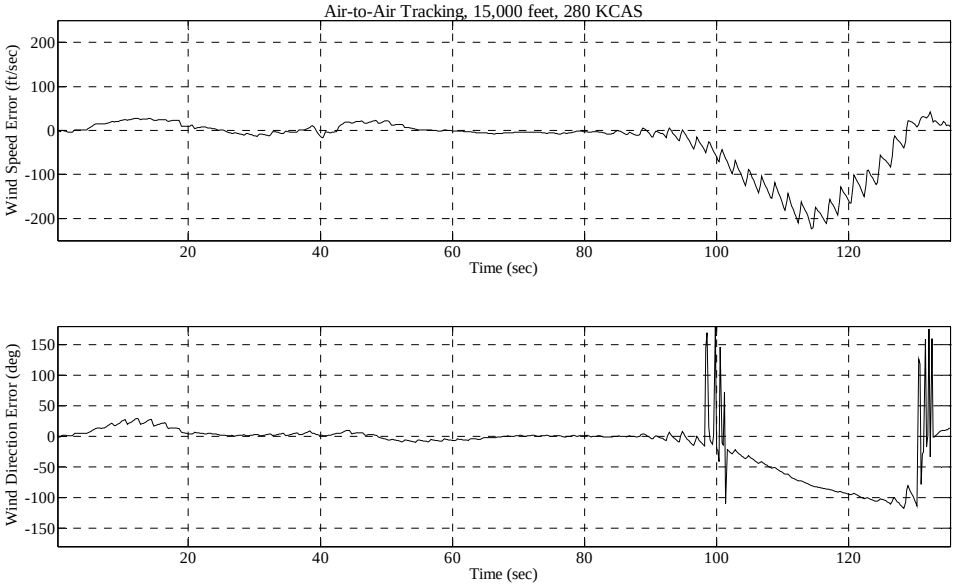

Test Point and Date: 060_21_Sep

WIND ERROR TIME HISTORY

Air-to-Air Tracking, 15,000 feet, 280 KCAS

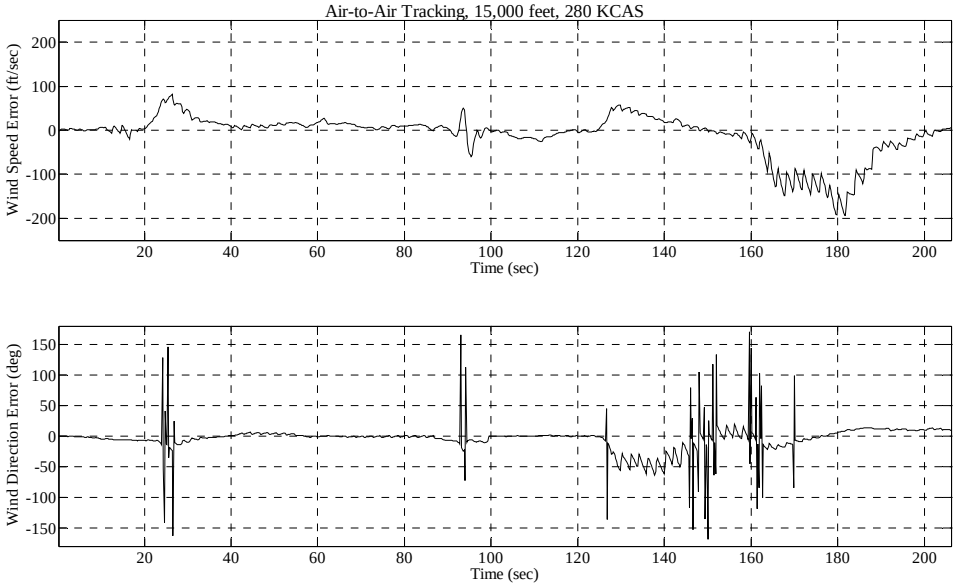

Test Point and Date: 061_21_Sep

WIND ERROR TIME HISTORY

Ground Attack, 17-13,000 feet, 220 KCAS

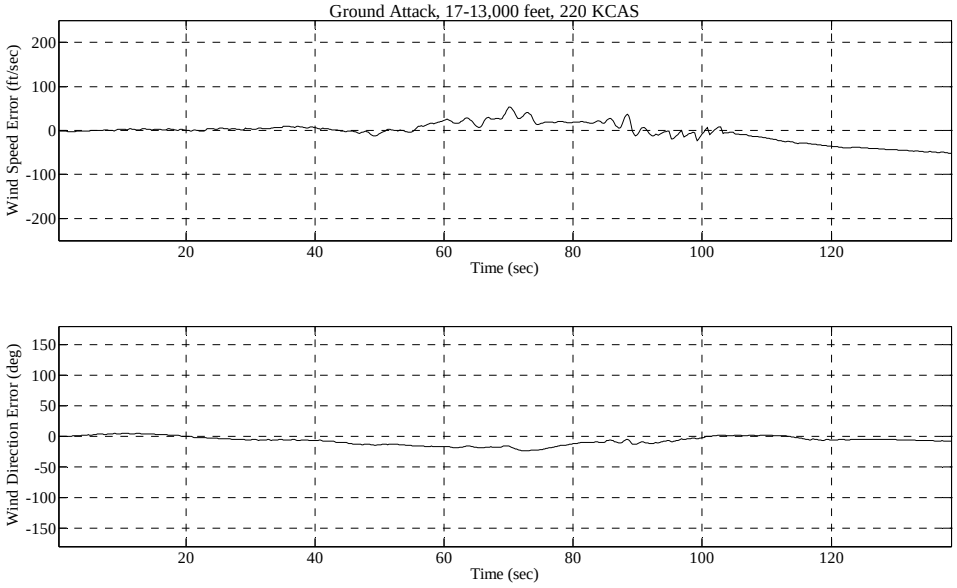

Test Point and Date: 070_19_Sep

WIND ERROR TIME HISTORY

Ground Attack, 17-13,000 feet, 220 KCAS

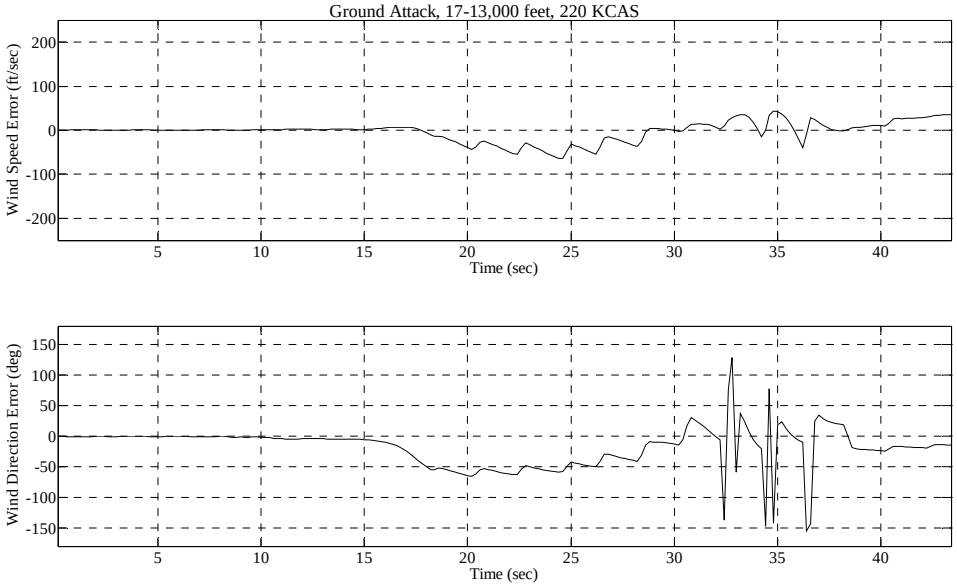

Test Point and Date: 071_19_Sep

WIND ERROR TIME HISTORY

Ground Attack, 17-13,000 feet, 280 KCAS

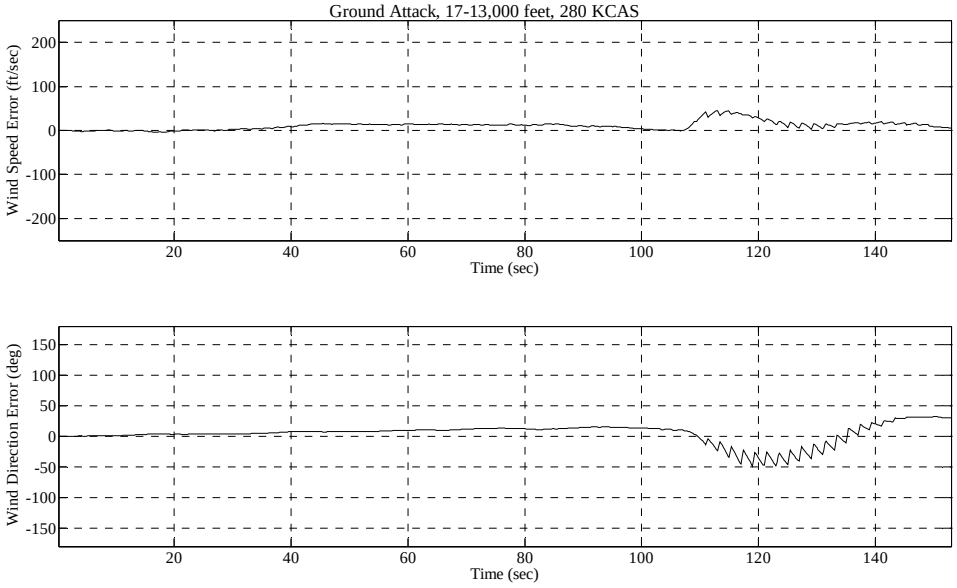

Test Point and Date: 072_19_Sep

WIND ERROR TIME HISTORY

Ground Attack, 17-13,000 feet, 280 KCAS

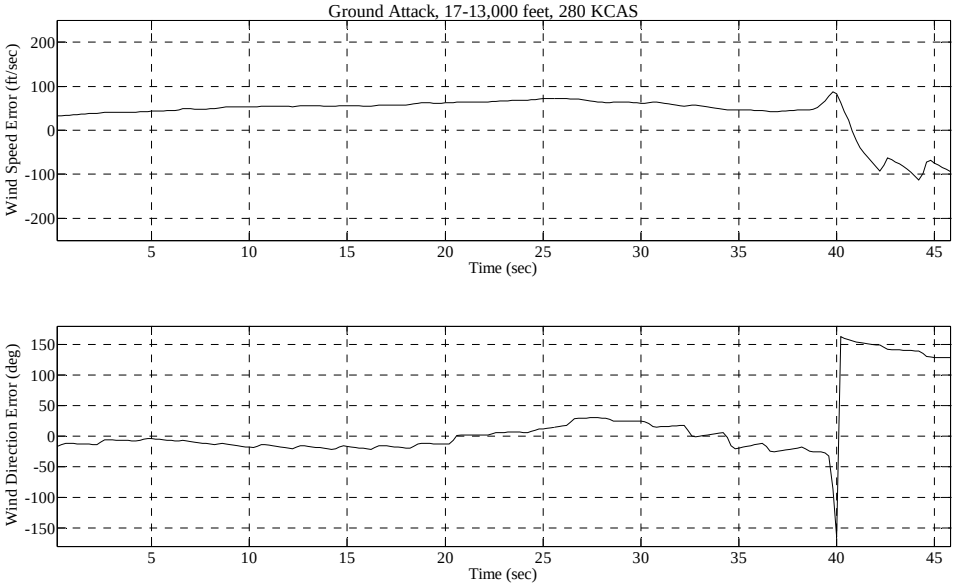

Test Point and Date: 073_19_Sep

G.5. Long Shot Flight Test Technique

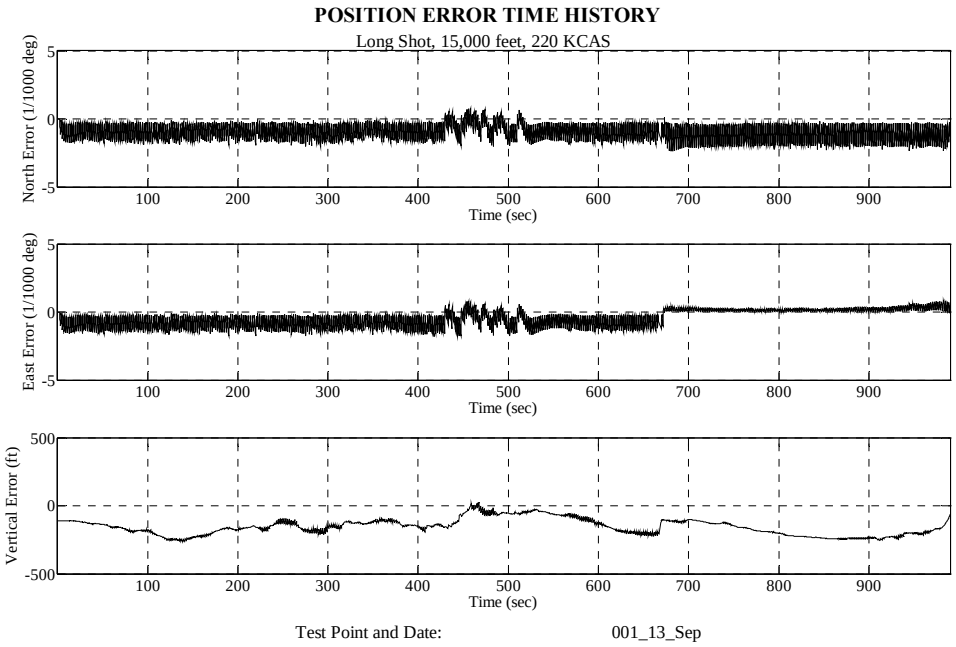

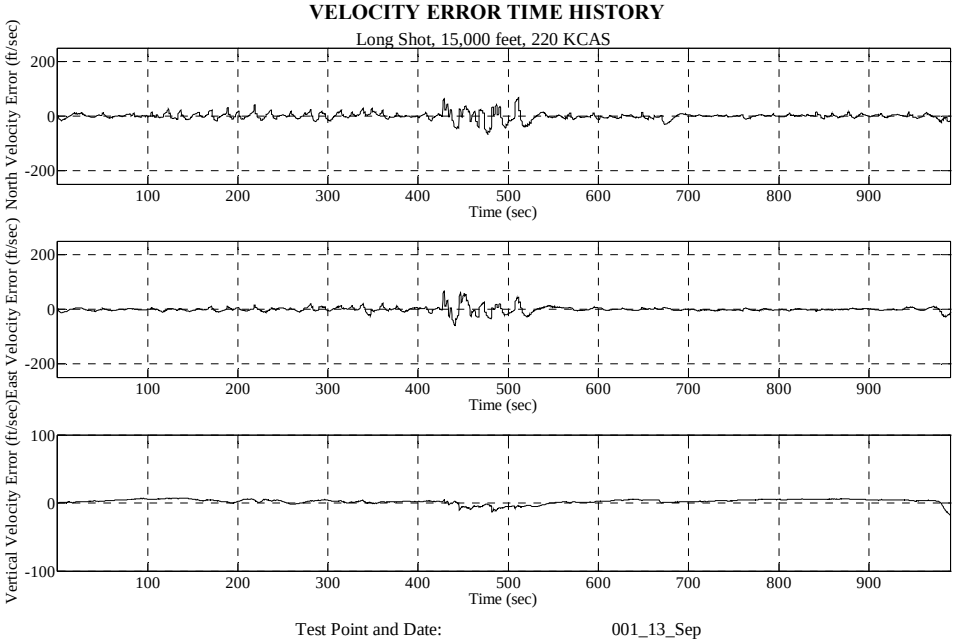

WIND ERROR TIME HISTORY

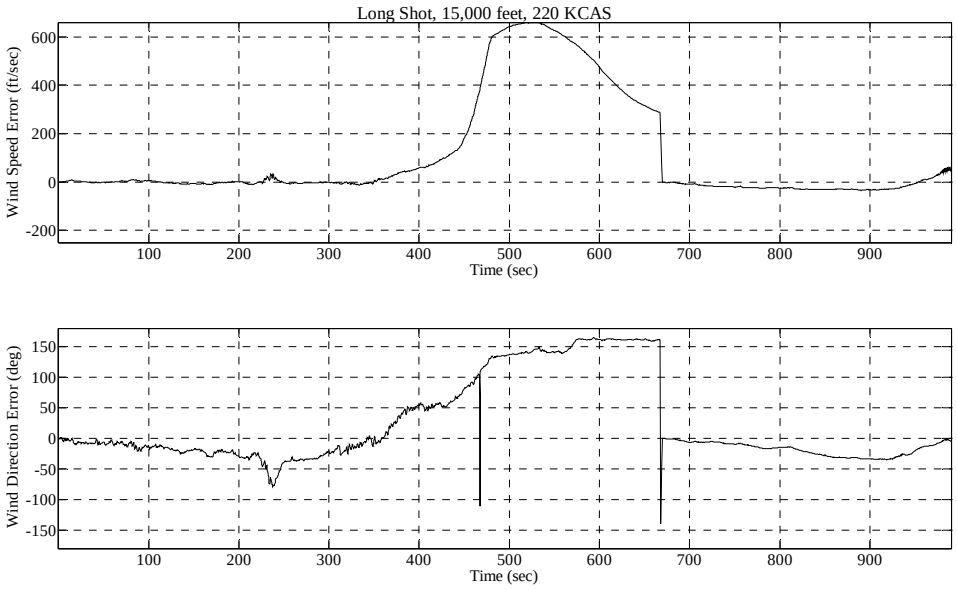

Test Point and Date: 001_13_Sep

POSITION ERROR TIME HISTORY

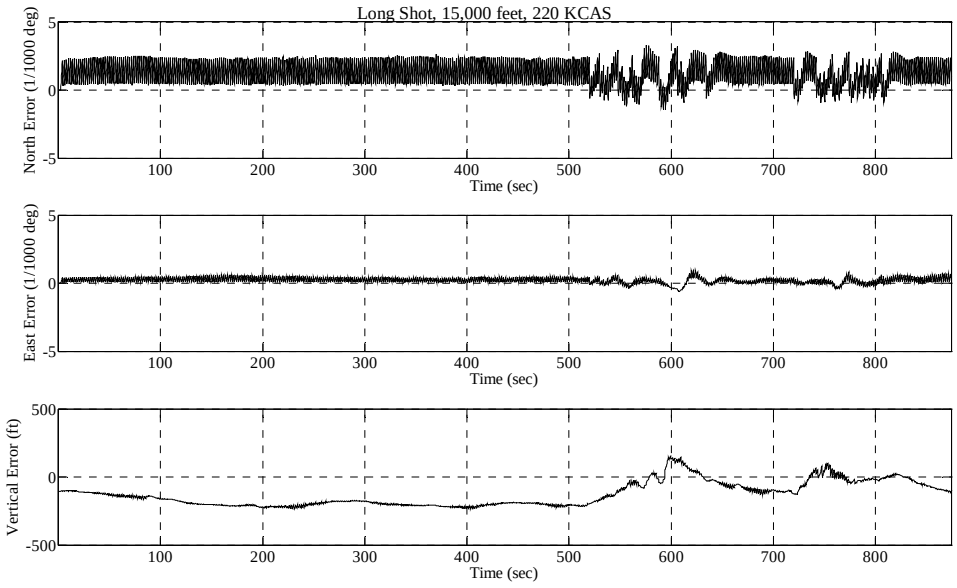

Test Point and Date: 002_13_Sep

VELOCITY ERROR TIME HISTORY

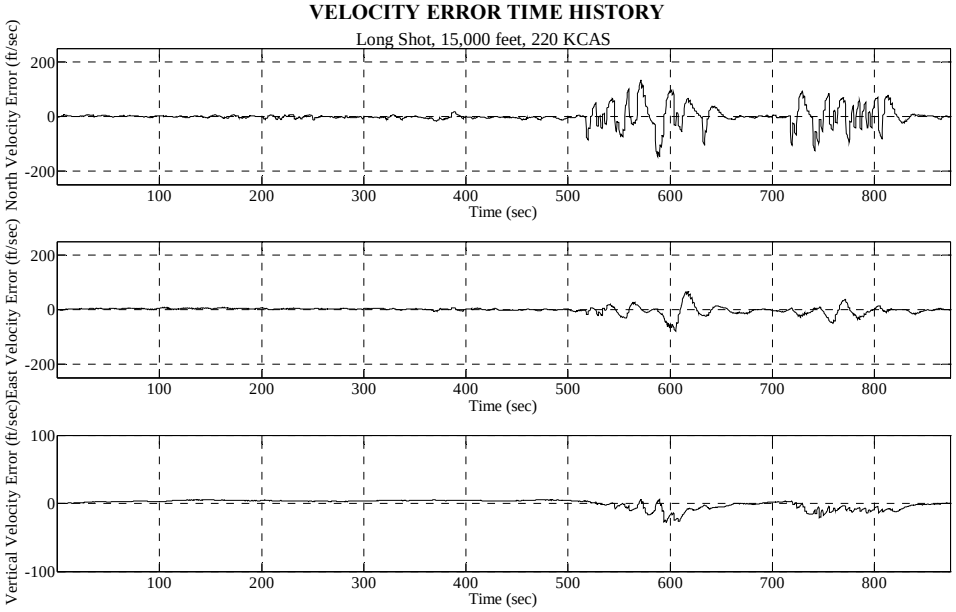

Test Point and Date: 002_13_Sep

WIND ERROR TIME HISTORY

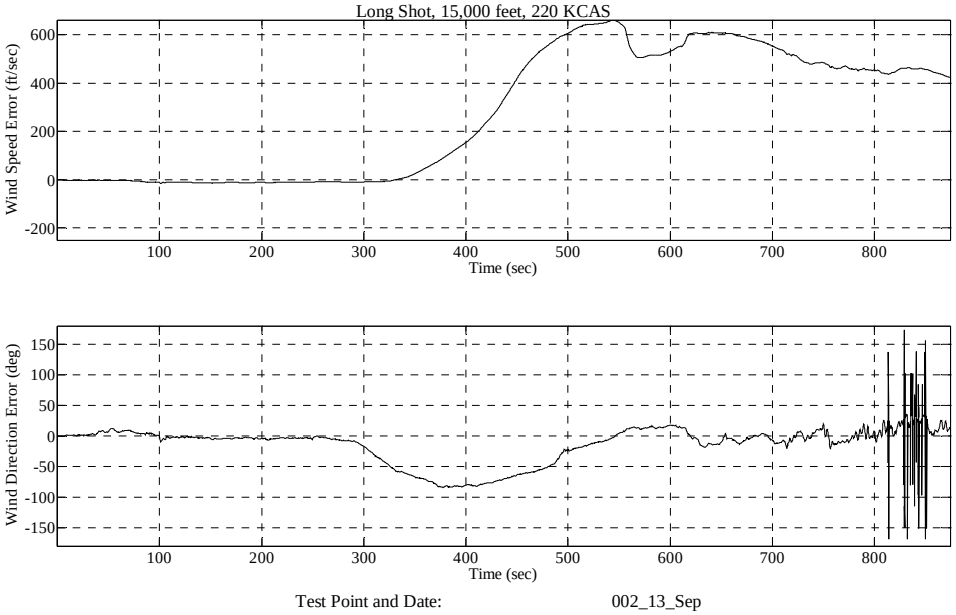

Test Point and Date: 002_13_Sep

POSITION ERROR TIME HISTORY

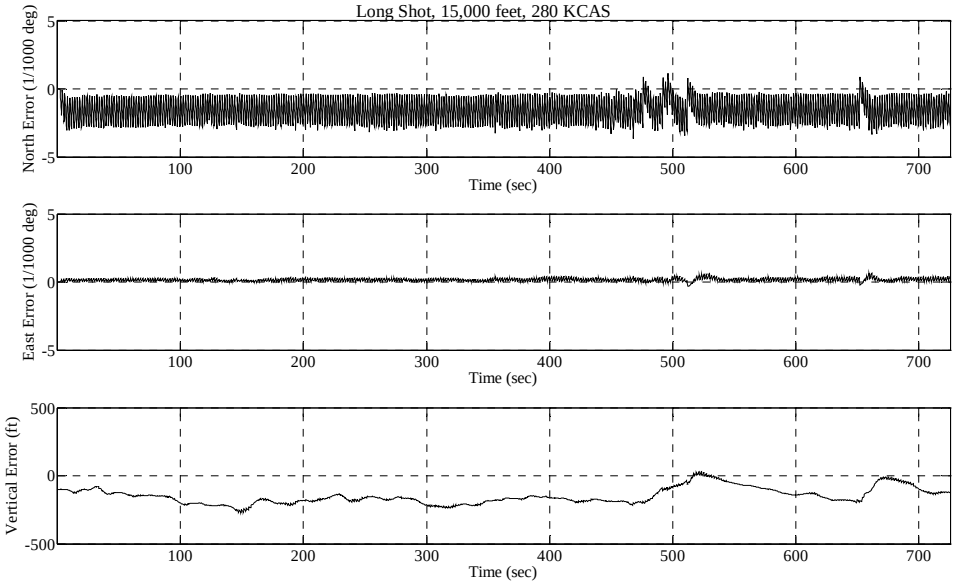

Test Point and Date: 003_17_Sep

VELOCITY ERROR TIME HISTORY

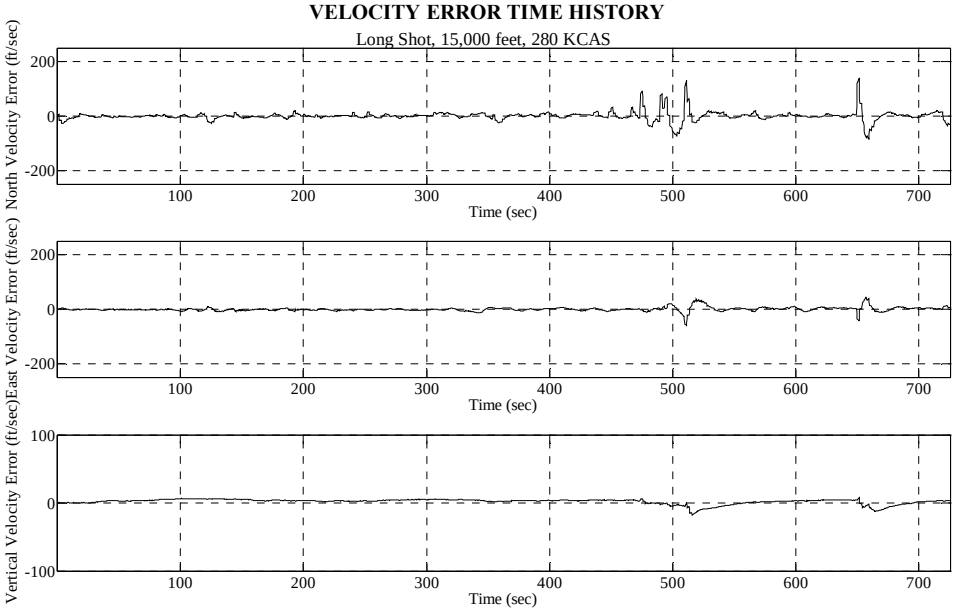

Test Point and Date: 003_17_Sep

WIND ERROR TIME HISTORY

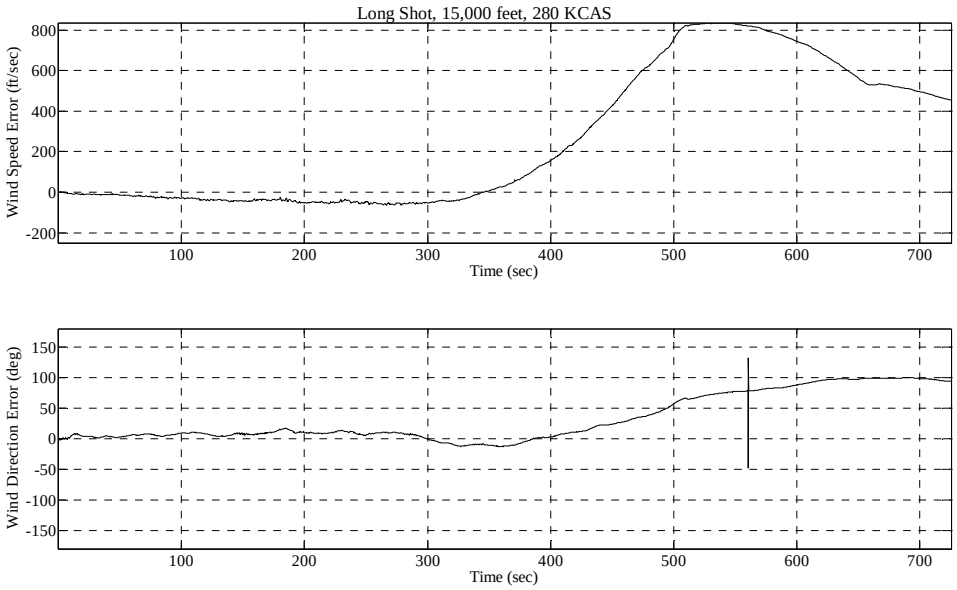

Test Point and Date: 003_17_Sep

POSITION ERROR TIME HISTORY

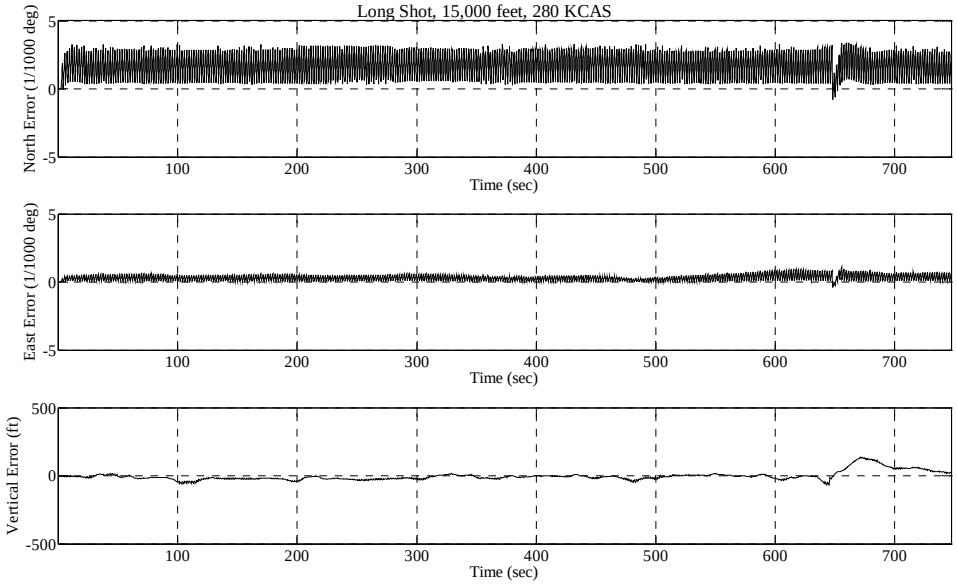

Test Point and Date: 004_19_Sep

VELOCITY ERROR TIME HISTORY

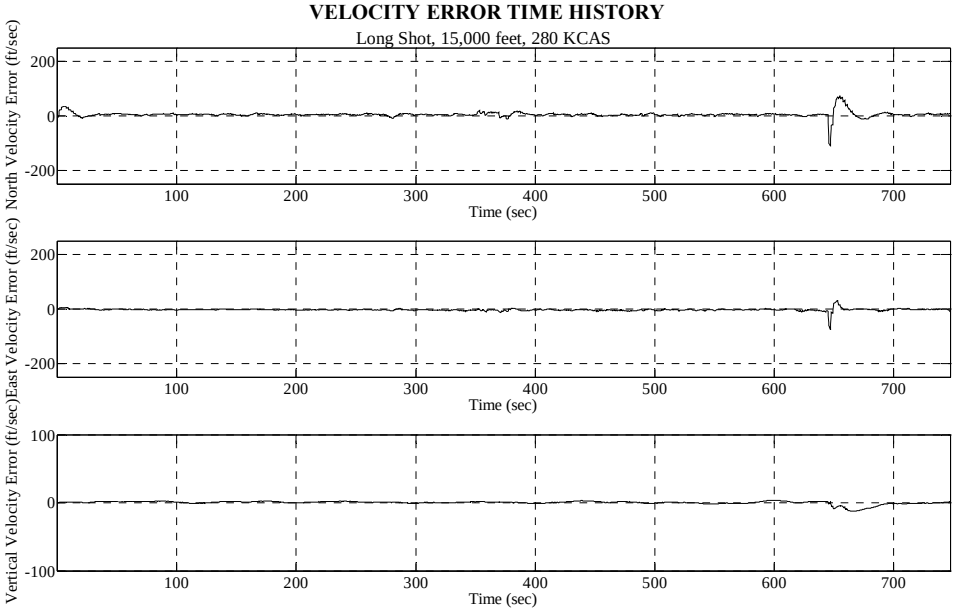

Test Point and Date: 004_19_Sep

WIND ERROR TIME HISTORY

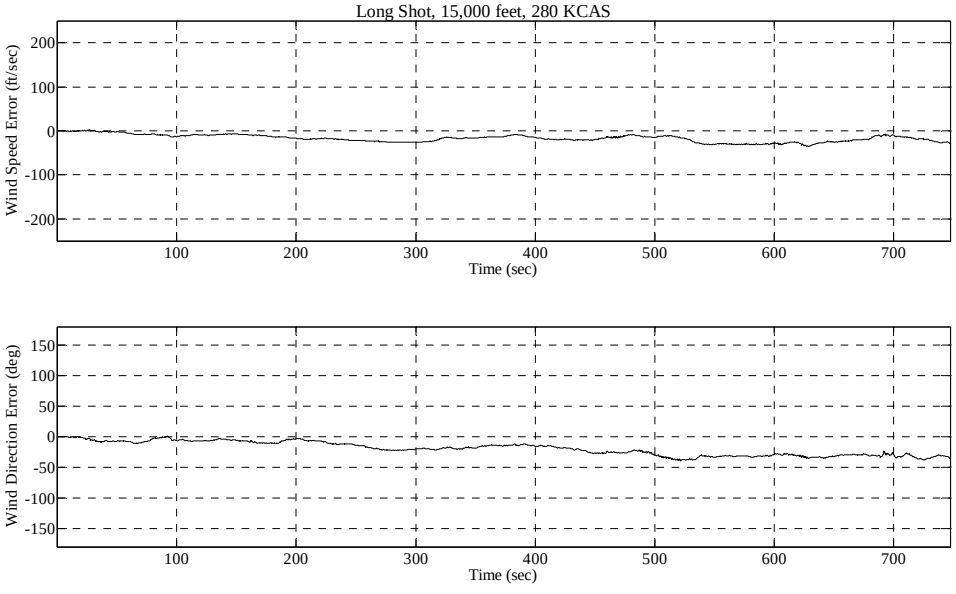

Test Point and Date: 004_19_Sep

G.6. Container Flight Test Technique

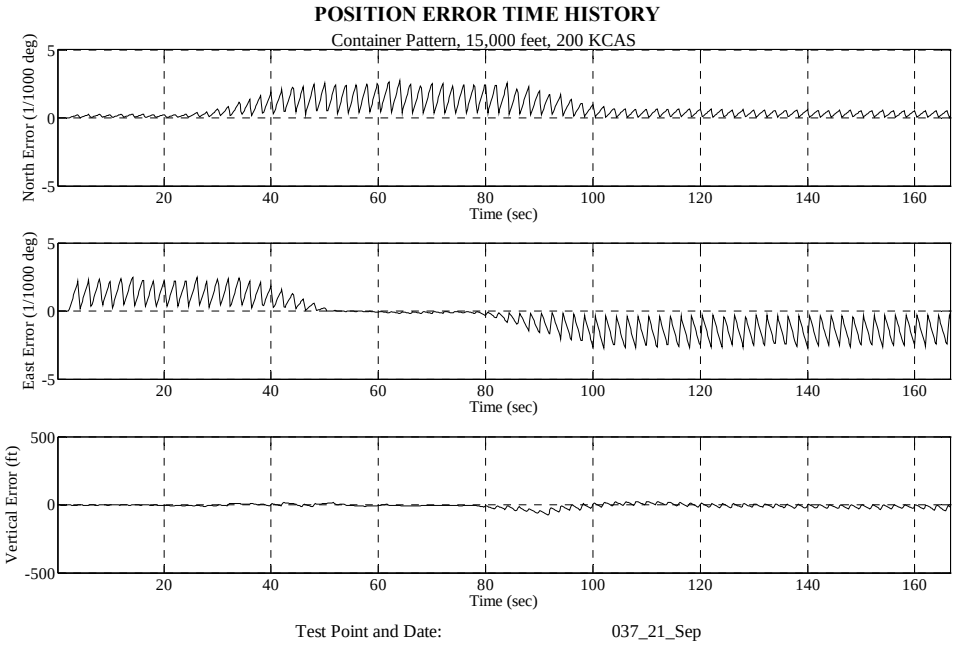

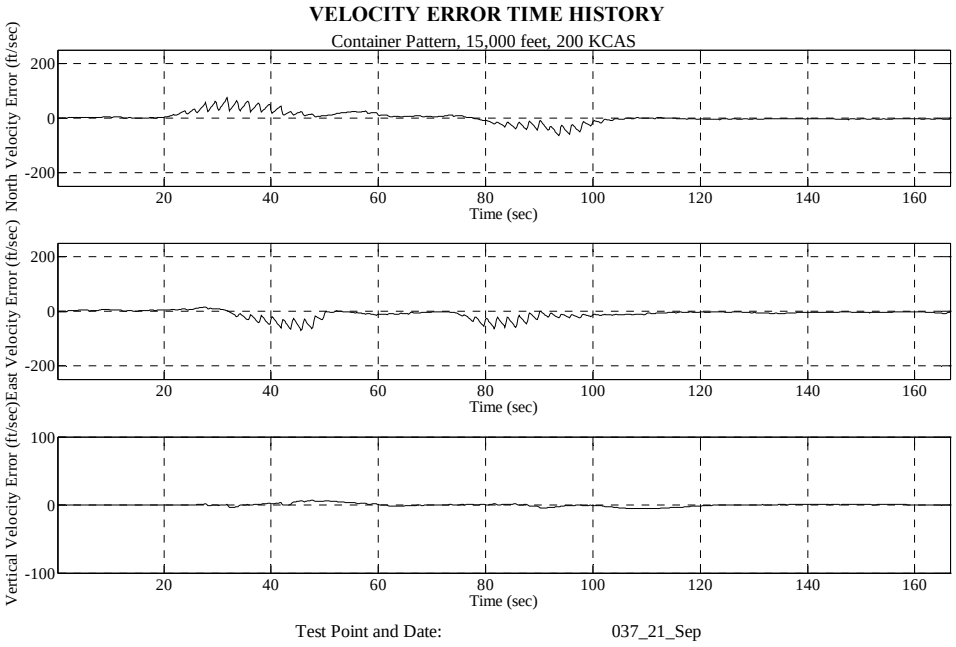

WIND ERROR TIME HISTORY

Container Pattern, 15,000 feet, 200 KCAS

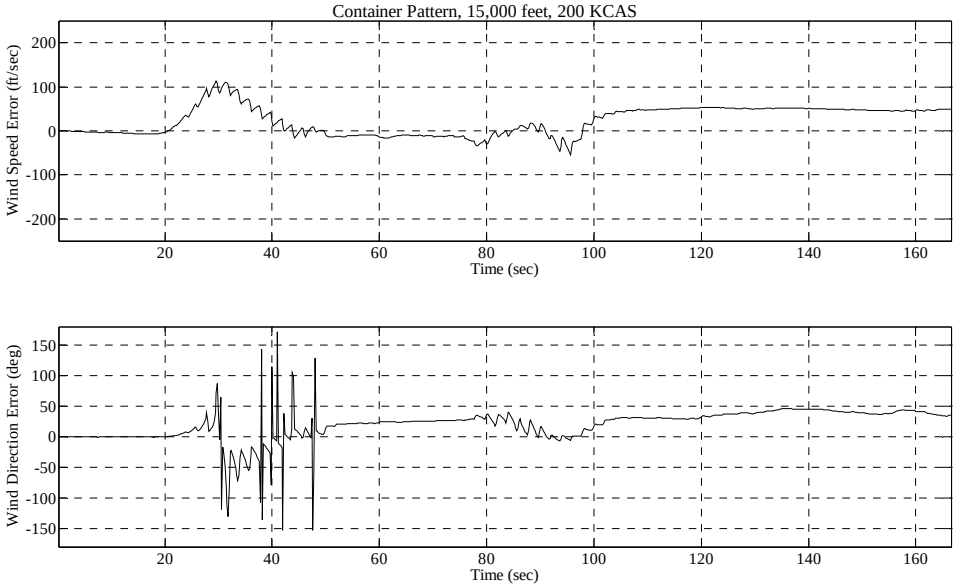

Test Point and Date: 037_21_Sep

POSITION ERROR TIME HISTORY

Container Pattern, 15,000 feet, 200 KCAS

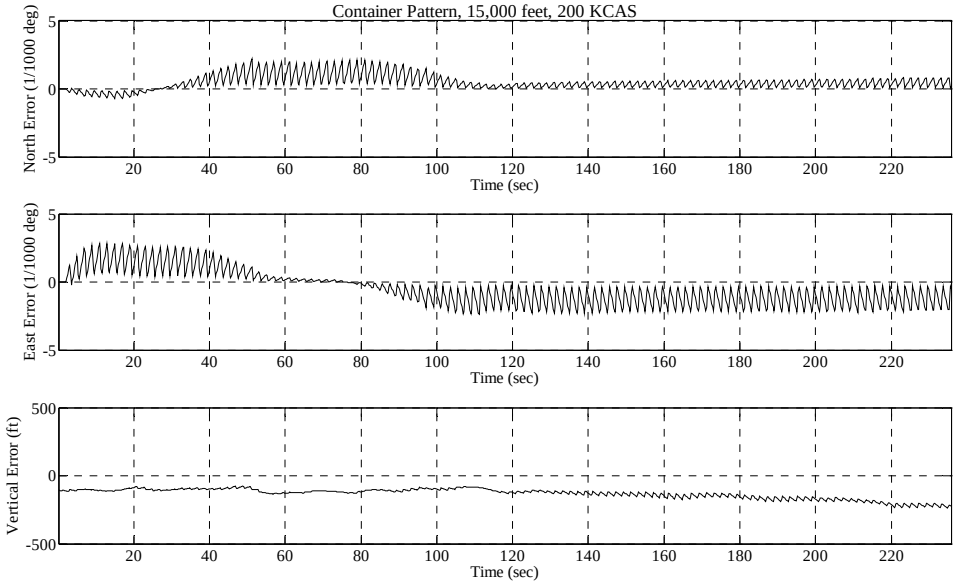

Test Point and Date: 038_17_Sep

VELOCITY ERROR TIME HISTORY

Container Pattern, 15,000 feet, 200 KCAS

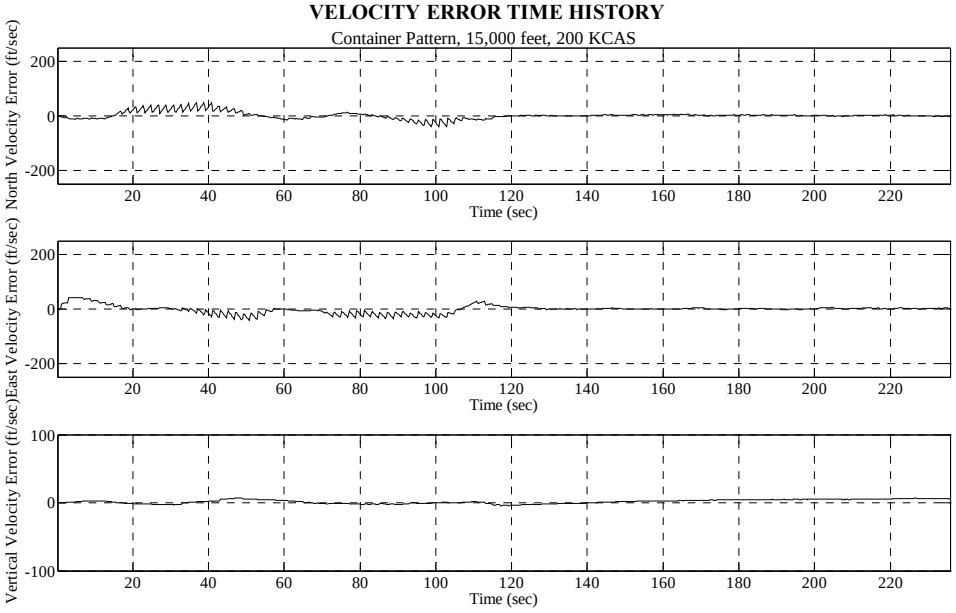

Test Point and Date: 038_17_Sep

WIND ERROR TIME HISTORY

Container Pattern, 15,000 feet, 200 KCAS

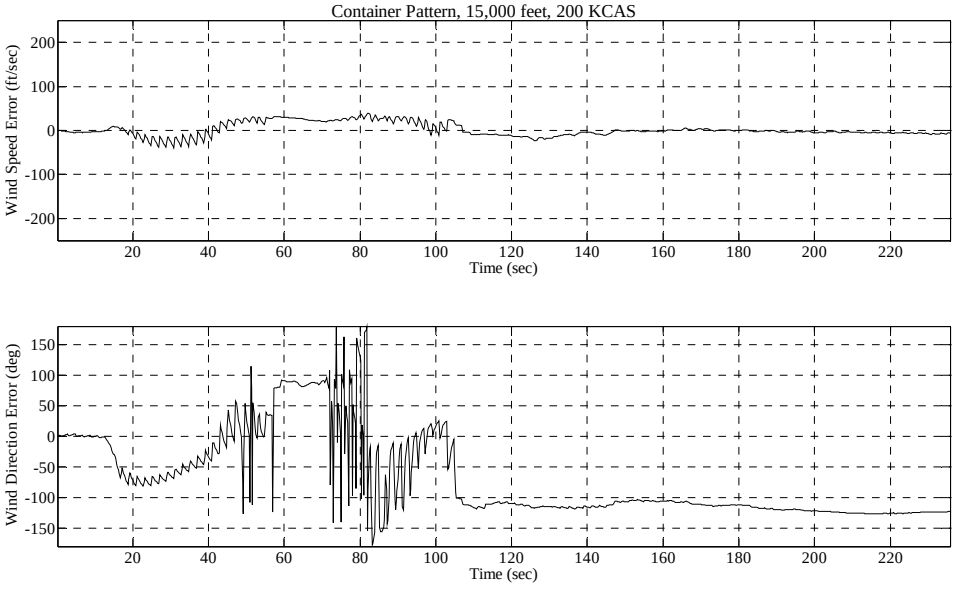

Test Point and Date: 038_17_Sep

POSITION ERROR TIME HISTORY

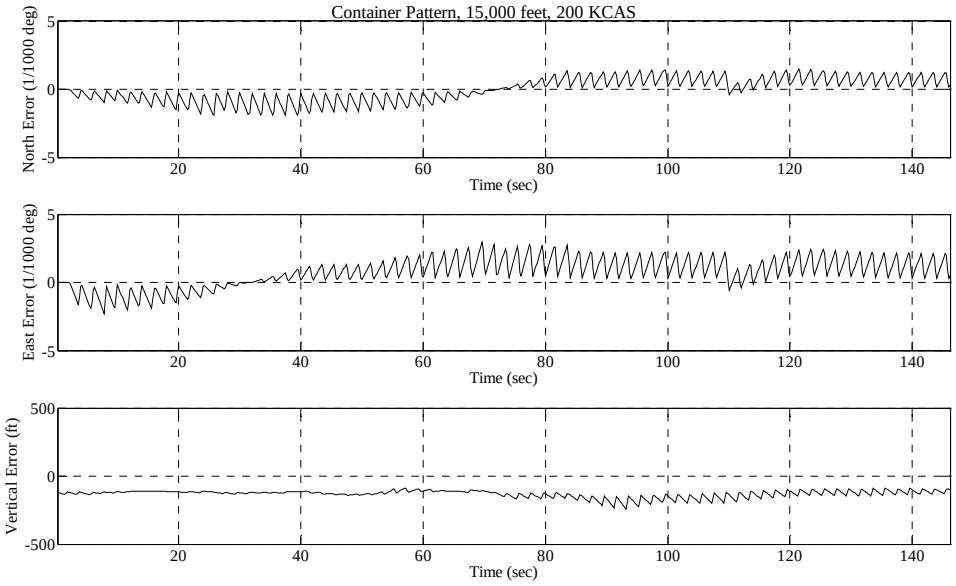

Test Point and Date: 039_13_Sep

VELOCITY ERROR TIME HISTORY

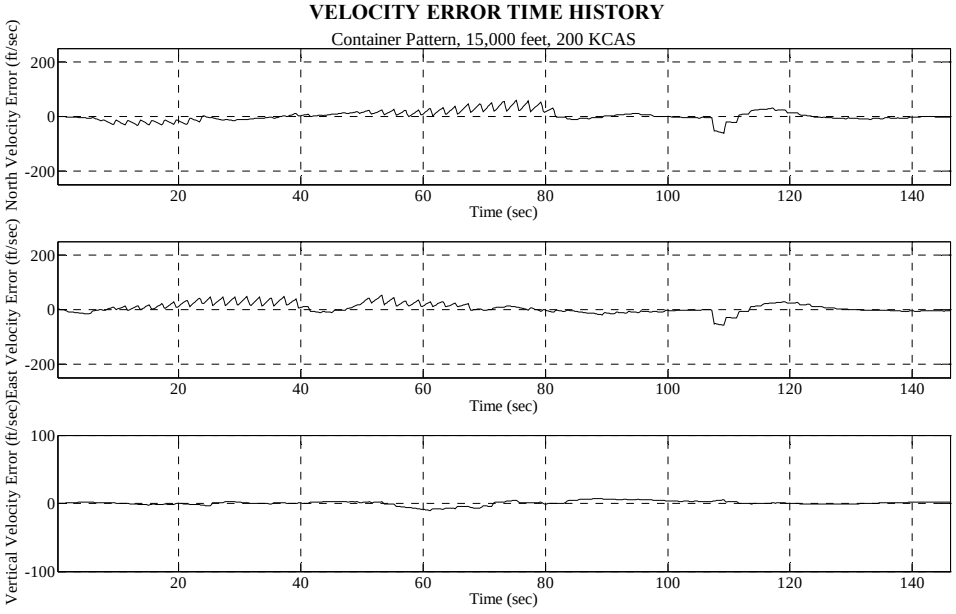

Test Point and Date: 039_13_Sep

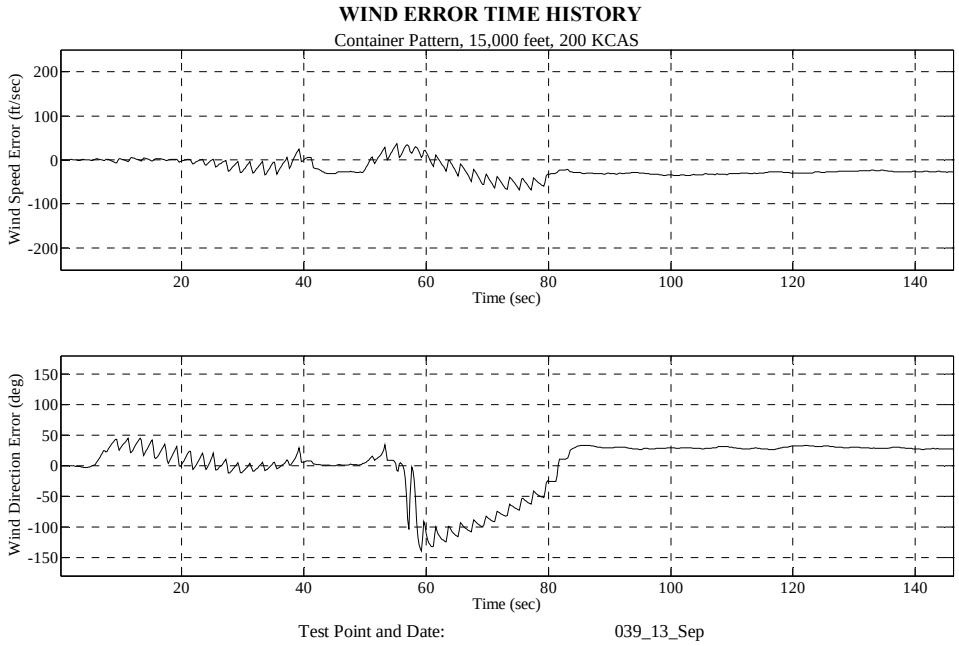

G.7. Landing Approaches

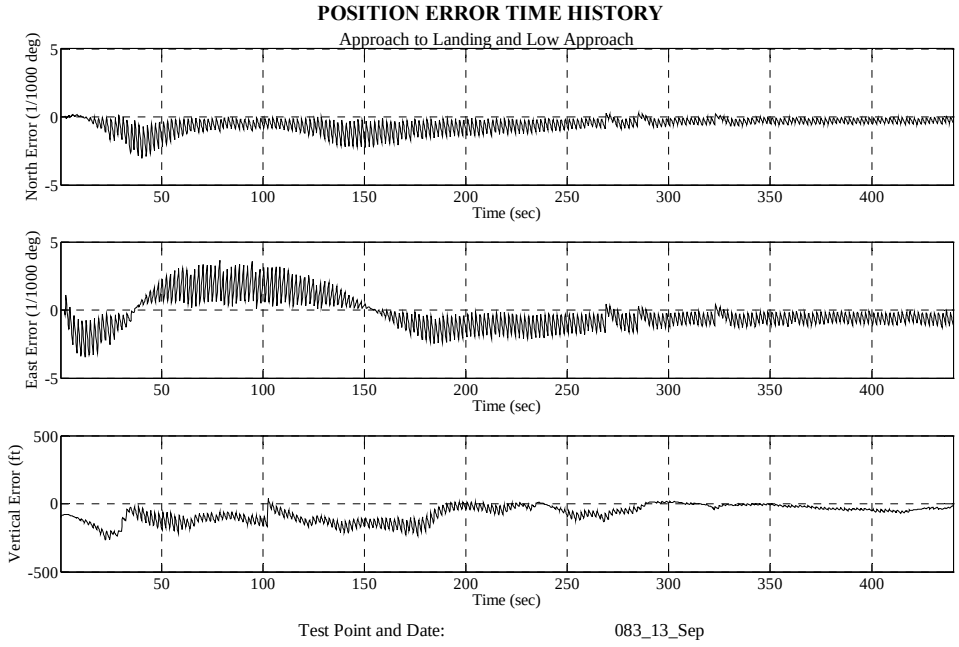

VELOCITY ERROR TIME HISTORY

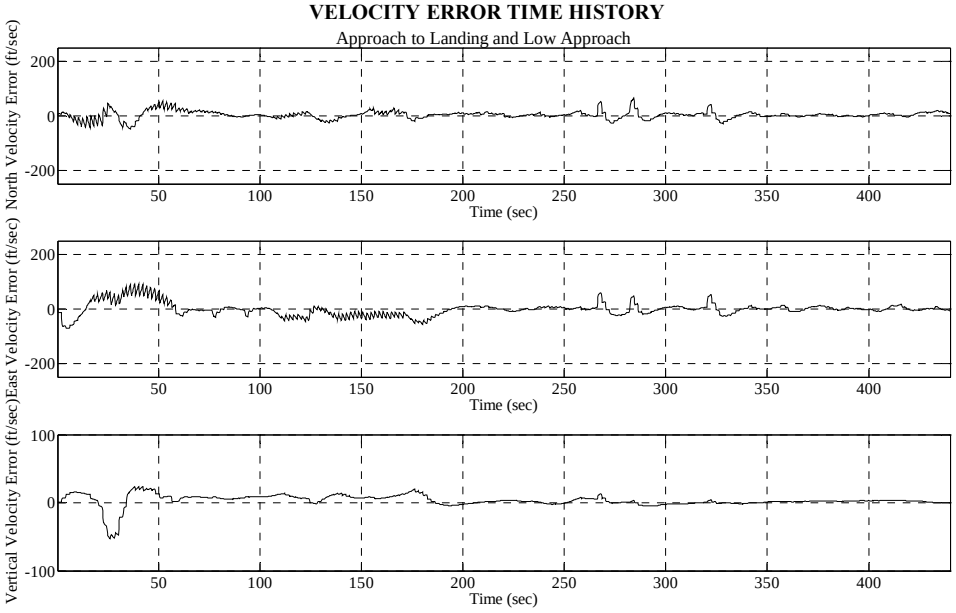

Test Point and Date: 083_13_Sep

WIND ERROR TIME HISTORY

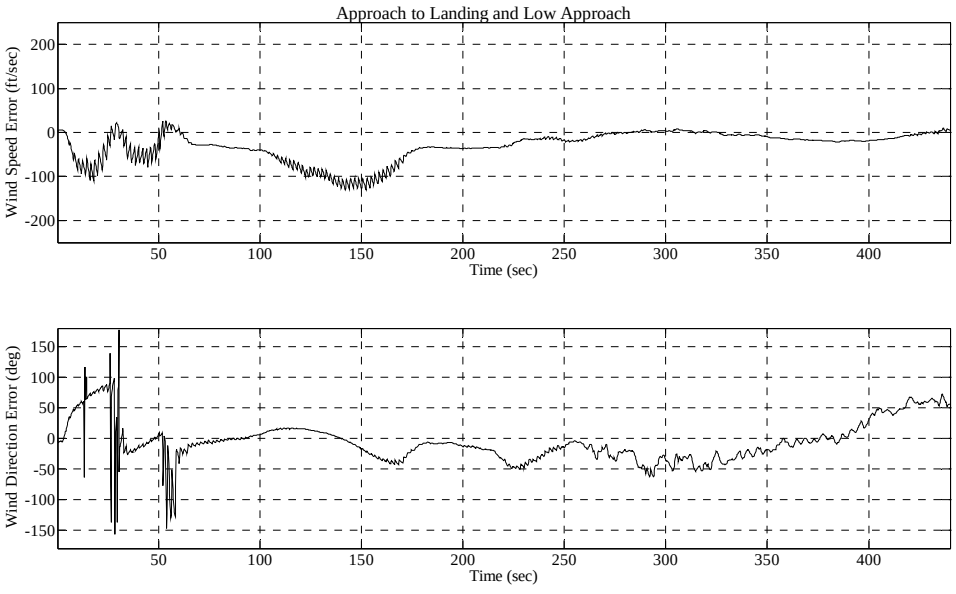

Test Point and Date: 083_13_Sep

POSITION ERROR TIME HISTORY

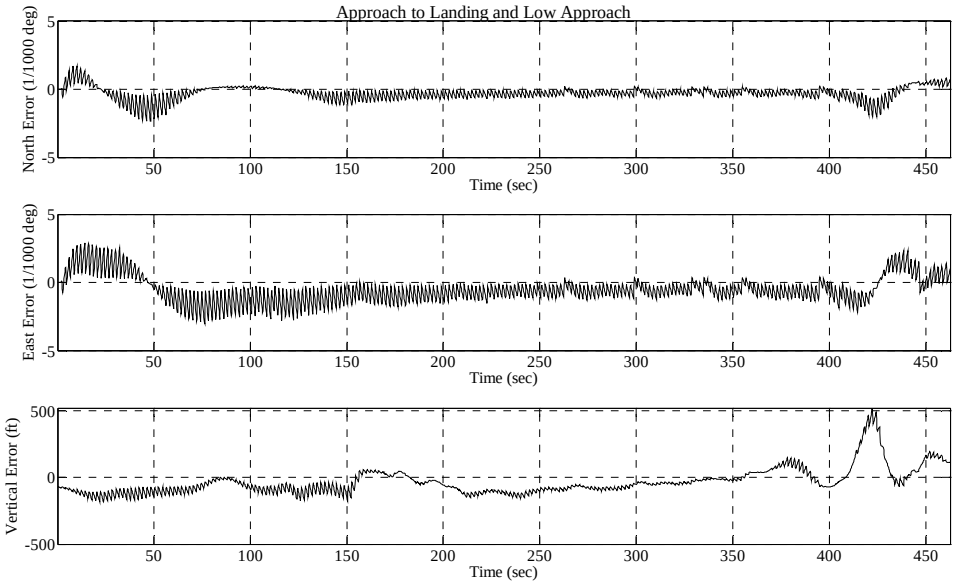

Test Point and Date: 084_17_Sep

VELOCITY ERROR TIME HISTORY

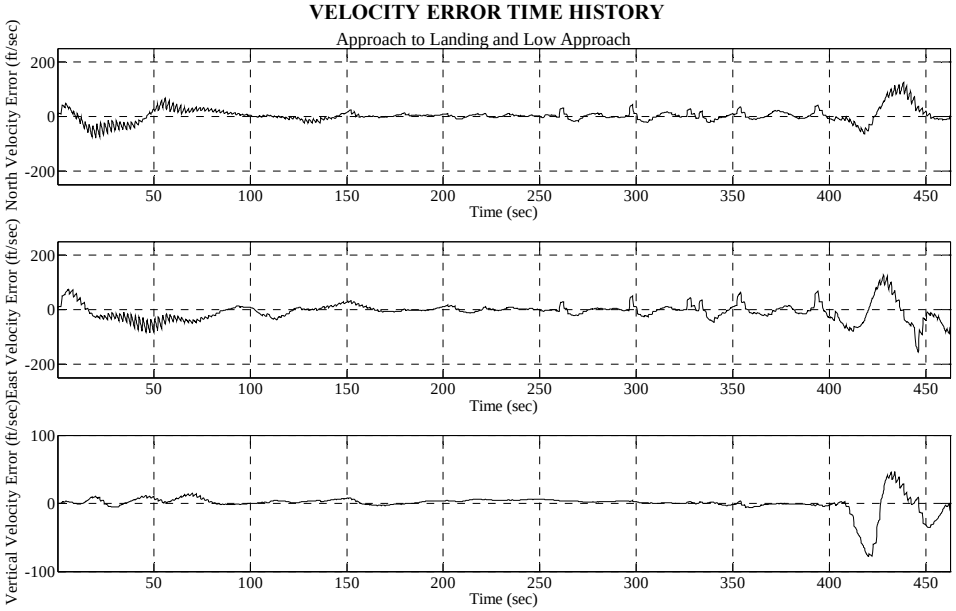

Test Point and Date: 084_17_Sep

WIND ERROR TIME HISTORY

Approach to Landing and Low Approach

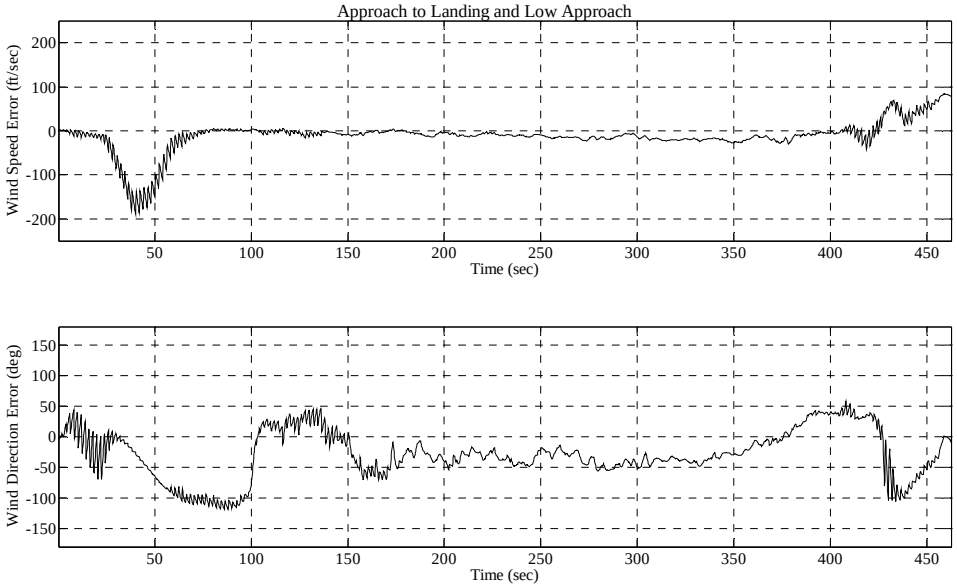

Test Point and Date: 084_17_Sep

POSITION ERROR TIME HISTORY

Approach to Landing and Low Approach

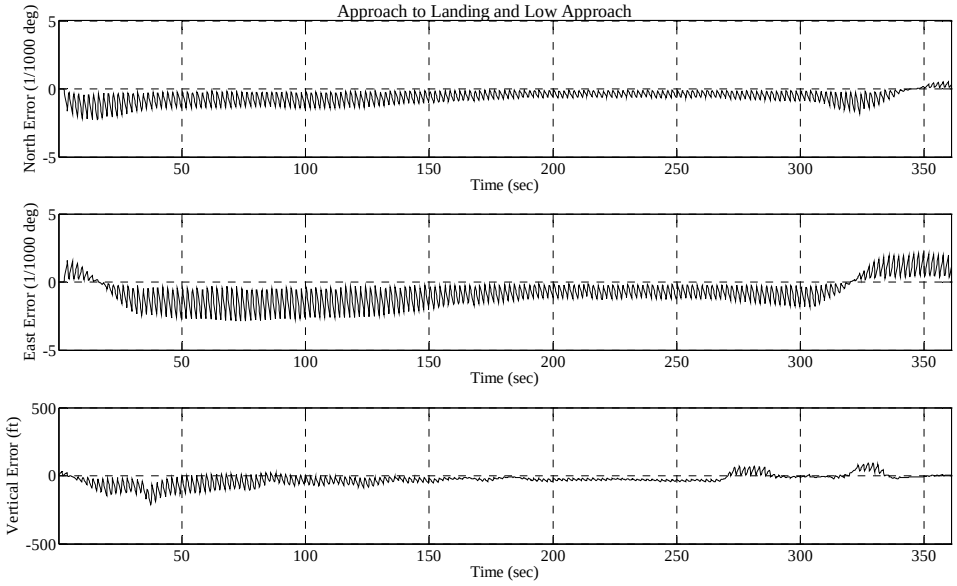

Test Point and Date: 085_18_Sep

VELOCITY ERROR TIME HISTORY

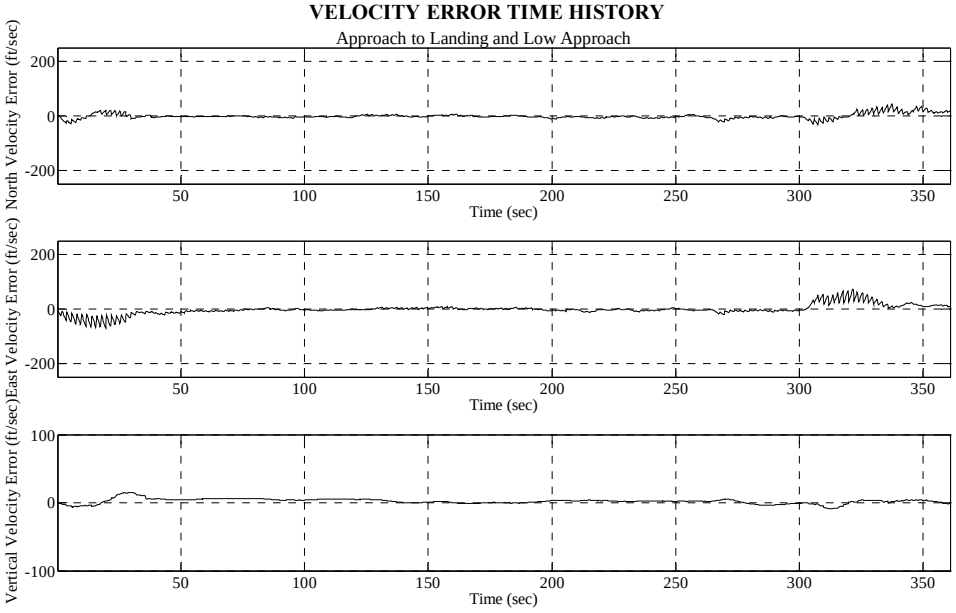

Test Point and Date: 085_18_Sep

WIND ERROR TIME HISTORY

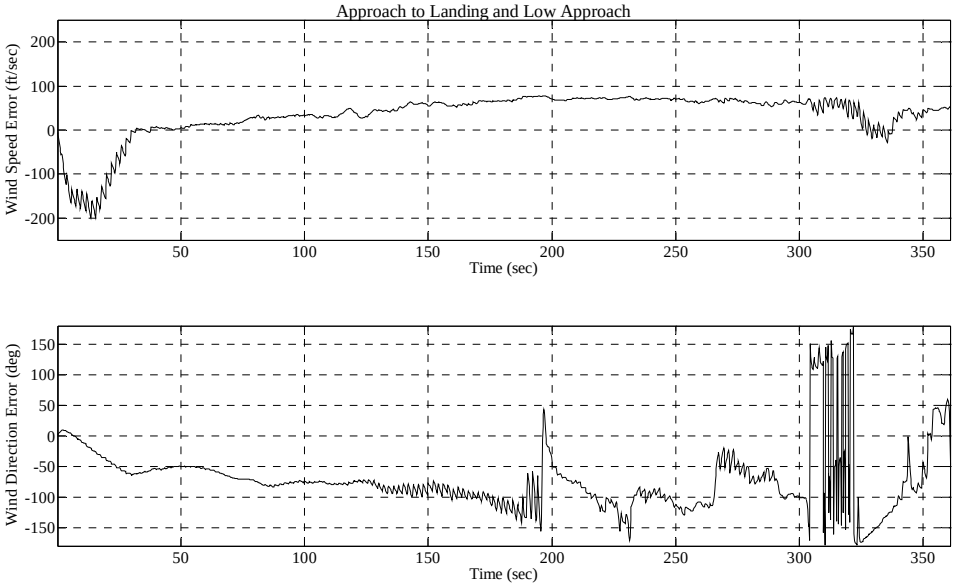

Test Point and Date: 085_18_Sep

POSITION ERROR TIME HISTORY

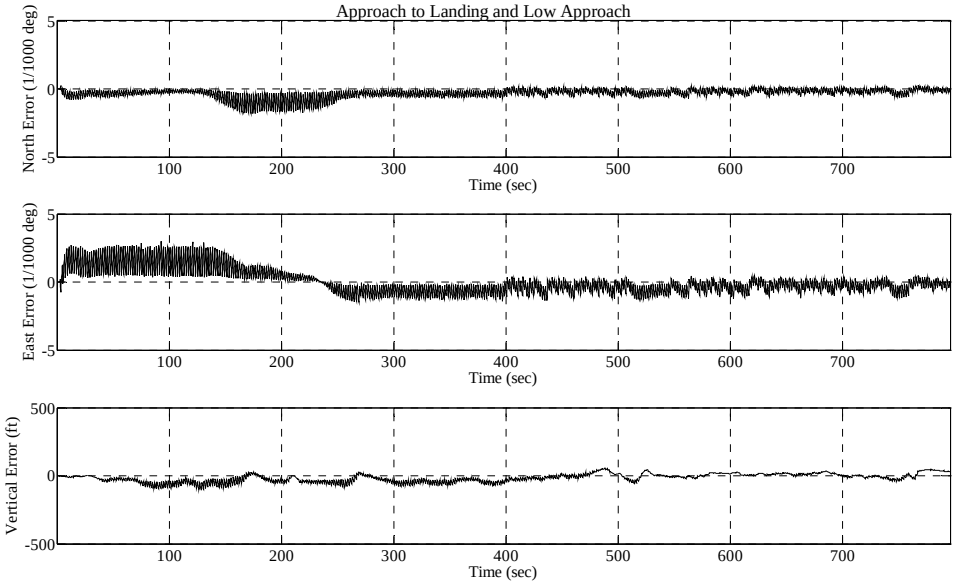

Test Point and Date: 086_19_Sep

VELOCITY ERROR TIME HISTORY

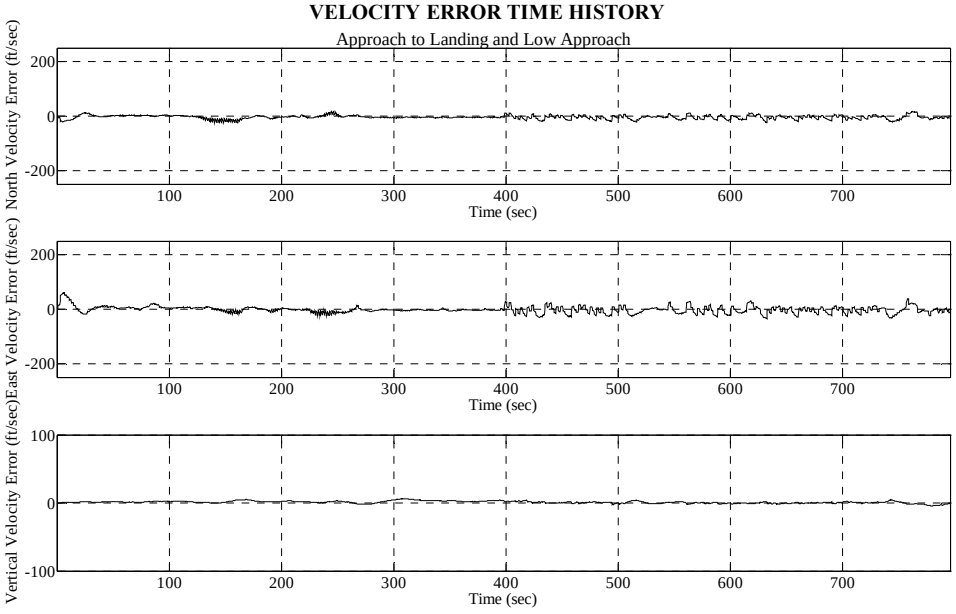

Test Point and Date: 086_19_Sep

WIND ERROR TIME HISTORY

Approach to Landing and Low Approach

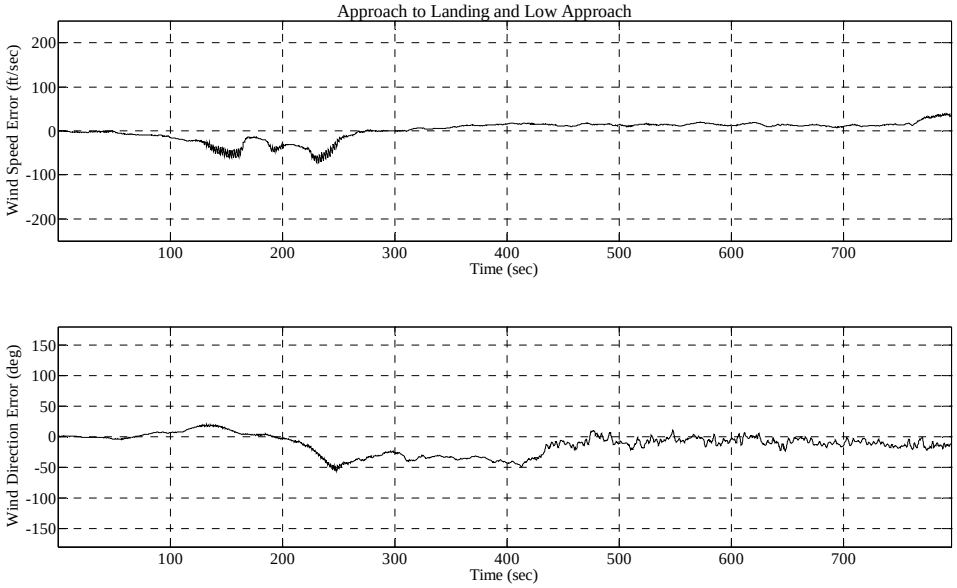

Test Point and Date: 086_19_Sep

POSITION ERROR TIME HISTORY

Approach to Landing and Low Approach

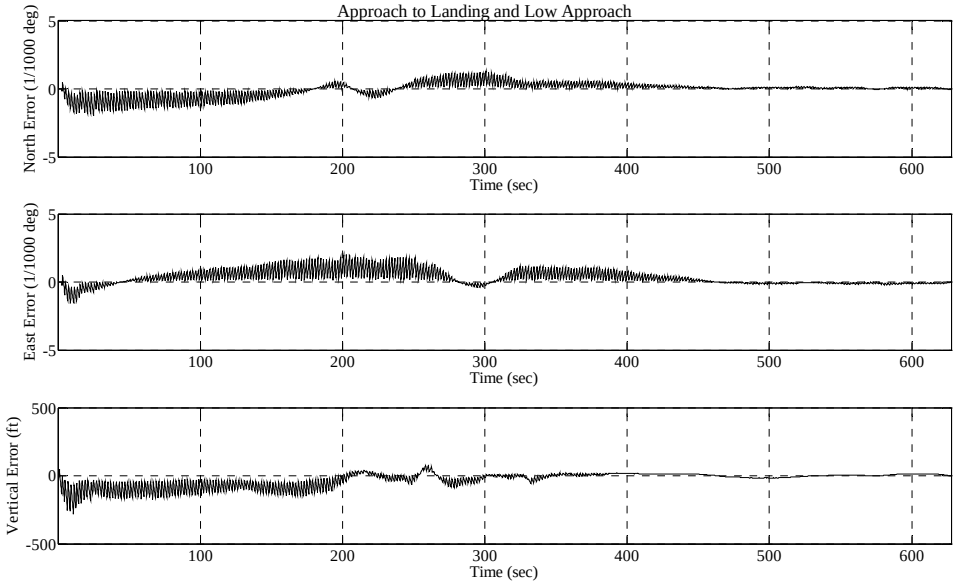

Test Point and Date: 087_21_Sep

VELOCITY ERROR TIME HISTORY

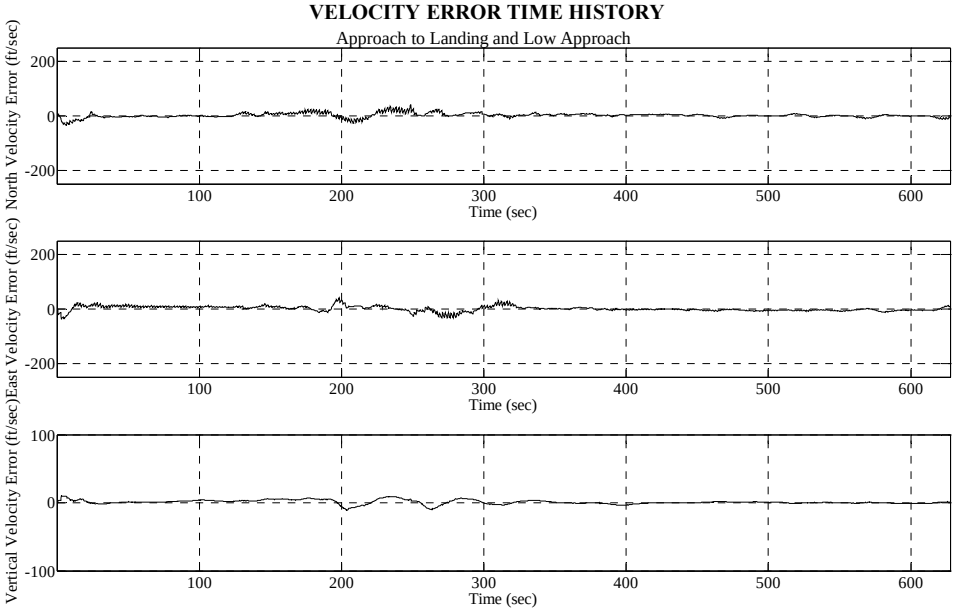

Test Point and Date: 087_21_Sep

WIND ERROR TIME HISTORY

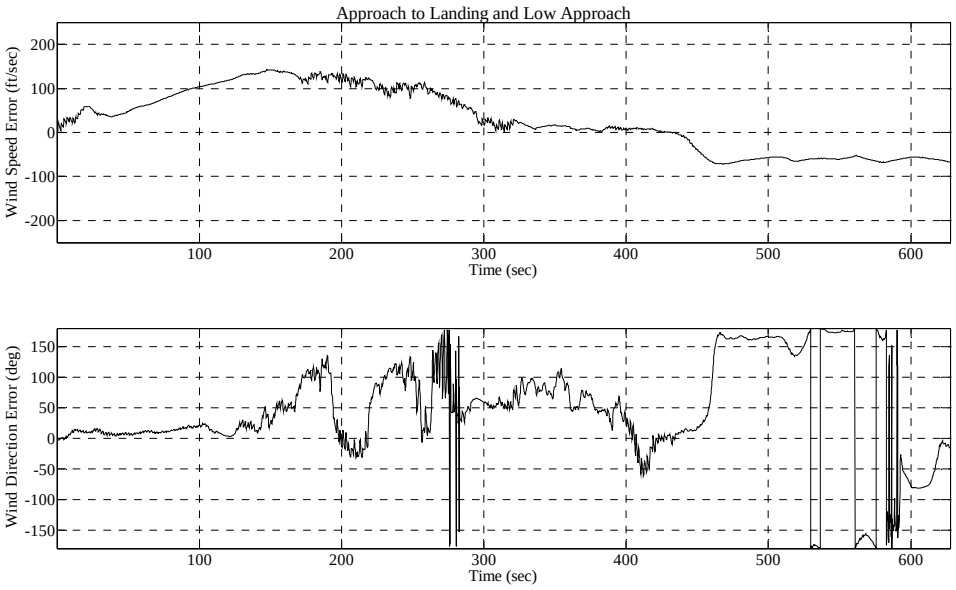

Test Point and Date: 087_21_Sep

Appendix H. Analog Pilot Rating Scales

Pilot Comment Analog Scales for Air-to-Air, Air-to-Ground and Air Refueling Tasks

Initial Delay in Pitch Response:

None — Gross Delay

Onset of Pitch Response:

Very Smooth — Too Abrupt

Sensitivity of Pitch Response:

Extremely — Extremely Sluggish

Tendency to initially o.s./u.s. pitch:

No — 2-3 deg — Overshoots (>5 deg)

Stabilize on new pitch att. Rapidly:

Very Easy — 2-3 O.S. — Overshoots (>5 O.S.)

Pilot Comment Analog Scales for Landing Task

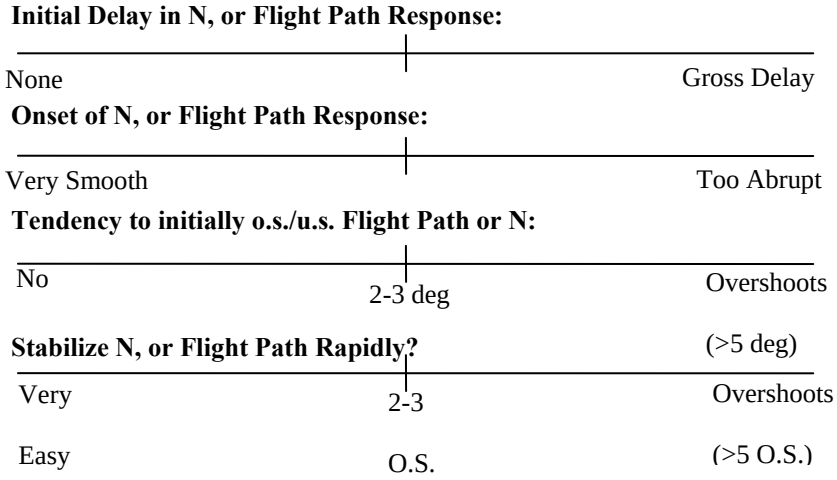

PIO Rating Scale

PIO RATING SCALE

Did I experience a PIO?

No

Did I experience undesirable motion?

No.....1

Yes

Did undesirable motion *tend to occur?* 2

Was undesirable motion *easily induced?* 3

Yes

While attempting maneuvers or tight control?

Was the PIO *bounded*?.....4

Was the PIO *divergent*? 5

While exercising normal control*?*.....6

REPORT DOCUMENTATION PAGE

Form Approved
OMB No. 074-0188

1. REPORT DATE *(DD-MM-YYYY)*	2. REPORT TYPE	3. DATES COVERED *(From – To)*
March 2008	Master's Thesis	September 2006 – March 2008

4. TITLE AND SUBTITLE

VELOCITY ESTIMATE FOLLOWING AIR DATA SYSTEM FAILURE

5a. CONTRACT NUMBER

5b. GRANT NUMBER

5c. PROGRAM ELEMENT NUMBER

6. AUTHOR(S)

McLaren, Scott A., Major, USAF

5d. PROJECT NUMBER

5e. TASK NUMBER

5f. WORK UNIT NUMBER

7. PERFORMING ORGANIZATION NAMES(S) AND ADDRESS(S)
Air Force Institute of Technology
Graduate School of Engineering and Management (AFIT/EN)
2950 Hobson Way, Building 640
WPAFB OH 45433-8865

8. PERFORMING ORGANIZATION REPORT NUMBER

AFIT/GAE/ENY/08-M21

9. SPONSORING/MONITORING AGENCY NAME(S) AND ADDRESS(ES)
Test Pilot School, ATTN: Mr. Aldrich, 220 South Wolfe Av., Edwards AFB CA 93524

10. SPONSOR/MONITOR'S ACRONYM(S)

11. SPONSOR/MONITOR'S REPORT NUMBER(S)

12. DISTRIBUTION/AVAILABILITY STATEMENT

APPROVED FOR PUBLIC RELEASE; DISTRIBUTION UNLIMITED.

13. SUPPLEMENTARY NOTES

14. ABSTRACT

The purpose of this research was to investigate a method of determining an aircraft's velocity in the event of total air data system failure. The process combined GPS aided inertial velocity with a continuously estimated wind velocity. A velocity estimator (VEST) algorithm was developed to combine the inertial and wind velocities to provide an estimate of the aircraft's current true velocity to be used for command path gain scheduling and for display in the cockpit. The culmination of this effort resulted in a flight test program as part of a Test Management Project at the United States Air Force Test Pilot School. The project consisted of two ground test and six flight test evaluation sorties. The average true airspeed from the estimator algorithm during in-flight maneuvers was determined to be 12 knots, non-divergent, and minimally variable. The research identified the potential of the algorithm to determine an aircraft's airspeed in the event of an air data system failure.

15. SUBJECT TERMS
Have VEST Velocity Estimation Calspan Variable Stability Learjet Learjet N101VS In-flight Simulator Flight Test Ground Test Gain Scheduling Air Data System Failure

16. SECURITY CLASSIFICATION OF:			17. LIMITATION OF ABSTRACT	18. NUMBER OF PAGES	19a. NAME OF RESPONSIBLE PERSON
a. REPORT	b. ABSTRACT	c. THIS PAGE			Paul A. Blue, Maj, USAF
U	U	U	UU	307	19b. TELEPHONE NUMBER *(Include area code)* (937) 255-6565, ext 4714 (paul.blue@afit.edu)